VNIVERSITAT DE VALÈNCIA

Departamento de Física Atómica, Molecular y Nuclear
Instituto de Física Corpuscular
Doctorado en Física

Development of a reconfigurable multi-plane Compton telescope for hadrontherapy dose monitoring

Tesis Doctoral

Enrique Muñoz Albaladejo

Directores:
Gabriela Llosá LLácer
Josep F. Oliver Guillén

Septiembre 2019

Declaración

Dra. Gabriela Llosá Llácer
Investigadora Ramón y Cajal, CSIC, y
Dr. Josep F. Oliver Guillén
Técnico Superior de Investigación de la Universidad de València

CERTIFICAN:

Que la presente memoria "**Development of a reconfigurable multi-plane Compton telescope for hadrontherapy dose monitoring**" ha sido realizada bajo su dirección en el Departamento de Física Atómica, Molecular y Nuclear de la Universidad de València por Don Enrique Muñoz Albaladejo y constituye su tesis para optar al grado de Doctor en Física. Y para que así conste, firman el presente certificado.

Dra. Gabriela Llosá Llácer **Dr. Josep F. Oliver Guillén**

Visto bueno del tutor,

Dr. Juan Zúñiga Román

València, Septiembre 2019

A mis queridos padres,
por dedicar a esta tesis, al menos,
tanto esfuerzo como yo.

Table of contents

List of figures

List of tables

List of abbreviations

ADC Analog-to-digital converter

APD Avalanche photodetector

ASIC Application-specific integrated circuit

CoR Cone of response

DAC Digital-to-analog converter

DAQ Data acquisition

DP-IVI Double proton interaction vertex imaging

EM Expectation maximization

ENVISION European novel imaging systems for ion therapy

FoV Field of view

FPGA Field programmable gate array

FWHM Full width at half maximum

GM-APD Geiger mode avalanche photodetector

HB Hybrid board

HZDR Helmholtz-Zentrum Dresden-Rossendorf

IFIC Instituto de Física Corpuscular

IVI Interaction vertex imaging

MACACO Medical applications compact Compton camera

ML Maximum likelihood

MLEM Maximum likelihood expectation maximization

MPPC Multi-pixel photon-counter

PDE Photon detection efficiency

PET Positron emission tomography

PG Prompt gamma

PGS Prompt gamma spectroscopy

PGT Prompt gamma timing

SiPM Silicon photomultiplier

SM System matrix

SOE Stochastic origin ensembles

SP-IVI Single proton interaction vertex imaging

SPECT Single photon emission computed tomography

TSV Through silicon via

UDP User datagram protocol

Preamble and outline

The present manuscript contains the main results obtained during the course of my thesis. The work reported here has been carried out in the IRIS (Image Reconstruction, Instrumentation and Simulations for medical imaging applications) group, in the context of the MACACO (Medical Applications CompAct COmpton camera) project, aimed at the design and construction of a Compton telescope for real time monitoring of treatment delivery in hadrontherapy; this project already existed before my incorporation to the research group, and its development continues beyond my thesis. In particular, it should be mentioned that a fully functional version of the experimental prototype had already been built before the beginning of this work, which has been upgraded during my thesis. The experimental prototypes enabled the extraction of the experimental data and, thus, the realization of the different studies reported in this work. My contributions to the MACACO project can be classified in two main aspects: the performance evaluation of the first experimental device and the development of the reconstruction software employed to obtain images from the measurements.

The thesis is divided in six chapters. The first chapter introduces hadrontherapy and provides a short overview of the physical background necessary to understand the functioning of the experimental device. The second chapter is dedicated to explaining the principles of Compton imaging. The third chapter describes in detail our experimental device and the different generations of detectors employed throughout the thesis. Chapter four presents the performance evaluation tests carried out with different configurations of the experimental prototype, and shows the results obtained from measurements with sources of energies in the range between 511 keV and 4.439 MeV. The last two chapters report the software developments achieved during my thesis. Chapter five is used to derive a complete physical model for the detection of an event in a two-plane Compton camera produced by a photon of known initial energy. The model is employed to obtain an expression for the system and sensitivity matrices used in image reconstruction. Special emphasis is given to the impact of the sensitivity matrix in the final images, which is assessed through image reconstruction of several sources with different distributions of activity. In chapter six, the physical model

presented in chapter five is extended to sources of unknown initial energy. The model is employed to implement a spectral reconstruction code to reconstruct simultaneously the spatial distribution and the spectral emission of the source, which is later evaluated through reconstruction of a variety of sources. Finally, the thesis finishes with a short summary and the general conclusions.

Chapter 1

Introduction

1.1 Hadrontherapy

1.1.1 General principles

Radiation therapy plays an essential role in cancer treatments. It is applied to more than 50% of patients with localized malignant tumors, being the most frequent and successful form of therapy after surgery [75]. In addition to conventional radiotherapy with X-rays, ion beam therapy or hadrontherapy was first proposed by Wilson in 1946 [104]. Today there are more than 80 active hadrontherapy treatment centers and, per end of 2018, more than 220,000 patients have been treated worldwide with hadrontherapy, from which about 86% have been treated with protons and 13% with carbon ions [66].

Hadrontherapy is a cancer treatment technique that consists in the irradiation of tumors with light ions. The useful therapeutic properties of employing light ions arise from their energy deposition profile when travelling through matter. Considering the Coulomb interactions as the main mechanism of energy loss, the Bethe-Bloch formula [11, 13] describes the stopping power (S) of heavy charged particles in a medium:

$$S \equiv -\left\langle \frac{dE}{dx} \right\rangle = \frac{4\pi n_e z^2}{m_e c^2 \beta^2} \left(\frac{e^2}{4\pi\varepsilon_0} \right)^2 \left[\log\left(\frac{2m_e c^2 \beta^2}{I(1-\beta^2)} \right) - \beta^2 \right], \tag{1.1}$$

where c is the speed of light, ε_0 is the vacuum permittivity, m_e and e are the mass and charge of the electron, n_e and I are the material electron density and mean excitation potential, z is the particle charge (in multiples of e) and β is the particle velocity (as a fraction of c).

Equation 1.1 allows the computation of the energy deposition profile of heavy charged particles inside a material. Figure 1.1 represents a plot of equation 1.1 for proton beams with different initial energies impinging on a water target. As can be seen in the plot, the energy

deposition of heavy charged particles when traversing a medium slowly increases as they penetrate deeper along their path. Most of the particle energy is lost at the end of the beam range, producing a steep peak just before the point where they are finally absorbed, known as the *Bragg peak*. The *range* of a charged particle of initial energy E_0 is defined as the distance beyond which no such particles can penetrate, and it depends on the beam energy and the target composition. Beyond this point, the beam is completely stopped and there is no direct transfer of energy to the target. For an initially monoenergetic beam, statistical fluctuations in the energy deposition processes lead to a broadening of the particle energies (*energy straggling*) that in turn causes the beam stopping point not to be completely sharp.

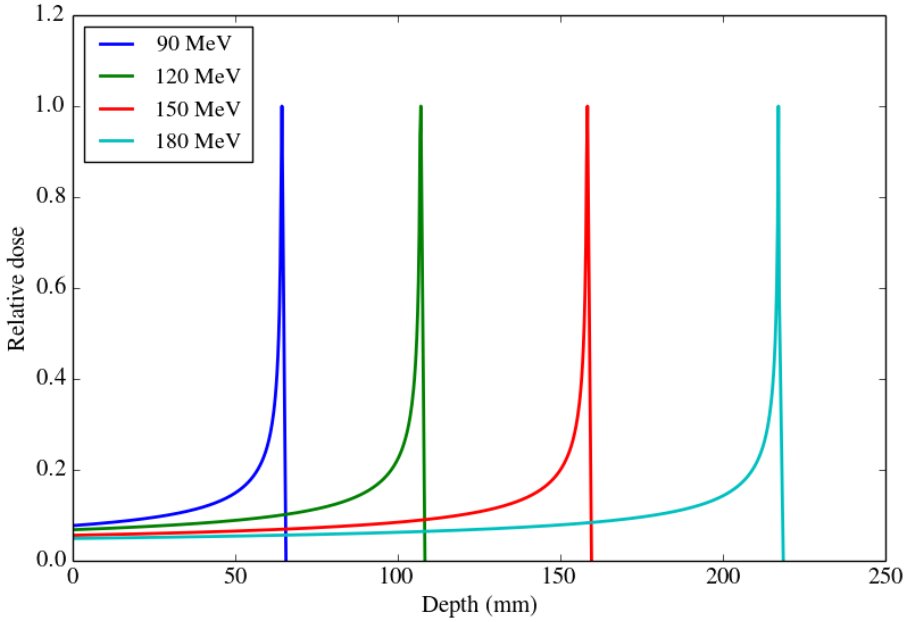

Figure 1.1 Energy deposition profile of proton beams with different initial energies impinging on a water target.

The Bragg peak is the key feature that makes hadrontherapy such an interesting option for patient treatment in some clinical scenarios. As the majority of the energy deposited by the beam is concentrated at the end of its range, the dose delivery can be focalized in the tumor region, with minimal damage to the tissue along the beam path and preserving the organs beyond the particle range. In contrast, the dose delivered in conventional radiotherapy treatments with X-rays can be neither so precisely concentrated nor completely stopped. Due to the physical processes that govern the interactions of photons and matter (see section 1.2), X-rays are either completely absorbed or scattered away from the beam direction. This results

in a beam with progressively diminishing intensity and a maximal energy deposition near the entrance surface.

Despite the advantageous dose deposition profile that the Bragg peak represents, there are also several aspects that constrain the wider application of hadrontherapy. One controversial topic is the question whether there is enough conclusive evidence about the clinical superiority of hadrontherapy with respect to photon radiotherapy to justify this substantially more expensive treatment. This has been (and still is) subject to debate [79], and, although the acquired evidence points towards higher patient survivability [28] and reduced side effects [81] for some kinds of cancers, long-term clinical studies are still necessary [55]. An important limiting factor of the therapy is the beam range uncertainty [34]. This uncertainty can be due to various aspects: biological changes during treatment, organs motion, energy straggling, etc. In order to prevent the range uncertainty from causing damage outside the tumor region, treatment plans are designed with large safety margins. If these margins could be reduced with no risk to the patients, the advantageous features of hadrontherapy could be exploited more efficiently. To that end, a real-time monitoring system for dose delivery would be highly beneficial, as it would allow for online assessment of any deviation from the treatment plan.

1.1.2 Beam monitoring

As discussed in the previous section, in hadrontherapy the beam particles are fully stopped and absorbed in the patient's body. Therefore, treatment monitoring systems cannot employ the beam particles directly, and they must rely on indirect measurements instead. A possible approach is to detect the secondary radiations issued from nuclear reactions between beam and target nuclei. Nuclear reactions occur along the particle path until close to the Bragg peak region, so the secondary radiation is correlated to the beam range [38]. There are three main secondary by-products of the nuclear interactions that can be used for dose monitoring: secondary protons, positrons and *prompt gammas*.

The use of secondary protons for monitoring purposes can be achieved through the so called *interaction vertex imaging* (IVI) technique [25]. It is based on the detection of secondary protons to reconstruct their nuclear emission vertices, which can provide information about the ion range by comparing the distributions of the vertices calculated in the treatment plan and those measured during irradiation. In [25], two detection techniques are considered: single-proton detection (SP-IVI) and double-proton detection (DP-IVI). In SP-IVI, one forward-located tracker is used to detect single protons in time coincidence with the incoming beam, measured with a hodoscope. In DP-IVI, two protons need to be detected in time coincidence by different trackers, so the beam hodoscope is not required.

Positrons emitters, most abundantly ^{11}C, ^{15}O and ^{13}N [93], are produced within the patient body. The emitted positrons are subsequently annihilated with an electron from the surrounding tissue, producing two anti-parallel 511 keV gammas that can be imaged employing conventional Positron Emission Tomography (PET). Depending on whether the PET scan is performed during or after irradiation, we can speak of *in-beam* or *off-line* PET. On the one hand, in-beam PET is considered as an attractive option because it provides better statistics (since both long and short-lived positron emitters contribute), it is less affected by biological washout and yields the fastest feedback on treatment monitoring [15]. On the other hand, the integration of the PET scanner and the beam line is technically demanding, mainly due to the geometrical constrains imposed by the mobility required for both the beam delivery system and the patient positioning [107]. In addition, a high background of prompt radiations during beam delivery is present during irradiation, so PET recordings must be performed between beam-pulse delivery periods [38]. The main advantage of off-line PET is the possibility of using full-ring conventional PET scanners, whereas the metabolic washout and decrease of positron activity taking place during patient transportation pose its major drawbacks. In the modality known as *in-room* PET, the PET scanner is placed in the delivery room, but it is not integrated with the beam line, which also allows employing conventional scanners. Comparison studies between in-beam and offline PET may be found in [62, 107, 93].

Regarding prompt gammas (PG), they are photons generated when the nuclei that interact with the beam particles are de-excited. The PG spectrum is a quasi-continuous distribution up to a few tens of MeV, and shows prominent lines from the nuclear reactions with highest probability. The emission spectrum depends on the composition of the irradiated material. In human tissues, the most important lines are found at 4.44 MeV, coming from the de-excitation of ^{12}C, and at 6.13 MeV, produced by ^{16}O. Figure 1.2 shows the region between 2 and 7.5 MeV of the PG spectrum [101], obtained from the irradiation of a water target with a proton beam, where the nuclei responsible for the different lines are indicated. The PG production distribution is closely correlated to the absorbed dose and their emission takes place within ns of irradiation [53, 97], so it is not affected by metabolic washout.

Several methods are under investigation for ion beam therapy dose monitoring through the detection of PG distributions:

- *Mechanical collimation*: this modality aims at imaging the PG distribution by restricting the acceptance detection angles with a collimator, which also shields the detector from unwanted particles. Depending on the geometry of the collimator, these systems are known as *pinhole* [80, 31], *multislit* [54, 64] or *knife edge* [89] cameras.

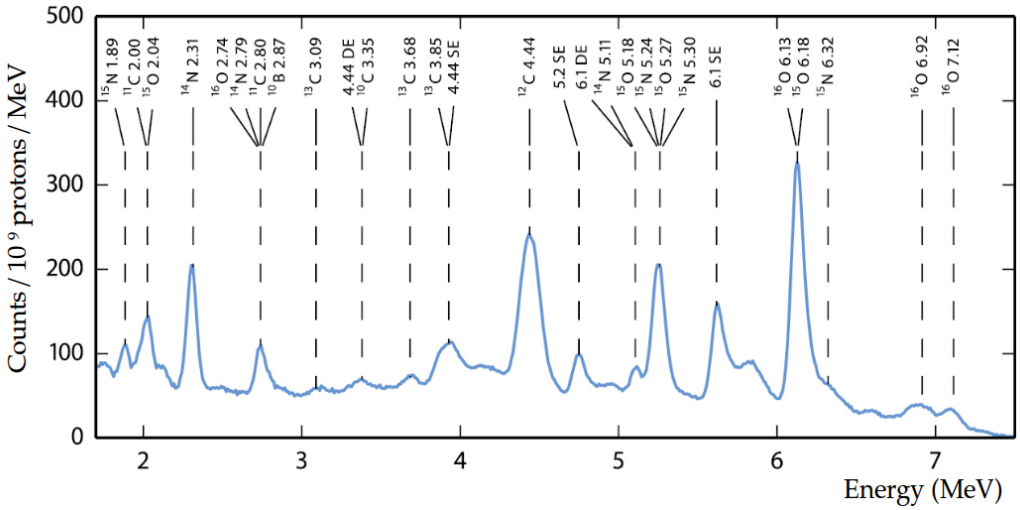

Figure 1.2 Prompt gamma energy spectrum measured from a water target irradiated with a proton beam. Extracted from [101].

- *Prompt-Gamma Timing (PGT)*: this technique exploits the correlation between the particle range and its transit time. Range variations are reflected in the time of flight spectra obtained by measuring the time difference between the beam entrance in the target and the detection of PG, and shifts of 2 mm are expected to be detectable [22].
- *Prompt-Gamma Spectroscopy (PGS)*: this method is based on the identification of characteristic PG spectral lines and their relative contributions. The correlation of the measured spectrum with models of proton-nuclear interactions allowed attainment of the range of proton beams in [101].
- *Compton cameras*: these systems use Compton kinematics to reconstruct the spatial distribution of a gamma source. Their operation principle is based on the measurement of a Compton scattering followed by a subsequent interaction from the scattered gamma, which provides directional information about the incident photon. In hadrontherapy, Compton cameras can be used to detect the emitted PG and reconstruct the distribution map of their production. Since this modality was chosen for this work, Compton imaging is described in detail in chapter 2.

1.2 Interactions of gamma-rays with matter

When a beam of photons travels through matter, there are different processes through which they can interact. These interactions result in the removal of photons from the original beam

direction, either by scattering or by full absorption of individual photons. The most relevant processes involved in radiation measurements are:

- Coherent scattering: in this process, also known as Rayleigh scattering, a photon interacts with an absorber atom coherently, stimulating the dipole emission of a photon with the same phase and energy as the initial photon. Although virtually no energy is lost in the interaction, the direction of the photon can be altered. This process is only significant at low energies, being of particular importance in the optical region, and its role for energies beyond X-rays can often be neglected. Since the gamma energies studied in this work are well above that region, this process will not be considered hereafter.

- Photoelectric absorption: the incoming photon is fully absorbed by a single electron in the inner atomic shells. Since the electron is energetically bound to the atom, this process is only allowed for photon energies E_γ greater than the binding energy, E_b, of the interacting electron. As a consequence of the interaction, the photoelectron escapes the atom with a kinetic energy $T_e = E_\gamma - E_b$, leaving a vacancy in its shell that is subsequently filled by an upper shell electron. In this process, the released energy results in the additional emission of either the characteristic X-rays or Auger electrons. The probability of the photoelectric process depends highly on the atomic number Z of the material and the photon energy. No single expression is valid for all ranges of energies and atomic numbers, but for the most widely used detector materials the photoelectric cross section is proportional to $\sigma^{ph} \propto Z^{[4-5]} E_\gamma^{-3.5}$, which indicates that the probability of the photoelectric interaction drops steeply as energy increases.

- Compton scattering: an incident photon transfers part of its energy to an electron. As a result, the electron is stripped from its atom and a scattering photon is produced at an angle θ from the original direction of propagation and with a lower energy. The energy transferred to the recoil electron and the scattered photon is directly related to the scattering angle. The Compton cross section increases linearly with the material atomic number, $\sigma^C \propto Z$. Since the Compton interaction is the process upon which the operating principle of Compton cameras is based, it will be described in more detail in section 1.2.1.

- Pair production: when the incident gamma energy is higher than the combined mass of a particle-antiparticle pair, it is possible that such a pair is produced. The threshold for e^+e^- pair production is 1.022 MeV, which corresponds to twice the mass of the electron. As a result of the interaction, the two particles are produced with the same

kinetic energy $T = \frac{1}{2}(E_\gamma - 2m_e c^2)$. After the e^+ loses all of its energy through multiple interactions, it is annihilated and two anti-parallel 511 keV photons are generated. Once this process takes place in a detector, each of these photons can either be absorbed or escape the detector material. If both photons are absorbed, the total energy deposited in the detector is equal to the initial E_γ; if one or both photons escape, the total energy measured will be $E_\gamma - m_e c^2$ or $E_\gamma - 2m_e c^2$, respectively. These energies correspond to the characteristic single escape and double escape peaks in the measured spectrum (see Figure 1.7 in section 1.3). The cross section for this interaction is proportional to $\sigma^{pp} \propto Z^2 \log E_\gamma$. Although the pair production process is permitted from the mentioned threshold, it is not until until energies above several MeV that it begins to dominate.

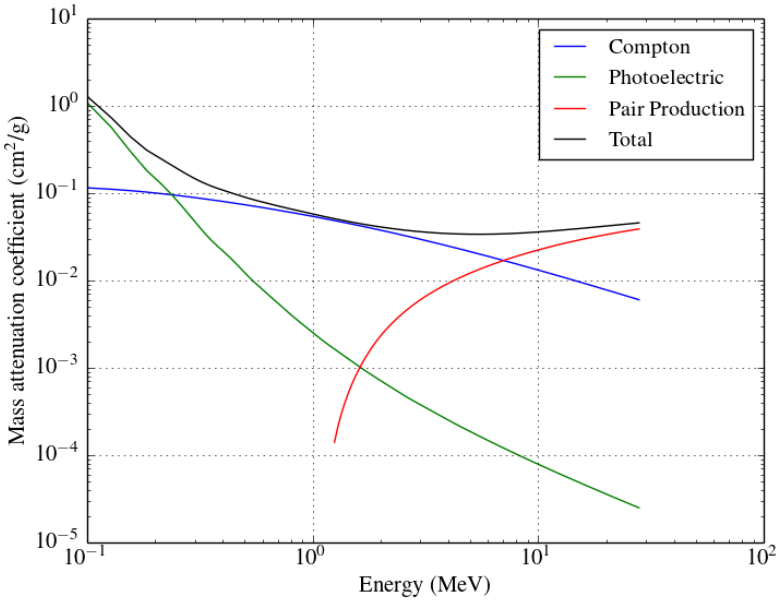

Figure 1.3 Mass attenuation coefficients of the different interactions in $LaBr_3$ [10].

The total probability of interaction is defined by the total photon cross section, which is given by the sum of the previous cross sections

$$\sigma^{tot} = \sigma^{ph} + \sigma^{C} + \sigma^{pp}. \tag{1.2}$$

An important quantity to characterize the penetration and diffusion of gamma radiation in matter, directly related to the photon total cross section, is the linear attenuation coefficient μ, with dimensions of inverse length. If we consider a collimated, monoenergetic gamma beam of initial intensity I_0 traversing an extended medium, the μ of the material determines

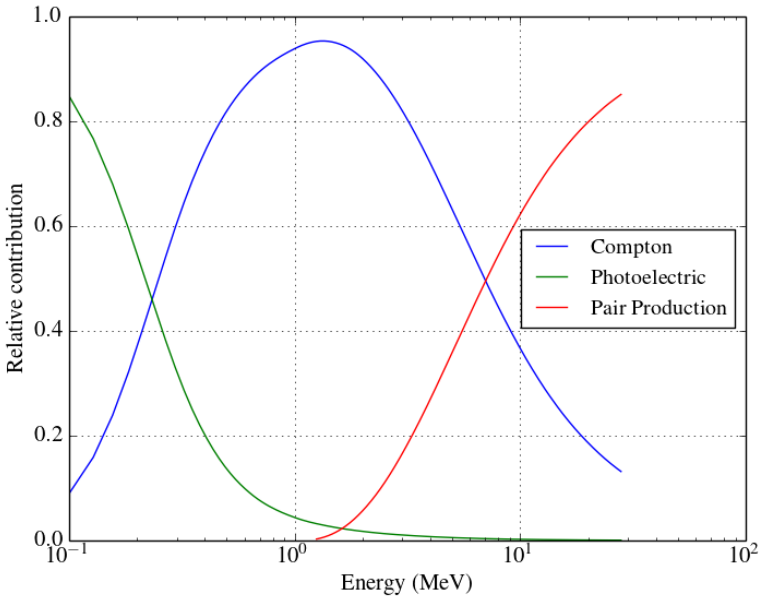

Figure 1.4 Relative contributions to the total mass attenuation coefficient in $LaBr_3$ [10].

the intensity I after the beam travels a distance ℓ:

$$I(\ell) = I_0 e^{-\mu\ell}. \tag{1.3}$$

The material distance ℓ in which the the beam intensity is reduced by a factor e is called the mean free path, $\lambda = \mu^{-1}$, also defined as the average distance travelled by a gamma in the medium. Since the linear attenuation coefficient is proportional to the density ρ of the material, which to some extent depends on its physical state, it is convenient to remove this dependency by defining the mass attenuation coefficient as μ/ρ. The mass attenuation coefficient is proportional to the atomic cross section as:

$$\frac{\mu}{\rho} = \sigma \frac{N_A}{M}, \tag{1.4}$$

where N_A is Avogadro's number and M is the atomic mass of the material. The mass attenuation coefficients in $LaBr_3$ (which is the scintillator crystal employed in our system, see section 1.3.1) for the different physical processes are plotted in Figure 1.3, where the changing tendency with increasing gamma energy can be appreciated. Figure 1.4 shows the relative contribution of each interaction to the total coefficient, showing that each of them is dominant at a different energy range.

1.2.1 Physics of the Compton interaction

When a photon (γ) and an (initially at rest) electron (e) interact via Compton effect, the energies of the scattered photon (γ') and the recoil electron (e') are uniquely determined by the initial photon energy and the scattering angle. A diagram of the particles and angles involved in the interaction is represented in Figure 1.5.

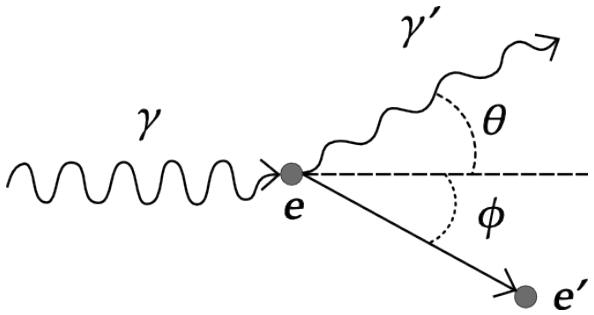

Figure 1.5 Diagram of the Compton interaction.

In order to derive an expression for the scattering angle θ, let us employ the relativistic formalism of four-vectors. Considering an electron initially at rest, the energy-momenta of the particles before and after the interaction are

$$p_\gamma = \left(E_\gamma, \vec{p}_\gamma\right) \; ; \quad p_e = \left(m_e, \vec{0}\right) \quad \rightarrow \quad p'_\gamma = \left(E'_\gamma, \vec{p}_\gamma{}'\right) \; ; \quad p'_e = \left(E'_e, \vec{p}_e{}'\right) \; ,$$

where $\vec{p}$ is the relativistic three-momentum, m_e is the electron mass and the convention $c \equiv 1$ is followed for simplicity. By conservation of the energy-momentum before and after the interaction, one obtains the following relation:

$$\begin{aligned} p_\gamma + p_e &= p'_\gamma + p'_e \\ \left(p_\gamma - p'_\gamma\right)^2 &= \left(p_e - p'_e\right)^2 \\ p_\gamma^2 + p_\gamma'^2 - 2p_\gamma p'_\gamma &= p_e^2 + p_e'^2 - 2p_e p'_e. \end{aligned}$$

Employing the relation $E^2 = m^2 + |\vec{p}|^2$, the scalar product in the Minkowski space yields $p^2 = E^2 - |\vec{p}|^2 = m^2$. This result implies that $p_\gamma^2 = p_\gamma'^2 = 0$ and $p_e^2 = p_e'^2 = m_e^2$. After this modification:

$$\begin{aligned} E_\gamma E'_\gamma - |\vec{p}_\gamma||\vec{p}_\gamma{}'|\cos\theta &= p_e p'_e - m_e^2 \\ E_\gamma E'_\gamma(1 - \cos\theta) &= m_e(E'_e - m_e). \end{aligned}$$

Finally, by conservation of energy, $E_\gamma + m_e = E'_\gamma + E'_e$, we can obtain the well known Compton scattering formula:

$$(1-\cos\theta) = m_e \frac{E_\gamma - E'_\gamma}{E_\gamma E'_\gamma}$$

$$\cos\theta = 1 - m_e\left(\frac{1}{E'_\gamma} - \frac{1}{E_\gamma}\right). \tag{1.5}$$

The recoil electron angle, ϕ, can also be derived from the conservation of the three-momentum. Requiring that the momentum is equal to $|\vec{p}_\gamma|$ in the direction of the incident photon and 0 in the perpendicular direction:

$$\left.\begin{array}{l} E'_\gamma\cos\theta + |\vec{p'_e}|\cos\phi = E_\gamma \\ E'_\gamma\sin\theta - |\vec{p'_e}|\sin\phi = 0 \end{array}\right\} \quad tan\phi = \frac{\sin\theta}{\frac{E_\gamma}{E'_\gamma} - \cos\theta}$$

From equation 1.5, $\frac{E_\gamma}{E'_\gamma} = 1 + \frac{E_\gamma}{m_e}(1-\cos\theta)$, which allows to obtain an expression for the recoil electron angle as a function of the initial gamma energy and the scattering angle:

$$tan\phi = \frac{1}{1+\frac{E_\gamma}{m_e}}\frac{\sin\theta}{1-\cos\theta}. \tag{1.6}$$

In the detection of Compton interactions, it is usually the kinetic energy transferred to the electron, T'_e, what can be measured by the detector. For that reason, it is often convenient to rewrite the Compton scatter formula in terms of T'_e or, equivalently, the energy lost by the incident gamma, $\tilde{E}_\gamma = E_\gamma - E'_\gamma$, so that equation 1.5 is expressed as

$$\cos\theta = 1 - \frac{m_e\tilde{E}_\gamma}{E_\gamma(E_\gamma - \tilde{E}_\gamma)}. \tag{1.7}$$

From equation 1.7 it is easy to see that the lower limit $\theta = 0$ corresponds to no energy lost ($\tilde{E}_\gamma = 0$), i.e no interaction. On the other hand, the maximum energy lost by the gamma is given by the upper limit $\theta = \pi$, for which $\tilde{E}_\gamma = \frac{E_\gamma}{1+m_e/(2E_\gamma)}$. Since all scattering angles between $[0,\pi]$ are possible, the measured spectrum of a monoenergetic gamma source presents a continuous distribution of deposited energies, usually referred to as the Compton continuum. The maximum transferable energy gives rise to a characteristic feature in the measured spectrum, known as the Compton edge (see Figure 1.7 in section 1.3).

So far, it has been proved that the energy transferred from the initial gamma is uniquely determined by the Compton scattering angle, although nothing has been said about which

scattering angles are more likely. The angular probability distribution of the scattered photons is given by the Klein-Nishina [33] formula for the Compton differential cross section:

$$\frac{d\sigma}{d\Omega}(E_\gamma,\theta) = \frac{\alpha^2 r_c^2}{2} P(E_\gamma,\theta)^2 [P(E_\gamma,\theta) + P(E_\gamma,\theta)^{-1} - \sin^2(\theta)] \tag{1.8}$$

$$P(E_\gamma,\theta) \equiv \frac{E'_\gamma}{E_\gamma} = \frac{1}{1+\frac{E_\gamma}{m_e}(1-\cos\theta)}, \tag{1.9}$$

where α is the fine structure constant and $r_c = \frac{2\pi}{m_e}$ is the electron Compton wavelength. The total Compton cross section can be obtained after integration over the whole solid angle, which yields:

$$\sigma(E_\gamma) = \frac{\pi\alpha^2 r_c^2}{\varepsilon^3}\left[\frac{2\varepsilon[2+\varepsilon(1+\varepsilon)(8+\varepsilon)]}{(1+2\varepsilon)^2} + [\varepsilon(\varepsilon-2)-2]\log(1+2\varepsilon)\right], \tag{1.10}$$

where $\varepsilon \equiv \frac{E_\gamma}{m_e}$.

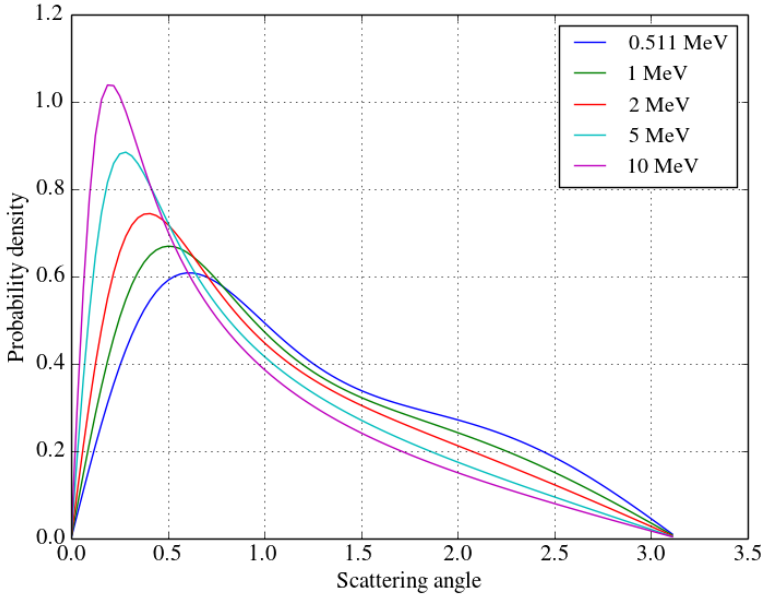

Figure 1.6 Probability density distributions of Compton scattering angles.

In order to represent the likelihood of an incident gamma (with energy E_γ) to be scattered with an angle θ, it is convenient to define de probability density function $f(\theta, E_\gamma) = \frac{2\pi}{\sigma}\frac{d\sigma}{d\Omega}\sin\theta$, which satisfies the normalization condition $\int_0^\pi f(\theta, E_\gamma)d\theta = 1$ for all energies. This function is represented in Figure1.6, where it can be appreciated that the maximum probability shifts

towards smaller scattering angles (or forward scattering) for higher energies. One can also notice that for low energy photons the probability of being scattered with angles greater than $\pi/2$ (backscatter) is significant, whereas this contribution is substantially lower for higher energies.

1.3 Detectors for medical imaging

Radiation detectors rely in general on the transformation of the energy deposited by the incident particle into an electrical signal. The existing detector technologies achieve this transformation through different means. In the case of semiconductor detectors and ion gas chambers, the detector active volume is ionized by the particle interacting in it and free charge carriers are generated. The charge must then be collected to generate the basic electrical signal. In the case of scintillator crystals, the interaction of an incident particle produces optical photons, which need to be measured by a photodetector coupled to the crystal in order to generate the electrical signal.

An important feature of the detector performance is its energy response function. The measured energy is proportional to the collected charge, arising from the total number of carriers generated, which in turn is proportional to the energy deposited in the detector. Since the amount of carriers is discrete, their number is subject to statistical fluctuations for different measured events, even if the deposited energy is the same. These statistical fluctuations, together with other factors (such as small changes in the detector parameters during the measurement or noise in the electronics), determine the energy resolution of the system. The energy resolution of a detector is conventionally defined as the full width half maximum (FWHM) of an energy peak over its center, $R = \frac{FWHM}{E_0}$. Considering the peak as a Gaussian function, the FWHM is related to the width of the distribution as FWHM = 2.35σ. The dimensionless energy resolution is usually expressed as a percentage at a certain energy. A spectrum of a monoenergetic source emitting gammas of energy E_γ (above the pair production threshold) measured by a detector with an arbitrary energy resolution is depicted in Figure 1.7.

In order to obtain an image employing high energy gamma radiation, the emitted photons must be measured and their trajectories reconstructed. For that purpose, the detector system must meet different requirements depending on the imaging modality, but mainly the following conditions must be fulfilled:

- High detection efficiency, so that a high fraction of the photons that reach the detector are measured. This allows to accumulate the necessary statistics for the required image quality. A high detection efficiency may lead to a reduced patient exposure to radiation.

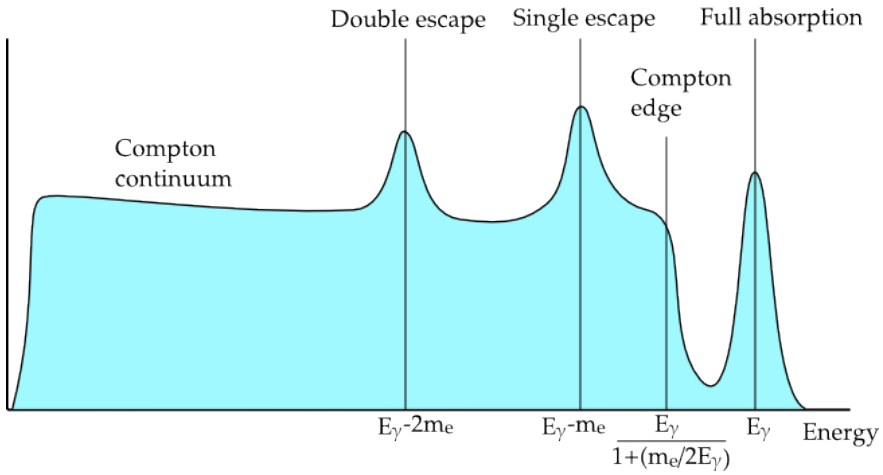

Figure 1.7 Generic measured spectrum of a source emitting photons of energy E_γ above the pair production threshold.

- Good spatial resolution, which translates into the determination of the gammas interaction positions inside the detector with reduced uncertainty and, therefore, into more precise final images.
- Fast time response for detectors operating in time coincidence, so that the time window can be narrowed to reduce random coincidences.
- Good energy resolution to measure the amount of energy deposited by the gammas in the detected interaction. This parameter is of particular importance in Compton imaging, since uncertainty in the energy deposition directly translates into the uncertainty in the determination of the scattering angle, needed to reconstruct the gamma origin.

Scintillator crystals are the most widely used radiation detectors in medical applications, due to their simple operation at room temperature and good performance at a moderate price. Since the prototype being developed in our research group employs scintillator crystals coupled to silicon photomultipliers, the following sections are dedicated to introducing their physical principles.

1.3.1 Scintillator crystals

The scintillation process occurs when external ionizing radiation deposits energy in the material, inducing the jump of electrons to excited states, which are de-excited through the emission of photons after a short time. In scintillator crystals, this process can be understood by considering the energy band structure of the different allowed states, represented in Figure 1.8. In a regular crystal lattice, the electrons in the lower energy discrete states of

the *valence* band are bound to the lattice, whereas those in the *conduction* band can move throughout the material. In between those bands, there is a forbidden energy space known as the *band gap*, where electrons can never be found in the pure crystal.

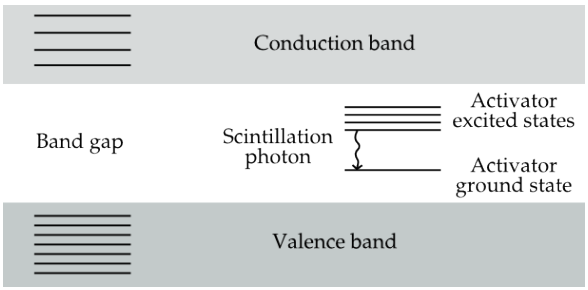

Figure 1.8 Diagram of a scintillator crystal band structure.

An electron can travel from the valence to the conduction band if it is transferred enough energy from an external particle to overcome the band gap. The posterior de-excitation to a valence band state could take place through the emission of a photon with the energy difference. Since it corresponds precisely to the transition energy between two sates, it has a high probability of being reabsorbed by another electron from the valence band, meaning that the pure crystal is not transparent to its own scintillation light. Furthermore, the band gap energy is such that the emitted photon usually lies in the ultraviolet or soft X-ray region for common lattices, while photomultiplier detectors achieve their peak performance in the visible range.

The emission of visible light can be enhanced by adding impurities to the crystal lattice. These impurities, called *activators*, modify the lattice band structure around their sites, creating intermediate energy states in the band gap through which electrons can be de-excited back to the valence gap. It is in these special sites, known as *luminiscence centres* or *recombination centres*, where the scintillation process takes place. When a charged particle travels through the crystal (in the case of gamma radiation, the recoil electron ejected in the interaction undergoes multiple collisions in the crystal before stopping), it induces the excitation of a large number of valence band electrons to the conduction band, thus creating electron-hole pairs. The holes in the valence band drift towards the activator sites, recombining with an electron and ionizing the activators; the electrons in the conduction band move throughout the lattice until they reach an ionized activator, where they are captured. The activator sites have their own energy structure, as depicted in Figure 1.8, and such an electron capture can result in the formation of an excited state. Finally, the de-excitation to the activator ground state is accomplished through the emission of a scintillation photon. Given that the energy difference between the activator states is smaller than the lattice band gap, scintillation photons cannot excite the valence band electrons, so the crystal is transparent

to this light. The characteristics of the scintillation light (emission wavelength, decay time, ...) depend on the chosen activator and its energy band structure within the lattice. The most relevant properties of some of the scintillator crystals most widely used in medical imaging are listed in Table 1.1 [95, 74].

Table 1.1 Properties of some commonly used scintillator crystals.

Name	Density (g/cm^3)	Z_{eff}	Emission λ (nm)	Light yield (photons/MeV)	Decay time (ns)
NaI(Tl)	3.67	51	410	$40 \cdot 10^3$	230
BGO	7.14	75	480	$4 \cdot 10^3$	300
LYSO(Ce)	7.1	65	420	$32 \cdot 10^3$	40
$LaBr_3$(Ce)	5.08	47	380	$63 \cdot 10^3$	16

1.3.2 Silicon detectors

Silicon, being a semiconductor material, presents an electron energy structure in which the band gap between the conduction and valence bands is reduced in comparison to insulator materials. At zero temperature, all the electrons would be placed in the valence band and the conduction band would be empty. However, thermal excitation causes some of the valence electrons to overcome the small band gap and jump to the conduction band, leaving a positively charged hole in the valence band. In semiconductors, both the conduction band electrons and the holes act as charge carriers. In a pure or *intrinsic* semiconductor lattice, the concentration of both carriers is the same. The concentration of carriers can be enhanced by the addition of impurities, process known as *doping*.

In order to understand how the presence of impurities modifies the number of carriers, let us consider the configuration of the silicon lattice. A silicon atom has four valence electrons, which in the lattice form four covalent bonds with its neighbors. If an element with five valence electrons is included in the lattice, it will still form four covalent bonds, and the remainder electron will be lightly bound to the impurity atom, jumping to the conduction band with very little thermal energy. These impurities are called *donors* (n-type), because one of their electrons is moved to the conduction band. Conversely, the *acceptor* (p-type) impurities are achieved by including elements with three valence electrons. In this case, only three covalent bonds are formed, so other electrons from the lattice valence band can fill this vacant with little extra energy, creating a hole with no corresponding electron in the conduction band.

The PN junction

The interesting properties of semiconductor materials as detectors arise at the contact boundary between p-doped and n-doped regions. Due to the different concentrations of charge carriers, diffusion will take place at the junction. Excess conduction electrons will cross from the n to the p side, leaving a positive charge balance in the lattice, and conversely with the excess holes. The result of the two-way diffusion of both carriers is the generation of two distinct regions with non-zero charge of opposite signs, which creates an electric field that eventually halts the carriers diffusion. The charge unbalance extends over what is known as the *depletion region*, which penetrates in both p and n materials to a depth dependant on the impurity concentration.

The existing electric field leaves the region *depleted* of free carriers, since they are attracted to the extremes of the field. When an incoming particle interacts in the depletion region, the deposited energy creates electron-hole pairs. These new carriers are swept in opposite directions by the electric field, creating an electrical signal that can be collected. The described PN junction acts thus as a radiation detector; nevertheless, the small thickness and the low potential of the depletion region result in a poor performance. The performance of the PN junction as a detector is greatly enhanced by the application of a *reverse bias* voltage. Reverse biasing is accomplished by setting a negative voltage to the p-side with respect to the n-side: this attracts the minority carriers across the junction, and both the potential difference and the area of the depletion region are increased. Semiconductor detectors operating in this way are known as *photodiodes*.

If the electric field is large enough, the generated electrons acquire sufficient energy to produce new electron hole pairs, which are in turn accelerated and can produce new pairs. This avalanche results in a net charge amplification. Devices operated in this regime are called Avalanche Photodetectors (APD). However, if the reverse voltage is too high, the *breakdown voltage* can be reached, point at which the junction behaves as a conductor material.

Silicon Photomultipliers

A Silicon Photomultiplier (SiPM) is a matrix of APDs operated with a reverse bias (V_{bias}) a few volts over the breakdown voltage (V_{bd}). The voltage above the breakdown limit is referred to as *overvoltage*. In this regime, the voltage is so high that both electrons and holes have enough energy to generate new secondary particles, creating a self-sustaining avalanche with a signal no longer proportional to the deposited energy. In this operation mode, an APD behaves as binary detector, indicating only whether or not it is excited, and

it is said to be working in *Geiger Mode* (GM-APD). The equivalent circuit of a GM-APD is shown in Figure 1.9a, where C_d is the diode capacitance and R_s is the silicon substrate resistance [1]. Each GM-APD is connected in series to a quenching resistor (R_q) to stop the avalanche following a detection.

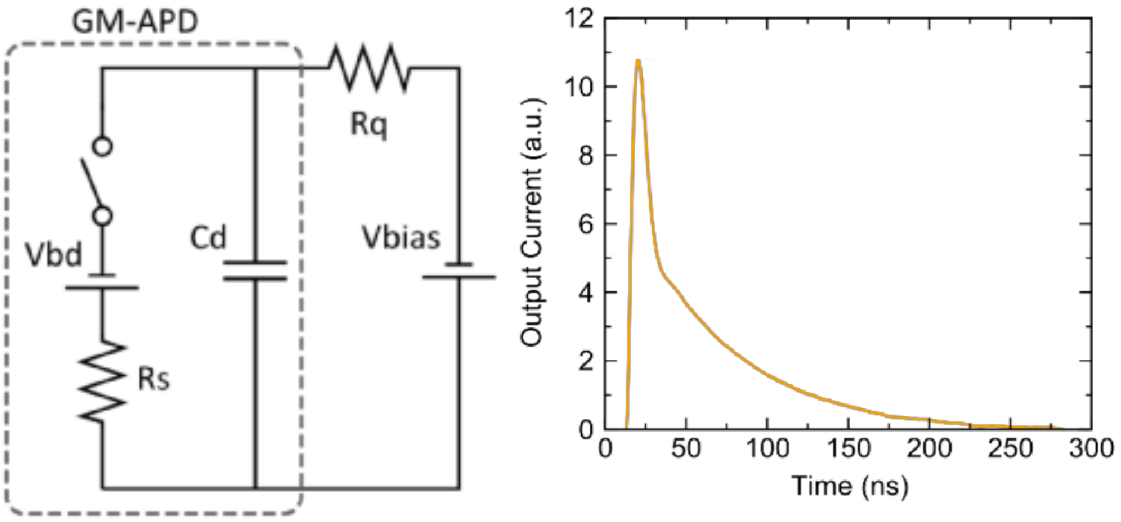

(a) (b)

Figure 1.9 (a) Equivalent circuit of a GM-APD with series quenching resistor and external bias. (b) Current pulse produced by a microcell after a photon detection. Both figures have been extracted from [1].

A GM-APD presents three fundamental states: *quiescent mode, discharge phase and recovery phase*. In quiescent mode, the switch in the equivalent circuit (Figure 1.9a) is open, the diode is reverse biased with V_{bias} and ready for photon detection. The discharge phase starts when an avalanche is triggered: the switch closes and C_d is discharged from V_{bias} to V_{bd}. The discharge phase lasts until the avalanche is quenched, point at which the switch opens and C_d starts recharging back to V_{bias} and the GM-APD returns to quiescent mode. This phase is known as the recovery phase, and has characteristic *recovery time* determined mainly by R_q and C_d. The current pulse shape and duration is represented in Figure 1.9b, where the fast raising edge corresponds to the discharge phase and the slower trailing edge to the recovery phase [1].

In order to obtain a signal proportional to the number of photons impinging the detector, SiPM elements are made of a large number of very small APDs, typically below $100\times100\ \mu m^2$, known as *microcells* or *micropixels*. The matrix of a dense pack of microcells connected in parallel constitutes a pixel. Pixels can be arranged in 2D arrays to conform position sensitive photodetectors. The signal measured from a pixel is given by the sum

of the signals generated in all its microcells, connected in parallel. Ideally, each photon interacts with a microcell, so the measured signal will be proportional to the number of photons entering the detector surface as long as the number of microcells is significantly larger than the number of photons.

It is worth mentioning the following operational parameters:

- The photon detection efficiency (PDE): it is the probability that a photon impinging on the detector surface produces a detectable signal. It can be expressed as the product of three factors:

$$PDE = QE(\lambda)P_A(V)f_{geo},$$

  where $QE(\lambda)$ is the quantum efficiency of the material, $P_A(V)$ is the probability of triggering an avalanche (which increases with overvoltage) and f_{geo} is the geometrical fill factor, given by the ratio of active area over the total detector surface.

- Dynamic range: it is the signal range over which the detector provides a proportional output. SiPMs show a linear response only when the number of microcells is substantially larger than the number of impinging optical photons. As the number of photons impinging the photodetector approaches that of microcells, the system response becomes sub-linear. Saturation is reached when all microcells are activated. For a given pixel size, a larger dynamic range can be obtained by reducing the microcell size and increasing its number, since the total number of microcells will be increased; conversely, the total active area of the detector will be reduced, resulting in a lower PDE.

- Dark count rate: it is the rate of events triggered by thermal creation of electron-hole pairs. It increases with temperature and overvoltage. Its contribution adds noise to the signal and cannot be completely removed. It can be reduced by setting a detection threshold, which limits the smallest measurable energies.

- Afterpulsing: it is the generation of a new avalanche during the micro-cell recovery phase. It is due to carriers generated in the avalanche being trapped in the silicon lattice defects. The afterpulse originates when a trapped carrier is released after the avalanche is quenched, producing a secondary avalanche. Afterpulsing originates from an existing pulse, and it therefore represents a source of correlated noise. The probability of this effect increases with overvoltage and microcell size.

- Optical crosstalk: it is the probability that an avalanche in one microcell produces a new avalanche in a neighboring microcell. This process occurs because the carriers,

accelerated in the high electric field, radiate photons, which can travel to a second microcell. This source of noise is also correlated and increases with overvoltage and microcell area.

1.3.3 Position determination in monolithic scintillator crystals

The resolution of reconstructed images is related to the precision with which interaction positions in the detector can be determined. In scintillator crystals, position determination depends on the crystal type, which in this aspect can be divided in two categories: pixelated and continuous (or monolithic). In pixelated crystals, determination of the interaction position is done by identifying the pixel in which the optical photons are generated, and usually the pixel center is taken as the interaction position. In the case of monolithic crystals, the generated photons can travel through the crystal unconstrained, so in general scintillation light can reach all photodetector elements. The distribution of the light detected by the different elements depends on the position where the photons are produced, so the interaction position can be inferred from the measurement.

Each of the detectors used in our prototype consists of a monolithic scintillator crystal coupled to a SiPM array of 64 channels, so a position determination method is necessary. The method employed for the determination of interaction positions of primary gammas in the scintillator crystal was not developed within the context of this thesis, and a detailed explanation of its implementation and performance can be found in [17]. It is based on the model of scintillation light transportation presented in [44], in which the number of photons detected by pixel i (np_i) is described by the equation:

$$np_i = C_{est} + A_0\Omega(x,y,z) + A_0\sum_j \Omega(x_j,y_j,z_j), \tag{1.11}$$

where A_0 is the total number of scintillation photons, $\Omega(x,y,z)$ is the solid angle subtended by pixel i from position (x,y,z) (within the crystal) and C_{est} is a constant that accounts for the contribution of the diffuse reflections around the crystal. The term $A_0\Omega(x,y,z)$ represents the number of photons impinging directly on the pixel, while $A_0\Omega(x_j,y_j,z_j)$ is the number of photons that arrives in the pixel after being reflected on the crystal surface j (each of the five surfaces not coupled to the photodetector). These reflections are modelled as contributions from *virtual sources* placed at a position symmetric to (x,y,z) with respect to surface j. The parameters in equation 1.11 are estimated by fitting np_i to the signal detected by each pixel of the SiPM array. The fit is performed with an iterative least squares algorithm, from which the interaction position of the primary gamma is extracted.

Chapter 2

Image reconstruction in Compton cameras

Compton imaging systems are gamma detectors that employ Compton kinematics to reconstruct images of the emission origin of the detected gamma rays. In the literature, these devices have been referred to as Compton telescopes or as Compton cameras depending on the geometry and application; without loss of generality, both terms are used indistinctly throughout this entire manuscript. This chapter is dedicated to explaining the working principles of Compton cameras and the process between measurement and image formation. The parameters affecting the quality of the reconstructed images are also discussed. Finally, the chapter concludes with a brief review of the history and state of the art in Compton camera research.

2.1 Operating principle

The working principle of Compton imaging systems is based on the detection in time coincidence of a Compton scatter from an incoming photon followed by a successive interaction from the scattered photon. If the initial gamma energy is known and the energy deposited in the Compton interaction is measured, the Compton scattering angle is given by the formula

$$cos\theta = 1 - \frac{m_e c^2 \tilde{E}_1}{E_0(E_0 - \tilde{E}_1)}, \tag{2.1}$$

which is equivalent to equation 1.7 in section 1.2.1*.

*Note that in this case the c^2 term is explicitly included and that the variables E_γ, $\tilde{E}_\gamma$ have been rewritten as E_0, $\tilde{E}_1$ in order to preserve the usual nomenclature employed in the literature

If a subsequent interaction is detected, under ideal detection conditions, the two interaction positions determine unambiguously the path followed by the scattered photon. The combination of the scattering angle and the path taken by the scattered photon provides directional information about the origin of the incident photon. Indeed, the origin of the photon can be constrained to a conical surface with its apex at the first interaction position, an axis given by the vector connecting the two interaction positions and an aperture angle equal to the Compton scattering angle. Figure 2.1 illustrates the path followed by an incident photon producing a signal event. From the measured parameters, the directional recovered information limits the origin of the photon to the depicted conical surface.

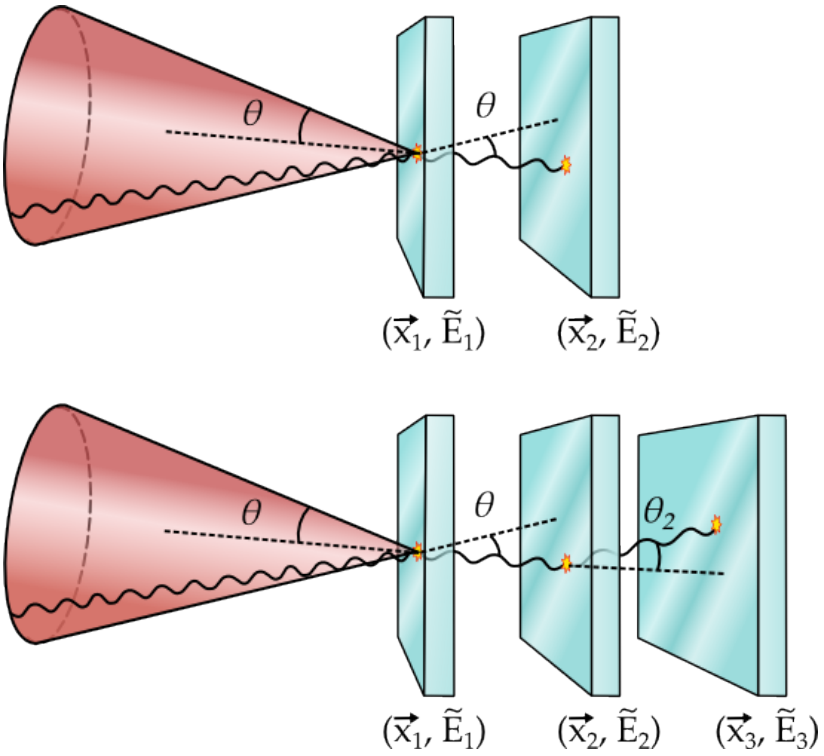

Figure 2.1 Operating principles of a Compton camera with two and three detector planes.

The applicability of Compton cameras is restricted to the energy range in which the Compton interaction probability is dominant, or at least sufficiently high to produce a significant percentage of signal events. That restricts their use to imaging sources in the energy range from a few hundred keV up to about 10 MeV. In order for a system to operate as a Compton camera, it needs to be able to measure the interaction positions and deposited energies of at least two interactions derived from a single incident photon. This usually leads to the design of systems based on multiple independent stages or planes operated in time coincidence, which allow to distinguish and read out independently the different interactions. As explained, the directional information about the photon origin is provided

by the measurement of two subsequent interactions, without the need for any mechanical collimation.

In order to calculate the aperture angle of the Cone of Response (CoR) associated to a measured signal event, it is mandatory to know both the initial energy of the incident gamma and the energy deposited in the Compton interaction, as seen from equation 2.1. If there is no prior knowledge of the initial energy, this can be achieved by requiring full absorption of the scattered photon. For that reason, the most basic cameras consist of two separate detector planes, in which the first one (also known as scatterer) aims at maximizing the probability of producing a single Compton interaction and the second one (absorber) is designed to maximize the probability of full energy absorption.

The physical interactions involved in the detection process make conventional two-plane Compton cameras suitable for imaging sources of gammas below 1 MeV, for which complete absorption in the second interaction has a high probability; however, full absorption becomes increasingly less likely for higher initial energies. If the photon energy is not fully absorbed in the second interaction, it is still possible to recover its initial energy without requiring full absorption if a third interaction is also detected. In such cases, the initial energy can be calculated as [16, 40]:

$$E_0 = \tilde{E}_1 + \frac{1}{2}\left(\tilde{E}_2 + \sqrt{\tilde{E}_2{}^2 + \frac{4\tilde{E}_2 m_e c^2}{1 - cos\theta_2}}\right), \tag{2.2}$$

where $\tilde{E}_2$ is the energy deposited at the second interaction and θ_2 is the scattering angle of the second Compton interaction (see Figure 2.1).

The addition of a third detector plane enables the measurement of three-interaction events, which allow calculation of the initial photon energy through equation 2.2. Therefore, when the measured sources emit gammas of multiple different energies or in an unknown spectrum, three-interaction events are in principle more advantageous than those with only two interactions. Nevertheless, since an additional interaction must be registered, the efficiency of detection of three-interaction events is significantly lower. To the end of exploiting the higher efficiency of two-interaction events in scenarios where total absorption is unlikely, another possible approach is to extend the reconstruction algorithms to include a spectral dimension, in which the initial energy must be inferred from the incomplete depositions measured.

For every detected event, a single CoR can be built and backprojected onto the image space. The intersection of the CoRs built from different measurements constitutes the basis for image reconstruction in Compton imaging systems. This idea is represented in Figure 2.2,

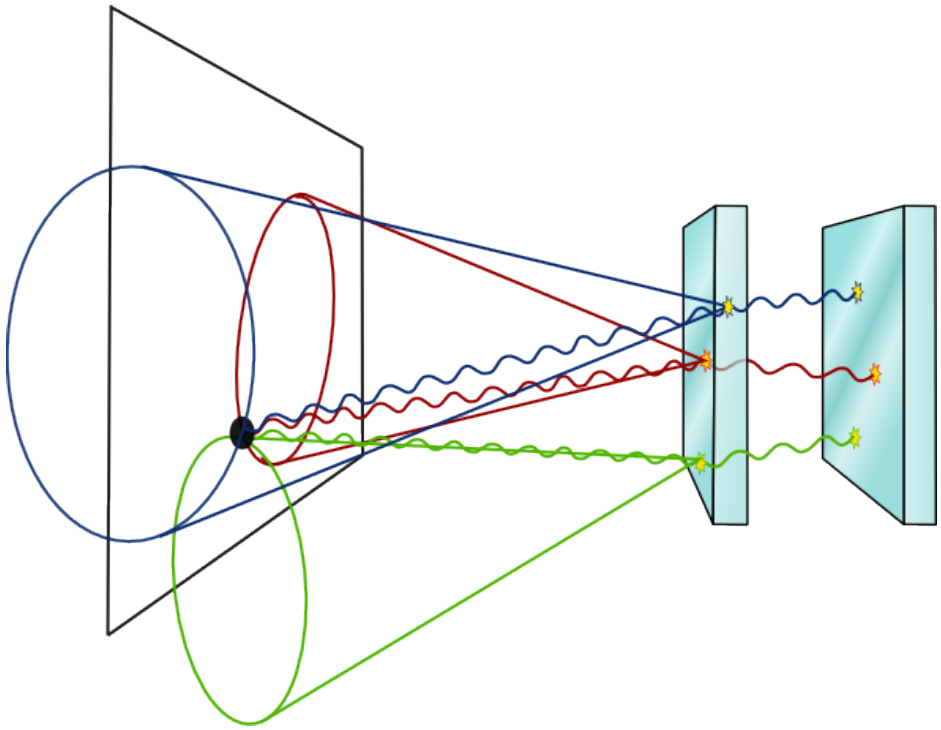

Figure 2.2 Intersection of different Compton conical surfaces at the image plane.

showing the intersection of three different CoRs and the image plane at the position where three different primary photons have been emitted.

2.2 From measurements to image

The aim of the image reconstruction process is to obtain an image of the source distribution that generated the measured data. The image can be modelled as a continuous scalar function $\lambda(\vec{x})$, where $\vec{x}$ describes a location in the image space. Defining $\vec{\eta}$ as the measurement coordinates vector, the relation between the expected number of events $y(\vec{\eta})$ (measured with coordinates $\vec{\eta}$) and the source distribution can be expressed as

$$y(\vec{\eta}) = \int T(\vec{x},\vec{\eta})\lambda(\vec{x})dx, \tag{2.3}$$

where the function T is the system response function and represents the conditional probability that an event measured at location $\vec{\eta}$ was emitted from the source at position $\vec{x}$.

For computing purposes, the reconstructed image cannot be represented as a continuous function, and the image space is described in a discrete domain made up of *pixels* (in the 2D case) or *voxels* (in the more general 3D case). Thus, the estimated $\vec{\lambda}$ is a sampled version of

the image. In the case of nuclear medical imaging, each element $\lambda_j, j = 1,\ldots,J$ represents the estimated activity at voxel j. The measurement space is also discretized into *bins*, understood as sets of measurement coordinates (in two-plane Compton cameras, $\vec{\eta} = [\vec{x}_1, \tilde{E}_1, \vec{x}_2, \tilde{E}_2]$), and the vector $\vec{y} = [y_1,\ldots,y_N]$ can be defined as the expected number of events in each of the N discrete bins. Figure 2.3 represents the projection of information from the discrete image space to a discrete measurement space through a Compton camera. In Compton imaging, each measurement bin is associated to a specific CoR; nevertheless, due to the large number of possible CoRs (which tends to infinity in continuous systems), the *list-mode* approach is often followed, in which each individual event from the measured set is identified directly as a bin (see sections 2.2.2 and 2.3.2), so the elements $y_i, i = 1, \ldots, M$ correspond to each of the M detected events.

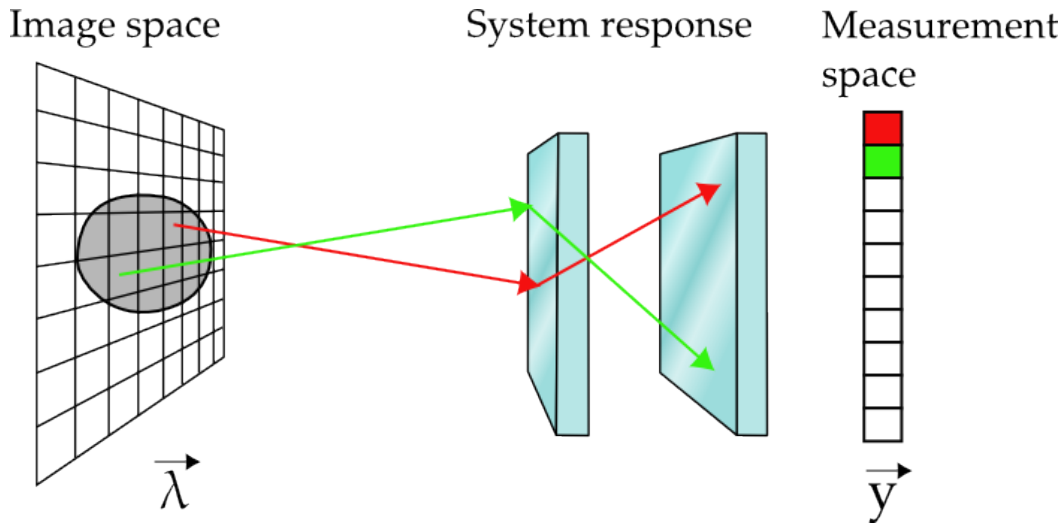

Figure 2.3 A discrete model of the measurement process in a Compton camera.

Taking into account the above considerations, the relation between the source distribution and the expected values in each measurement bin can be written in the matrix form

$$\vec{y} = T\vec{\lambda}, \tag{2.4}$$

where the function T is identified as the system matrix. T is a $N \times J$ matrix, in which each row represents a measurement bin and each column corresponds to a voxel in the image space. The system matrix is characteristic of the measurement device, and it establishes the relation between the image and the measurement spaces. Equation 2.4 is often written as

$$y_i = \sum_j t_{ij}\lambda_j, \tag{2.5}$$

where it is more explicit that the system matrix element t_{ij} represents the probability that a photon emitted from voxel j be detected in terms of measurement i.

The image reconstruction problem is to find the image $\vec{\lambda}$ that maximizes the probability of the measured set $\vec{y}$. One could think that the problem could be solved by calculating the inverse of T. However, in general the system matrix T is non-invertible and ill-conditioned, so this is in fact not possible. In order to find a solution, there are different strategies that can be followed. The next section provides a short overview of the most common approaches followed in Compton image reconstruction.

2.2.1 Image reconstruction algorithms

In Compton imaging, different methods have been proposed to solve analytically the inverse problem. In [14], the authors develop an analytical solution for the 3D reconstruction problem, adapted for a system based on two infinitely extending parallel planes. Other approaches based on the employment of spherical harmonics as the sets of orthogonal functions to diagonalize the inversion operator have also been proposed [9, 63]. However, analytical inversion methods present several shortcomings, mainly the difficulty to include all the physical processes involved in the detection (e.g. attenuation, statistical nature of the emission, random coincidences,...) and the fact that they in general require a complete set of projections.

Iterative reconstruction procedures can avoid the limitations faced by analytical solutions. One widely used iterative method is the maximum likelihood expectation maximization (MLEM) approach. In medical imaging, the MLEM algorithm was demonstrated in [83] for PET, and a list-mode version was adapted to Compton imaging in [102]. Since then, the list-mode MLEM algorithm has likely become the most popular method for image reconstruction in Compton cameras (e.g. see [106, 20, 50, 76]). A list-mode MLEM algorithm has been employed for the reconstruction of all the images contained in this thesis, and next section is thus dedicated to the derivation of its iterative formula.

It is also worth mentioning that the Stochastic Origin Ensembles (SOE) iterative algorithm has recently gained importance in the field of Compton imaging. The algorithm was presented for PET reconstruction in [88] and adapted to Compton image reconstruction in [4], and it has since been employed with promising results [5, 48].

2.2.2 List mode MLEM

The Maximum Likelihood (ML) criterion is to find an image $\tilde{\lambda}$ such that maximizes the likelihood of obtaining the measured data. Assuming that the measurements are random variables, the probability of detecting y_i events in bin i is given by

$$y_i \sim Poisson(\mu_i) = \frac{\mu_i^{y_i}}{y_i!} e^{-\mu_i}, \tag{2.6}$$

where μ_i is the mean value of y_i, modelled as

$$\mu_i = \sum_j t_{ij} \lambda_j. \tag{2.7}$$

Considering that the measurement bins are conditionally independent, the log likelihood is expressed as

$$\begin{aligned} \mathscr{L}(\vec{y}|\vec{\lambda}) &= \log p(\vec{y}|\vec{\lambda}) = \log\left(\prod_i \frac{\mu_i^{y_i}}{y_i!} e^{-\mu_i}\right) \\ \mathscr{L}(\vec{y}|\vec{\lambda}) &= \sum_i \left(y_i \log \mu_i - \mu_i - \log y_i!\right). \end{aligned} \tag{2.8}$$

Equation 2.8 must be maximized with respect to λ to find the most likely solution. One approach is to employ the Expectation Maximization (EM) algorithm, for which the log likelihood must be expressed in terms of the *complete* data set. One natural choice for the complete data set is to use the unobservable data vector $\vec{z}$, with elements z_{ij} defined as the number of photons emitted from voxel j and detected in bin i. The complete data set is related to the measured projection as

$$y_i = \sum_j z_{ij}, \tag{2.9}$$

and its conditional expectation for the current estimation $\vec{\lambda}^{(n)}$ is given by

$$E(z_{ij}|\vec{y}, \vec{\lambda}^{(n)}) = \frac{y_i t_{ij} \lambda_j^{(n)}}{\sum_k t_{ik} \lambda_k^{(n)}}. \tag{2.10}$$

Introducing the variable $\vec{z}$, the log likelihood over the complete data set reads

$$\mathscr{L}_C(\vec{z}|\vec{\lambda}) = \sum_i \sum_j \left(z_{ij} \log(t_{ij}\lambda_j) - t_{ij}\lambda_j - \log z_{ij}!\right). \tag{2.11}$$

The EM algorithm can now be applied on equation 2.11. In the E-step, the expectation of the log likelihood is taken, which yields

$$E[\mathscr{L}_C] = \sum_i \sum_j \left(\frac{y_i t_{ij} \lambda_j^{(n)}}{\sum_k t_{ik} \lambda_k^{(n)}} \log(t_{ij}\lambda_j) - t_{ij}\lambda_j - \log\left(\frac{y_i t_{ij} \lambda_j^{(n)}}{\sum_k t_{ik} \lambda_k^{(n)}} \right)! \right). \tag{2.12}$$

In the M-step, the derivative with respect to λ_j is taken and set to zero, resulting in the final iterative MLEM equation:

$$\frac{\partial E[\mathscr{L}_C]}{\partial \lambda_j} = \frac{1}{\lambda_j} \lambda_j^{(n)} \sum_i \frac{y_i t_{ij}}{\sum_k t_{ik} \lambda_k^{(n)}} - \sum_i t_{ij} = 0 \tag{2.13}$$

$$\lambda_j^{(n+1)} = \frac{\lambda_j^{(n)}}{s_j} \sum_i \frac{y_i t_{ij}}{\sum_k t_{ik} \lambda_k^{(n)}}, \tag{2.14}$$

where $s_j = \sum_i t_{ij}$ is the sensitivity matrix, defined as the probability that a photon emitted from voxel j is detected by the system in any measurement bin.

In systems with high granularity, the number of bins required to store the measurable data increases exponentially with the number of measured coordinates. In continuous systems, this number of bins is actually infinite, so a different approach must be taken. In the list-mode version of the algorithm, only the measured events are considered, and each of them is considered a separate bin. This is equivalent to setting $y_i \to 1$ for all bins with a measured event, and $y_i \to 0$ otherwise. After this modification, summation is only performed over the M measured events, and the equation reads:

$$\lambda_j^{(n+1)} = \frac{\lambda_j^{(n)}}{s_j} \sum_{i=1}^{M} \frac{t_{ij}}{\sum_k t_{ik} \lambda_k^{(n)}}. \tag{2.15}$$

2.3 Reconstruction parameters

2.3.1 Field of View

The Field of View (FoV) is the region of the image space considered in the reconstruction process and modelled as a set of ordered voxels. Depending on the measurement conditions and the image reconstruction method, different FoV geometries may be more adequate than others. Under the far-field assumption, the detector is modelled as point-like, since its size is negligible compared to the distance between source and detector, and a 2D spherical space is the most convenient. In the near-field scenario, the detector size must be considered,

and cartesian coordinates (in 2D or 3D) are usually employed. Figure 2.4 represents the intersection between a Compton conical surface and the FoV in the two mentioned coordinate systems. Given the geometrical configuration of our system and sources in the experimental measurements, our reconstruction algorithm is built based on a cartesian coordinate system.

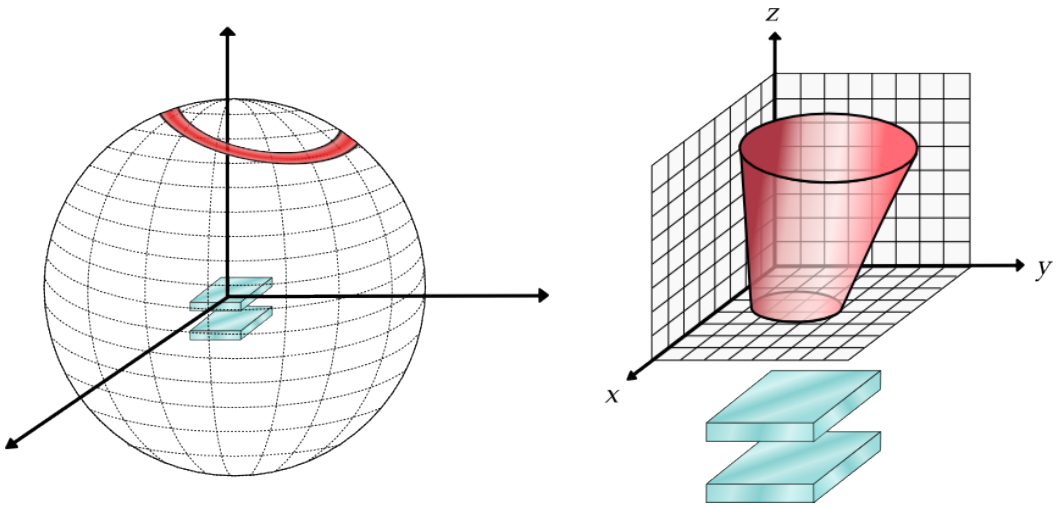

Figure 2.4 Intersection between a CoR and the FoV. Left: 2D spherical space. Right: 3D cartesian space.

So far, only the spatial coordinates of the FoV have been mentioned, since the object of the reconstruction is usually the spatial distribution of the source. However, it can be extended to additional dimensions, without loss in the algorithm functionality, as long as the measurement parameters convey information that allows their reconstruction (i.e. that can be included in the system matrix). For instance, if the time dimension is considered in the FoV, the reconstruction process yields an image for each of the defined time slices, which allows for motion visualization. This can be useful in some cases, such as studies of substance diffusion inside living organisms.

For Compton imaging, especially when aimed at PG imaging, the most interesting extension of the FoV is to include the spectral dimension. In such cases, each voxel is associated to a (small 4D volume centered in a) spatial position and a photon emission energy. Figure 2.5 depicts a diagram of the backprojection of an arbitrary signal event onto a 4D FoV with an energy dimension. It shows that, for a realization in the measurement space, the aperture angle of the Compton cones (used to build the system matrix) decreases for higher emission energies, according to equation 2.1. The product of the reconstruction process is an image in the combined spatial-spectral space, which reconstructs simultaneously the position of the measured source and its emission spectrum. Since this approach allows extracting a separate spatial distribution for each of the measured spectral lines, it is well suited for

imaging sources with continuous emission spectra. A model for spectral reconstruction in Compton cameras was developed and studied during this thesis, which will be explained in detail in Chapter 6.

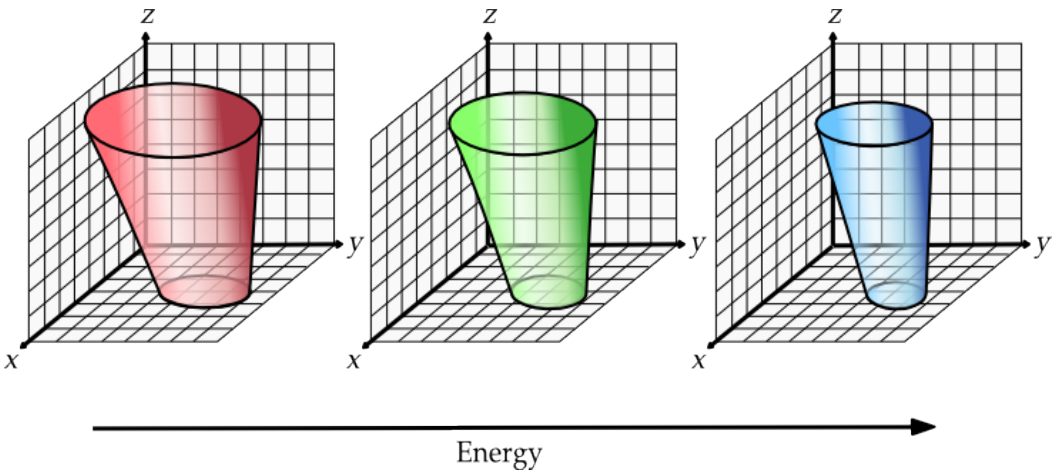

Figure 2.5 Backprojection of a measured event onto a 4D FoV. The three conical sections belong to different energy slices within the same FoV.

2.3.2 The system matrix

The system matrix encodes all the processes that cause an emission in the image space to produce an entry in the measurement space. As explained, the matrix elements t_{ij} must be understood as the probability that a photon emitted from voxel j be measured with the parameters of the detected event i. For a given event i, a CoR is built from the measured parameters employing Compton kinematics, and only the elements t_{ij} containing the voxels contained in such CoR are activated. The specific value of those elements depends on the adopted criterion (i.e. weighted distance to the cone surface), and it must be derived from a complete model taking into account the physics involved in the detection process. Sometimes it can be useful to approximate the system matrix as composed of a geometrical and a physical part. In this approximation, the intersection of the conical surface and the FoV constitutes the geometrical part of the system matrix, and determines which voxels are activated for a measured event. The physical part is derived from a detailed model and is used to assign the specific values to the activated elements. Before we endeavour to deduce the physical contribution (see chapter 5), let us start by defining the geometrical aspects of the system matrix in Compton imaging.

Building the system matrix

We have already seen that the information carried by a signal event allows the generation of a CoR. In the list-mode method, each measured event corresponds to a system matrix row, so the cones need to be transformed into the row elements. In order to do so, it is necessary to find which voxels are intersected by the conical surface. In a FoV defined in the cartesian coordinate system, there are two main approaches that are usually followed for this purpose:

- Voxel-driven approach: it consists in calculating the angle α formed by the voxels and the cone axis at the point of its apex. The voxel weights are then assigned according to the difference between this angle and the Compton scattering angle θ obtained from the measured parameters. An important drawback of this approach is that, as the number of voxels in the FoV can be very large (especially in higher dimensions) and only a small fraction of them yield an α compatible with θ, a lot of computation time is wasted on the rest of the voxels.

- Ray-tracing approach: the conical surface is modelled as a dense set of rays, which are backprojected to the image space. The weight assigned to a voxel is proportional to the length of the rays contained inside it. This quantity can be very efficiently calculated for FoVs built upon parallel planes [84], and only those voxels traversed by a ray are involved in the computation.

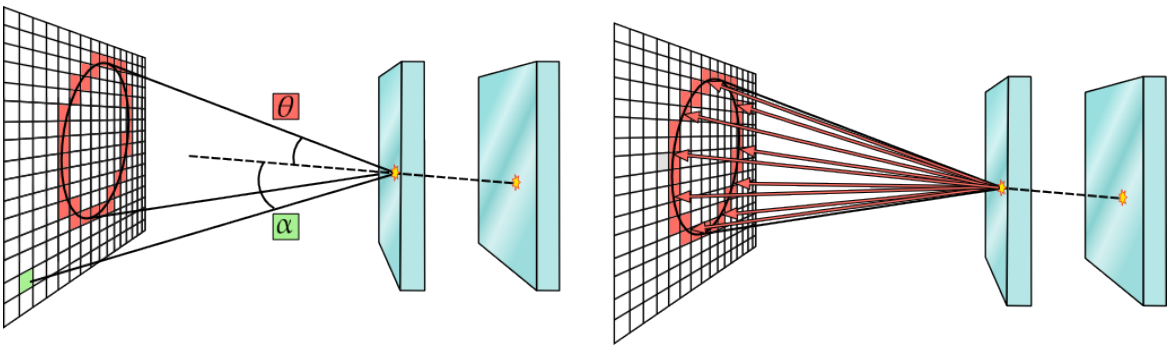

Figure 2.6 Backprojection of a CoR onto the FoV. Voxel-driven (left) and ray-tracing (right) approaches.

In the reconstruction code implemented during this thesis, the system matrix is built based on the ray-tracing technique. In addition to the faster computation time, this method also provides directly the length of the rays inside a traversed voxel, which in our physical model is related to the probability of emission from inside it (see chapter 5 section 5.1.1). The calculation of the rays that comprise a cone is performed following the steps:

1. Compute the Compton scattering angle θ.

2. Calculate the rotation R that transforms a vector defined parallel to the scattered photon direction $(\vec{x_1} - \vec{x_2})$ to the $\vec{z}$ direction.

3. Define N_r vectors $\vec{r_i}$ uniformly distributed over the surface of a cone with its axis parallel to the $\vec{z}$ direction and with aperture angle θ. It can be easily seen that these vectors are $\vec{r_i} = (\cos\phi_i \sin\theta, \sin\phi_i \sin\theta, \cos\theta)$, with $\phi_i = i(2\pi/N_r), i = 1, \ldots, N_r$.

4. Apply the inverse rotation R^{-1} to the vectors $\vec{r_i}$, so the final parametric equation of the rays is $\vec{\xi_i} = \vec{x_1} + \lambda \cdot (R^{-1}\vec{r_i})$.

Once the rays are defined, they are backprojected to the FoV, which provides the basis for the computation of a system matrix row. The system matrix (row) elements corresponding to the voxels traversed by the different rays are thus updated and saved as a pair *[index, value]*. The value of the different elements is given by $t_{ij} \propto \ell_{ij}$, where ℓ_{ij} is the total length of all the rays from event i contained in voxel j. Voxels not intersected by any ray are given the value 0, and are not stored in the system matrix to save memory space. After the backprojection of the generated rays, the next event is selected and the process is repeated until the calculation is completed for the whole measured data set.

2.4 Image degradation

2.4.1 Signal and noise

As mentioned before, the signal events in two-plane Compton cameras are those in which an incident photon is Compton scattered in the first plane and the scattered photon is subsequently detected in the second one. Although the different possible physical processes in the second interaction may require to be treated differently, useful information can always be extracted from these events, as long as the interaction positions and deposited energies are measured. However, since the system needs to capture coincidental detections in both planes inside a time window, an acquisition can also be triggered by other unwanted events:

- Random coincidences: these are produced when two different primary gammas interact in the detector planes within the coincidence time window. They are inevitable, and their number can only be reduced by systems with high time resolution.

- Backscatter events: if an incoming photon reaches the second plane directly and is Compton scattered with a large angle, the scattered photon may then reach the first

plane and produce a second interaction there. If the order of interaction in the different planes is not properly assigned, the CoR generated by these backscatter events will not contain the actual origin of the gamma and it will contribute to add noise to the reconstructed image. These events become increasingly less likely for higher energy gammas, which have a lower probability of being scattered with large angles.

- Multiple interactions in one plane: when a photon enters a detector plane, it may interact more than once inside it. Because these interactions occur within a very short time, they are often detected as a single interaction. In such cases, the measured energy and impact position do not correspond to the parameters of the initial interaction, thus leading to a deviation in the constructed CoR. However, if the designed system were able to precisely discriminate multiple interactions within a single plane, the additional information given by a third detection could be used to reconstruct the initial energy as in equation 2.2.

- *Jumping* electrons: the electrons stripped from their nucleus after taking part of the initial gamma energy (or all of it, if the gamma is completely absorbed), lose their acquired energy through different interactions inside the detector material, ideally depositing it all and being reabsorbed. Nevertheless, if an electron reaches the surface with enough energy, it can escape the detector. In such cases, there is a non-zero probability that the escaped electron *jumps* into a separate detector plane, thus producing a new energy deposition and triggering a coincidental acquisition.

- Annihilation photons: as the gamma energy increases, the e^+e^- pair production cross section gains more importance, and it becomes more likely that it is the first and only interaction undergone by the primary gamma in the detector. After the e^+ loses its energy and is annihilated, it is possible that one of the two annihilation photons reaches a separate detector plane and is detected in time coincidence. Because the annihilation photons are always produced with 511 keV, it is frequent to cut off this energy in order to avoid such events.

- Other particles: in addition to photons, other unwanted particles can reach the detectors during the measurement time. In the case of hadrontherapy, there is a high background of neutrons and secondary protons escaping the patient's body, which can trigger a coincidence detection and add noise to the signal.

2.4.2 Detection uncertainties

Experimental measurements are inevitably subject to the detector resolution, so even the true signal events produce blurred data. The impact of the different experimental resolutions on the image reconstruction process is briefly discussed in this section.

Scattering Angle Uncertainty

When dealing with real detectors with finite energy resolution, the Compton scattering angle can only be determined with limited precision. If the incident energy is known and the main source of error is the energy resolution of the first detector, the angular uncertainty of the scattering angle is given by:

$$\sigma(\theta) = \frac{m_e c^2}{\left(E_0 - \tilde{E}_1\right)^2 \sin\theta} \sigma(\tilde{E}_1). \tag{2.16}$$

Equation (2.16) indicates that a better angular resolution can be achieved for higher energy incident gammas. The angular uncertainty results in the broadening of the cone surface where the source must be contained, which turns into a cone shell whose width depends on the detector resolution.

Doppler broadening

Another factor limiting the angular uncertainty of Compton cameras is the *Doppler broadening*. This effect is due to the electron momentum prior to the Compton interaction, which causes the broadening of the photon scattering angle. The Compton formulas in section 1.2.1 have been derived under the assumption of an ideal free electron at rest. Equation 2.1 can be restated in terms of the scattered photon energy E_1[†] as

$$E_1 = \frac{E_0}{1 + E_0(1-\cos\theta)/m_e c^2}. \tag{2.17}$$

When the electron momentum prior to the collision is taken into account, equation 2.17 transforms into [61]

$$p_z = -m_e c \frac{E_0 - E_1 - E_0 E_1 (1-\cos\theta)/m_e c^2}{\sqrt{E_0^2 + E_1^2 - 2E_0 E_1 \cos\theta}}, \tag{2.18}$$

[†]Note the distinction between $\tilde{E}_i$ (energy transferred in interaction i) and E_i (gamma energy after interaction i). This notation is kept throughout the text.

where p_z is the projection of the electron pre-collision momentum along the incident gamma direction. Consistently, equation 2.18 reduces to equation 2.17 when $p_z = 0$. Since p_z of the bound electrons is described by a distribution (the Compton profile), the energy deposited by the gamma in the interaction will also follow a distribution for a given scattering angle. This effect, known as Doppler broadening, is an uncertainty source independent of the detector resolutions. The uncertainty derived from the Doppler broadening is more relevant for small scattering angles and in detector material with high atomic number, and the effect is reduced as the gamma energy increases [61, 35].

Uncertainty in E_0 calculated for 3 interactions

If the incident energy is calculated by the detection of a third interaction, the energy and spatial resolution of the measured interactions will contribute to the uncertainty in the reconstructed initial energy. From equation (2.2), it is easy to see that the error of the calculated incident energy will have contributions from the energy resolution of the two scatter detectors and the uncertainty in the second scattering angle, which depends on the precision of the measured interaction positions. The total error of the reconstructed energy can be expressed as

$$[\sigma(E_0)]^2 = \left[\Delta\tilde{E}_1\right]^2 + \left[\Delta\tilde{E}_2\right]^2 + [\Delta\theta_2]^2, \tag{2.19}$$

where

$$\Delta\tilde{E}_1 = \sigma(\tilde{E}_1) \tag{2.20}$$

$$\Delta\tilde{E}_2 = \left(1 + \frac{\tilde{E}_2 + m_e c^2}{2\sqrt{\tilde{E}_2^2 + \frac{4\tilde{E}_2 m_e c^2}{1-\cos\theta_2}}}\right)\sigma(\tilde{E}_2) \tag{2.21}$$

$$\Delta\theta_2 = \frac{\tilde{E}_2 m_e c^2}{(1-\cos\theta_2)^2\sqrt{\tilde{E}_2^2 + \frac{4\tilde{E}_2 m_e c^2}{1-\cos\theta_2}}}\sigma(\cos\theta_2). \tag{2.22}$$

Whereas the contribution to the uncertainty in the reconstructed initial energy from the energy resolution is somewhat constant, the imprecision derived from the spatial resolution of the detector is dependent on the second scattering angle, and grows larger as the angle decreases (equation 2.22).

Intrinsic spatial resolution

The detector intrinsic spatial resolution affects the precision with which the gamma interaction position is determined. The error in $\vec{x}_1$ translates into an error in the positioning of the CoR apex, while the orientation of the cone axis is affected by the uncertainties in both $\vec{x}_1$ and $\vec{x}_2$.

As a result of both spatial and angular uncertainties, the CoR built from the experimentally measured values is deviated from the ideal one, and it may not contain the actual position of emission (Figure 2.7) if the model employed for the system matrix construction does not account for the detector resolutions.

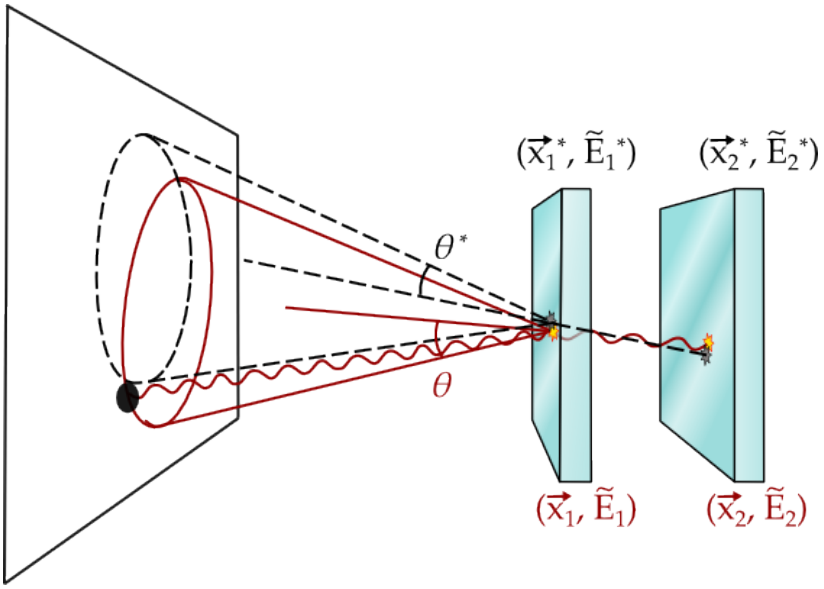

Figure 2.7 Effect of the detector uncertainties in the backprojection of a CoR.

2.4.3 Image filters

One drawback of the MLEM algorithm is that it yields noisy reconstructed images. The statistical criterion followed by the iterative algorithm is to find solutions that maximize the consistency with the measured data. Since the measurement process produces noisy data, the reconstruction algorithm will in turn generate noisy images. In addition to the already mentioned factors degrading the signal (unwanted events and detection uncertainties), the stochastic nature of the measured process entails a random noisy component. As the iterative procedure advances, and the algorithm approaches the ML solution, the high frequency noise increases. In practice, one extended option is to stop the algorithm before the noisy voxels are excessively amplified.

The results may also be improved through the application of a low-pass filter that suppresses the high frequency noise [60]. In this aspect, two image filters for image post-processing have been implemented in this work. Both filters re-scale the voxel values according to the values of their surrounding neighbors, taking always a cubical footprint

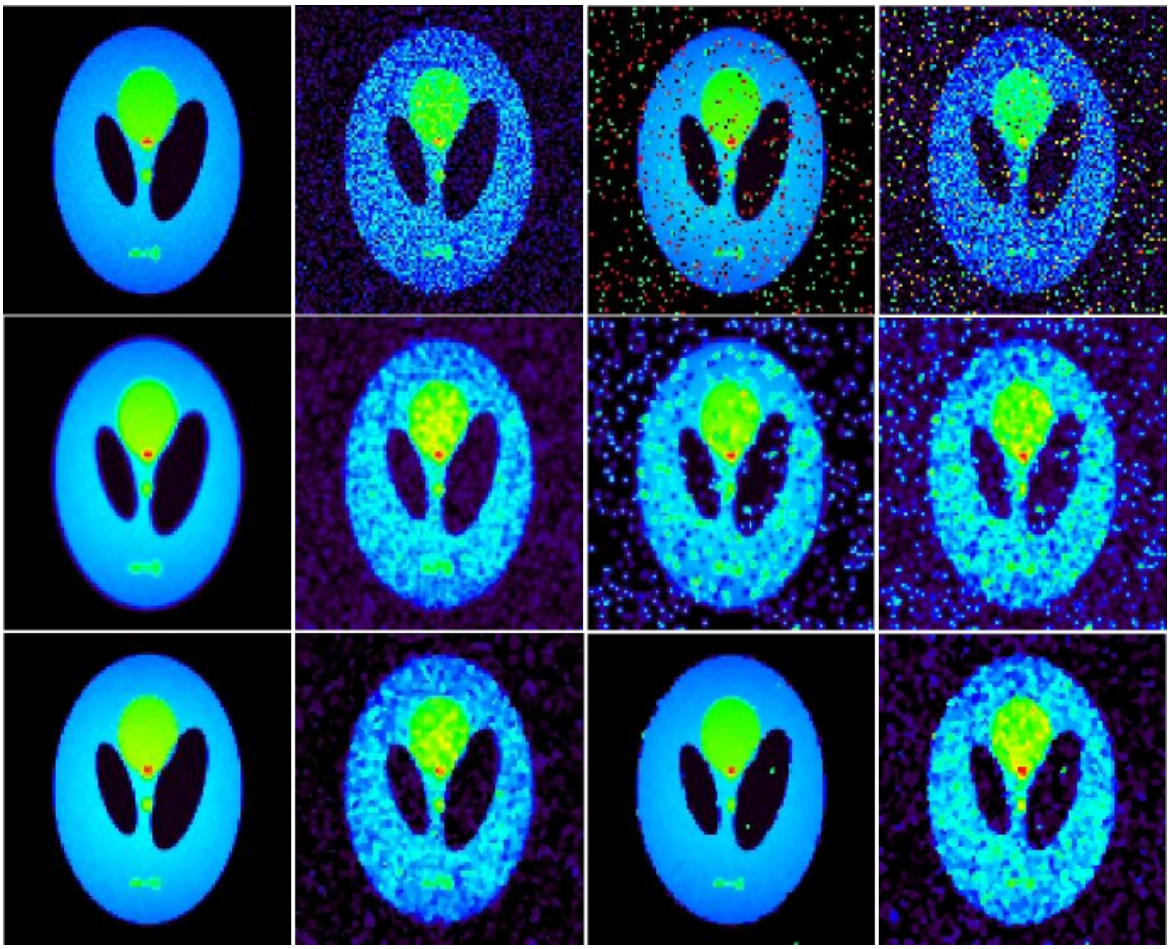

Figure 2.8 Effect of the employed image filters on noisy images. First row: original image and addition of noisy components. Second row: first row images after application of the Gaussian blur. Third row: first row images after application of the median filter.

and a windows size of $3 \times 3 \times 3$ voxels in the 3D space. The employed filters are based on different criteria:

- Gaussian blur: this filter is often employed to smooth random uniform noise. The value v_j of pixel j is replaced by

$$v_j = \frac{1}{N_i} \sum_i \frac{v_i}{\sigma^3 (2\pi)^{3/2}} \exp\left(-\frac{d_i^2}{2\sigma^2}\right),$$

  where the summation is taken over the N_i neighbors within the filter footprint, d_i is the distance between the centers of pixels i and j and σ is usually set to one voxel length.

- Median filter: it is a low-pass filter that can eliminate sparse voxels with values very different from its surroundings. For its application, the values of the pixel under

consideration and those of its immediate neighbors are first sorted, and the median value from the sorted list is assigned to the pixel at issue.

The effect of the described filters on noisy images can be appreciated in Figure 2.8. The first row of the figure shows the original picture (first column) and its degradation after the addition of random uniform noise (second column), *salt and pepper* noise (third column) and both forms of noise (fourth column). The results from the application of the filters on those images are shown in the second (Gaussian blur) and the third (median filter) rows.

2.5 History and application of Compton cameras

Compton cameras for gamma ray imaging were initially proposed in 1973 as an instrument for the observation of photons in the energy range from 1 to 10 MeV in astronomy [78]. The COMPTEL Compton telescope [77], which consisted of a liquid scintillator scatter detector and a NaI absorption detector, was developed and mounted on board of the satellite Compton Gamma Ray Observatory (CGRO), and its first measurements were reported in [105]. A second generation of Compton telescopes has been proposed, aiming at improving the system sensitivity and energy range. The prototype developed by the MEGA (Medium Energy Gamma-ray Astronomy) collaboration [6] employs a stack of double sided silicon strip detectors as scatterer and tracking detectors and pixelated CsI detectors as absorbers. The tracking of the recoil electron allows measuring its momentum, further limiting the origin of the incident gamma to an arc of the CoR. The TIGRE (Tracking and Imaging Gamma-Ray Experiment) collaboration [100] features a similar concept, in which the replacement of the CsI absorber by arrays of Ge or Cadmium Zinc Teluride (CZT) pixel detectors has been suggested for an improved resolution [12].

The use of Compton cameras in the field of medical imaging was proposed in 1974 [99], and a possible application of Compton imaging systems to Single Photon Emission Computed Tomography (SPECT) was described [18] for clinical diagnoses. Analytical and experimental results for a Compton camera prototype were reported [86, 87], employing pixelated Ge detectors as scatterer and a conventional Anger camera (without collimator) based on NaI as absorber. The C-SPRINT prototype presented in [42] employed the SPRINT scanner, a full ring of NaI scintillator crystal [73], as absorber, with the addition of a silicon pad detector placed at the ring axis to act as scatterer. In [43], the C-SPRINT camera demonstrated its capability of imaging a ^{99m}Tc and a ^{131}I radioactive sources. Despite the early promising results of the proposed prototypes and the increase of efficiency with respect to collimated systems, Compton cameras were never consolidated in clinical practice.

More recently, Compton cameras have emerged as a possible candidate for treatment monitoring in hadrontherapy. This application was first proposed in [30], where the authors perform a simulated study with a detector composed of a gaseous drift chamber and a CsI scintillator crystal, in which the drift chamber acts as scatterer and electron tracking system and the scintillator as absorber. The same concept was tested in [41] with Gadolinium Orthosilicate - Gf_2SiO_5 (GSO) scintillators, showing a correlation between the measured gammas and the dose falloff.

In the framework of the European project ENVISION (European NoVel Imaging Systems for ION therapy), aimed at developing solutions for non-invasive real-time dose monitoring in hadrontherapy, three Compton camera prototypes were designed. A prototype with a CZT scatterer and a LSO absorber was developed in Dresden [36]. This prototype reported a spatial resolution of 7 mm FWHM for a point-like ^{22}Na source placed at 7 cm from the scatterer [76]. Another prototype employing a stack of double sided silicon strip detectors as scatterers and a scintillator crystal of BGO or LYSO as absorber is under development by the CLaRyS (*Contrôle en Ligne de l'hadronthérapie par Rayonnements Secondaires*) collaboration at the University of Lyon [72, 71, 39, 19]. The third prototype designed in the context of the ENVISION project is MACACO (Medical Applications CompAct COmpton camera), developed at IFIC-Valencia [46, 45]. MACACO is a reconfigurable Compton camera that can be operated with two or three detector planes. The detector planes are based on $LaBr_3$ scintillator crystals coupled to SiPMs and the work presented in the remaining chapters of this thesis describes my contribution to the development of this prototype.

Other research groups are also investigating the use of Compton cameras for treatment monitoring in hadrontherapy. The system developed in [98] is thought to exploit the additional information carried by the recoil electron. Their design is similar to the prototype proposed by the CLaRyS collaboration, employing a stack of silicon detectors acting both as scatterer and electron tracker and a $LaBr_3$ scintillator as absorber [3]. A handheld camera based on pixelated GAGG:Ce scintillator crystals was presented in [32], where a spatial resolution below 7 mm FWHM was shown for point-like experimental sources. The first tests of this prototype with a proton beam were presented in [96]. Another promising system is the Polaris-J Compton camera [51], composed by four stages of CZT pixelated detectors. The prototype demonstrated the feasibility of detecting 3 mm range shifts with clinical proton beams on a water target [65].

Outside the field of prompt gamma imaging, possible applications of Compton cameras include their use as laparoscopic cameras for nuclide guided surgery [59, 37] and for molecular imaging with multiple radioactive tracers [32]. They have also been employed in the field of Homeland Security, due to their capability to localize remote radiation sources [85, 26].

In this field, they are used for control in nuclear power plants and can be applied to trace the distribution of radioactive material in large areas. Cameras designed for this purpose have been successfully used to visualize the distribution of the radioactive material leaked following the Fukushima nuclear power plant accident [94, 29].

Chapter 3

The MACACO prototype

All the studies reported in this work have been performed with the MACACO (Medical Applications CompAct COmpton camera) Compton telescope prototype developed at IFIC-Valencia. This chapter is dedicated to the description of the experimental prototype. A fully functional first version of the prototype had already been built before my incorporation into the research group. Therefore, I did not participate in the design or assembly of the experimental system, and my contribution to the experimental development is related to the system characterization and to the implementation of code required for measurement analysis.

3.1 Prototype description

3.1.1 Detector description

The MACACO prototype is a reconfigurable Compton telescope that consists of several detector planes (or layers) based on monolithic cerium doped lanthanum bromide ((Ce)$LaBr_3$) crystals (BrilLanCe^{TM} from Saint Gobain Crystals [74]) coupled to SiPM arrays. Each SiPM array is a multi-pixel photon-counter (MPPC) from Hamamatsu Photonics [24]. In the prototype development, different detector models have been tested. During the course of my thesis research, three generations of detectors have been employed (although older versions had been previously built in the context of the project [46]). The tests reported in chapter 4 were performed before the last generation of detectors was acquired, so the detectors built in the first and second generations were employed. The detectors built in the third generation were ready at the time of the experimental measurements used to reconstruct the images shown in chapter 5, so they were used for those studies, given their superior performance.

Table 3.1 Detectors employed in the experimental prototype.

Generation	Crystal dimensions (mm^3)	SiPM Array Version	Pixels	Pixel size / pitch (mm^2)
First	$36.0 \times 32.4 \times 5$	S11064-050P(X1)	16	3×3 / 4.50×4.05
First	$36.0 \times 32.4 \times 10$	S11064-050P(X1)	16	3×3 / 4.50×4.05
Second	$27.2 \times 26.8 \times 5$	S11830-3340MF	16	3×3 / 3.2×3.2
Third	$25.8 \times 25.8 \times 5$	S13361-3050AE-08	64	3×3 / 3.2×3.2

The most important characteristics of the three generations are listed in Table 3.1. In the first generation, two different detector planes were built using the MPPC model S11064-050P(X1), a 4 $\times$ 4 channel array. In each of them, four MPPCs are coupled respectively to a $36.0 \times 32.4 \times 5$ mm^3 and a $36.0 \times 32.4 \times 10$ mm^3 (Ce)$LaBr_3$ crystal. The 10 mm thick crystal is designed to be used as the last plane of the telescope, as an increase in the crystal thickness entails a higher probability of total energy absorption. The second generation employs four 4 $\times$ 4 MPPCs model S11830-3340MF coupled to a $27.2 \times 26.8 \times 5$ mm^3 (Ce)$LaBr_3$ crystal. One more plane was assembled with this technology. Finally, two more planes from the third generation were assembled. These latest detectors use a MPPC model S13361-3050AE-08 with 8 $\times$ 8 pixels, so only one array per plane is employed. This MPPC array works with TSV (Through Silicon Via) technology, which improves several aspects with respect to the SiPMs employed in previous versions (reduced crosstalk and dark count rate, better uniformity among pixels, higher PDE, ...), resulting in an overall better energy resolution. The scintillator in these new detectors is also a (Ce)$LaBr_3$ crystal, with dimensions $25.8 \times 25.8 \times 5$ mm^3 to match the MPPC size. In the three generations, the pixels have an active area of 3 $\times$ 3 mm^2 composed by 3600 microcells of 50 $\times$ 50 μm^2. A detailed view of the detector components is shown in Figure 3.1.

Each of the individual detector planes (scintillator crystal coupled to SiPMs) is mounted on a hybrid board (HB), to which the SiPMs are connected. The HB gives mechanical support to the detector, provides the bias voltage to the SiPM arrays and hosts the readout ASIC (Application-Specific Integrated Circuit). The bias voltage to the detectors is provided by a power supply specifically designed for SiPMs [68]. Each HB is connected to a custom made data acquisition (DAQ) board [92, 90] equipped with an FPGA (Field-Programmable Gate Array), model XC3S4000 from Xilinx, that manages the acquisition process. The 64 channels of each detector are read out by the ASIC VATA64HDR16 from Ideas [8, 52]. The first stage in the ASIC is a preamplifier, after which the signal enters the slow shaper, a semi-Gaussian filter that delivers the energy information either in a voltage or a current signal. An 8-bit

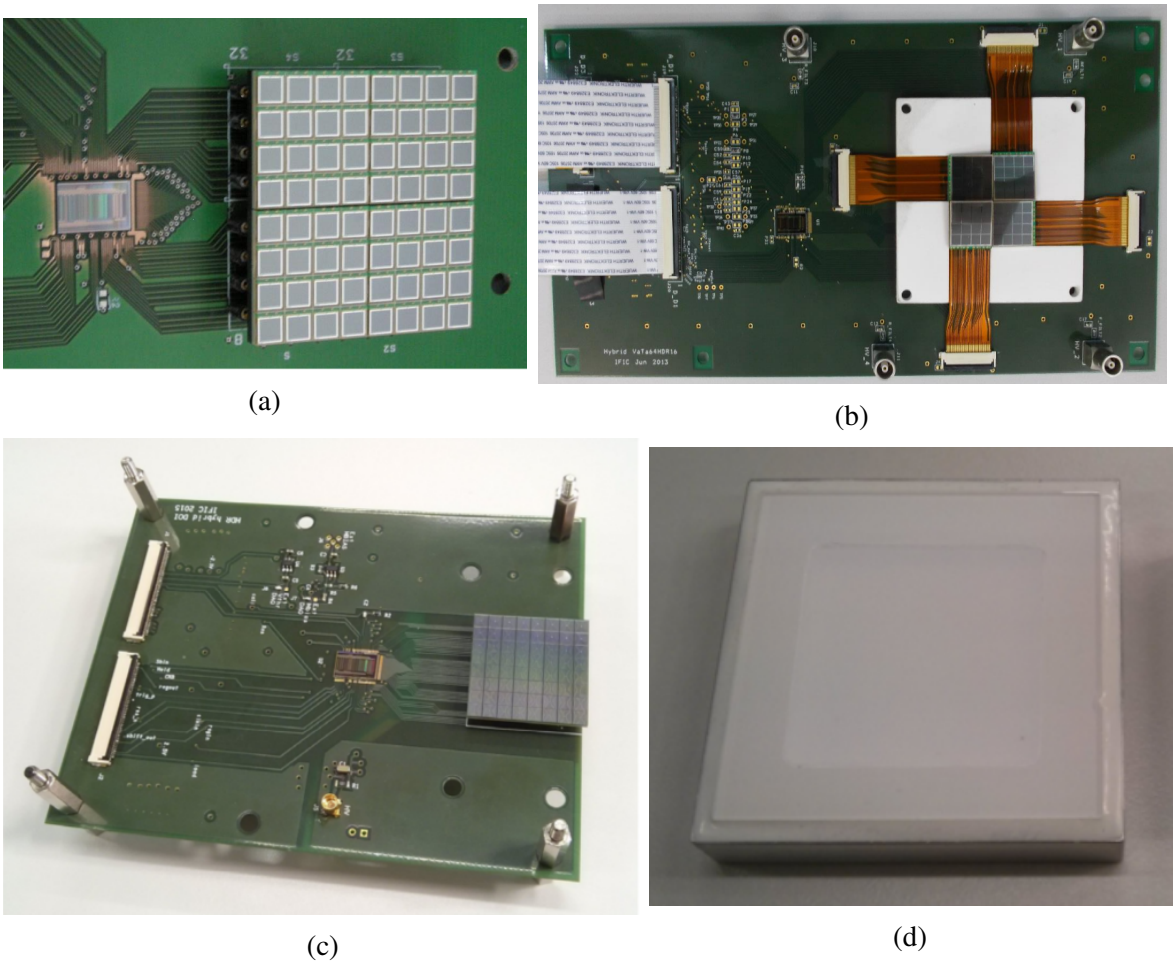

(a) (b)

(c) (d)

Figure 3.1 Components of the detector planes. HB with the VATA64HDR16 ASIC and the MPPCs employed in the different generations: first (a), second (b) and third (c). A $LaBr_3$ scintillator crystal of $25.8 \times 25.8 \times 5$ mm^3 is shown in (d).

digital-to-analog converter (input DAC) allows the user to fine-trim the input potential of the preamplifier. Through the application of the DACs, the input potential of individual channels can be decreased from the array bias voltage up to 1 V in steps of 3.5 mV. This allows the operating voltage of each pixel to be adjusted independently in order to achieve better uniformity across the whole matrix [8]. When an event takes place, the ASIC generates a signal that triggers the readout sequence. The analog data from the HB is transferred to the DAQ board, where it is amplified and digitized by a 12-bit Analog-to-Digital Converter (ADC) and assigned a time-stamp provided by the FPGA. The data is then formatted and sent to the computer for further processing.

A thermal sensor is also placed in the HB for temperature monitoring. The temperature is measured using an integrated thermometer (DS18B20-PAR from Maxim Integrated) which

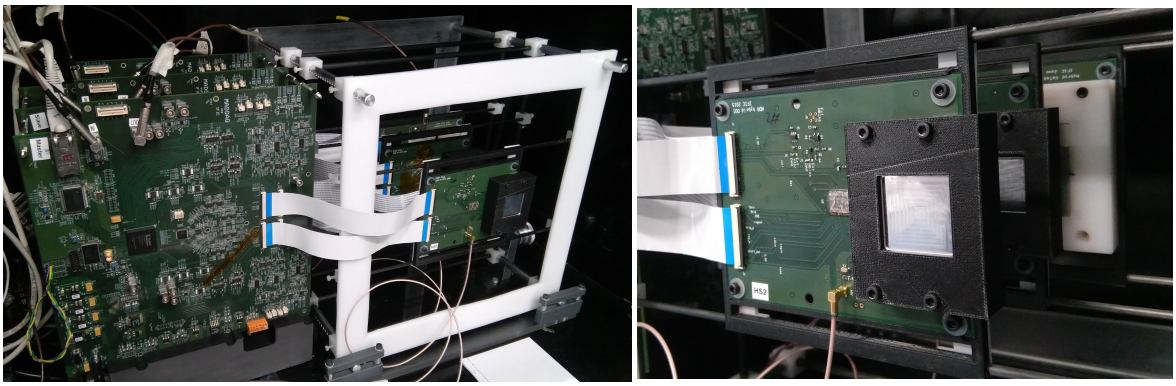

(a) (b)

Figure 3.2 Pictures of the experimental prototype assembled with three planes. Whole system (a) and detailed view of the detector planes (b).

communicates with the FPGA via I2C bus. The DS18B20 outputs the digitized temperature in a 12 bit code when the FPGA sends the corresponding command. This chip has an accuracy of 0.5°C in the range of -10°C to 85°C, in which the operation temperature of the system is always contained.

3.1.2 Data acquisition software

The acquisition process is controlled through a dedicated software from the PC. Each DAQ board communicates with the PC via Ethernet connection, using the UDP (User Datagram Protocol) protocol. The acquisition program allows the user to set different detector parameters before a measurement run starts. Among others, the low energy detection threshold, the input DACs for the individual pixels and the trigger pulse duration are defined in this program. It also allows the user to choose between two acquisition modes: *singles* (each detector plane is triggered independently) or *coincidences* (detectors working in time coincidence). A software-triggered acquisition mode is also available, which can be employed in verification tests and for pedestal measurement (see section 3.1.4).

3.1.3 Operation in time coincidence

The decoupling of the front-end (HB) and back-end (DAQ boards) readout electronics results in a flexible and modular design of the overall system. The different detector planes can be operated independently or assembled together into a Compton camera with either two or three stages. The system is equipped with a coincidence board that triggers the acquisition of data in time coincidence. The coincidence board is based on a Virtex 5 FPGA evaluation board.

The trigger signals from the detectors are connected to the input ports of the coincidence board.

If the system is assembled with only two detector planes, the coincidence board acts as a logic AND gate. The trigger signals from both detectors are delivered to the coincidence board. When these signals overlap, a trigger signal is sent from the coincidence board to the external trigger input of the two DAQ boards simultaneously, which starts the event acquisition of both detectors.

When three planes are mounted, two coincidence strategies can be selected remotely from the acquisition software. In the first mode, a logic AND operation is performed among the three trigger inputs, returning a logic '1' if all three inputs present overlapping trigger signals. In the second coincidence mode, the board outputs a logic '1' if two or more inputs present a trigger simultaneously. In both cases, when the coincidence condition is satisfied, the output signal is sent to all DAQ boards and the charge stored in the three detectors is read out.

3.1.4 Data processing

The signals acquired in the 64 channels of each detector in a measured event are pedestal-subtracted and summed up to obtain the total event signal. The pedestals indicate the offset of the ADC for each channel, which corresponds to the position of zero energy. Prior to a data run, the pedestals are determined by acquiring and averaging a few thousand events obtained in the absence of a source, through a software-triggered acquisition, to force a readout of the detector with no energy detection.

The signal is employed to generate the energy histograms. For energy calibration of the detectors, data are taken with radioactive sources in *singles* mode. Plotting the measured energy versus the peak position in the histogram allows the determination of the calibration curves that are employed for energy calibration of the coincidence data. When data are acquired in coincidence mode, the total ADC signal obtained in each event is converted to energy employing the calibration functions previously generated.

When the system is operated with three detector planes, data processing also includes determination of the detectors involved in the coincidence event. Since for each coincidence event the three detector planes of the telescope are read out independently of the number of detectors involved in the coincidence event, it is necessary to apply an energy cut in order to identify the planes in which the photon interacted. When an acquisition is triggered by only two of the three planes, the charge read out from the remainder plane corresponds to zero energy value. Thus, by applying a low energy cut, the actual planes involved in the coincidence are identified and the one with zero value can be discarded.

3.2 Simulation of the system

Parallel to the development of the experimental prototype, simulation studies are also carried out. Simulations are used to gain insight into the physical processes taking place in the detector, to test the system under experimentally unavailable situations or to evaluate image reconstruction algorithms. The simulated studies presented in this book have been performed with GATE version 7.0 [27], a Monte Carlo simulation toolkit based on Geant4 [2]. The standard electromagnetic physics list without optical photons has been employed in all cases. As a first approximation, the simulated Compton camera is modelled as two (or three) parallel $LaBr_3$ crystals with the dimensions of the experimental detectors*. The remaining elements of the experimental prototype (SiPMs and readout electronics) are not included in the simulation. GATE offers multiple possibilities to simulate the source. In the studies reported in this work, mainly two kinds of simulated sources have been employed: point-like radioactive sources and gamma sources with different geometries. The radioactive sources have been simulated with the same parameters as those experimentally measured, and have been employed for the characterization tests reported in chapter 4. In those cases, the material encapsulating the source was also included in the simulation. Gamma sources emit photons in a predefined energy distribution and direction, and they have been used in the imaging studies described in chapters 5 and 6.

The simulated data can be retrieved with different levels of precision. As the simulation runs, the program generates the primary particles one by one with the initial conditions set by the user. The paths of the generated particles are followed and, once they reach the defined detector system, their interactions are recorded. The result of the simulation is stored in two data sets, which are produced by the same interactions but convey information with different levels of detail: *hits* and *singles*. One hit is recorded every time that a physical interaction takes place, be it produced either by a primary or a secondary particle. The *hits* list contains the exact information of the generated processes, including the nature of the physical interactions and the particle that produced it. The information collected in the *hits* is thus ideal, but experimentally inaccessible. In order to present a more realistic approach, the *singles* list stores the information as it would be measured by a real detector. Each *single* event congregates all the processes undergone by the primary and its secondary particles at one interaction point. In a *single*, the total energy deposited by all particles constitutes the measured energy and the interaction position inside the crystal is given by a weighted average over all energy depositions. The spatial and energy resolutions of the system are

*Depending on the date of simulation, the crystal dimensions are chosen according to the latest acquired crystals. The crystal dimensions and geometrical configuration of the simulated detector are indicated for all the simulations mentioned hereafter.

also applied at the *singles* level in the simulation. Figure 3.3 represents schematically the simulation of a Compton interaction by a primary gamma in the detector. The recoil electron scatters multiple times in the crystal, producing one hit at each interaction, until it loses all of its energy and is again reabsorbed. The whole simulated sequence constitutes only one *single* event.

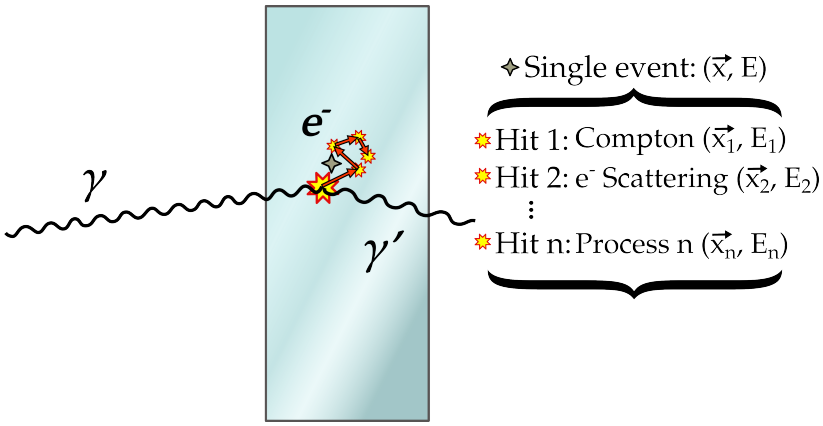

Figure 3.3 Diagram of the physical processes generated in a simulated Compton interaction.

Once the simulated data are generated, an external sorter is applied in order to select the events that are used for image reconstruction. The main purpose of the sorter is to extract from the simulated data those events occurring in time coincidence in different detector planes. The applied sorter can classify the coincidence events from the *hits* and *singles* lists independently. From the *singles*, the coincidences are extracted employing a time coincidence window and simply selecting the events taking place in different detector planes within that window. The *hits* list allows more detailed selections, since the information of all the physical interactions undergone by the different particles is available. From the *hits* list, the true signal events (excluding the unwanted coincidences described in section 2.4.1) can be extracted for reconstruction studies with more ideal data. The *hits* and *singles* lists can be related through a parameter called *event ID*, an event counter that remains constant for every generated primary particle and all sequences of secondary particles derived from it (in Figure 3.3, the depicted *hits* and *single* would have a unique event ID). The comparison between *hits* and *singles* coincidence detections helps understanding the measured data, and allows classification of the signal events and quantification of the background.

3.3 Detector characterization

In order for the whole prototype to achieve its optimal performance, it is important to test and adjust the independent planes individually. This section is dedicated to presenting the most relevant parameters of our detectors.

3.3.1 Uniformity

Small variations in the manufacturing process of the MPPCs produce photodetector elements with different operation voltages, which result in gain differences among the 64 pixels when a common bias voltage is applied to the entire array. In our detectors, the channels response is equalized through the input DACs in the ASIC, which allows the fine adjustment of the voltage applied to the individual pixels.

For each detector plane, under a given set of operation parameters (mainly bias voltage and temperature), the appropriate input DACs must be found. Experimentally, the DAC adjustment is performed by measuring the system response to a radioactive source (in our case, usually ^{22}Na) placed at a distance sufficiently far from the detector to ensure that the whole detector surface is uniformly irradiated [8]. The DAC value for the different channels is tuned manually until a homogeneous response is observed in all of them. Figure 3.4 shows the ADC output averaged over a few thousand events from the different pixels in a detector plane before (left) and after (right) application of the input DAC values.

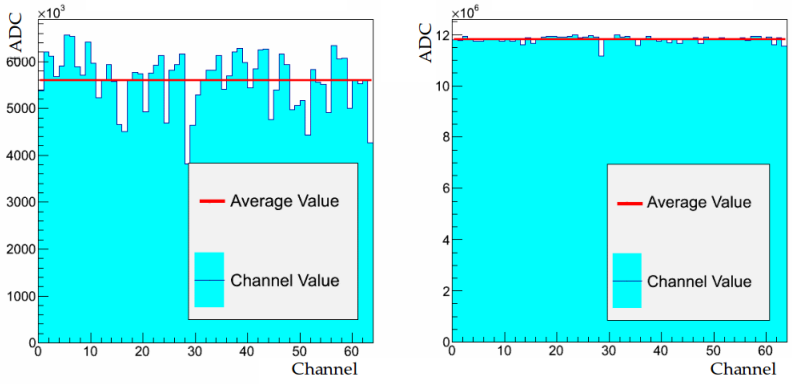

Figure 3.4 Equalization of the pixel response through application of the input DACs.

3.3.2 Energy response

The correct identification of the energy transferred by the incident gamma is essential in Compton imaging. Therefore, the energy response of the detector must be accurately

calibrated and its resolution as high as possible. After the equalization of the detector response, the energy response is calibrated with the aid of radioactive sources emitting gammas of known energy. The calibration parameters are then applied to the ADC values obtained for each event to find the measured energy.

The detector gain and, therefore, its calibration curve, depend on the the operation parameters at the given measurement conditions. At a fixed bias voltage, the most important gain variations are due to changes in the system temperature. The detector gain is proportional to the applied overvoltage, and its dependence with temperature arises from the increase of the breakdown voltage for higher temperatures: if the bias voltage is constant, the increase of the breakdown voltage causes the reduction of the overvoltage and, thus, the detector gain [69]. Because the system response changes with temperature, the optimal performance of the detectors is achieved with different bias voltage and input DACs at different temperatures. In order to prevent the application of incorrect calibration parameters due to temperature changes during the measurement, two experimental strategies are followed. The first and simplest of them is to ensure a constant temperature throughout the measurement time. This is usually achieved by allowing the system a warm-up period, in which the detector temperature slowly rises until reaching stability. In our laboratory conditions, the warm-up time is about one hour and the temperature is stabilized around 30^{o}C. The second strategy is to employ the thermal sensor attached to each detector plane to correct for the registered variations, through a previously calculated energy calibration curve as a function of the temperature. This method is more robust when the temperature cannot be maintained stable during a complete measurement run, but has one important shortcoming. Since the calibration must hold for all the temperatures in the considered range, the detector parameters need to remain constant, which means that the response is not fully optimized for the whole range. In practice, in most of the measurements carried out so far with our prototype the temperature has been kept stable, so the first strategy has been followed. The only exception was reported in [91], where the temperature calibration was needed and employed.

An important parameter of the detector energy response is its linearity within the measured range. In order to test the detector linearity, more than two gamma energies need to be measured. This can be achieved employing several radioactive sources of different isotopes or with a single source with a higher number of different gammas in its emission spectrum. An excellent isotope for that purpose is ^{152}Eu, which yields the photons listed in Table 3.2[†]. The spectra measured by three detector planes with a ^{152}Eu source are plotted in Figure 3.5. To understand the differences among the spectra, it should be noticed that the spectrum with the biggest crystal was taken when the whole system was assembled with three planes (working

[†]Only the emissions with intensity superior to 3% are mentioned.

in singles mode), and said crystal was placed in the third plane position. This explains the count decrease in the low energy peaks, as most of those photons are absorbed in the previous stages. The right hand side of Figure 3.5 shows the calibration curve corresponding to the $27.2 \times 26.8 \times 5$ mm^3 crystal, where the linear behaviour of the detector in the considered range can be seen.

Table 3.2 Gamma energies emitted by ^{152}Eu. Intensities are given with respect to all decay modes.

Energy (keV)	121.8	244.7	344.3	779.0	867.4	964.1	1085.9	1112.1	1408.0
Intensity (%)	20.6	5.5	7.4	3.6	3.1	10.5	7.4	9.8	15.1

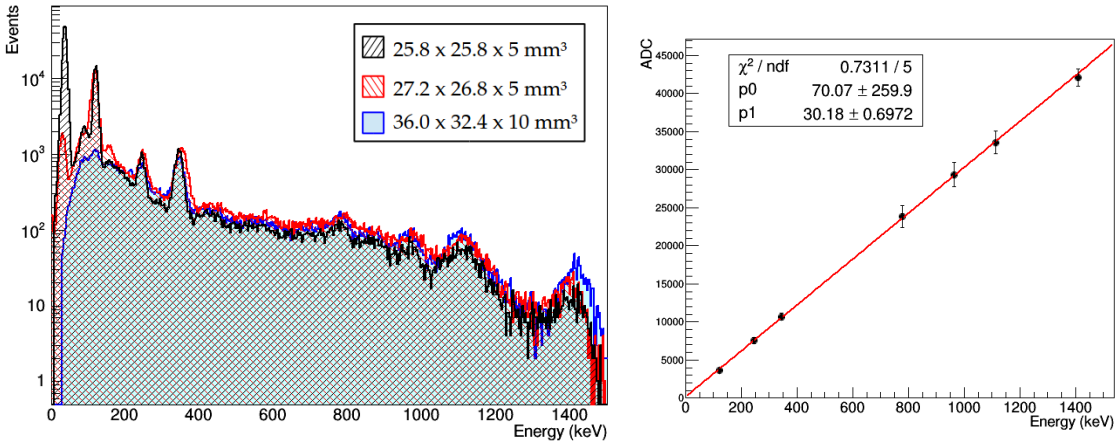

(a) (b)

Figure 3.5 Spectra of a ^{152}Eu source measured independently with three detector planes (left) and the calibration curve for one of them (right).

If the energies involved in the measurement are contained within the linear region of the detector, radioactive sources emitting just two different gamma ray energies can be used to fully calibrate the detector. It is the case of ^{22}Na sources, which emit 511 and 1275 keV photons (the 511 keV photons are generated in the positron annihilation following a β^+ decay). That is one of the reasons why a ^{22}Na source has been employed in most of the characterization tests carried out in our laboratory, the other main reason being that this isotope is widely used in most medical imaging research facilities, owing to its relatively long lifetime and its suitability for PET imaging. The calibrated spectra of a ^{22}Na source, measured separately with three of the developed detector planes, can be seen in Figure 3.6, where the increase in energy resolution of the newest detectors can be clearly seen in the

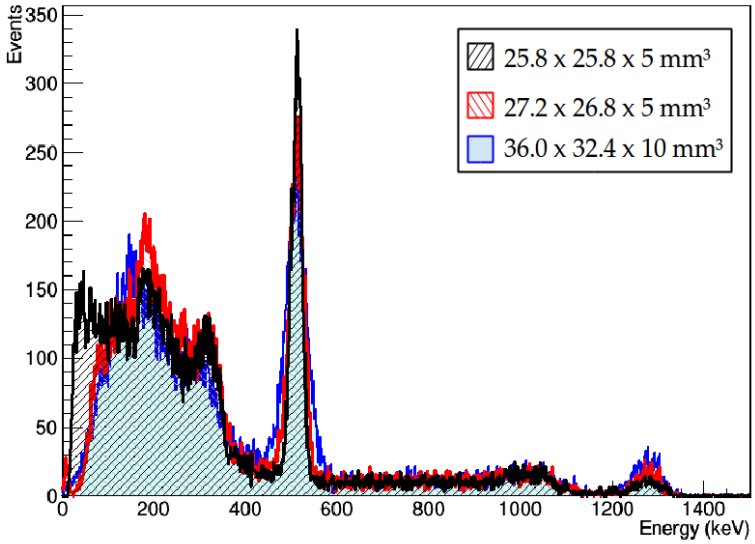

Figure 3.6 Spectra of a ^{22}Na source measured independently with three detector planes.

narrowing of the 511 keV peak. The energy resolution achieved for the different detectors is listed in Table 3.3.

Table 3.3 Energy resolution obtained with the different detectors employed in the experimental prototype.

Generation	Crystal dimensions (mm^3)	Best energy resolution (FWHM at 511 keV)
First	$36.0 \times 32.4 \times 5$	7.2
First	$36.0 \times 32.4 \times 10$	7.4
Second	$27.2 \times 26.8 \times 5$	6.4
Third	$25.8 \times 25.8 \times 5$	5.3

3.3.3 Coincidence timing resolution

The coincidence timing resolution of the system in the two-plane operation mode has also been characterized. This measurement was taken with a ^{22}Na source. The $27.2 \times 26.8 \times 5$ mm^3 crystal was used as the first plane and the $36.0 \times 32.4 \times 10$ mm^3 as the second one. Both the separation between detectors and the distance from the source to the first plane were approximately 40 mm. When the trigger signals of the two detectors generate a logic AND in the coincidence board, their time difference is registered by an oscilloscope

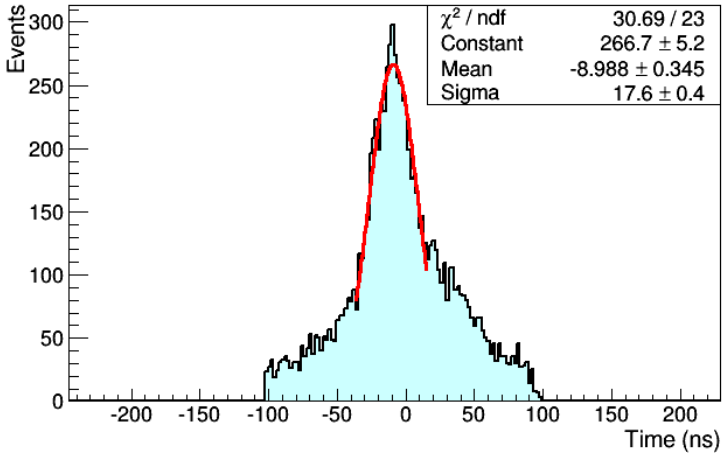

Figure 3.7 Coincidence timing resolution of 41 ns FWHM with two planes.

LeCroy WavePro 950. The result is plotted in Figure 3.7, where a coincidence timing resolution of 41 ns FWHM is achieved. This value is worse than the usual values for detectors employed in medical imaging. This poor timing resolution is due to the use of the 64-channel VATA64HDR16 ASIC with a continuous crystal: the trigger is generated when the signal in any of the channels surpasses the threshold level, more appropriate for pixellated crystals [8]. The experimental prototype is still in a development stage, in which its timing resolution will be considerably improved. In any case, the measurements reported in this thesis were carried out with low activity radioactive sources (below 1 MBq), so the fraction of random events introduced by the timing resolution is not significant in the reported results.

3.3.4 Spatial resolution

The interaction position of the gamma rays in the crystal is determined as described in section 1.3.3. In order to quantify the intrinsic spatial resolution of the detectors, an electronically collimated ^{22}Na source has been measured in time coincidence with a second smaller detector. The second detector employed in the experimental set-up is a $1 \times 1 \times 10$ mm^3 LYSO crystal coupled to a single SiPM of 1×1 mm^2. It is placed orthogonally to the detector surface at a distance of 30 mm between crystal surfaces, while the source is located between the two detectors at 5 mm from the LYSO crystal. With this geometrical configuration, the collimated 511 keV photons enter the crystal surface in a region with a diameter of approximately 0.21 mm. Figure 3.8a shows the reconstructed interaction positions in the plane parallel to the detector surface, for a measurement in which photons impinge on the detector center. The Gaussian fit over a profile along the maximum yields a FWHM of

1.1 mm (Figure 3.8c) in the measured position. Figure 3.8b shows the reconstructed depth of interaction (DoI) for those same events. A color map with the raw values read out by the different channels in the data acquisition can be seen in Figure 3.8d. Tests on position determination yielded a spatial resolution of approximately 1.5 mm FWHM for the 10 mm thick crystal and 1.2 mm FWHM for the 5 mm crystals in the whole crystal surface [47, 7].

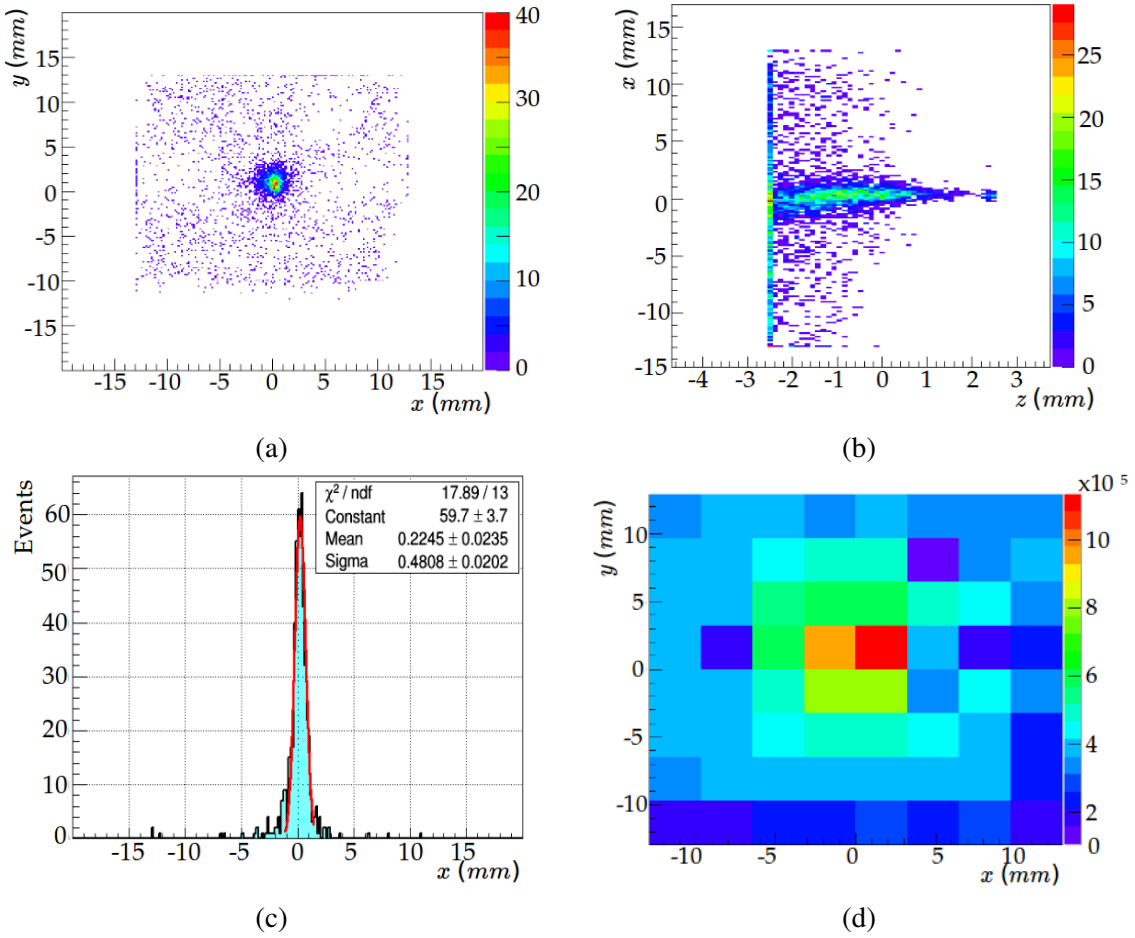

Figure 3.8 Reconstructed impact positions from an electronically collimated ^{22}Na source. (a) Reconstructed position in the *xy* plane. (b) Reconstructed position in the *xz* plane. (c) Profile along the maximum in the *x* direction. (d) Raw readout value by the different pixels.

Chapter 4

Experimental results with point-like sources

This chapter reports a series of experimental measurements conducted with the whole system working in time coincidence. Results are shown for both two- and three-plane operation modes in the laboratory with radioactive sources emitting photons in a range of energies from 511 to 1836 keV. Additionally, measurements performed with 4439 keV gammas produced in an accelerator facility are also presented. The results presented in this chapter are published in [58] and [56].

4.1 Coincidence measurements with radioactive sources

Measurements in time coincidence with the prototype in the two-plane and three-plane operation modes have been performed in the laboratory with radioactive sources. This section reports the performance evaluation tests carried out with ^{22}Na and ^{88}Y point-like radioactive sources. The most important characteristics of the employed sources are listed in Table 4.1.

Table 4.1 Radioactive sources employed in laboratory measurements.

Isotope	Photon energy (keV)	Activity (kBq)	Nominal diameter of active area (mm)
^{22}Na	511, 1275	847	0.5
^{88}Y	898, 1836	506	3

4.1.1 Two plane operation mode

A thorough characterization of the system assembled with two detector planes was carried out. In these tests, the $27.2 \times 26.8 \times 5$ mm^3 crystal was used as the first plane and the $36.0 \times 32.4 \times 10$ mm^3 as the second (as the latest detectors with improved energy resolution had not yet been acquired). The first reported measurements were taken with the ^{22}Na source placed at 53 mm from the first plane and an inter-plane distance of 50 mm.

Energy spectra

The results reported henceforth were measured with the system working in time coincidence, aiming at detecting only those events generated by one interaction at each plane derived from a single primary photon. Therefore, the spectra measured by the detector planes are qualitatively different from those obtained in singles mode. The spectrum in the first plane must be completely dominated by a Compton continuum, while the second plane spectrum will still have contributions from both Compton and photoelectric interactions by the scattered gammas. Since the initial photons deposit part of their energy in the first plane, the energy detected in photoelectric absorptions in the second plane will be shifted towards lower energies. Figures 4.1a and 4.1b show the spectra measured in the first and second planes respectively. The measurement has been reproduced in a simulation matching the experimental detector geometry and performance. In all simulated results presented in this chapter, the singles data with realistic experimental energy and spatial resolution have been employed. The simulated spectra are plotted together in those same figures along with the experimental results, showing good agreement in both data sets.

In contrast to the previous explanation regarding the expected spectra, small peaks appear at 511 and 1275 keV (the emitted photon energies) in the spectra measured by the different planes in time coincidence. These peaks are related to the full absorption of a primary gamma in a single plane, and therefore should not be measured in time coincidence. The reason why these peaks appear in the measurement is the time correlation of the two spectral lines from ^{22}Na, which are emitted quasi simultaneously. This leads to the possibility of detecting two separate primary gammas within the time coincidence window, and constitutes an important source of noise for this radioactive source. These noisy events can also be appreciated in the scatter plots shown in Figures 4.1c (experimental data) and 4.1d (simulated data), which represent in the x and y axis the energy measured by the first and second detectors, denoted as E_1 and E_2 respectively, for each coincidence event. In these plots, the random coincidences with full absorption in one detector are distinguishable as vertical and horizontal lines of 511 and 1275 keV. In the same graphs, true signal events generated by a Compton scatter

interaction in the first plane and a photoelectric absorption in the second one are identified in the visible diagonal lines, for which the sum of both energies add up to the initial gamma energy.

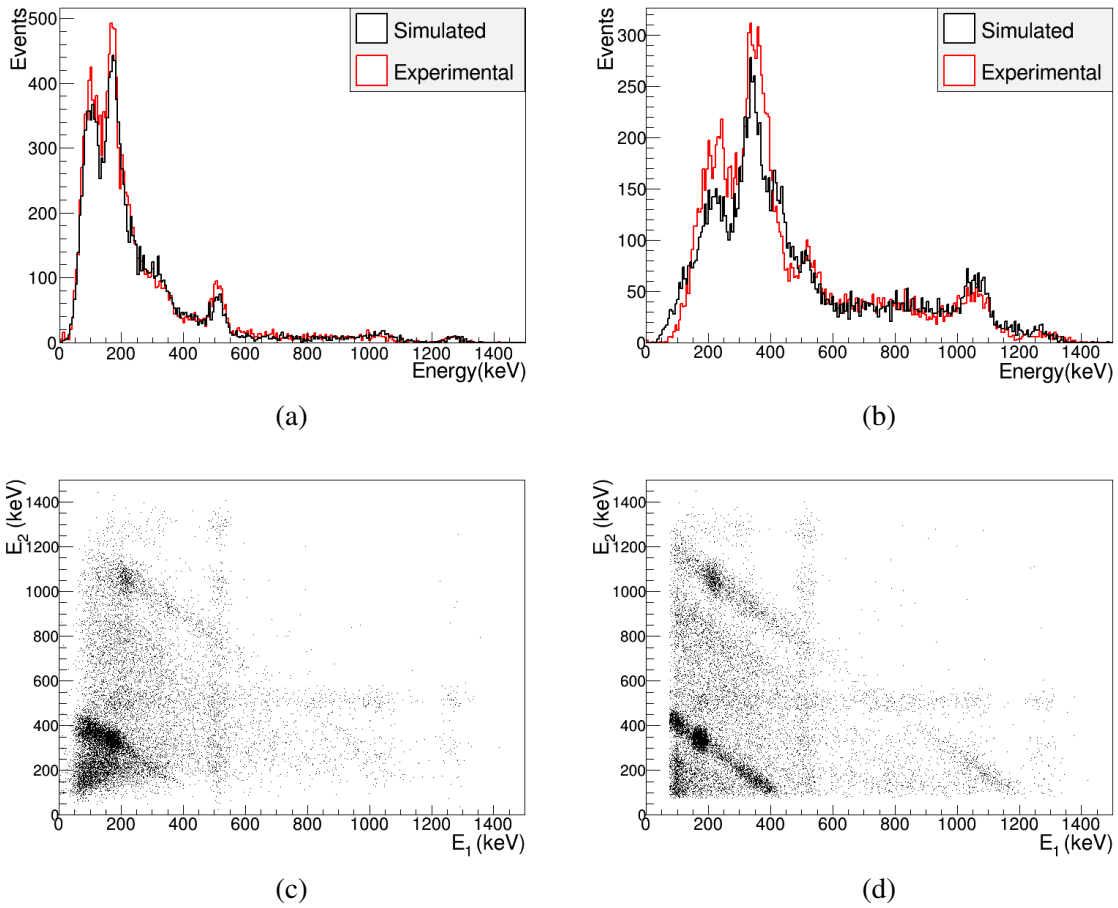

Figure 4.1 Spectra measured by the first (a) and second (b) detector planes working in time coincidence. The energy deposits in the second plane versus the energy in the first plane are shown for the real (c) and simulated (d) data.

Another interesting result is the summed energy spectrum, obtained by summing the energy depositions in both planes from the same coincident event. In the summed energy spectrum, the photopeaks at the emitted gamma energies are recovered if the photons scattered in the first plane are fully absorbed in the second one. We can also notice a small peak at the energy equivalent to the sum of both gammas (1786 keV), produced by the total absorption of two different photons, one in each plane. Again, this effect appears due to the time correlation in their emission. The correct assignment of the photopeak energies in this spectrum is a confirmation that all the involved detector planes are properly calibrated. The summed energy spectra for the aforementioned experimental and simulated results are plotted in Figure 4.2.

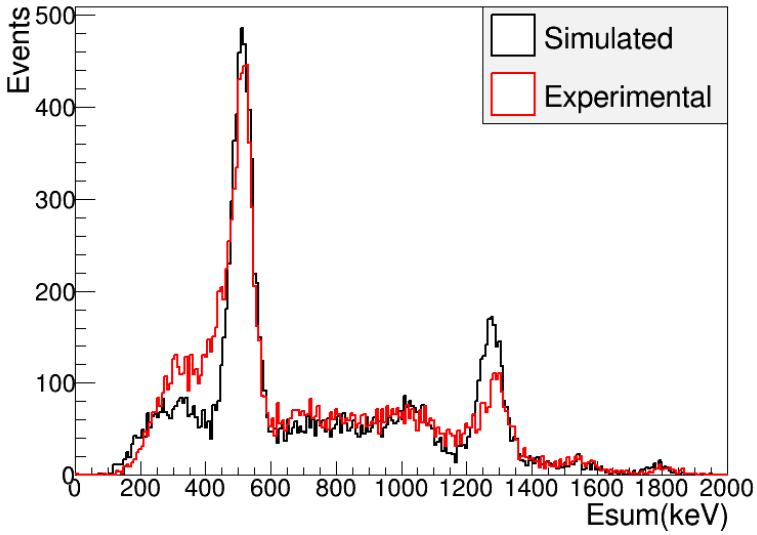

Figure 4.2 Experimental and simulated summed energy spectra of a ^{22}Na source obtained from the measurements in both planes operated in time coincidence.

Scattering angle

For the two plane case, the knowledge of the source position helps us to verify the proper functioning of the device. Taking the source location as a known parameter, the actual Compton scattering angle can be calculated employing only the measured positions of the interactions at both planes ($\theta_{geometrical}$), which can then be compared to the angle reconstructed by the Compton-scattering formula ($\theta_{Compton}$).

Figure 4.3b shows the comparison between both angles, reconstructed as just described, for the data obtained from the experimental (4.3a) and simulated (4.3b) ^{22}Na source. $\theta_{Compton}$ in those images has been calculated selecting events according to the energy deposited in both interactions: events with a summed energy between 600 and 1350 keV were assigned a gamma energy $E_0 = 1275$ keV, and events with summed energy below 600 keV were given an $E_0 = 511$ keV, in spite of contamination from partial depositions of the higher energy photon. True coincidence events produced by one incident gamma give rise to the diagonal line $\theta_{geometrical} = \theta_{Compton}$, whereas random and background events are found outside it. The width of the distribution is caused by the finite energy and spatial resolution of the detector.

Three noise lines are visible at $\theta_{Compton} \approx 0.4$, $\theta_{Compton} \approx 0.75$ and $\theta_{Compton} \approx 1.05$ rad. The $\theta_{Compton} \approx 1.05$ and $\theta_{Compton} \approx 0.4$ rad lines are created by backscatter events of 511 keV and 1275 keV gammas, respectively, which are detected in coincidence and assigned a wrong interaction order. Finally, the $\theta_{Compton} \approx 0.75$ rad line is due to random events produced by a full absorption of a 511 keV gamma in the first plane and an interaction from a different

photon in the second one, thus generating a background coincidence with an assigned initial energy of $E_0 = 1275$ keV.

Although real applications of a Compton camera require to reconstruct the origin of gamma rays without any previous knowledge of the source position, this agreement between the reconstructed scattering angles is taken as an experimental verification that our prototype is working as expected.

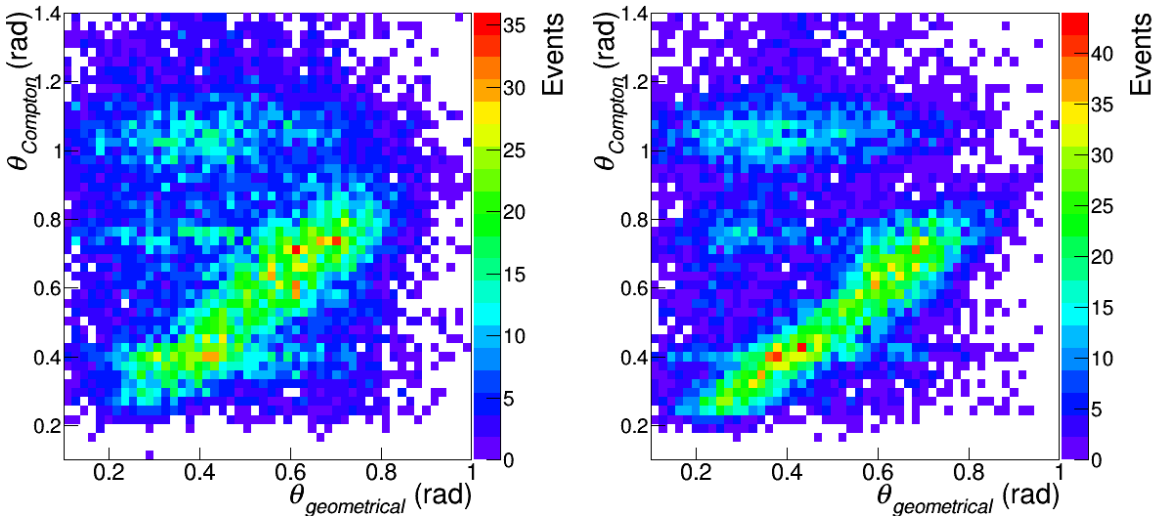

Figure 4.3 Experimental (a) and simulated (b) comparison of Compton scattering and geometrical angles for a ^{22}Na source.

Imaging tests

This section presents the imaging tests performed with the mentioned radioactive sources in the laboratory. In all cases, the employed FoV was a three-dimensional space of $101\times101\times51$ mm^3 divided into voxels of $1\times1\times1$ mm^3. To compare between different configurations, the number of iterations in the list mode MLEM algorithm employed for all reconstructed images is set to 20, although the image quality is not significantly improved between successive images for more than 10 iterations. In order to reduce the high frequency noise generated by the iterative algorithm, a median filter (see section 2.4.3) with cubical footprint and window size $3\times3\times3$ voxels in the 3D image space has been applied after final iteration to all images shown.

Measurements of the ^{22}Na source were taken for three different relative distances between the source and the detector planes (configurations 1, 2 and 3 in Table 4.2). This allows us to

assess how the geometrical configuration of the camera affects the final reconstructed images. For each of the geometrical configurations, the source was placed manually at nine different points within the defined FoV, forming a rectangular array with spacing of approximately 20 mm along the x and y axes.

Table 4.2 Distances in the geometrical configurations tested in the two-plane operation mode.

Distance (mm)	Source - Plane 1	Plane 1 - Plane 2
Configuration 1	53	50
Configuration 2	104	50
Configuration 3	53	100
Configuration 4	41	42

Figure 4.4 shows the reconstructed images of the ^{22}Na source in nine positions, where the different source positions are clearly visible. From left to right, the columns contain the images obtained for the first, second and third geometrical configurations described in Table 4.2. Since ^{22}Na emits photons of 511 and 1275 keV, coincidence events can be selected according to the energy of the photon that was measured. In these tests, the initial photon energy is given to the reconstruction algorithm as a known parameter. Events are selected as described in the previous section, assigning an initial energy of 511 keV to those events with summed energy below 600 keV and 1275 keV to those with summed energy above 600 keV. Thus, two different images from the same measurement can be obtained. The top row images in Figure 4.4 correspond to the events selected with 511 keV, and the bottom row to those with 1275 keV.

For each configuration and energy, images of the source at different positions were reconstructed independently, with 5000 coincidence events per image. Since the employed reconstruction algorithm produces three-dimensional images, the represented pictures correspond to the two-dimensional slices of the reconstruction where the voxel with maximum value is located. For each measurement, slices containing the maximum value voxel in the reconstructed three-dimensional space were selected. The slice containing the voxel with maximum value is not necessarily found at the same depth in all the reconstructed images, mainly due to small variations in the positioning of the source along the axis perpendicular to the detector planes. All slices selected to form the summed images are contained within an interval of ± 3 mm in depth with respect to the source-plane distances listed in Table 4.2. In the images shown in Figure 4.4, the selected two-dimensional slices were then summed to form a single image for a better image display.

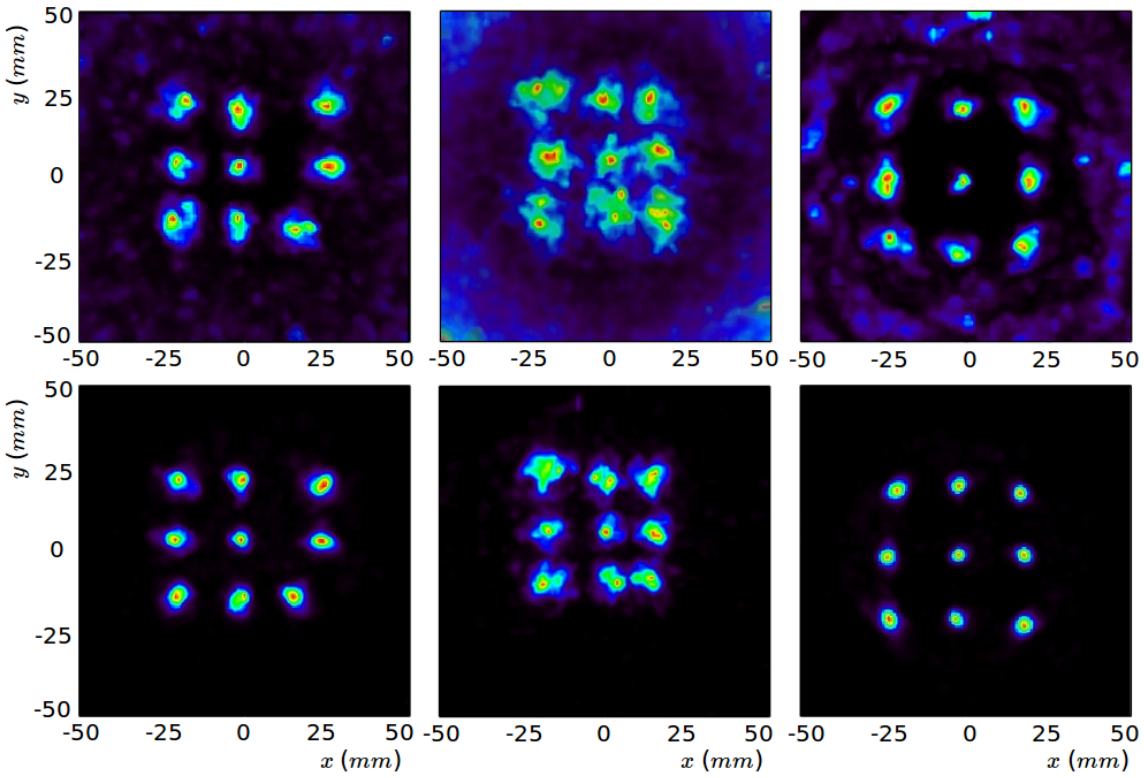

Figure 4.4 Reconstructed images of a ^{22}Na source at nine different positions for the three tested geometrical configurations. From left to right: configurations 1, 2 and 3. Images obtained for the two different gamma energies: 511 keV (top) and 1275 keV (bottom).

From the reconstructed images represented in Figure 4.4, two important aspects can be mentioned. In the first place, the source positions reconstructed with 511 keV match those reconstructed with 1275 keV. This was naturally expected, since they correspond to the same measurements, and was confirmed after the results analysis. A particular case is observed in the images obtained in configuration 1, where the source position in two measurements has been reconstructed outside the rectangular array. Since the radioactive source was moved manually for every measurement and this effect appears for both energies, the deviation of these two spots is attributed to a human error at the time of placing the source. In the second place, several trends regarding image quality are visible. From the two gamma energies measured, the images reconstructed with the 511 keV present more noise and worse resolution. This is due to three contributions, namely the higher fraction of backscatter events, bigger error in the Compton scattering angle for lower energies (see equation (2.16) in section 2.4.2) and the contamination of the data classified as belonging to 511 keV gamma interactions by partial depositions of 1275 keV gammas. With respect to the different geometries, better images are obtained when the source is placed closer to

the first plane, since in those cases the cone angle error has a smaller impact, and when the inter-plane distance is increased, since this reduces the uncertainty in the orientation of the cone axis.

The ^{88}Y radioactive source has also been imaged with our prototype. Similarly to the tests with ^{22}Na, the source was measured again at nine different points with spacing of approximately 20 mm along the x and y axes. In this case, the measurements were taken with only one geometrical configuration of the system, specified as Configuration 4 in Table 4.2. The images were reconstructed as discussed for the ^{22}Na source: the events corresponding to the different energies are separated through an energy cut in the summed spectrum and each position is reconstructed independently in a 3D FoV. The resulting image is median filtered and slice selected, and the images from all positions are then combined to form the displayed figures. The reconstructed images are shown in Figure 4.5, in which the image on the left was obtained for 898 keV and the one on the right for 1836 keV. Each point-like source image with 898 keV was reconstructed using 4000 coincidence events, and with 2700 coincidence events for the 1836 keV energy. In agreement with the results from the ^{22}Na source, in this case the highest energy photons also produce better quality images.

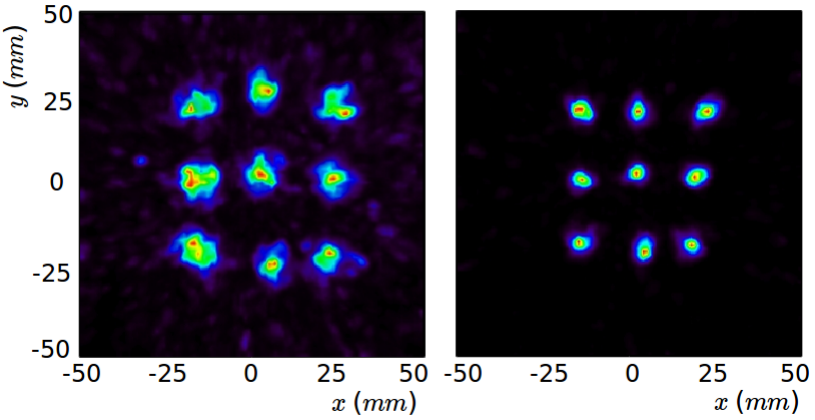

Figure 4.5 Reconstructed images of a ^{88}Y source at nine different positions. Images obtained for the two different gamma energies: 898 keV (left) and 1836 keV (right).

The ^{22}Na and ^{88}Y sources were also imaged in the same geometrical configuration in order to compare the reconstructed images corresponding to the four incident energies. Configuration 4 was chosen for these tests. Coincidence events from each source were measured independently, and one separate image is obtained for the events corresponding to each energy. The reconstructed images can be seen in Figure 4.6. The results from the ^{22}Na source are shown in the top row, and those from the ^{88}Y source in the bottom row. For both sources, the left column shows the image obtained from the lowest energy gamma and

the middle column the image from the highest energy gamma. In all cases, images were reconstructed with 5000 coincidence events. The right column represents the profiles along the x direction through the maxima of the previous images, where it can be appreciated that the images from the different energies of the same source are reconstructed in the same position.

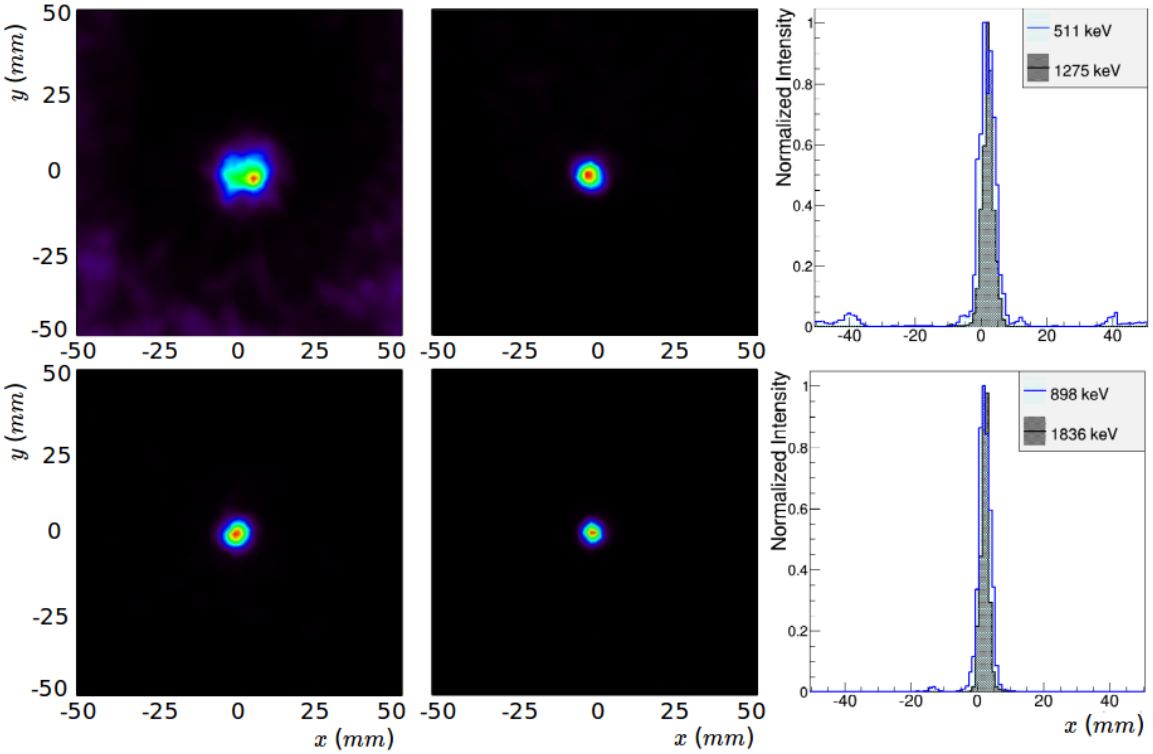

Figure 4.6 Reconstructed images of different photon energies for a the same system configuration (configuration 4 in Table 4.2). Top: image of the ^{22}Na source with 511 keV (left), 1275 keV (center) and their profiles (right). Bottom: image of the ^{88}Y source with 898 keV (left), 1836 keV (center) and their profiles (right).

Images obtained for different photon energies and geometrical configurations are compared in terms of spatial resolution. The figure of merit calculated is FWHM of Gaussian fits to the profiles along the x and y axes through the maximum value in the two-dimensional image. It should be noticed that, when reconstructing point-like sources with the MLEM algorithm in zero background, the apparent spatial resolution can be artificially enhanced due to the non-negativity constraint [23]. While the actual spatial resolution of the system is not precisely assessed, comparing the obtained results allows us to characterize the system performance in different configurations. The values obtained for each case are listed in Table 4.3, which confirm the trends appreciated visually in Figures 4.4 and 4.5: the reconstructed FWHM achieved in our measurements is better for higher energy gammas,

for smaller source-detector distances (configurations 1 and 3) and for bigger inter-plane separations (configuration 3).

Table 4.3 FWHM along x and y profiles of reconstructed images of the radioactive sources with the different initial energies at the employed geometrical configurations.

	FWHM$_{x,y}$ (mm)			
Energy (keV)	Configuration 1	Configuration 2	Configuration 3	Configuration 4
511	3.8, 4.0	6.2, 6.5	3.2, 3.6	5.2, 4.4
1275	3.7, 3.4	3.7, 4.4	2.8, 2.9	3.8, 3.7
898	-	-	-	4.0, 3.6
1836	-	-	-	2.7, 3.1

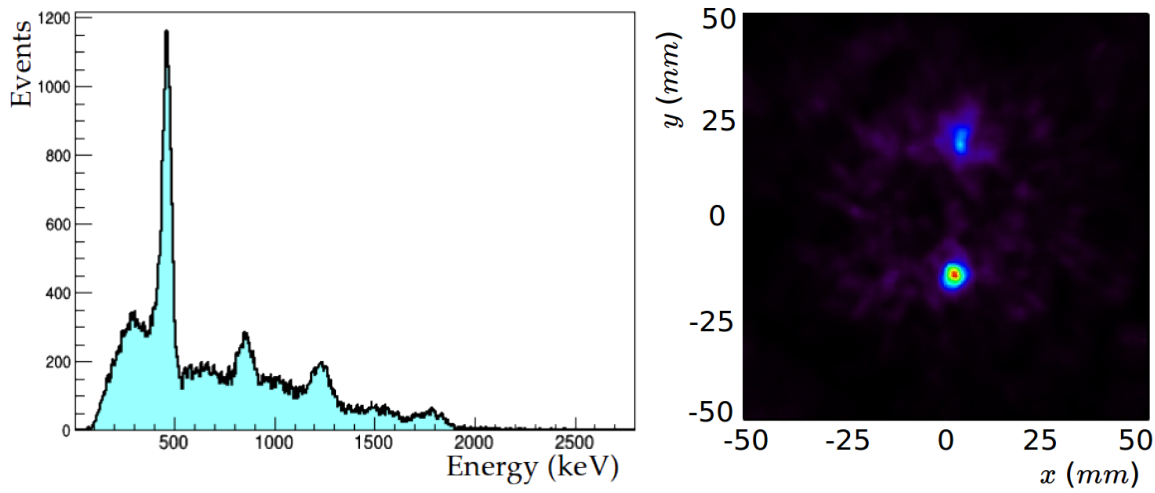

(a) (b)

Figure 4.7 Measurement with the ^{22}Na and ^{88}Y sources together in time coincidence. Summed energy spectrum (a) and reconstructed image (b).

An additional measurement was also performed with both radioactive sources together, placed on a plane parallel to the surface of the detectors. In this case, the data from both sources are reconstructed simultaneously. For the reconstruction of this data, only events with summed energy greater than 950 keV were used, in order to select the highest energy photons emitted by each source. Since the reconstruction is carried out from events produced by photons of different energies, in this case the algorithm does not take a predefined initial energy and it is instead calculated as the summed energy of each event; in practice, that means that only events with full absorption on the second detector will provide useful information,

while the rest will act as background. Figure 4.7 shows the resulting summed energy spectrum and the subsequent reconstructed image, where both sources are represented. The lower spot of picture 4.7b, corresponding to the ^{22}Na, source is brighter than the upper one, produced by the ^{88}Y source. This difference is due to the higher full absorption probability of lower energy photons and to the fact that the ^{22}Na source had a higher activity than the ^{88}Y one, which is also reflected in the summed energy spectrum shown in Figure 4.7a. After the cut imposed on the summed energy, a total of 14000 events were used for reconstruction.

4.1.2 Three plane operation mode

In the three plane configuration, the system performance was also tested with the same radioactive sources. In these tests, the $27.2 \times 26.8 \times 5$ mm^3 crystal was used as the first, the $36.0 \times 32.4 \times 5$ mm^3 as the second and the $36.0 \times 32.4 \times 10$ mm^3 as the third detector planes. The distances between the source and the first plane and between the planes in the reported measurements are listed in Table 4.4.

Table 4.4 Distances employed for the three-plane operation mode with the ^{22}Na and the ^{88}Y sources.

	Distance (mm)		
	Source - Plane 1	Plane 1 - Plane 2	Plane 2 - Plane
^{22}Na Source	32	36	39
^{88}Y Source	41	42	35

Reconstructed energy

As explained in chapter 2, the main advantage of three-stage Compton cameras lies in their capability of recovering the initial photon energy without any previous knowledge (equation (2.2)). The initial energy is a fundamental parameter to build the CoR of the measured events, and therefore it must be precisely calculated. The calculation of the initial energy is based on the measured energies and positions of the detected interactions, and thus has an associated uncertainty. As described in section 2.4.2, the uncertainty of the reconstructed energy is derived from the uncertainty of three parameters: the energy measured in the first plane, the energy measured in the second plane and the scattering angle of the Compton interaction in the second plane. The second scattering angle is calculated through geometrical considerations employing only the interaction positions in the three planes, so

its error is caused by the spatial resolution in the determination of those interactions. Thus, the initial energy uncertainty is ultimately given by the intrinsic spatial and energy resolution of the detectors. Nevertheless, the second scattering angle is specific of each particular event, and equation (2.22) states that smaller angle values lead to higher imprecision of the calculated energy.

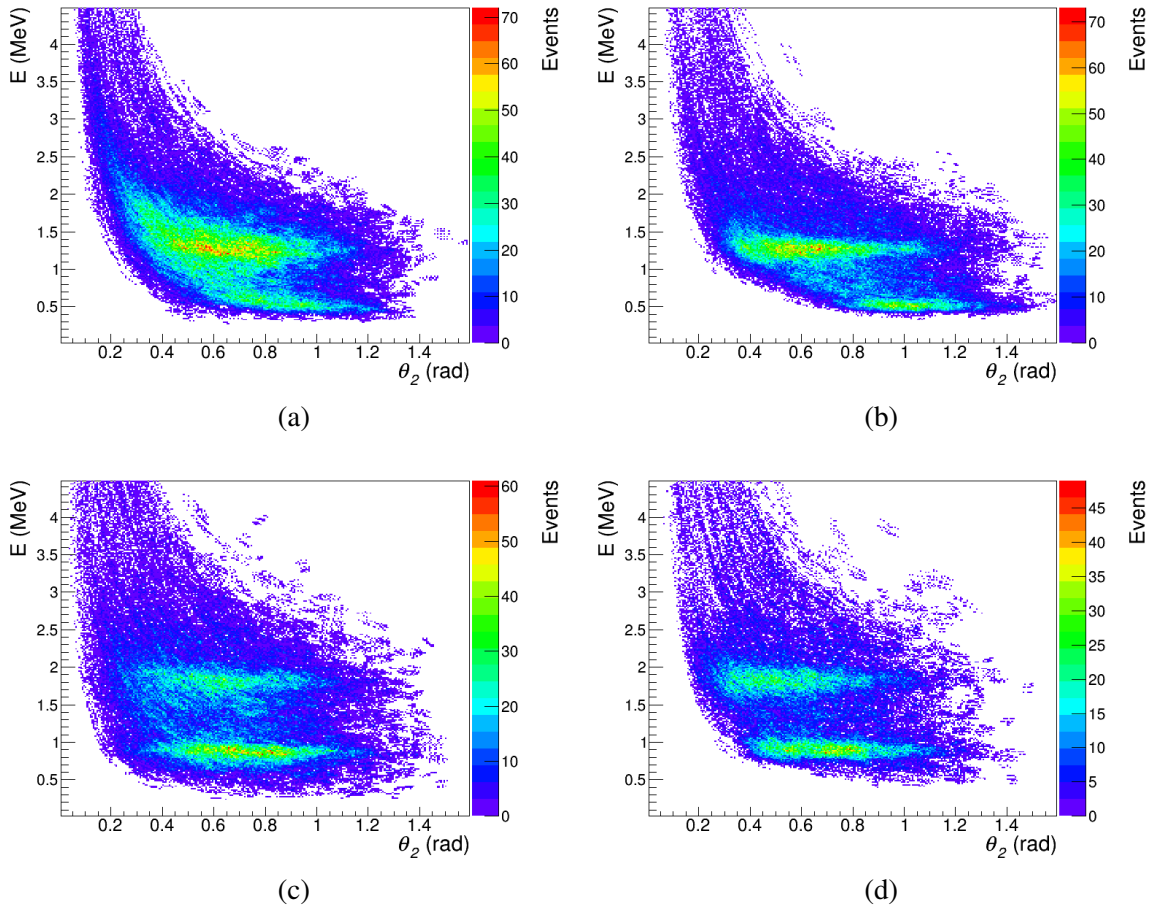

Figure 4.8 Incident energy reconstruction versus second Compton scattering angle for an experimental (a) and a simulated (b) ^{22}Na source and an experimental (c) and a simulated (d) ^{88}Y source.

The described dependence of the reconstructed initial energy on the scattering angle has been studied. Figure 4.8 shows the reconstructed initial energy as a function of the second scattering angle for a ^{22}Na (experimental (4.8a) and simulated (4.8b)) and an ^{88}Y (experimental (4.8c) and simulated (4.8d)) radioactive sources. A higher concentration of points can be found at the energies corresponding to the spectral lines of the sources (511 and 1275 keV for ^{22}Na, 898 and 1836 keV for ^{88}Y), produced by events whose energy is being reconstructed correctly. However, as the second scattering angle gets smaller, the calculated

energies tend to higher values, away from the real photon energies, and an increasing number of events is reconstructed with wrong energies. In order to minimize this effect, a lower limit for this angle can be established. In this study, such limit was chosen at 0.4 rad.

Figure 4.9 depicts the effect of the described filter on the measured spectra with the three-plane camera and the previously mentioned radioactive sources. Figures 4.9a and 4.9c show the spectra obtained by summing the energies deposited in the three detectors for each source. Figures 4.9b and 4.9d represent the energy calculated with equation (2.2), where it can be appreciated that the filter on the second scattering angle reduces the amount of events reconstructed with energies higher than the actual value, which would add noise to the reconstructed images.

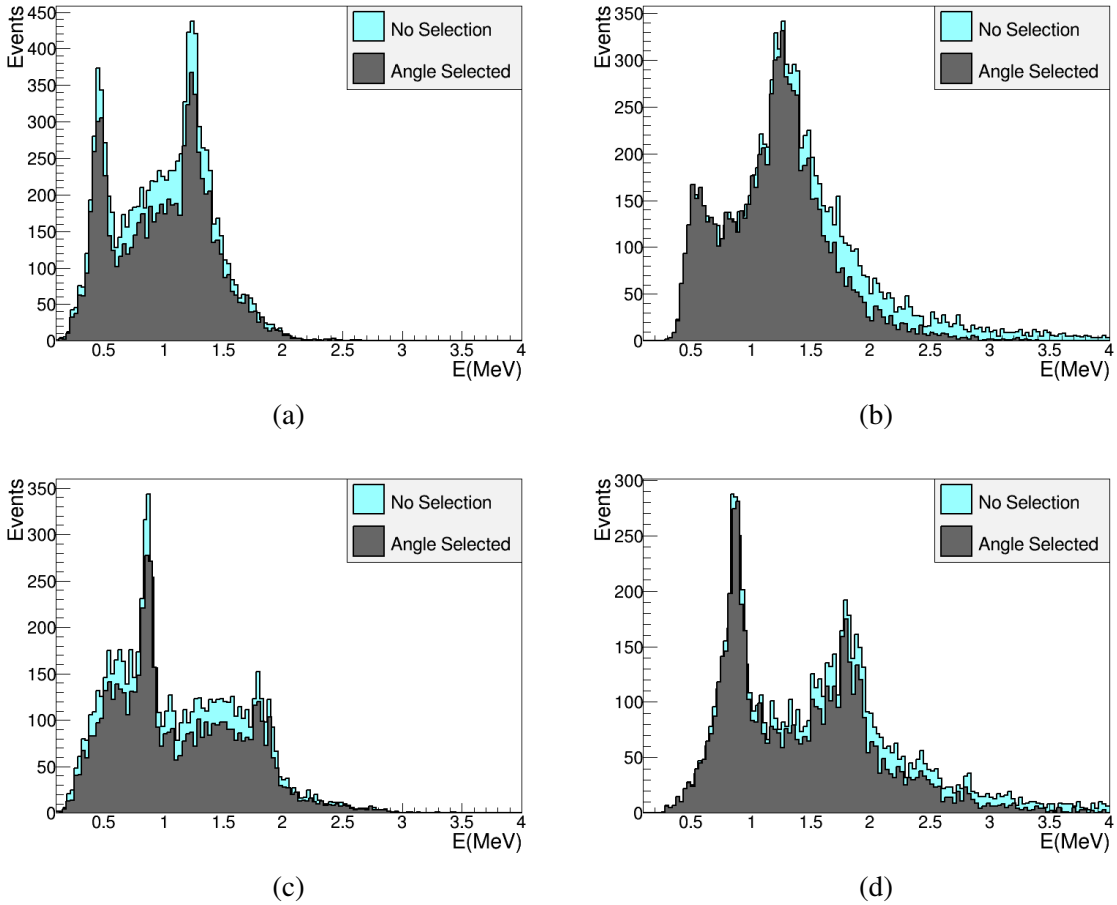

Figure 4.9 Effect of the applied filter for event selection in spectra obtained in time coincidence with three detector layers. (a) Summed energy ^{22}Na, (b) reconstructed energy ^{22}Na, (c) summed energy ^{88}Y, (d) reconstructed energy ^{88}Y.

Imaging tests

For the imaging tests, only events selected with the described angular filter were used. The ^{22}Na source was measured at three different positions, and the reconstructed images of the ^{22}Na source are shown in the top row of Figure 4.10, where the source is visible in all three cases. Similarly to the procedure in the two-plane operation mode, to test the performance of the algorithm at several energies, the data were also separated in different energy intervals by setting a cut in the summed energy spectrum. However, there is a fundamental difference: whereas in the two-plane operation the initial energy was used as an input parameter for the reconstruction algorithm, in the three-plane case the energy was reconstructed event by event as described previously. The top-left image in Figure 4.10 corresponds to 511 keV, and the one on the right to 1275 keV. In all cases, images were reconstructed with 5000 coincidence events.

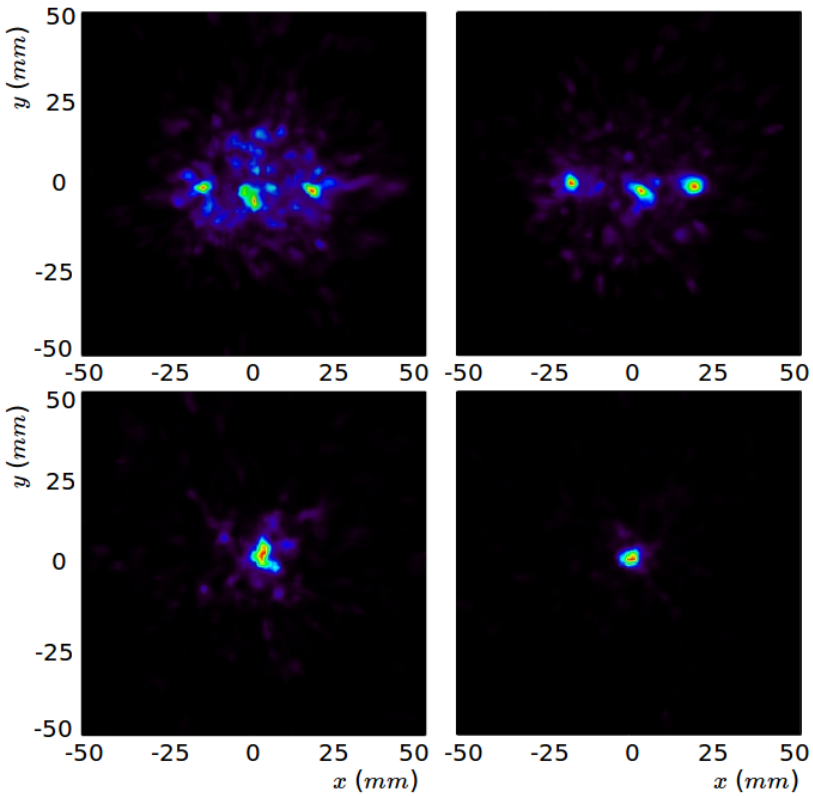

Figure 4.10 Reconstructed images in the three-plane configuration. Top: image of the ^{22}Na source with 511 keV (left) and 1275 keV (right). Bottom: image of the ^{88}Y source with 898 keV (left) and 1836 keV (right).

The ^{88}Y source was also imaged in the three-plane operation mode, in this case only at one centered position and with 2000 coincidence events for each energy. The reconstructed

Table 4.5 FWHM along x and y profiles of reconstructed images from different gamma energies with 3 planes and distances shown in Table 4.4 and the source in the central position.

Energy (keV)	511	898	1275	1836
FWHM$_{x,y}$ (mm)	5.4, 5.4	3.9, 4.6	3.6, 3.6	3.4, 3.0

images can also be seen in the bottom row of Figure 4.10, where the left column shows the image obtained for 898 keV and the right column shows the 1836 keV case. The FWHM of the reconstructed images obtained from the sources at the central position are listed in Table 4.5. In agreement with the two-plane results, a better image resolution is achieved for higher energies.

4.1.3 Detection efficiency

A factor limiting the quality of images produced by Compton cameras is the number of measured events, especially in applications which require short measurement times. The detection efficiency of our system has been studied with two and three detector planes for a variety of inter-plane distances. For this study, the detection efficiency has been measured and simulated at the energy of 1275 keV, both with two and three planes. In the case of three planes, the studies have been performed using the same distance between planes 1-2 and planes 2-3. The efficiency is calculated as the fraction of events entering the surface of the first detector that produce a detected coincidence event.

In the laboratory, the efficiency of our system for 1275 keV photons with two and three planes has been measured with the ^{22}Na source, by selecting coincidence events for which the summed energy is comprised between 600 and 1350 keV. Experimental results have been reproduced by simulations with a 1275 keV gamma source in good agreement with measurements. The results for the two-plane operation mode are shown in Figure 4.11a and those with three planes in Figure 4.11b. The small deviations from experimental to simulated data have two main contributions: overestimation of experimental coincidences due to coincidences produced by two different gammas (511 and 1275 keV), which cannot be rejected through energy cuts, and underestimation of *true* coincidence events that deposit a total energy below the threshold, set to 600 keV in order to select only events produced by a 1275 keV gamma.

Simulations have been extended to study a three-stage system capable of measuring coincidence events produced both in three or in any two planes, showing a greatly enhanced

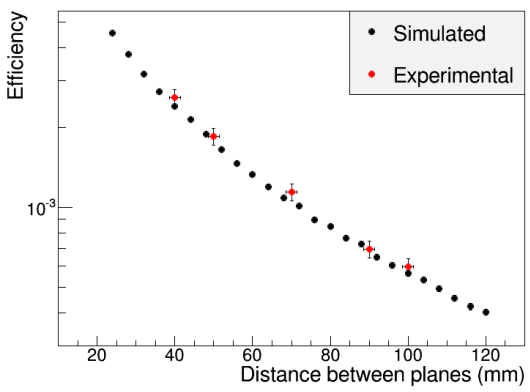

(a) 2 planes

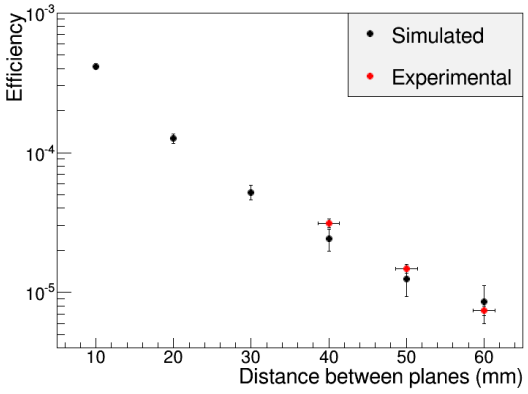

(b) 3 planes

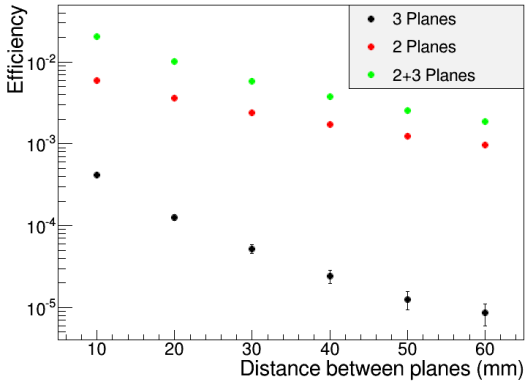

(c) 2+3 planes

Figure 4.11 Efficiency of coincidence detection at 1275 keV as a function of the inter-plane distance.

detection efficiency (Figure 4.11c) with respect to the two-plane configuration. Efficiency is increased between two and three times depending on the relative distances.

4.2 Tests with 4.44 MeV gammas

In addition to the imaging tests with radioactive sources in the laboratory, the system was tested at the Tandetron accelerator at Helmholtz-Zentrum Dresden-Rossendorf (HZDR). In this facility, quasi-mono-energetic gamma rays of 4.44 MeV can be produced [21]. As explained in section 1.1.2, this energy is relevant in hadrontherapy monitoring, being a prominent line in the prompt gamma emission spectrum. The MACACO prototype was tested with the aim of characterizing the detectors at high energies and assessing the possibility of obtaining images with 4.44 MeV gamma rays employing two and three detector planes.

4.2.1 Experimental setup

Production of 4.44 MeV photons

In order to achieve the production of 4.44 MeV photons, an accelerated 6.6 MeV $^{15}N^{2+}$ beam was shot onto a Ti target, inducing the proton-capture resonance reaction

$$^{15}N\,(p,\alpha\gamma_{4.439})^{12}C. \tag{4.1}$$

The nuclear de-excitation of the produced $^{12}C^{*}$ nuclei yields the $\gamma_{4.439}$ photons of the desired energy [49, 70]. The resonance reaction results in a clean gamma production with very low background, perfect for conducting tests at this energy. However, one drawback of this method is the low production rate, which can limit the acquisition of data in time coincidence.

Setup description

The target employed was a 300 nm thick Ti target, implanted with hydrogen on a 220 μm thick Ta backing, enclosed in a stainless steel chamber and placed at an angle of 55^{o} with respect to the beam (Figure 4.12a). It is equipped with a water cooling system. In this experiment, the ion beam made a spot of 10 mm width and 4 mm height at the target location. The beam current oscillated from 0.3 to 0.7 μA during the experiment. A high purity germanium (HPGe) detector [49] placed at 159 mm from the target encapsulation surface measured the rate of 4.44 MeV gammas interacting in it. Figure 4.12b shows the 4.44 MeV gamma emission rate over 4π for the whole measurement period.

In all the coincidence measurements performed during this campaign, the system was assembled with three planes, and two- and three-event data were acquired simultaneously. As in the measurements with three planes carried out in the laboratory, for these tests the $27.2 \times 26.8 \times 5$ mm^3 crystal was used as the first, the $36.0 \times 32.4 \times 5$ mm^3 as the second and the $36.0 \times 32.4 \times 10$ mm^3 as the third detector planes. A photograph of the telescope and the beam line employed for the measurements can be seen in Figure 4.13. For the measurements in beam, the system was placed next to the beam target, at 44 mm from its center. The relevant distances between the detectors and from the system to the target employed for the measurements are listed in Table 4.6.

Data with 4.44 MeV photons were taken first in singles mode with all three planes for characterization and calibration purposes, and later on in coincidence mode. In order to simulate target displacements, coincidence measurements were carried out with the camera

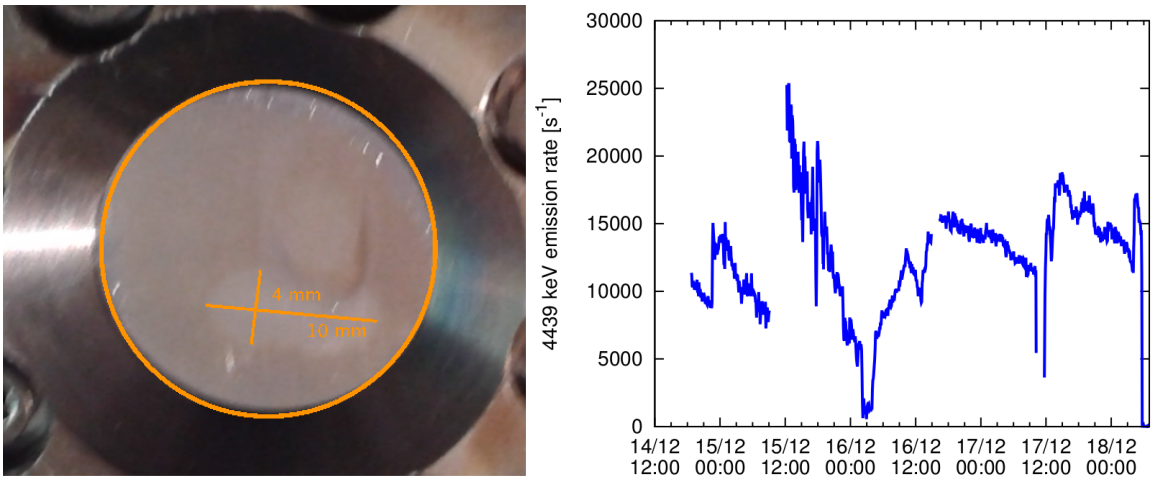

(a) (b)

Figure 4.12 (a) Ti target in which the spot made by the ion beam can be seen. (b) Rate of gamma rays over 4π, calculated from the rate detected in the HPGe detector.

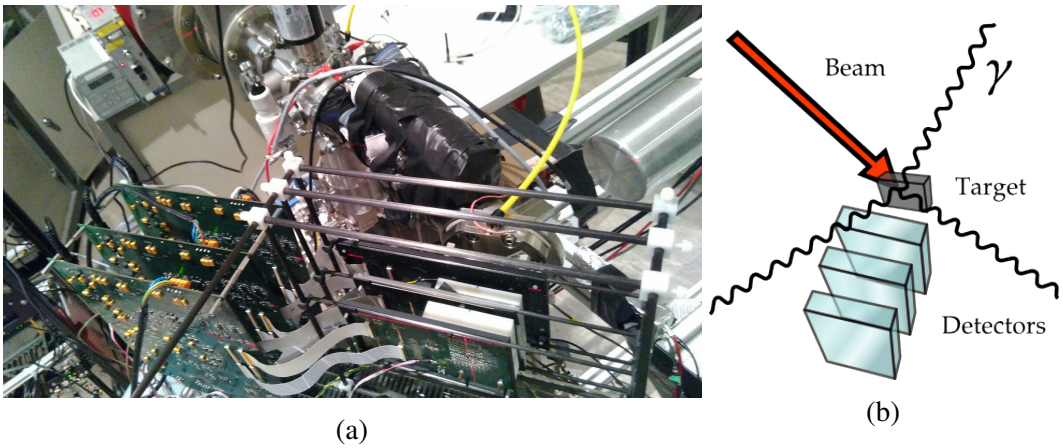

(a) (b)

Figure 4.13 Photograph (a) and diagram (b) of the experimental setup showing the beam line, target and the MACACO prototype assembled with three planes.

Table 4.6 Geometrical configuration of the telescope employed during measurements.

Distances (mm)		
Target - Plane 1	Plane 1 - Plane 2	Plane 2 - Plane 3
44	28	32

in three different positions with respect to the target, moving in each case the system in steps of 10 ± 1 mm along the horizontal axis.

4.2.2 Detector response at high energies

Measurements of the beam were taken in the singles acquisition mode in order to calibrate the detector response. The calibrated spectra recorded by each of the individual detector planes are plotted in Figure 4.14.

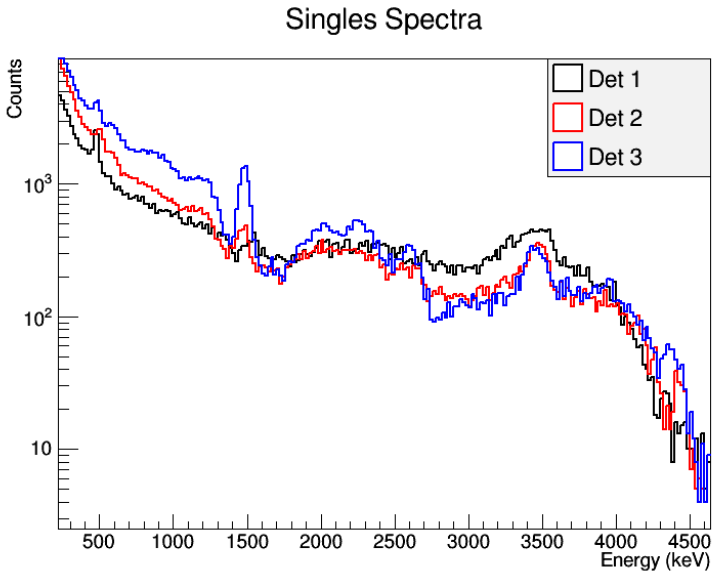

Figure 4.14 Energy spectra measured in singles mode with the three detector planes.

The peaks corresponding to 511, 1470, 3417 and 4439 keV can be identified in the energy spectra and have been employed for energy calibration. The 4439 peak corresponds to full absorption of the gamma rays produced in nuclear reactions and the 3417 keV peak is due to double escape. The single escape peak, at 3928 keV, is not clearly visible in the measured spectra, and has therefore not been used. The 511 keV photons are generated by the annihilation of positrons produced by pair production reactions. The 1470 keV peak comes from the de-excitation of ^{138}Ba, produced by electron capture of ^{138}La. In addition to this peak, other features appearing in the spectrum, not employed for calibration, are characteristic of the use of $LaBr_3$ detectors [67]. The contamination in the spectra below the mentioned 1470 keV peak is produced by the activity of^{138}La, while the contamination in the region between 1.6 and 2.7 MeV is due to the detection of α particles emitted by the radioactive isotope ^{227}Ac and daughters, residually present in the $LaBr_3$ crystal lattice. These features are more prominent in the third detector, since it holds the thickest crystal, which has the highest intrinsic activity and absorption probability. The fact that the peaks associated to the intrinsic radioactivity of the crystals are so clearly visible in the spectra acquired during beam time is indicative of the low gamma production rate. While the low rate can hinder the

measurements in coincidence mode, the presence of those peaks in the spectrum was used for the detectors energy calibration without the need for external radioactive sources.

The calibration curves of the three detectors are shown in Figure 4.15, where the peak position in ADC units are plotted versus the different peak energies. The linear fit indicates the correspondence between ADC and energy units, given by $ADC = p0 + p1 \cdot E(keV)$. The plot obtained for each detector was fitted with a straight line and the fit parameters were employed to calibrate the data taken in coincidence acquisition mode. The three detectors showed a linear response up to the highest energies tested.

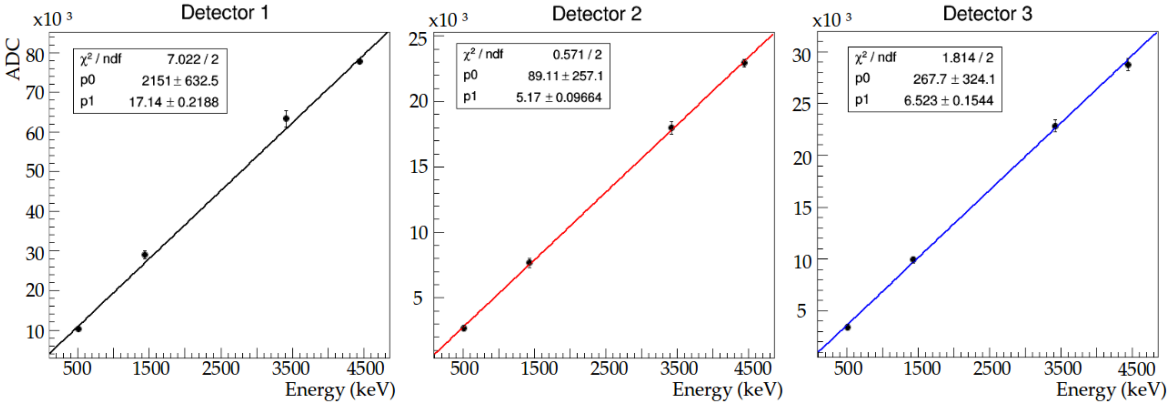

Figure 4.15 Calibration curves of the three detectors, showing a linear behaviour in the measured range.

4.2.3 Coincidence measurements

Beam measurements were taken with the detector placed at three different positions with respect to the target: centered, displaced 10 mm to the left and 10 mm to the right in the beam direction. The measurement with different system positions emulates the displacement of the target, whose fixed position could not be changed. In the three measurements, the system was assembled with three planes, and data were classified according to the planes involved in their detection, which can be divided into two-plane events in any of the three possible detector pairs (1 - 2, 1 - 3 or 2 - 3) or three-plane events (1 - 2 - 3). The number of events registered for the different combinations are listed in Table 4.7 for the three measured positions, where the percentage of events detected in each combination is also indicated. It can be seen that the detection efficiency of three-interaction events is much lower than that of two-interaction events. This fact, in combination with the relatively low rate of photon production and the limited beam time available during the experiment, resulted in insufficient statistics for image reconstruction with three-interaction events. In consequence, the imaging

studies in this experiment are restricted to the results measured with the three combinations of detector pairs.

Table 4.7 Number of coincidence events acquired in each detector configuration and percentage of events per run in each position.

Detectors	Number | percentage of events per run		
	Position 1	Position 2	Position 3
1-2	14517 | 48.7 %	9513 | 46.7 %	22348 | 48.7 %
1-3	4957 | 16.6 %	3380 | 16.6 %	7545 | 16.4 %
2-3	9594 | 32.2 %	7029 | 34.5 %	14851 | 32.3 %
1-2-3	747 | 2.5 %	449 | 2.2 %	1176 | 2.6 %
Total	29815	20371	45920

The energy spectra measured in time coincidence by the three possible detector pairs are shown in Figure 4.16, plotted for the measurement performed at the central position. For the three combinations, the spectra measured in the detectors acting as the first and second planes are depicted in Figures 4.16a and 4.16b. The summed energy spectra, resulting from the sum of the previous two, are plotted in Figure 4.16c. In the summed energy spectra, a protuberant region can be seen between 3 and 4.5 MeV. This region includes the 3.4 MeV, 3.9 MeV and 4.4 MeV peaks, although the individual peaks can not be identified.

4.2.4 Reconstructed images

For each measured position, an image was reconstructed with the three combinations of detector pairs. In all cases, the image reconstruction process considered all the measured events, without any further selection, as listed in Table 4.7, and the initial photon energy was given as a known parameter to the algorithm. The obtained results are shown in Figure 4.17, where a separate image is shown for each detector pair: planes 1-2 (left), planes 2-3 (center) and planes 1-3 (right). Images at different positions have been reconstructed independently, and plotted together for a better visualization of the relative displacement between target and detector. The shown images correspond to iteration number 5 in the iterative algorithm. Iteration 5 was chosen because it is sufficient to identify the target position in all cases, and successive iterations do not significantly improve the image quality. The FoV considered in the reconstruction process was $101 \times 101 \times 51$ mm^3, divided into voxels of 1 mm^3. Since the reconstruction algorithm produces three-dimensional images, Figure 4.17a represents the two-dimensional slices where the voxel with maximum value is located. In addition to the

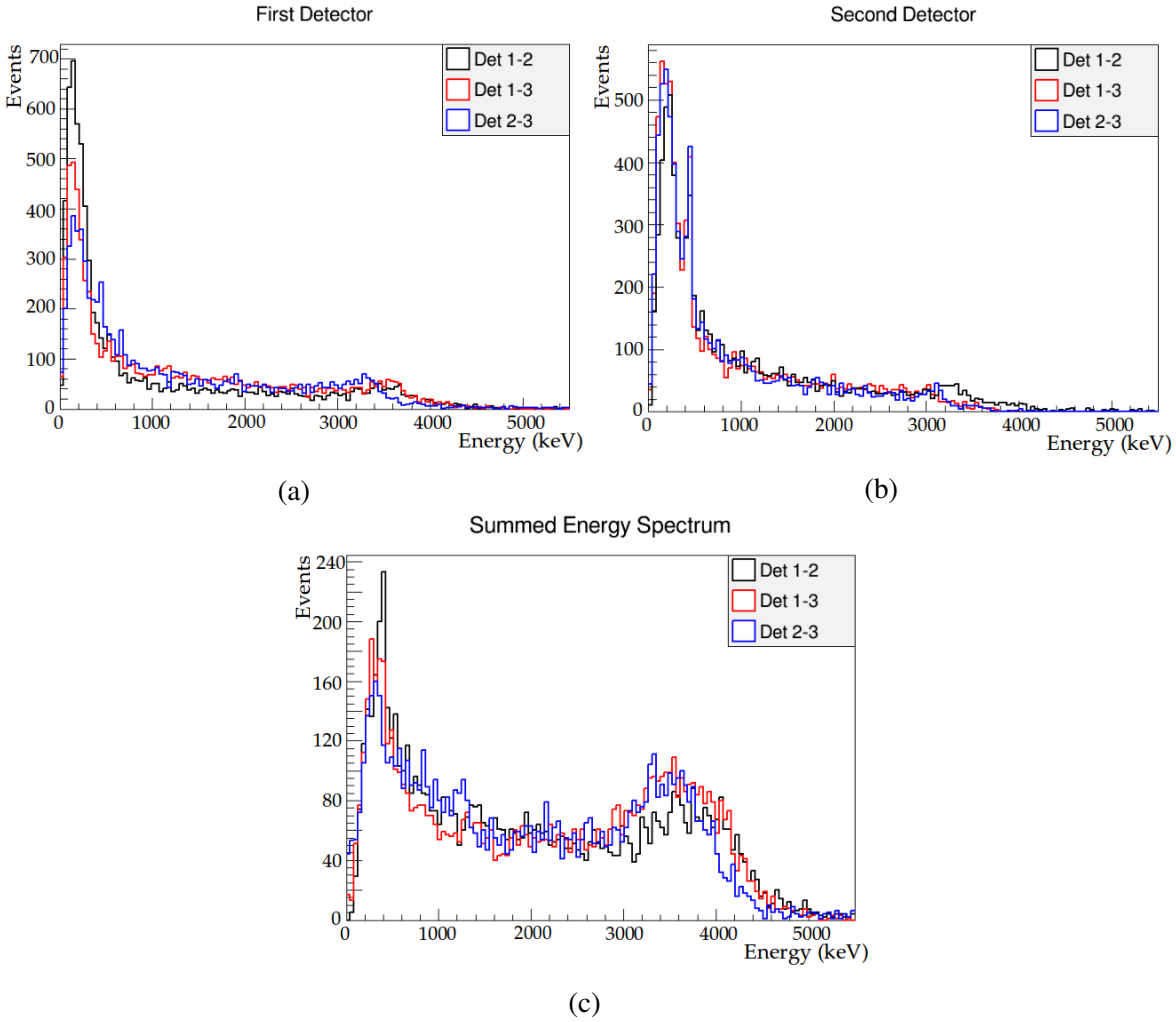

Figure 4.16 Coincidence spectra obtained for the three possible combinations of two detector planes: 1-2, 1-3, 2-3. (a) Energy spectra recorded in the first detector, for the three possible combinations. (b) Energy spectra recorded in the second detector. (c) Summed energy spectra in all three cases.

two-dimensional slices, Figure 4.17b shows the respective profiles along the y axis through the maximum of the images, where the displacements can be better appreciated.

In order to quantify the reconstructed displacements, the reconstructed positions are extracted from the images by fitting a Gaussian function to the previous profiles. Figure 4.18 shows the reconstructed positions versus the nominal positions in the three cases. The errors in the y axis correspond to one sigma in the respective Gaussian fits along the profiles containing the maxima for each image, while the errors in the x axis correspond to the estimated uncertainty in the manual positioning of the system (1 mm). It can be seen that, in all cases, the position obtained from the reconstructed images matches the nominal positions

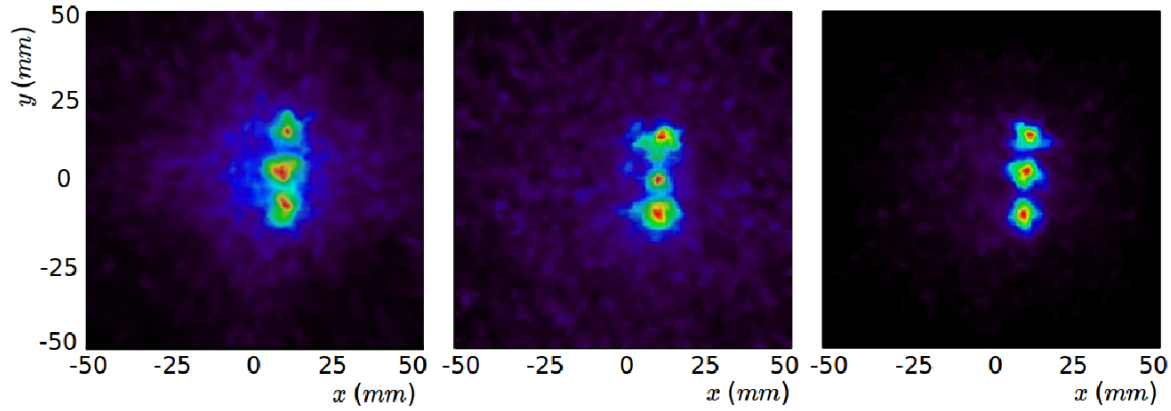

(a)

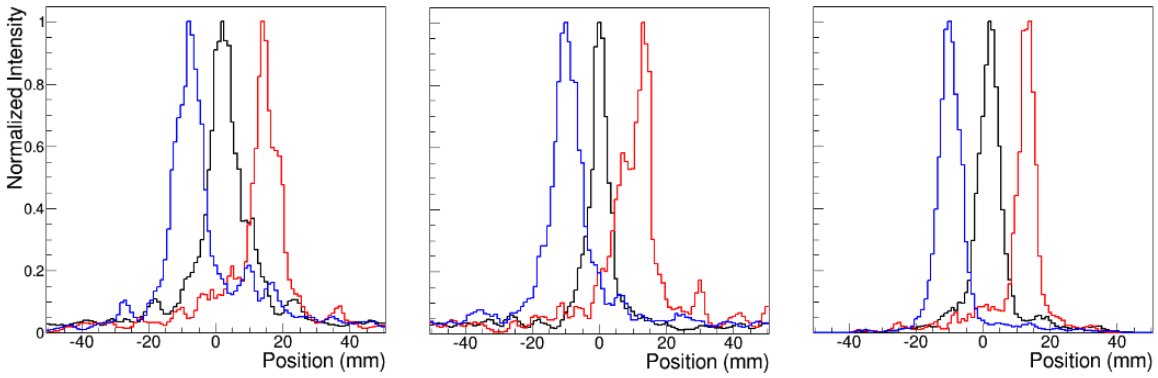

(b)

Figure 4.17 Reconstructed images (a) and profiles (b) with datasets from the detectors at three different positions, and with coincidence events from the three possible combinations of two planes: planes 1-2 (left), 2-3 (center) and 1-3 (right).

within the errors. It can also be noticed that all the reconstructed positions are above the nominal position, represented in the plot with a dashed line. This is due to the bias error associated with the manual positioning of the detector in front of the target. The target encapsulation and geometry complicate the exact positioning of the first detector with respect to the target and, since the imaging tests are aimed at measuring differences between the reconstructed positions, an exact absolute positioning is not necessary. Given that the second and third positions are selected taking the first one as a reference, there is a common shift in the three reconstructed positions. In agreement with the results seen in section 4.1.1, the best performance is obtained with the first detector closest to the source and the second detector furthest from the first one (pair 1-3).

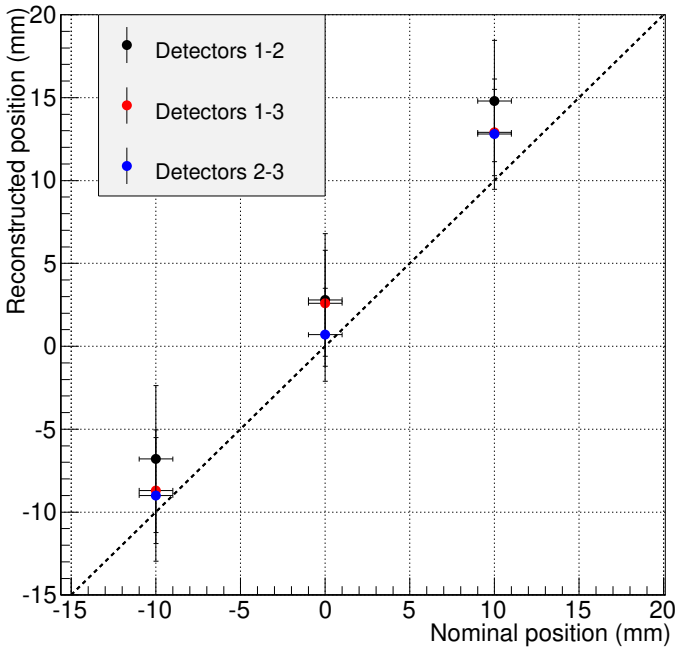

Figure 4.18 Reconstructed positions of the target with respect to the telescope versus the nominal position for the three measured positions and for each pair of detectors. The dashed line represents the perfect match.

4.3 Conclusions

The tests in time coincidence under different conditions prove that the experimental prototype can be employed for image reconstruction, both with two and three detector planes. In all the studied cases, the source could be identified and the distances between the different source positions were correctly recovered.

The data taken in the laboratory in the two-plane operation mode with radioactive sources show that imaging is feasible in the range between 511 and 1836 keV. In this energy range, the spatial resolution of the reconstructed images improves for higher energy photons. This effect is due in the first place to the lower uncertainty associated to the Compton scattering angle for higher gamma energies (equation (2.16) in section 2.4.2). In the second place, the fraction of backscatter events is significantly reduced as the initial energy increases (recall Figure 1.6 in section 1.2.1), so these noisy events have a smaller weight. Concerning this aspect, simulation studies of our prototype show that the percentage of backscatter events decreases from around 17% at 511 keV to 5% at 1275 keV, which explains in part the noisier images obtained for the low energy gammas. Lastly, it should be kept in mind that both sources employed for this study emit gammas of two different energies and that

the classification to each of them is based only on an energy cut applied on the summed energy spectrum. Therefore, the data associated to the lower energy gamma will inevitably be contaminated by partial depositions of the higher energy photon, which add noise to the reconstructed image. The quality of the images also depends on the separation distances between the planes and between source and the first plane. In that sense, the results show that the source is imaged with better quality when it is closer to the first detector and when the inter-plane distance is increased.

In the three-plane operation mode, the system was able to reconstruct the initial energy of the incident gammas for the four energies emitted from the employed sources. Images were successfully recovered for all the energies measured in the laboratory. As in the two-plane case, image resolution improved for higher energy photons in the considered range. It can be noticed that images obtained with three planes are in general noisier than those recovered with two planes. This is because the two-plane data have been reconstructed using the initial photon energy as a known parameter. The main advantage of employing a third plane is that it allows recovery of the initial energy; however, the recovered energy is subject to the detection uncertainties, which can lead to deviations in its determination that in turn degrade the final image. Therefore, the two-plane scenario is more favourable when the emitted energy is known beforehand, as in radiotracer imaging. Nevertheless, the tests show that our three-plane prototype can reconstruct images without any prior knowledge of the emitted photon energy. The preliminary study also showed that the uncertainty in the initial energy determination is higher for events with small second scattering angle, so it can be more accurately reconstructed when these events are cut off. Since the initial energy is necessary for the construction of the Compton cone, this leads to better final images.

Tests at the HZDR with 4.44 MeV photons have served us to characterize the detectors at this energy, which was unavailable for us in the laboratory. The coincidence measurements were carried out with the prototype assembled with three planes, with all events producing a detection in any two of the three detectors triggering an acquisition. The data were afterwards classified according to the detector pairs involved in their measurement, which allows the independent reconstruction of the source for each combination of detectors. Indeed, images of the three different target positions have been obtained for the tree available detector pairs. Images from the three detector combinations are compatible and the recovered source positions in agreement with the expected values. Unfortunately, no image could be retrieved with the three-plane operation mode, which is attributed to the lack of statistics caused by our limited beam time and the low gamma production rate. Nevertheless, the measurements with 4.44 MeV photons confirm that the prototype can also produce useful images with high energy photons.

Chapter 5

Imaging of monochromatic sources of known energy

The results obtained in the previous chapter prove that our Compton camera prototype can successfully reconstruct experimental point-like sources of known energy. In order to image more complex sources, a detailed physical model must be considered and included in the image reconstruction process. This chapter is dedicated to the derivation of a detailed physical model of the measurement process of a known energy gamma by a two-plane Compton camera. The model is used to obtain an expression for the system and sensitivity matrices. Special emphasis is given to the sensitivity matrix, and a study of its impact on the reconstructed images is conducted with a variety of simulated and experimental sources. The results presented in this chapter are published in [57].

5.1 Physical model

In order to fully exploit the information conveyed by the events detected by the system, we need a detailed model of the signal formation. This section is dedicated to introducing the physical probabilities involved in the detection process, which are then employed to derive an expression for the system and sensitivity matrices. In this chapter, the emission is assumed to be monochromatic of known energy.

It should be noted that the general model presented in the following sections can be applied to any configuration of a two-plane Compton camera. In the validation tests performed afterwards, all simulated studies reported in this chapter were carried out with two detector planes of $LaBr_3$ with the dimensions of the latest version of our experimental prototype

($25.8 \times 25.8 \times 5$ mm^3) introduced in section 3.1, which are also the planes employed for the reported experimental studies.

5.1.1 System matrix calculation

The output provided by the telescope consists of the value of the energy deposited by the photon due to an interaction with the detection plane and the position of this interaction, $(\tilde{E}_p, \vec{r}_p)$, for each of the two planes, $p = 1, 2$. Specifically, we need to compute the probability that an emission from a small region, V, generates a given signal. For concreteness, we will identify V with a voxel. A diagram describing the detection of an event is shown in Figure 5.1.

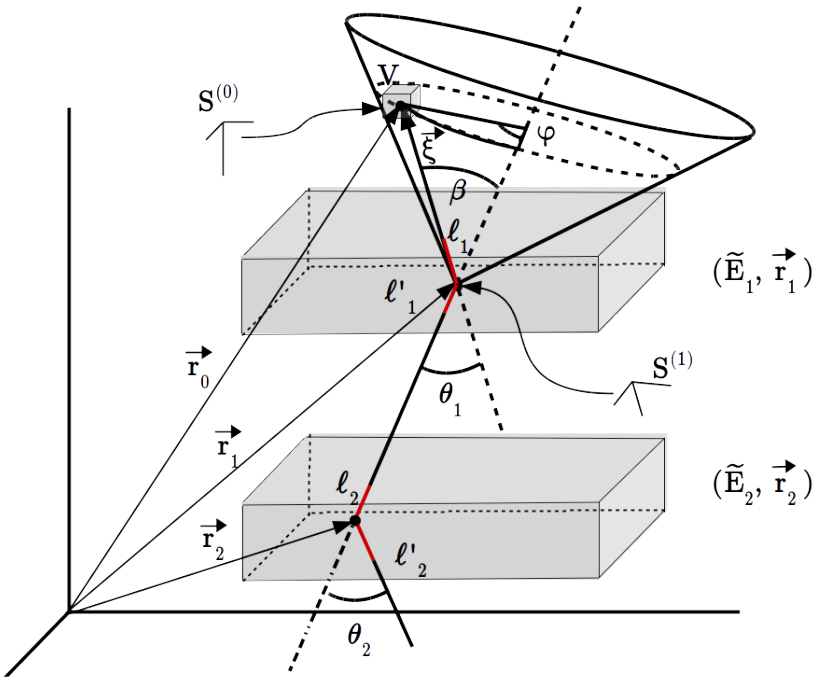

Figure 5.1 Diagram of a Compton camera measured event. The diagram indicates the position of emission of the gamma, the lengths travelled inside the detectors, the interactions positions, the scattering angle and the cone of response.

If we do not infer the incoming photon energy from the measurements but, instead, assume it is a known parameter with value E_0, the Compton scattering angle is fully determined by $\tilde{E}_1$. In addition, only the interaction points, $\vec{r}_1$ and $\vec{r}_2$, are required to build the CoR. Therefore, any interaction in the second plane is accepted as long as we can determine its

position. Under this assumption, the probability of the event depicted in Figure 5.1 can initially be written as:

$$dP = \frac{d^3r_0}{V} \cdot \frac{d\Omega_0}{4\pi} \cdot e^{-\mu_0 \ell_1} \cdot n_e^{eff} \frac{d\sigma_0^c}{d\Omega_1} d\Omega_1 d\ell_1 \cdot e^{-\mu_1(\ell_1' + \ell_2)} \cdot \mu_1 d\ell_2 \cdot \Theta_V(\vec{r}_0), \tag{5.1}$$

where $d\Omega_i = d\varphi_i d\theta_i \sin\theta_i$ stands for the i-th solid angle as defined in the i-th reference system. For convenience the $i-th$ reference system is defined with its center at $\vec{r}_i$ and its z-axis aligned along $\vec{r}_i - \vec{r}_{i-1}$. The value of the $LaBr_3$ linear attenuation coefficient for a photon of energy E_i is referred to as μ_i. The distance travelled by the photon inside the plane p is denoted as ℓ_p and the total distance travelled by a photon of energy E_k inside any plane will be denoted as λ_k. Thus, $\lambda_0 = \ell_1$, $\lambda_1 = \ell_1' + \ell_2$ and $\lambda_2 = \ell_2'$. The n_e^{eff} stands for the effective number density of electrons for the material of the detector planes ($LaBr_3$ in our case). The $d\sigma_i^c/d\Omega_j$ stands for the usual Klein-Nishina formula with the subscript indicating the energy of the photon, E_i. Finally, $\Theta_V(\vec{r}_0)$ is equal to 1 if $\vec{r}_0$ is inside V and 0 otherwise. After these definitions, each term in equation (5.1) can be easily understood. The first term is the probability that the emission takes place inside the elementary volume d^3r_0 within V. The second term stands for the probability of emission of the photon from $\vec{r}_0$ with angles θ_0 and φ_0. The third term stands for the probability of the photon to penetrate ℓ_1 in the first plane. The fourth term stands for the probability of a Compton scattering in ℓ_1 with final emission angles θ_1 and φ_1. The fifth term stands for the probability of escaping the first plane and penetrating ℓ_2 in the second plane. The next term stands for the probability of the photon to undergo *any* interaction in ℓ_2 and the last term stands for the fact that we only consider emissions from inside V.

It is extremely convenient to re-write equation (5.1) in terms of measured magnitudes. This can be achieved by noting that variables $\ell_1, \theta_0, \varphi_0$ and $\vec{r}_1$ are essentially related by a transformation of coordinates from spherical to Cartesian, and similarly for $\ell_2, \theta_1, \varphi_1$ and $\vec{r}_2$. The variables Ω_i and $d\ell_i$ are defined in terms of the $\vec{r}_i$ variables as $d\Omega_i d\ell_{i+1} = d^3r_{i+1}/|\vec{r}_{i+1} - \vec{r}_i|^2$. Upon application of these transformations equation (5.1) reads

$$dP(\vec{r}_0\vec{r}_1\vec{r}_2 |\, V) = \frac{d^3r_0}{V} \frac{d^3r_1}{4\pi|\vec{r}_1 - \vec{r}_0|^2} \frac{d^3r_2}{|\vec{r}_2 - \vec{r}_1|^2} \frac{d\sigma_0^c}{d\Omega_1} n_e^{eff} \mu_1 e^{-\mu_0\lambda_0} e^{-\mu_1\lambda_1} \Theta_V. \tag{5.2}$$

In order to introduce the energy deposited in the first plane $\tilde{E}_1$ we change $\vec{r}_0$ to spherical coordinates in a reference system centered in $\vec{r}_1$ and with its z-axis aligned along $\vec{r}_2 - \vec{r}_1$. Thus, $d^3r_0 = d\varphi \, \sin\beta \, d\beta \, d\xi \, \xi^2$. As can be seen in Figure 5.1, the angle β in this reference system equals the Compton scattering angle in the first plane, which is related to the energy deposited in the interaction through Compton kinematics. From equation (2.1):

$$cos\theta = 1 - \frac{m_e c^2 \tilde{E}_1}{E_0(E_0 - \tilde{E}_1)} \quad \rightarrow \quad \sin\theta \, d\theta = d\tilde{E}_1 \frac{m_e c^2}{(E_0 - \tilde{E}_1)^2} \tag{5.3}$$

Which leads to

$$\frac{d^3 r_0}{|\vec{r}_1 - \vec{r}_0|^2} = d\varphi \, \sin\beta d\beta d\xi = d\varphi \, d\xi \, d\tilde{E}_1 \frac{m_e c^2}{(E_0 - \tilde{E}_1)^2} \tag{5.4}$$

After this change of variables, the probability reads:

$$dP(\varphi \xi \tilde{E}_1 \vec{r}_1 \vec{r}_2 | \, V) = d\varphi d\xi d\tilde{E}_1 d^3 r_1 d^3 r_2 \frac{m_e c^2 n_e^{eff}}{4\pi V} \frac{e^{-\mu_0 \lambda_0} e^{-\mu_1 \lambda_1}}{(E_0 - \tilde{E}_1)^2 |\vec{r}_1 - \vec{r}_2|^2} \frac{d\sigma_0^c}{d\Omega_1} \mu_1 \Theta_V . \tag{5.5}$$

The variables $\tilde{E}_1, \vec{r}_1, \vec{r}_2$ can be measured, but φ and ξ cannot. Finally, to obtain the probability (density) that an emission in V produces the measurement of $\tilde{E}_1, \vec{r}_1, \vec{r}_2$, the non-measurable variables φ and ξ must be integrated out:

$$\frac{dP(\tilde{E}_1, \vec{r}_1, \vec{r}_2 | \, V)}{d\tilde{E}_1 \, d^3 r_1 \, d^3 r_2} = \int d\varphi d\xi \frac{m_e c^2 n_e^{eff}}{4\pi V} \frac{e^{-\mu_0 \lambda_0} e^{-\mu_1 \lambda_1}}{(E_0 - \tilde{E}_1)^2 |\vec{r}_1 - \vec{r}_2|^2} \frac{d\sigma_0^c}{d\Omega_1} \mu_1 \Theta_V . \tag{5.6}$$

Equation (5.6) constitutes the expression of our System Matrix, SM. It can be seen from Figure 5.1 that the integration over φ and ξ is the integration over a conical surface. This conical surface contains the geometrical components of the SM, which can be computed as

$$C(\tilde{E}_1, \vec{r}_1, \vec{r}_2) = \int_0^{2\pi} d\varphi \int_0^{\infty} d\xi \; e^{-\mu_0 \lambda_0} \Theta_V = \sum_{n=1}^{N_r \to \infty} \frac{2\pi}{N_r} \Delta\xi^{(n)} e^{-\mu_0 \lambda_0^{(n)}} . \tag{5.7}$$

It represents the integration of the smooth-varying function $e^{-\mu_0 \lambda_0}$ over a surface defined by the intersection of a cone and the spatial extent of voxel V. The conical surface corresponds to the usual Compton CoR: the cone axis is given by $\vec{r}_1 - \vec{r}_2$ and the aperture angle β is obtained from E_0 and $\tilde{E}_1$ (equation (2.1)). For its numerical calculation, the integral over φ is discretized in N_r pieces, which effectively amounts to decomposing the conical surface into a set of N_r rays ($d\varphi \approx \Delta\varphi = 2\pi/N_r$). For each ray, the integration over ξ inside the small volume of a voxel V equals the length of the ray inside the voxel. In equation (5.7), the integral value is calculated as the sum of all the individual contributions of each ray, where $\Delta\xi^{(n)}$ stands for the length of the n-th ray contained in the voxel and $\lambda_0^{(n)}$ stands for the length of the n-th ray contained inside the first detection plane. Equation (5.7) is particularly well suited for using conventional ray-tracing techniques, which justifies the choice made in section 2.3.2.

Thus, the probability that an emission in voxel V is detected in the projection defined by $\vec{\eta} = \{\tilde{E}_1, \vec{r}_1, \vec{r}_2\}$ can be approximated as

$$\frac{dP_V}{d\vec{\eta}} = \frac{m_e c^2 n_e^{eff}}{4\pi V} K(\vec{\eta})\, C(\vec{\eta}), \tag{5.8}$$

where the first fraction is a constant and $K(\vec{\eta})$ is a real number that depends *only* on the measured event

$$K(\tilde{E}_1, \vec{r}_1, \vec{r}_2) = \frac{\mu_1\, e^{-\mu_1 \lambda_1}}{(E_0 - \tilde{E}_1)^2 |\vec{r}_1 - \vec{r}_2|^2} \frac{d\sigma_0^c}{d\Omega_1}. \tag{5.9}$$

Equation (5.8) shows that the spatial dependencies inside the FoV are essentially encoded by a geometrical component, $C(\vec{\eta})$ (the CoR associated to $\vec{\eta}$), which is further modulated on an event-by-event basis by $K(\vec{\eta})$.

5.1.2 Implementation of the code

The previous section presented a complete expression for the calculation of the SM elements, which must be implemented for its numerical computation in the reconstruction code. In the list mode approach followed in our reconstruction algorithm, each measurement $\vec{\eta}_i$ gives rise to a CoR that is used to compute the V elements in a row of the SM, t_{iv}. The complete sequence of the calculation process of an individual SM row is represented schematically in Figure 5.2. The left hand side of Figure 5.2 describes how the CoR is built: the position of interaction inside the first detector plane, $\vec{r}_1$, is the apex of the cone. The interaction point in the second detector, $\vec{r}_2$, is used to calculate the cone axis, given by $\vec{r}_1 - \vec{r}_2$. The cone aperture angle is obtained through the Compton scattering formula, employing the measured energy deposited in the first detector, $\tilde{E}_1$, and the initial gamma energy, E_0, which is taken as an input parameter at this stage. When the cone is determined, its surface is represented as a set of N_r rays (recall section 2.3.2). These rays are then projected onto the FoV, which consists of a predefined grid of voxels.

For each CoR, the event-dependent function $K(\vec{\eta})$, defined in equation (5.9), is computed. In order to do so, the linear attenuation coefficients are stored in a lookup table obtained from the National Institute of Standards and Technology (NIST) database [10]. The contribution of the individual rays to the weight of the different voxels is then computed separately for each of the N_r rays into which the cone surface is divided. The length covered by the photon of E_0 before scattering, which depends on its path inside the detector, must also be calculated separately for each ray.

The contribution of a ray to the weight of a voxel is calculated as the multiplication of $K(\vec{\eta})$, the constant factors, the exponential $e^{-\mu_0 \lambda_0}$ and the length of that ray contained

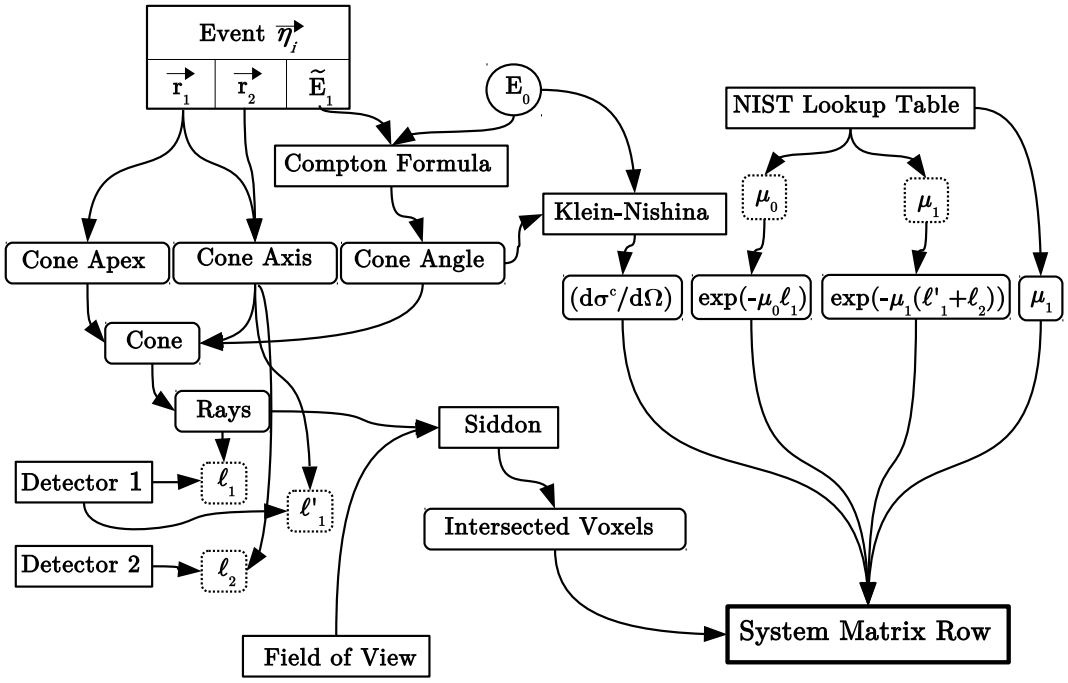

Figure 5.2 Diagram showing the process of construction of the SM row corresponding to one coincidence event.

inside the voxel. The intersection lengths of individual rays with the voxels in the FoV are computed with a ray tracing method [84]. The integral is finally computed as the sum of the contribution of all the rays in an event $\vec{\eta}_i$ to the voxel V.

After the complete SM is calculated, the list mode MLEM algorithm (equation 2.15) is used to obtain the reconstructed images. In addition to the SM, the reconstruction algorithm requires a sensitivity matrix. An accurate sensitivity image is necessary for quantitative image reconstruction, since it is used by the algorithm to correct the weight given to the different voxels according to the detection probability of gammas emitted from them. The following section presents an expression for the sensitivity matrix derived from our model, which can be pre-calculated prior to the image reconstruction process.

5.1.3 Sensitivity matrix calculation

The value of the sensitivity image is defined at each voxel, V, as the sum of the SM over all possible measurements, i.e., $s_v = \sum_i t_{i,v}$. It represents the probability of an emission from V

to be detected by the imaging device. However, obtaining the sensitivity image directly from its definition is often impractical due to the large number of possible measurement outcomes. Actually, for systems whose signal does not take discrete values, the sensitivity must be understood as the integration over all possible outcomes. This integration can be performed in any set of variables that describes all the possible final outcomes. In particular, we use the set $\{\vec{r}_0, \vec{r}_1, \vec{r}_2\}$. From equation (5.2), the sensitivity in voxel V can be expressed as:

$$s_V = \frac{n_e^{eff}}{4\pi V} \int_V d^3 r_0 \int_{P_1} d^3 r_1 \frac{e^{-\mu_0 \lambda_0}}{|\vec{r}_1 - \vec{r}_0|^2} \int_{P_2} d^3 r_2 \frac{e^{-\mu_1 \lambda_1}}{|\vec{r}_2 - \vec{r}_1|^2} \frac{d\sigma_0^c}{d\Omega_1} \mu_1, \tag{5.10}$$

where the integrals are extended to the volumes of the voxel, V, the first detection plane P_1 and the second detection plane P_2. Given a configuration of the telescope, this image can be pre-computed once and used in the image reconstruction process. We compute s_V numerically by applying conventional Monte Carlo integration techniques, which allow to compute simultaneously the value of the integration and an estimation of its error. An example of the sensitivity images obtained from integration of equation (5.10) is shown in Figure 5.3. The integration was performed with the dimensions of our detectors, with an initial energy of 1275 keV and a planar FoV placed in parallel and at a distance of 50 mm from the first detector. The plot represents the expected variation of our system sensitivity, which decreases for positions further from the detector center (placed at coordinates $(0,0)$).

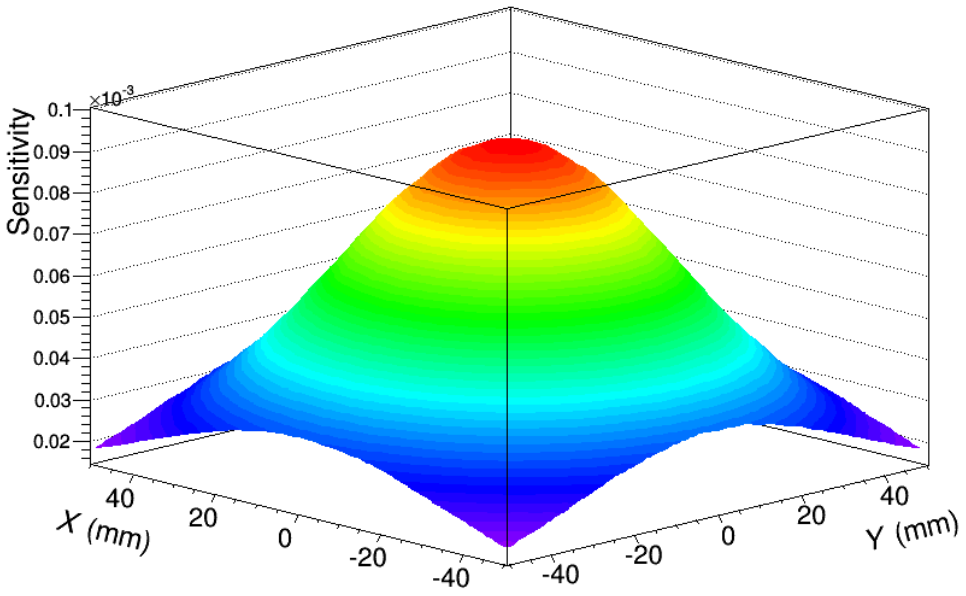

Figure 5.3 Sensitivity image obtained from integration of equation (5.10).

Other (simplified) models have been proposed in the literature, and we have compared some of them against our model. Apart from the trivial model where sensitivity is taken as uniform, s_v^{I}, the models described in [50] and [103] were also implemented. We will refer to them as s_v^{M} and s_v^{W} respectively.

$$s_v^{\mathrm{M}} \propto \sum_{l=1}^{L} \frac{|\cos(\theta_0^l)|}{|\vec{r}_1^{\,l} - \vec{r}_0|^2} \qquad s_v^{\mathrm{W}} \propto s_v^{\mathrm{M}} \left[1 - e^{-\mu_0 \lambda_0}\right] \qquad s_v^{\mathrm{I}} = 1 \ . \tag{5.11}$$

Both models rely on the assumption that the main contribution to the sensitivity of a voxel with center at $\vec{r}_0$ is given by the solid angle subtended by the scatterer. This approximation is valid for large source to first detector distances and large area second detectors. The scatter detector is divided into L volume elements, being $\vec{r}_1^{\,l}$ their respective centres and θ_0^l the angle formed by $\vec{r}_1^{\,l} - \vec{r}_0$ and the normal to the entrance surface of the scatterer. The model s_v^{W} also takes into account the interaction probability inside the scatterer.

The systems for which those models were developed differ substantially from our device. Those systems employ thin silicon pad detectors as scatterers and a thick scintillator absorber with high angular coverage with respect to the scattered photon. However, they have also been employed in this study in order to assess the quality of the images that may be obtained with our system when simpler (easier to implement) sensitivity models are used. A comparison study between the different models for the calculation of the sensitivity matrix is conducted in section 5.2. They are compared following two methods: by directly comparing the matrix values against Monte Carlo simulations, and by using them in the reconstruction of images.

5.1.4 Validation of the physical model

The validity of the presented physical model for a two-plane Compton telescope has been evaluated through a comparison to simulations. This evaluation concerns both the system and the sensitivity matrices. The comparison between simulation and model is more direct for the case of the sensitivity matrix, since its computation from Monte Carlo simulations is straightforward. In order to obtain the simulated sensitivity value for voxel V, a monoenergetic point-like source is simulated inside it, emitting isotropically a fixed number of gammas. The sensitivity is given simply by the fraction of detected signal events over the total emissions, which can be compared directly to the value obtained from integration of equation (5.10).

In fact, a small modification in equation (5.10) can provide more insight in the weights of the different processes involved in the signal formation. As stated in the derivation of the physical model, we are assuming that the initial gamma energy is known, and therefore the energy deposited in the second plane does not play a role. This is equivalent to saying

that we are accepting all detected interactions in the second plane, regardless of their nature: photoelectric absorptions, second Compton scatters or e^+e^- pair productions. This is reflected in the choice of the total linear attenuation coefficient of the scattered photon, μ_1, in equation (5.10). This coefficient can be split as the sum of three contributions, $\mu_1 = \mu_1^{pe} + \mu_1^{C} + \mu_1^{pp}$, where the superscripts refer to each of the mentioned processes. In order to calculate the sensitivity of the system to the different processes in the second plane, μ_1 in equation (5.10) must be replaced by their corresponding term. Of course, the contributions of the different processes can also be easily extracted from the simulated data. In the processing of the simulated data, the generated coincidence events are classified according to the physical process undergone by the photon in the second plane, and the sensitivity to each of them is given by the number of that particular type of events measured, divided by the total emissions.

The comparison between the simulated and calculated sensitivity is shown in Figure 5.4*. Figures 5.4a and 5.4b represent the sensitivity of the system to the each of the mentioned pairs of interactions calculated with the analytical model, compared to the one extracted from simulations, for sources in an energy range between 200 keV and 5 MeV placed at two positions along the x axis in the FoV. Figures 5.4c and 5.4d show the sensitivity profiles of those same interactions for points located along a line in the FoV for two fixed energies. For this test, energies of 1275 and 4439 keV have been chosen, due to their frequent use in our experimental measurements. In all cases, almost perfect agreement is found between simulations and our model, which indicates that all probabilities are being properly taken into account.

A simplified methodology has been developed to validate the SM model described in section 5.1.1. The data space is described by the continuous variables $\vec{r}_1$, $\vec{r}_2$ and $\tilde{E}_1$, which yield an infinite number of possible CoRs. In order to reduce the complexity of the problem, the detector planes are discretized into N_i, N_j boxes, so that $\vec{r}_1 \in P_1^{i=1,\dots,N_i}$, $\vec{r}_2 \in P_2^{j=1,\dots,N_j}$, and all energy depositions on the first plane are divided into $N_{\tilde{E}}$ elements. With this binning of the data, the number of possible CoRs is limited to $N_i \times N_j \times N_{\tilde{E}}$. For simplicity, we will group all the energy depositions on the first plane in a single bin, $N_{\tilde{E}} = 1$. The value of each SM element is calculated by integrating equation (5.5) in the appropriate detector volume elements. The integral of the element defined by P_1^i, P_2^j at voxel V reads:

$$t_{ij,V} = \int_0^{\tilde{E}_1^{\max}} d\tilde{E}_1 \int_{P_1^i} d^3 r_1 \int_{P_2^j} d^3 r_2 \int_0^{2\pi} d\varphi \int_0^{\infty} d\xi \, \frac{dP}{d\varphi \, d\xi \, d^7\eta} \, , \tag{5.12}$$

*All studies presented in this section were carried out for a Compton camera with our system dimensions and an inter-plane distance of 40 mm.

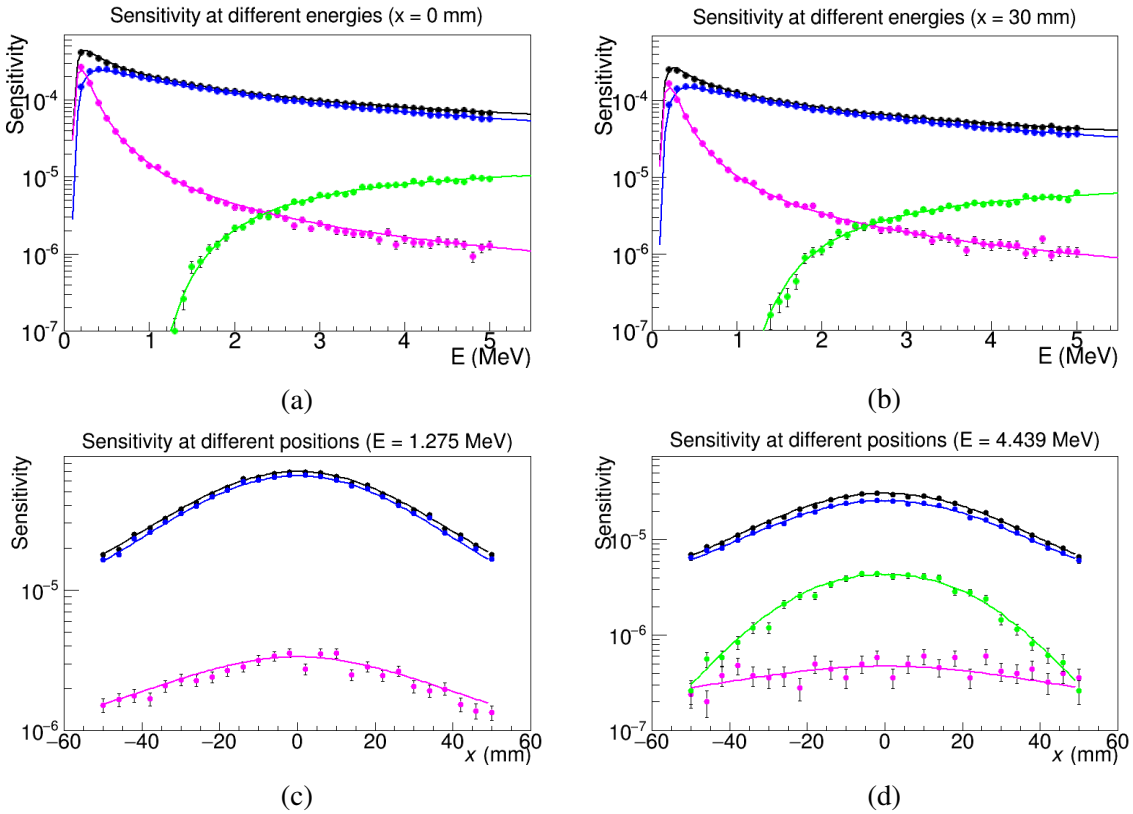

Figure 5.4 Top row: sensitivity to the possible interactions of the photon in coincidence events over a range of energies for a source placed at $x = 0$ mm (a) and $x = 30$ mm (b). Bottom row: comparison of sensitivity profiles of the possible interaction types obtained for sources at different positions with energies of 1275 keV (c) and 4439 keV (d). In all plots, the points are obtained from simulated data and the continuous lines from the integration of equation 5.10. The different colors indicate the interaction experienced by the photon in the second plane: Compton scatter (blue), photoelectric absorption (pink), pair production (green) or any of the three (black).

where $\tilde{E}_1^{\max}$ is the maximum energy that a photon of energy E_0 can deposit in a Compton scatter, previously defined in section 1.2.1. The numerical integration of equation (5.12) yields an estimation of the probability of the CoR defined by detector elements P_1^i, P_2^j to have been generated by an emission in voxel V. Figure 5.5 illustrates this discretization and the activation of one of the finite CoRs (i.e., pairs of detector elements) by an emission from one voxel in the FoV. To assess the validity of the physical model, we check that the analytically calculated SM elements are in accordance with those that could be obtained from Monte Carlo simulations. This oversimplified classification of CoRs is only used to check the compatibility of the SM derived from our model with simulations, and has not been used for image reconstruction.

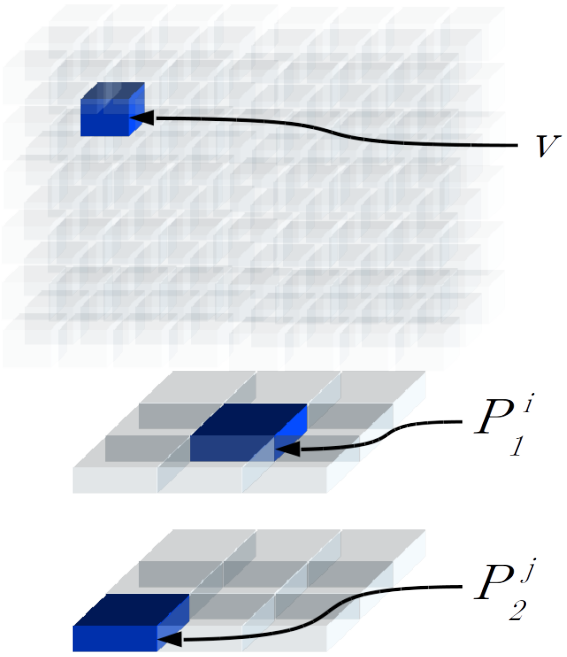

Figure 5.5 Diagram of a Compton camera showing the discretization of the detector volume used for the validation of the SM model.

For the numerical computation of equation (5.12), each of the two considered detector planes was divided into 3×3 detector elements of equal dimensions, as represented in Figure 5.5. Since the model considers the whole size of the scintillator crystals, the number of elements into which they are discretized is arbitrary. Because the number of possible CoRs allowed increases multiplicatively with the number of divisions, for this assessment the division into 3×3 detector elements was chosen, which yields 81 possible CoRs for the comparison between model and simulations. This number is high enough for the comparison while still remaining manageable. Equation 5.12 has been calculated via Monte Carlo integration with $5 \cdot 10^6$ events, randomly generated over the whole integration region and then assigned to the corresponding CoR. For each event, a cone surface is obtained and projected onto the FoV, which allows to calculate the values of the traversed voxels. Since all voxels in the FoV are considered for this projection, in practice this process yields one image for each pair of detector elements, which corresponds to one row of the SM. The equivalent to one SM column (the probability of an emission from a specific voxel V to be measured in each of the possible CoRs) can be recovered by selecting the value of element V in all the obtained images (see Figures 5.6a and 5.6b).

From simulations, the SM elements have been calculated for a source emitting $2.5 \cdot 10^9$ photons of 1275 keV. The simulated events are classified in the CoR index according to the detector elements in which the interactions took place. For this assessment, only ideal events

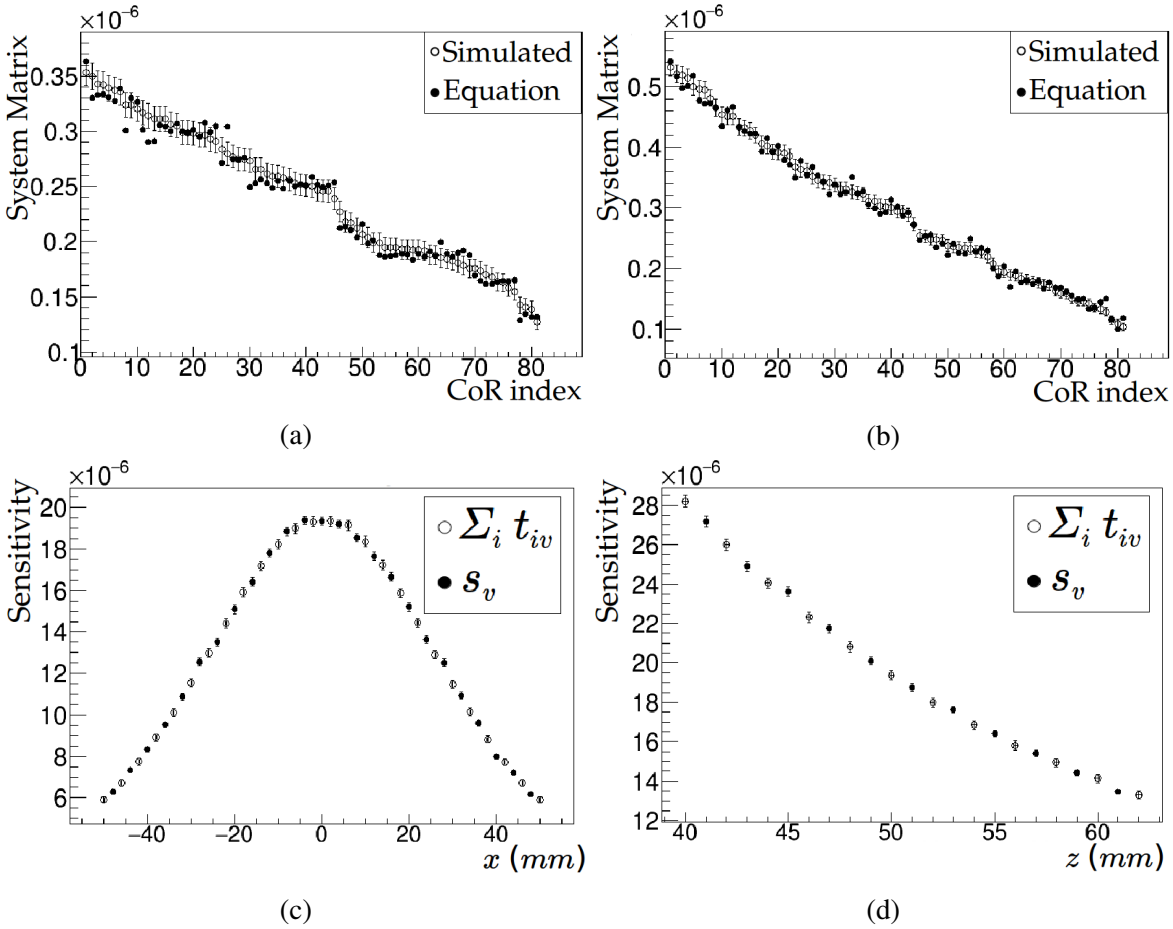

Figure 5.6 Top row: values obtained for all the possible CoRs in the SM with the considered discretization of the detector elements. CoRs for voxels located at (0,0,0) mm (a) and (10,10,10) mm (b), being the first detector plane centered at (0,0,50) mm and the second one at (0,0,100) mm. Bottom row: sensitivity matrix profiles along the x (c) and z (d) axes, obtained through numerical integration of equation (5.10) and by summing all the SM elements given by integration of equation (5.12).

with no spatial or energy resolution have been considered. The simulated sources have been placed in two different voxels, located at the coordinates (0,0,0) mm and (10,10,10) mm. This allows the comparison of two SM columns between simulated and numerically integrated results. The simulated results (hollow circles) are plotted next to the calculated values (filled dots) in Figures 5.6a and 5.6b. Both values are in agreement within the statistical error, which is taken as a validation of the employed physical model.

Another consistency check on the validity of the SM can be performed by comparing the sum of all CoRs to the sensitivity matrix. In order to do so, all the SM rows have been summed, producing a new sensitivity image that can be compared to the one obtained by

numerical integration of equation (5.10). Figures 5.6c and 5.6d show profiles of these two images along the x and z axes[†], showing the agreement between the values of s_v (filled dots) and $\sum_i t_{iv}$ (hollow circles).

5.2 Impact of the sensitivity on reconstructed images

A good agreement between our analytical model and the simulations has been shown in the previous section, demonstrating that the most relevant physical processes are being taken into account to a high level of accuracy. The next step is to test the model in the image reconstruction process. As mentioned before, the developed reconstruction code implements a list mode MLEM algorithm, for which the SM is built as explained in section 5.1.2. The algorithm also employs the sensitivity matrix, which is precomputed and loaded by the code before the iterative procedure begins. Sensitivity matrices obtained from different models can be plugged in the algorithm at this stage.

The calculation of the sensitivity matrix derived from our complete model requires the numerical integration of equation (5.10). This may be an excessive computational effort for some applications, so the use of approximate models for the sensitivity can be preferable in some cases. Before we assess the impact of the tested sensitivity models on the final reconstructed images, the different sensitivity models are compared with results obtained from simulations. This comparison is shown for two initial gamma energies (1275 and 4439 keV) and with two different relative distances between sources and detector planes, in order to study the accuracy of the sensitivity models in situations with different angular coverage over the scattered photons. In the first case, the sources are placed on a plane 40 mm from the first detector and the distance between detectors is 40 mm. In the second case, the distance to the source is 50 mm and the inter-plane distance is 100 mm. Given the dimensions of the detector planes, the solid angles subtended by the second plane relative to the center of the first one are 0.416 and 0.067 sr for the first and second cases respectively. We will henceforth refer to these two configurations as high angular coverage and low angular coverage scenarios.

Figure 5.7 shows profiles along the x axis of the sensitivity images given by the different models considered. These profiles have been obtained from our implementation of the two approximate models considered, s_v^W and s_v^M, and with our analytical model, s_v, and are plotted together with the values obtained from simulations. It is worth to mention that the approximate models are not taking into account a constant factor that is present in the analytical model. However, in general, these constants can be ignored for image

[†]The z position in Figure 5.6d represents the distance as measured from the first detector plane.

reconstruction. In order to plot the profiles together, the approximate models have been normalized to the maximum value in the profile given by our analytical model. It should be noticed that our analytical model considers all the factors involved in the interactions, and so it matches the simulated values without the need for any normalization. The sensitivity profiles have been calculated for the two described geometrical configurations. The results obtained in the high angular coverage scenario are shown in Figures 5.7a and 5.7b, and those obtained in the low angular coverage scenario are shown in Figures 5.7c and 5.7d.

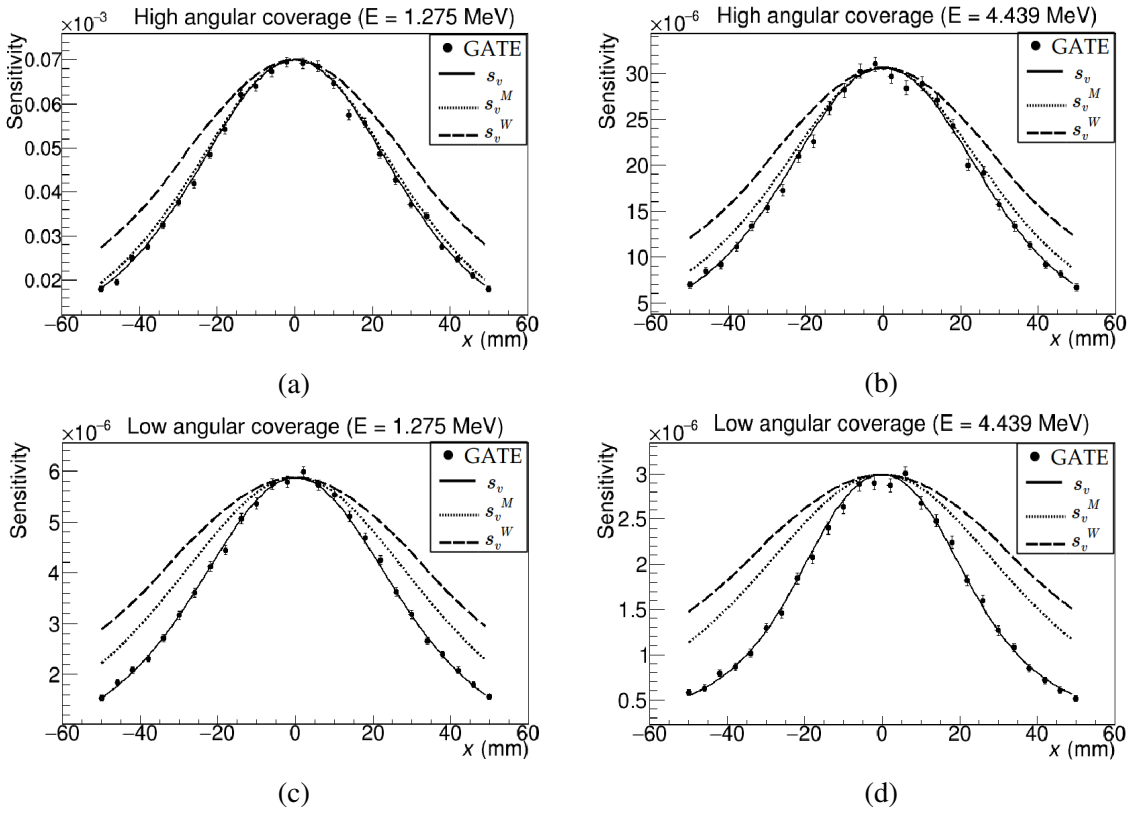

Figure 5.7 Comparison of sensitivity profiles obtained for models reported in the literature (s_v^M,s_v^W), our analytical model (s_v) and from Monte Carlo simulations, for two different energies and configurations. Top row: high angular coverage of the second plane relative to the first one and energies of 1275 keV (a) and 4439 keV (b). Bottom row: low angular coverage of the second plane relative to the first one and energies of 1275 keV (c) and 4439 keV (d). The plots of the approximated models (s_v^M,s_v^W) have been renormalized to the maxima given by our analytical model (s_v).

It can be seen in the profiles that, in general, the approximate models tend to overestimate the system sensitivity for positions located further away from the detector center with respect to our model. The deviation between the approximated models and the Monte Carlo results is larger for the case with lower angular coverage. This was expected, since the approximated

models assume that the sensitivity is mostly due to the detection probability in the first plane. In low angular coverage scenarios, however, the probability that the scattered photon reaches the second plane has an important contribution to the overall sensitivity that should be considered. As will be shown in the remainder of this chapter, these deviations have an effect on the reconstructed images of different source distributions.

5.2.1 Simulated sources

Point-like sources

Nine point-like monoenergetic sources placed along a horizontal line, contained in a plane parallel to the first detector, have been simulated and reconstructed with the tested sensitivity models. The point-like sources are defined in the simulation as spheres with a radius of 10^{-6} mm and are left to emit isotropically $5 \cdot 10^8$ photons during the simulation time. Each point-like source is simulated independently at a distance of 5 mm from the previous source position, covering the range between (0,0) and (40,0) mm with respect to the center of the detector. The effect of the sensitivity matrix on the reconstruction process is evaluated by comparing the intensity of the point-like sources in the reconstructed images. This is done by selecting the values of the voxels where the source is recovered. To avoid partial volume effects caused by the spread of the active point, these values are completed by summing the closest neighbors in a radius of 4 voxels.

Images of simulated monoenergetic point-like sources have been reconstructed in a FoV of $101 \times 101 \times 25$ voxels of $1 \times 1 \times 1$ mm^3, using the different models for the sensitivity matrix in the MLEM equation. In order to compare quantitatively the different results obtained for each sensitivity model, the values of the voxels where the source is reconstructed are plotted together in Figure 5.8. The two different data sets generated from simulations, introduced in section 3.2, have been used, which consist of either ideal (Hits) or realistic (Singles) events. Figures 5.8a, 5.8b, 5.8c and 5.8d represent the cases with high angular coverage over the scattered photon, in which the distance to the source is 40 mm and the distance between planes is 40 mm. In Figures 5.8e, 5.8f, 5.8g and 5.8h the distance to the source is 50 mm and the distance between planes is 100 mm (low angular coverage scenario). The plots represent the maximum value for each case with the ideal (left column) and realistic (right column) events, measured with a 1275 keV and a 4439 keV sources. The dashed line shows the ideal case.

Several interesting features can be noted from the results in Figure 5.8. If the approximation of a constant sensitivity is employed, sources of the same activity placed in regions of different sensitivity in the FoV are reconstructed with different intensities. When only ideal

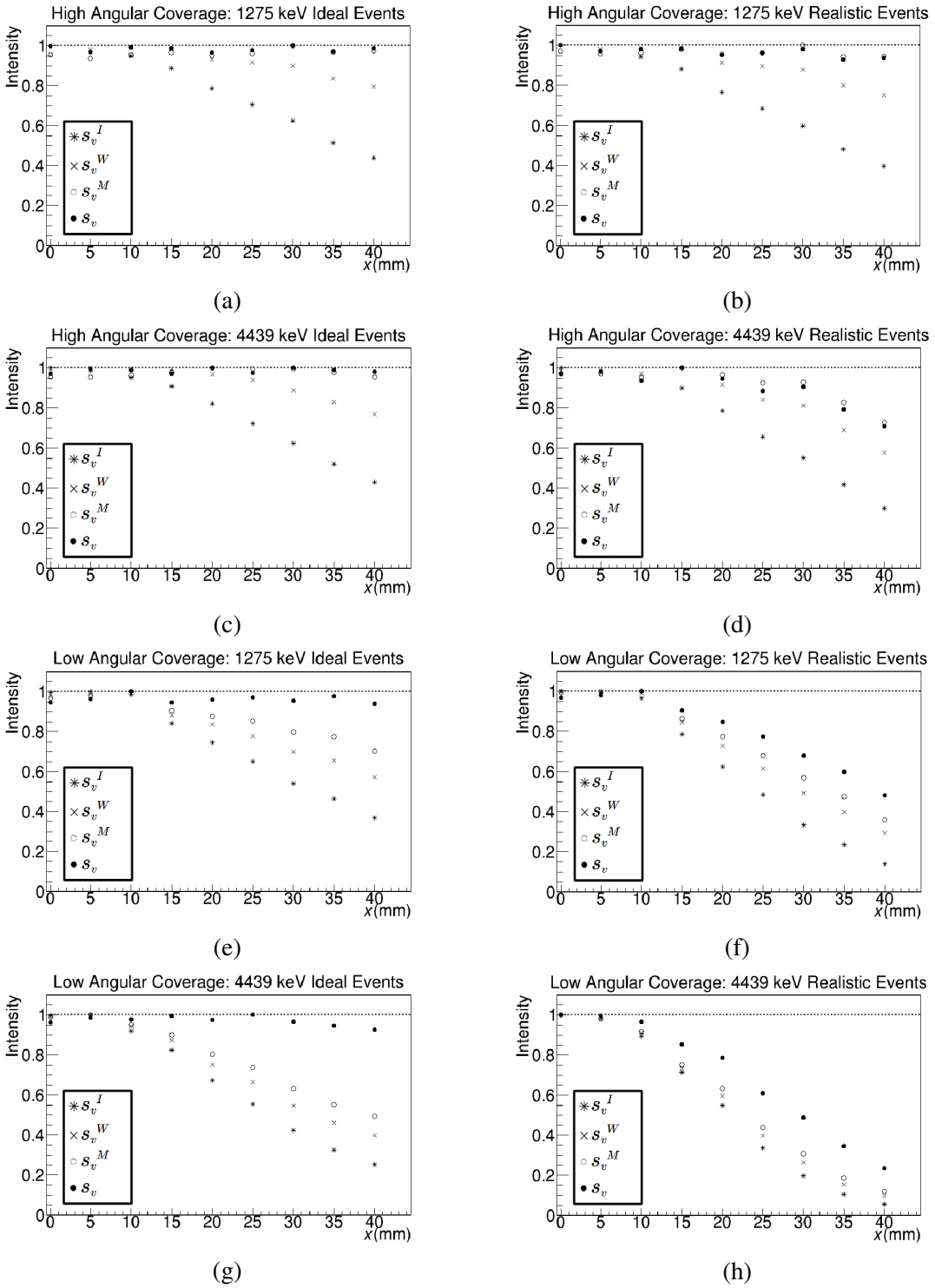

Figure 5.8 Comparison of reconstructed images of point-like sources, in the high and low angular coverage scenario, using ideal and realistic data with the different sensitivity models.

events (without energy or spatial resolution) are considered, the results show that, by using our sensitivity model, we are able to reconstruct the activities of the sources in all cases, even for those placed outside the region of direct coverage. The other models considered, s_v^W and s_v^M, are able to correct for this effect partially. In particular, the results obtained with the s_v^M model in the high angular coverage configuration are practically indistinguishable from those obtained with our model. It is in the low angular coverage scenario where our model clearly improves the results, as the approximate sensitivities cannot compensate the image intensity for positions placed further away from the region of direct coverage.

When realistic events are considered, the activity of the source cannot be recovered correctly, and sources closest to the detector surface are given higher intensities than those placed further away. This degradation, which appears for all sensitivity models employed, is not surprising, since the detector resolutions have not been included in the derivation of the physical model. In any case, the images reconstructed with our sensitivity model still achieve the most uniform results.

Homogeneous regions

The impact of the sensitivity model on regions of homogeneous activity filling the entire FoV has also been studied. For these tests, two phantoms with homogeneous activity have been simulated: a planar phantom of $101 \times 101 \times 1$ mm^3 and a thick phantom of $101 \times 101 \times 25$ mm^3. In both cases, the phantoms were simulated emitting 4439 keV photons, at 40 mm from the first detector and with an inter-plane distance of 40 mm (high angular coverage scenario)

The homogeneous planar source phantom has been reconstructed with the different sensitivity models in a FoV of $101 \times 101 \times 1$ mm^3 divided into $51 \times 51 \times 1$ voxels. Approximately 10^5 signal events were used, and the resulting images can be seen in Figure 5.9. Since the simulated phantom is simply a homogeneous source filling the entire FoV with the same activity, a representation of the original phantom is not shown. In order to compare the images quantitatively, the standard deviation of the voxel values has been calculated for the four cases at every iteration step, which can be seen in Figure 5.10a. In this case, there is little difference between the images obtained from the singles and the hits data, so the quantitative study compares only the results from the different sensitivity models with ideal hits. Figure 5.10b shows the standard deviation for the case of the $101 \times 101 \times 25$ mm^3 homogeneous source phantom, which was also reconstructed (but not shown) with all the considered sensitivity models, in a FoV equal to its extension and divided into $51 \times 51 \times 13$ voxels.

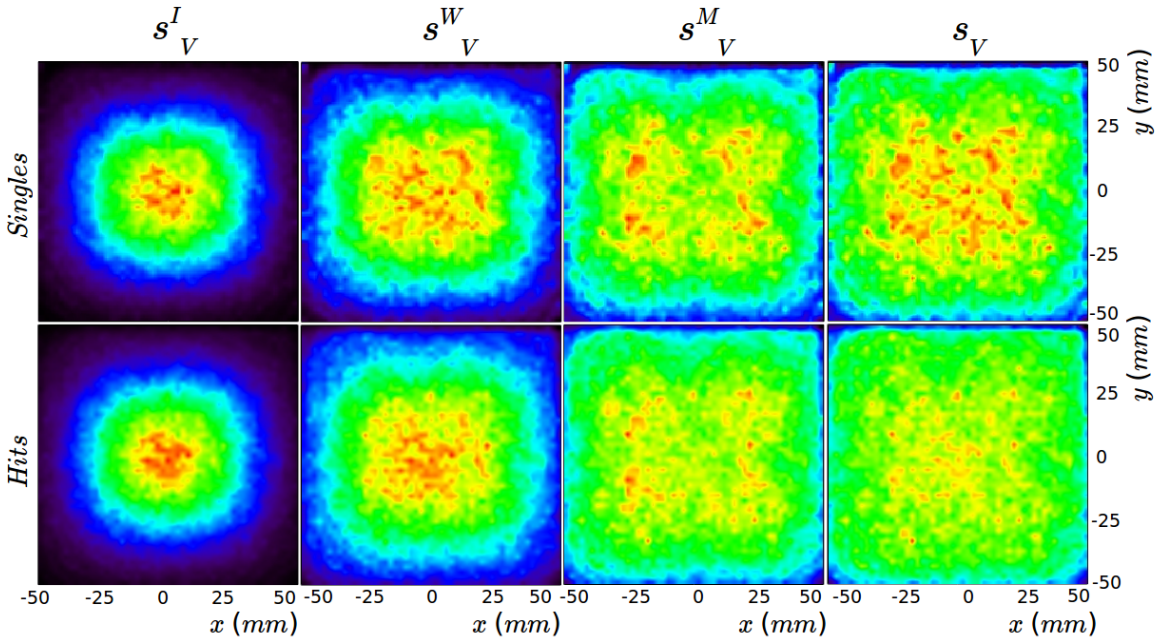

Figure 5.9 Reconstructed image of a homogeneous planar source phantom reconstructed with the different sensitivity models. Images represented here correspond to iteration 3, since it is the iteration number with the smallest standard deviation (see Figure 5.10a).

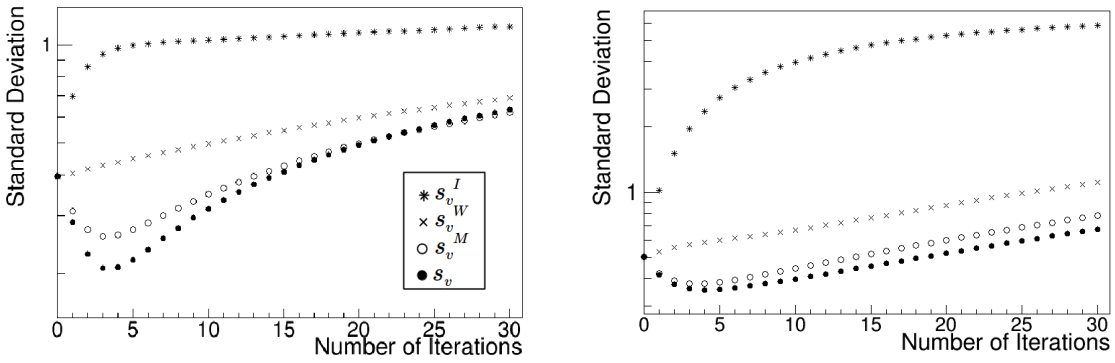

Figure 5.10 Comparison of reconstructed images of homogeneous activity regions with the different sensitivity models. The plots represent the standard deviation of all voxels in the reconstructed space for a $101 \times 101 \times 1$ mm^3 (a) and a $101 \times 101 \times 25$ mm^3 phantom (b).

The results show that the use of a sensitivity model makes an important difference. Under the assumption of a constant sensitivity, only the region directly covered by the detector footprint is reconstructed with maximum intensity, which decreases smoothly for voxels placed further from it. A clear improvement is seen with s_v^W, although the intensity in the

image edges is still underestimated. The study shows that s_v and s_v^M yield similar images, although the noise is diminished with our analytical model (Figure 5.10).

Shepp-Logan phantom

The different sensitivity models have also been tested with a two-dimensional Shepp-Logan-like phantom [82], in order to assess the performance of the image reconstruction method and the impact of the sensitivity on a more complex scenario. The Shepp-Logan phantom was simulated emitting 1275 keV photons, at 40 mm from the first detector and with an inter-plane distance of 40 mm (high angular coverage scenario). A diagram of the simulated phantom is shown in Figure 5.11, which also shows the region directly covered by the simulated detector.

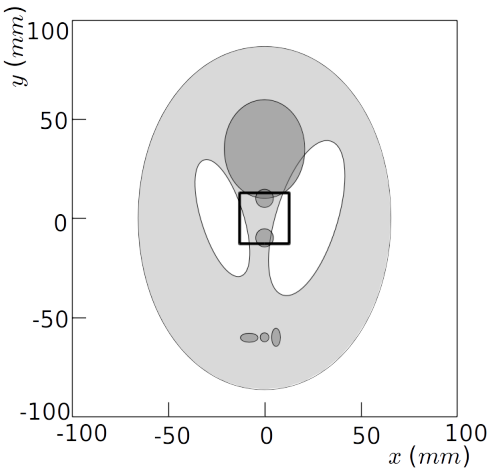

Figure 5.11 Simulated Shepp-Logan phantom.

Figure 5.12 shows the images recovered with the different models of the sensitivity, for both the realistic singles (top row) and the ideal hits (bottom row) selected from the simulation. The reconstructed FoV is $201\times201\times25$ mm^3 divided into $51\times51\times25$ voxels. The images shown correspond to iteration 20 of the reconstruction algorithm. The iterative procedure was stopped at this point, since no improvement in the identification of the different phantom structures was observed for higher iterations.

The importance of the sensitivity model in the imaging of spatially distributed sources is obvious in Figure 5.12. In this case, the footprint of the detector only covers a small fraction of the phantom, and in the image obtained with a constant sensitivity no structure beyond this size can be recovered, so the phantom cannot be recognized. The three employed models improve notably this result. Looking at the images obtained with the hits data, the edge of the phantom is clearly delimited from the empty background in the images obtained from the three models. Regarding the interior structure, again s_v^W performs worse than the other

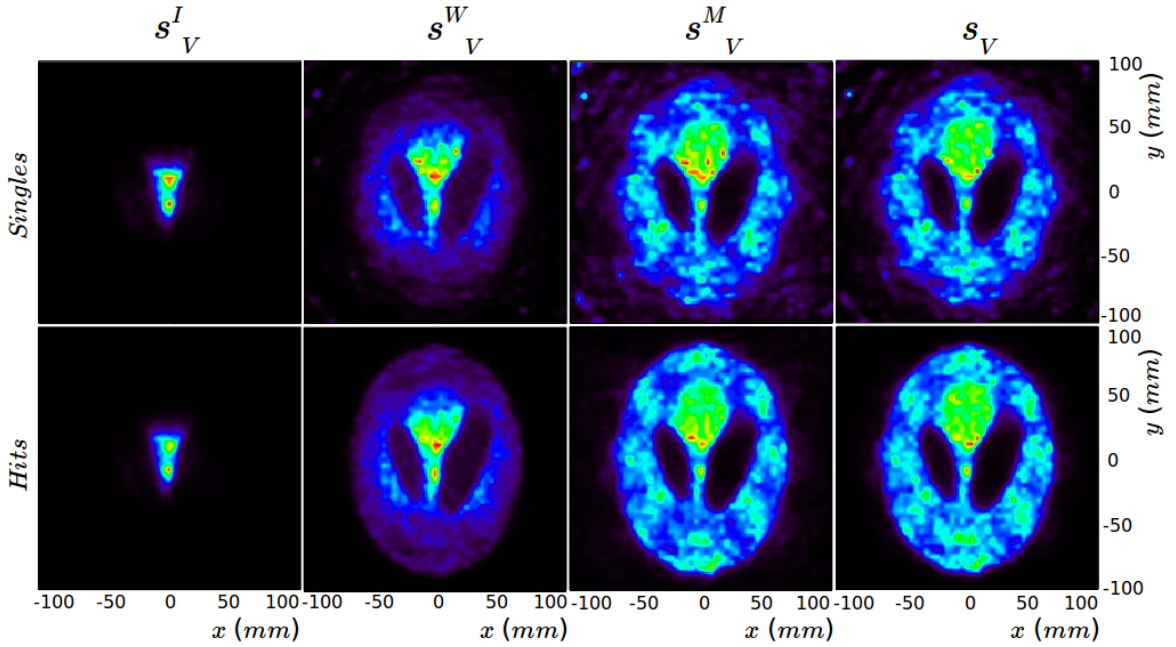

Figure 5.12 Reconstructed images of the two-dimensional Shepp-Logan phantom with the different sensitivity models.

two, especially in the compensation of intensity for points further to the detector. In this case, there is little difference between our model s_v and s_v^M, and only a slight increase of the noise around the phantom edge can be appreciated with s_v^M. This is in accordance with the results discussed in previous sections, as the simulations were performed in the high angular coverage scenario. The reconstructed images from the singles events show degradation when the measured data is subject to the detector resolutions. In this case, this can be appreciated mainly in the image blurring, most noticeably around the phantom edges, and in an increase of noisy pixels in the empty background.

5.2.2 Experimental sources

The effect of the different sensitivity models has also been tested with experimentally measured data. For that purpose, a first study was performed with a ^{22}Na point-like source. Data from this source have been taken placing it at six different points on a fixed plane parallel to the detector surface, in a similar fashion to the simulated point-like sources studied in section 5.2.1. Each position was separated 5 mm along a fixed line from the previous one, covering the range between 0 and 25 mm as measured from the center of the detector. A schematic view of the source positions with respect to the detector in the different measurements can be seen in the left column of Figure 5.13. Since the edge of the detector

is 12.9 mm from its center, only the three inner positions are contained inside the region of direct detector coverage. The activity of the source at the time of measurement was 537 kBq, and every measurement lasted a fixed time of 20 minutes. The distance from the plane of the source to the first detector was 40 mm, and the distance between detectors was 80 mm. The reconstruction of images was performed after applying a low energy threshold at 600 keV in the summed energy, in order to select only the data produced by the 1275 keV photon emitted by ^{22}Na. For this study, the energy of 1275 keV was chosen because, as we saw in the previous chapter, the data generated by the 511 keV photons emitted by the source leads to noisier images. Another reason to perform the study with the highest energy photon is that, since our ultimate goal is to use the camera for prompt gamma imaging, its energy is more similar to the range in the final application.

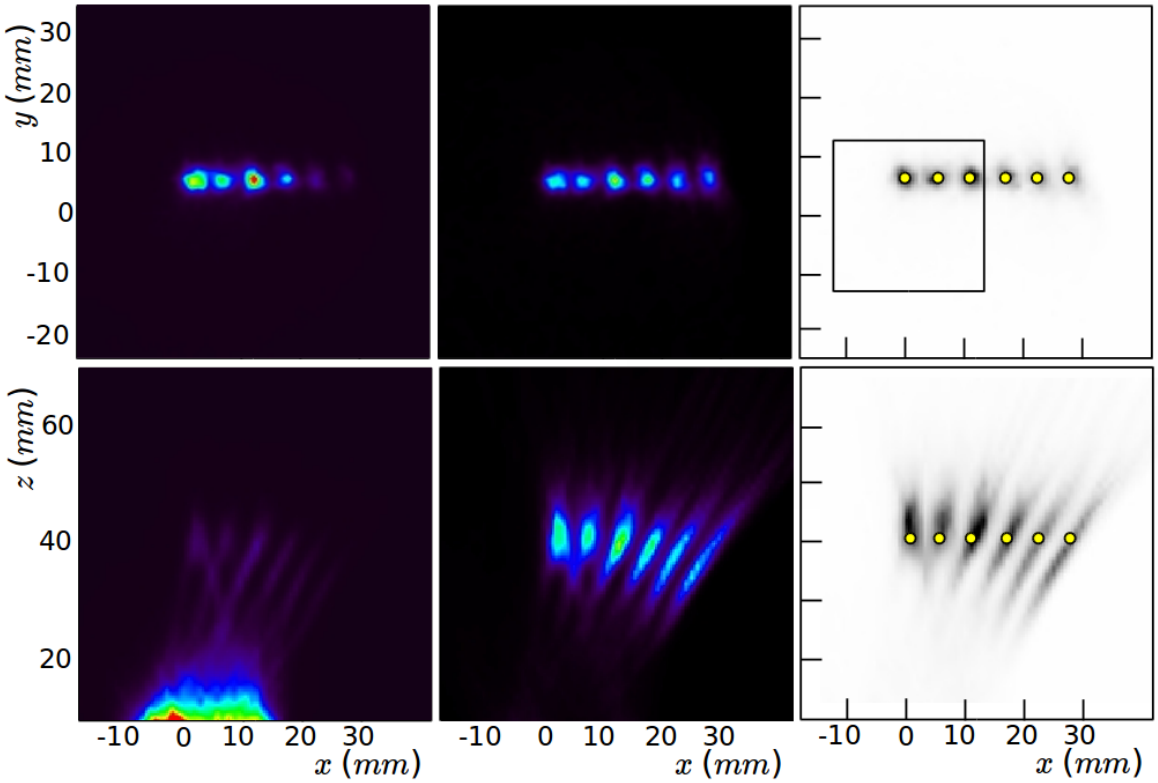

Figure 5.13 Sum of the individually reconstructed images of the experimentally measured data with a point-like ^{22}Na source. The left column shows the transverse (top) and coronal (bottom) views of the image obtained with s_v^I. The equivalent images obtained with our sensitivity model are shown in the middle column. These are also shown in the right column, plotted in gray scale for a better visualization of the true source positions, indicated in yellow.

The data taken with the point-like ^{22}Na source was reconstructed independently for every measurement and with each of the sensitivity models. The images, obtained after 5 steps in

the iterative algorithm, are shown in Figure 5.13, where the top row shows the transverse view of the summed image and the bottom row shows the coronal view. Images in the left column correspond to the image recovered with the sensitivity matrix set to 1, s_v^I. In this case, most of the activity is assigned to the voxels closest to the detector surface. In order to enhance the visibility, the image intensities have been renormalized independently for each slice of the reconstructed 3D image. With this renormalization, the three positions of the point-like source placed inside the region of direct detector coverage are visible; the fourth position, placed 2.1 mm away from the edge of the detector, can also be identified. The remaining two positions are barely visible, with a very attenuated activity. The middle column represents the result obtained when our analytical sensitivity model is used by the reconstruction algorithm, where it can be observed that the activity assigned to the voxels closest to the detector surface is properly compensated and corrected, and so it is not necessary to renormalize the intensities for each slice. In this case, the six different positions measured are clearly visible in the image and their activities are compensated. The right column in Figure 5.13 shows images equivalent to the middle column (obtained with our model), which in this case have been plotted in gray scale for a better visualization of the true source positions, indicated as yellow circles. The other sensitivity models considered yield visually similar results to the ones obtained with our model, and are therefore not shown.

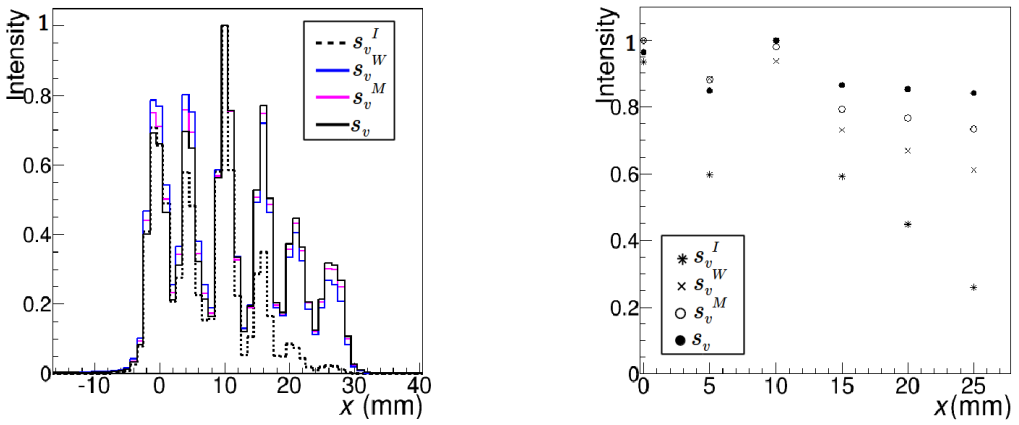

(a) (b)

Figure 5.14 Profiles along the maxima with all the sensitivity models (a) and intensity of the different images after correcting for partial volume effects (b).

In order to compare the results obtained with the tested sensitivity models quantitatively, the numerical values assigned to the different source positions are represented in Figure 5.14 (normalized independently for each model). Figure 5.14a shows the profiles along the x axis through the maximum for all the images obtained. The profiles recovered from the images

with the three tested sensitivity models have a similar shape, and all of them achieve better uniformity than the constant case. In order to compensate for partial volume effects and correctly compare the reconstructed intensity of the source in each position, the values of the neighbors in a radius of 4 voxels around the maximum have been summed and plotted together in Figure 5.14b, following the same procedure as for the simulated point-like sources in section 5.2.1. This allows to correct partially for the spread of activity in the image around the source position, which can be clearly seen in the elongated shapes in the z direction in the bottom row of Figure 5.13. In this plot, it can be appreciated that our model yields the most uniform results over the whole tested range of positions. Again, the most significant difference between the models appears at the points placed outside the detector footprint, where the approximated sensitivities tend to underestimate the source intensity.

In addition, an array of 37 ^{22}Na sources was also measured and imaged. Each of the sources conforming the array has an active area of 1 mm in diameter and is separated 10 mm in the x and y directions from its closest sources. A diagram of the positions of the active points within the encapsulated source is shown in Figure 5.15, in which the detector footprint is also indicated. The total activity of the ensemble of sources was 754 kBq at the time of measurement. For this measurement, the distance between detectors was 80 mm and the source plane was separated 30 mm from the first detector. The acquisition time of the experimental data was approximately 4 hours, yielding a total of $1.9 \cdot 10^5$ coincidence events.

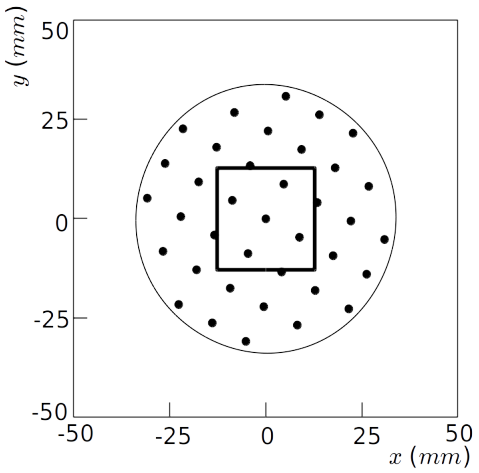

Figure 5.15 True positions of the sources and the region of direct detector coverage.

The reconstructed images obtained from the experimentally measured data, employing the different sensitivity models, are shown in Figure 5.16. These images were obtained after 50 iterations, with a FoV of $101 \times 101 \times 25$ voxels of $1 \times 1 \times 1$ mm^3. The images shown are two-dimensional slices of the three-dimensional reconstruction, corresponding to the depth

at which the source is located. A three-dimensional median filter with cubical footprint and $3\times3\times3$ voxels window size has been applied after final iteration in order to remove the high frequency noise present in the four experimental images shown.

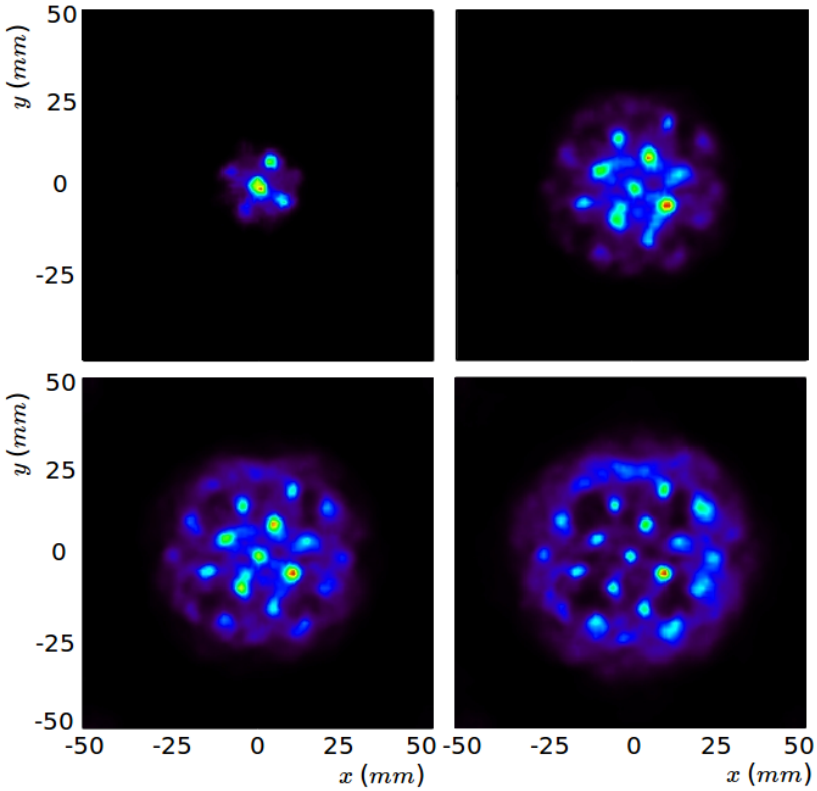

Figure 5.16 Reconstructed images of experimentally measured data of the ^{22}Na array source with the different sensitivity models: s_V^I (top-left), s_V^W (top-right), s_V^M (bottom-left) and s_V (bottom-right). $1.9 \cdot 10^5$ coincidence events were used for the reconstruction of the displayed images.

In Figure 5.16 we can see that, when sensitivity corrections are ignored (s_v^I is used) only the central sources can be distinguished. The image is significantly improved when s_v^W or s_v^M are used, and especially when our model is used. In the image obtained with our sensitivity model, the sources in the central region of the image are better delimited and present a higher contrast with the background. As in the simulated studies, the intensities assigned to the different sources present higher uniformity in this case than in the others. The most external point-like sources of the array, which lie well outside region of direct coverage, are not visible with any of the three models.

5.3 Discussion

An analytical model for the calculation of the system and sensitivity matrices of a Compton camera has been derived and presented in this chapter. The analytical model has been validated taking Monte Carlo simulations as a reference. A good agreement has been obtained for the system and sensitivity matrices. In order to validate the SM, the detector planes have been divided into a small number of boxes, so that the SM contains only a small number, 81, of CoRs. The values of the resulting SM elements have been calculated for two different source positions, and are found to be in agreement with those obtained from Monte Carlo simulations. Regarding the sensitivity matrix, results have shown that the analytical model can predict the sensitivity of the system to all possible pairs of physical processes experienced by a photon producing a coincidence event, and that all normalization constants are properly taken into account. This agreement has been reproduced for all the positions and energies of the point-like sources studied in this work.

Our sensitivity model has been compared with other simplified models, which can be more easily implemented in the reconstruction code and are computationally less expensive: s_v^W and s_v^M. The comparison of these models, taking the Monte Carlo results as reference, shows that the simplified models reproduce the sensitivity profiles with good accordance in some of the considered scenarios, especially s_v^M. However, our analytical model, despite its higher computational cost, offers several advantages. Firstly, since all the physical factors are being considered, the global constant of the sensitivity matrix is automatically calculated and it does not require any further normalization. This global constant is generally not necessary for sensitivity correction in the reconstruction algorithm, but it also conveys useful information; for instance, it is necessary for the direct comparison with the Monte Carlo results, and could be used to calculate the overall efficiency of the system. Secondly, simplified models provide the sensitivity matrix up to a normalization constant. This constant depends on the initial gamma energy. Our model includes implicitly this energy dependence, so it could be useful in scenarios in which it is interesting to image sources of various energies or in spectral reconstruction codes, which estimate both the source position and spectral emission simultaneously (see next chapter). Finally, only our model considers explicitly the dependence of the sensitivity on the inter-plane distance. This distance plays an important role in image reconstruction: the uncertainty in the positioning of the cone axis is reduced for longer inter-plane distances, thus improving image resolution, but the number of measured coincidences also decreases. In some cases, it may be desirable to increase this distance, leading to a situation in which the assumption that most photons scattered on the first plane will be detected by the second one cannot be made. In this scenario, the simplified models will perform worse, since the assumptions on which they are based cease to be correct.

In a quantitative analysis of the reconstructed images, the sensitivity matrix plays an important role. In this sense, we have studied the reconstruction of regions with homogeneous activity. The results (Figure 5.9) show that the use of a sensitivity model makes an important difference. The sensitivity correction allows to recover the regions of the FoV placed outside the area directly covered by the detector. The study shows that the simplified models yield similar images, although the noise is diminished with our analytical model (Figure 5.10).

If the approximation of a constant sensitivity is employed, sources of similar activities placed in regions of different sensitivity in the FoV are reconstructed with different activities. In order to study this effect, we have evaluated the impact of the sensitivity model on the image reconstruction of point-like sources simulated with the same activity at different positions and with different energies. When only ideal events (without energy or spatial resolution) are considered, the results show that, by using our sensitivity model, we are able to reconstruct the activities of the sources in all cases, even for those placed outside the region of direct coverage. The other models considered, s_v^W and s_v^M, are able to correct for this effect partially, but they perform worse as the source is placed further away from the region of direct coverage. However, the activity of these point-like sources can no longer be properly reconstructed when spatial and energy resolutions are considered. This degradation, which appears for all the sensitivity models, is expected, since the detector resolutions were not included in the construction of the SM.

The reconstruction of images of a Shepp-Loggan phantom was also studied. This phantom represents a more complex scenario than the previous cases, since it consists of several regions of different activity with an internal structure. When the sensitivity is ignored, the phantom structure cannot be identified. The use of any of the sensitivity models produces a significant improvement. In the image obtained with s_v^W, the cold areas and external contour of the phantom are well delimited, but regions of homogeneous activity are not reconstructed with uniform intensity. The images obtained with s_v^M and with our analytical model are very similar, and present more uniformity in the regions of homogeneous activity, but the smallest structures are still not visible.

The sensitivity models were also tested in the laboratory with a point-like source of ^{22}Na. Figure 5.13 shows that the sources located in the region of direct coverage of the detector can be reconstructed even if we ignore the sensitivity, although the intensities given to points located at different positions are not compensated. In this case, the points placed outside this region are not visible. Furthermore, the voxels closest to the detector surface are given the highest intensities. These artifacts are compensated by the three sensitivity models studied. In this case, the use of the simplified models, s_v^M in particular, gave results which are visually very similar to those obtained with our model. With all the models, the recovered images

present some elongation in the direction radial to the center of the detector, which is more visible as the source is placed further from it. This elongation is due to the finite surface of the detectors, which truncates the available projections. After correcting artifacts by taking into account all the voxels into which the activity is spread, the effect of the sensitivity model in compensating the reconstructed activities at different positions can be seen in Figure 5.14b. While all three models considered clearly improve the case of s_v^I, our model yielded the most uniform results, especially for the points furthest from the region directly covered by the detector.

The above descriptions can also be applied to the results obtained for the experimentally measured array of ^{22}Na sources. Figure 5.16 illustrates the impact of the sensitivity model on the final image. When a constant sensitivity is employed in the algorithm, only the central sources can be distinguished, and the sources placed outside the detector footprint cannot be recovered. The image is significantly improved when s_v^W or s_v^M are used, and the best results were reconstructed when our model was used. In the image obtained with our sensitivity model, the sources in the central region of the image are better delimited and present a higher contrast with the background. As in the simulated studies, the intensities of all the visible sources are more uniform in the image produced by the algorithm with our analytical sensitivity model.

5.4 Conclusions

This chapter presents a detailed physical model of the processes involved in the detection of a coincidence event in a two-plane Compton camera. Through a comparison with Monte Carlo simulations, the model has proven to predict correctly the sensitivity and the SM of the camera. This model has been assessed for sources located at several positions and with different energies. The inclusion of all terms and physical processes makes this model suitable for most systems, regardless of the detector material and the geometrical configuration. It can be used in scenarios where the approximation that the second detector offers a high coverage is not valid. The model also includes the sensitivity dependence on the incident gamma energy.

The impact of the sensitivity on the reconstructed images has been studied, and the performance of our sensitivity model has been compared with other simplified models: s_v^W and s_v^M. While the simplified models have proven to work correctly in many circumstances, especially s_v^M, the approximations upon which they are based may not always be correct for our system. Thus, we have developed a more detailed analytical model for our system.

In summary, the derived model allows reconstructing homogeneous regions with reduced noise and correcting properly for the sensitivity dependences over the FoV, including regions outside the area directly covered by the detector, and it remains valid for any of the configurations of interest of our system.

Chapter 6

Imaging of sources of unknown emission spectrum

The previous chapter introduced a detailed physical model that was employed to successfully reconstruct monoenergetic sources with extended distributions of activity. Keeping in mind that the final goal of the project is to develop a Compton camera for hadrontherapy dose monitoring, and given the continuous spectrum of creation of prompt gammas and the necessity for high detection efficiency, the employment of spectral reconstruction algorithms for two-interaction events appears as highly desirable. Spectral reconstruction algorithms for Compton cameras have been previously proposed in the literature. A detailed model aimed at spectral reconstruction of radioactive sources was presented in [106], which was employed in the reconstruction of sources with spectral emission below 1 MeV with great accuracy. A different model, targeting prompt gamma imaging, was proposed in [20]. Although this last method did not include a detailed physical model for the system or sensitivity matrices, it was successfully employed in [91] to measure shifts in the Bragg peak.

In this chapter, our approach towards the development of a spectral reconstruction algorithm is presented, which is tested with various distributions of simulated and experimental multi-energy sources. The principle that constitutes the basis of the algorithm is the fact that the second interaction can be either a full or a partial absorption of the energy carried by the scattered photon, and so the coincidence event must have been produced by a photon with an initial energy equal or superior to the sum of the energies deposited in both interactions. This allows the formation of a set of conical surfaces with a different aperture angle for each of the initial energies tested. In turn, each conical surface is built taking into account the probability that the considered initial energy produces the measured outcome; in order to do so, the probabilities assigned to the system matrix elements are calculated as described in the previous chapter, with an extension to the spectral dimension. An expression for a

four-dimensional sensitivity matrix is derived from the physical model and employed in the reconstruction process.

6.1 System matrix

When the energy of the incoming photons is known, the image reconstruction algorithm can exploit this information. However, when it is not, the reconstruction algorithm should somehow compensate for this lack of information. The approach followed in this work is to simultaneously estimate the (spatial) distribution and the (energy) spectrum of the photon emission.

To this end, we extend the method presented in the section 5.1.1 in two aspects: first, four dimensional voxels (the three coordinates of the emission point plus the energy) are used and, second, an explicit model of the type of interaction in the second detection plane is kept.

In order to obtain the expression of the SM elements, we start from an expression similar to equation (5.1). In this case, we want to compute the probability of detection of a photon emitted from inside one of the (hyper) voxels V characterized by the position $\vec{r}_0$ and the energy E_0 [*]. The probability reads:

$$dP = \frac{d^3 r_0\, dE_0}{V} \cdot \frac{d\Omega_0}{4\pi} \cdot e^{-\mu_0 \ell_1} \cdot n_e^{eff} \frac{d\sigma_0^c}{d\Omega_1} d\Omega_1 d\ell_1 \cdot e^{-\mu_1(\ell_1' + \ell_2)} \cdot (dP^c + dP^e + dP^g) \cdot \Theta_V, \quad (6.1)$$

where most terms are identical to those in equation (5.1). Note that, unlike in the previous chapter, in this case we are considering four-dimensional (hyper) voxels, so the integral includes dE_0 and now Θ_V is defined as 1 if $\vec{r}_0$ and E_0 are inside V and 0 otherwise. The other important modification is visible in the terms $(dP^c + dP^e + dP^g)$. These terms stand for the differential probability of the photon to undergo in ℓ_2 a Compton, photo-electric or pair-production interaction respectively. Specifically, for the Compton and photo-electric interactions:

$$dP^c = n_e^{eff} \frac{d\sigma_1^c}{d\Omega_2} d\Omega_2 d\ell_2 \cdot e^{-\mu_2 \ell_2'}\,; \qquad dP^e = \mu_1^e d\ell_2, \quad (6.2)$$

where in the first case we have included the probability of escape of the scattered photon. Similarly, for the pair-production the escape probability of the two annihilation photons must also be considered. In this case we use the expression

$$dP^g = \mu_1^g d\ell_2 \frac{d\Omega_\gamma}{4\pi} e^{-\mu_e \ell}, \quad (6.3)$$

[*]It is frequent to use E_0 to refer to different parameters. In order to avoid confusion, here we refer as E_0 to the energy associated to a (hyper) voxel and denote the (unknown) initial photon energy as E_γ.

where Ω_γ stands for the angles of the direction that contains the two annihilation photons and ℓ is the total length traversed in the second plane by them. As a first approximation, these photons are taken as collinear, with energy $E_e = m_e c^2 = 511\ keV$, and being created at the point of creation of the positron. It should also be noticed that the linear attenuation coefficients associated to the specific interactions, μ^e and μ^g, have been employed in equations (6.2) and (6.3), where the superscript indicates the nature of the interaction.

Following the same procedure as in section 5.1.1, it is convenient to express dP from equation (6.1) as much as possible in terms of measured variables. The first step in this direction is to rewrite the variables Ω_i and ℓ_i in terms of the $\vec{r}_i$ variables ($d\Omega_i d\ell_{i+1} = d^3 r_{i+1}/|\vec{r}_{i+1} - \vec{r}_i|^2$), which yields:

$$\begin{aligned} dP(\vec{r}_0\vec{r}_1\vec{r}_2\ldots|V) \;=\; & \frac{d^3r_0 dE_0}{V}\frac{d^3r_1}{4\pi|\vec{r}_1-\vec{r}_0|^2}\frac{d^3r_2}{|\vec{r}_2-\vec{r}_1|^2}e^{-\mu_0\lambda_0}n_e^{eff}\frac{d\sigma_0^c}{d\Omega_1}e^{-\mu_1\lambda_1}\cdot \\ & \cdot\left(n_e^{eff}\frac{d\sigma_1^c}{d\Omega_2}d\Omega_2 e^{-\mu_2\lambda_2} + \mu_1^e + \mu_1^g\frac{d\Omega_\gamma}{4\pi}e^{-\mu_e\ell}\right)\Theta_V, \end{aligned} \tag{6.4}$$

As in the case with known emission energy (equations (5.2) and (5.10)), this expression is well-suited for computing the sensitivity probability. Since the sensitivity is defined as the probability that an emission in V is detected (in any form), we can obtain its expression by integrating over all the possible outcomes

$$\begin{aligned} S_V \;=\; & \int_V \frac{d^3r_0 dE_0}{4\pi V}\int_{P_1} d^3r_1\frac{e^{-\mu_0\lambda_0}}{|\vec{r}_1-\vec{r}_0|^2}\int_{P_2} d^3r_2\frac{e^{-\mu_1\lambda_1}}{|\vec{r}_2-\vec{r}_1|^2}n_e^{eff}\frac{d\sigma_0^c}{d\Omega_1}\cdot \\ & \cdot\left(\int_{\Omega_2} d\Omega_2 n_e^{eff}\frac{d\sigma_1^c}{d\Omega_2}e^{-\mu_2\lambda_2} + \mu_1^e + \mu_1^g\int_{\Omega_\gamma}\frac{d\Omega_\gamma}{4\pi}e^{-\mu_e\ell}\right), \end{aligned} \tag{6.5}$$

where the first integrals are extended to the volumes of the voxel, $V = \Delta x\Delta y\Delta z\Delta E_0$, and the detection planes, P_i. Note that the function Θ_V is no longer necessary, since the integration limits coincide exactly with the region where $\Theta_V \equiv 1$. In fact, Θ_V is a mathematical artifact to constrain the calculation to the voxel volume, so in this case keeping both Θ_v and the integration limits would be redundant. The second integrals add up all the possible outgoing angles of the photon after the Compton scatter and the angle of the two annihilation photons. Equation (6.5) allows computing the sensitivity matrix without having to resort to the very expensive conventional method of computing and summing all the possible cones of response (see below). The last integration in equation (6.5) will be referred to as the *double escape probability*, $S(\vec{r}_2)$ in the following, and it represents the probability that the two photons escape after being created at $\vec{r}_2$ inside the second plane.

Finally, Compton kinematics can be employed to transform the polar angles into the energy deposited in the Compton interactions. Equation (5.4) is employed again to introduce the measured energy in the first plane. Similarly, when the interaction in the second plane is a second Compton scatter, from equation (5.3) we have

$$\sin\theta_2\, d\theta_2 = d\tilde{E}_2 \frac{m_e c^2}{(E_0 - \tilde{E}_1 - \tilde{E}_2)^2}. \tag{6.6}$$

Upon application of these changes of variables, and after integrating out those variables which are not measured, we obtain

$$\frac{dP_V}{d^3 r_1 d\tilde{E}_1 d^3 r_2 d\tilde{E}_2} = \int \frac{dE_0}{4\pi V} \frac{e^{-\mu_1 \lambda_1}}{|\vec{r}_2 - \vec{r}_1|^2} \frac{m_e c^2}{(E_0 - \tilde{E}_1)^2} n_e^{eff} \frac{d\sigma_0^c}{d\Omega_1}\, T^{ceg}\, C \tag{6.7}$$

where T^{ceg} encodes the kinematics of the second interaction

$$\begin{aligned} T^{ceg} = & \frac{m_e c^2}{(E_0 - \tilde{E}_1 - \tilde{E}_2)^2} n_e^{eff} \frac{d\sigma_1^c}{d\Omega_2} \int d\varphi_2 e^{-\mu_2 \lambda_2} + \mu_1^e \delta(E_0 - \tilde{E}_1 - \tilde{E}_2) + \\ & + \mu_1^g S(\vec{r}_2) \delta(E_0 - \tilde{E}_1 - \tilde{E}_2 - 2m_e c^2), \end{aligned} \tag{6.8}$$

and acts as a weight for the geometrical terms encoded in $C(\vec{\eta})$, defined as in equation (5.7). If the energy width of the voxels is sufficiently small that dependencies over E_0 within the voxel are negligible, the integral over E_0 can be performed (see next section). Equation (6.7) can be interpreted as the probability of an emission from voxel V, around $\vec{r}_0$ and E_0, being detected by the telescope as an event given by $\vec{\eta} = \{\vec{r}_1, \tilde{E}_1, \vec{r}_2, \tilde{E}_2\}$. Therefore, equation (6.7) constitutes the sought mathematical expression for the SM elements of our system. It should be emphasized that both T^{ceg} and $C(\vec{\eta})$ depend on E_0. Since the voxels in the considered FoV are associated to an E_0, the backprojection of a measured event $\vec{\eta}$ requires the calculation of a T^{ceg} and $C(\vec{\eta})$ for each of the energies in the FoV. The practical details on the implementation are explained in the following section.

6.2 Practical considerations

6.2.1 Implementation of the code

The equations described in the previous section were implemented as an extension of the already existing reconstruction code, described in section 5.1.2. In the previous code, the initial gamma energy was assumed as a fixed parameter; thus, each measured coincidence event led unambiguously to the determination of a single CoR, whose backprojection onto

the FoV constituted the calculation of one SM row. In the spectral reconstruction approach, however, the initial energy is unknown. Therefore, the algorithm needs to try different possible energies for each measured event.

For a measurement $\vec{\eta}$, the initial gamma energy must satisfy the condition $E_\gamma \geq \tilde{E}_1 + \tilde{E}_2$. It should be stressed that the FoV in this method is defined as four-dimensional, which means that the different (hyper) voxels contain a finite volume element and are associated to an energy bin. The energy dimension is divided into a finite number of bins, sufficiently narrow so that energy variations within it are negligible. Thus, each bin is represented by a single E_0, and only discrete values of E_0 are employed. Taking into account the above considerations, the energy condition is equivalent to saying that, for a specific $\vec{\eta}$, only the voxels associated to energies greater than the measured value can be activated. For each of these energies, a different CoR is constructed with an aperture angle given by equation (2.1). From that equation, for a fixed $\tilde{E}_1$, the Compton scattering angle decreases as the initial energy increases, and so the CoR with maximum aperture angle will be obtained for $E_0 = \tilde{E}_1 + \tilde{E}_2$, as illustrated in Figure 6.1a. Because the individual CoRs correspond to different E_0, they also have different probabilities T^{ceg}, which are calculated as defined by equation (6.8). Considering all possible energies given by the measured values, the corresponding SM row is thus a set of CoRs with different aperture angles and probabilities. Figure 6.1b represents qualitatively a set of CoRs built for an arbitrary event, with different relative probabilities assigned to different E_0.

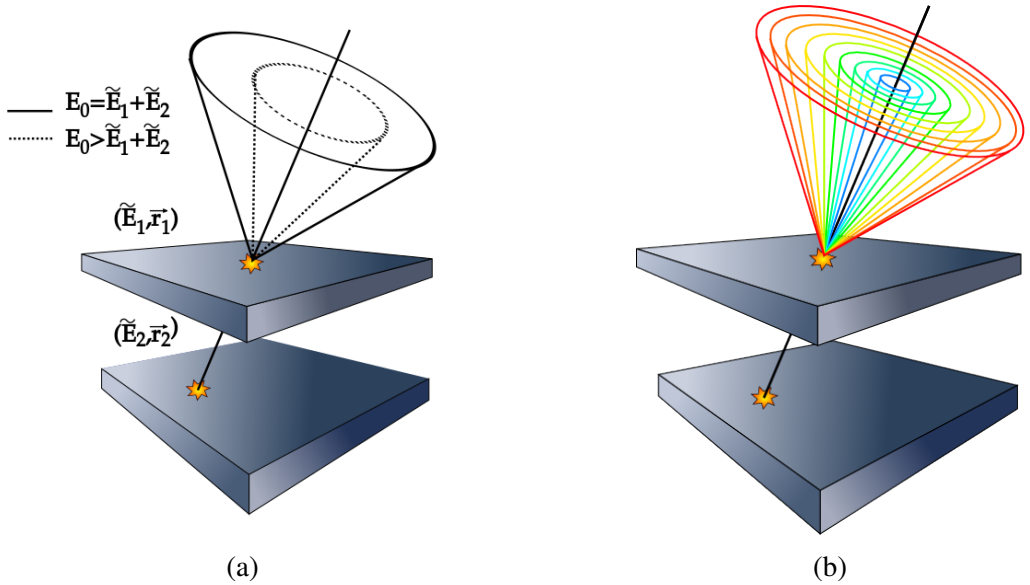

(a) (b)

Figure 6.1 Diagram of the different CoRs that arise from one coincidence event. (a) Shows the decrease in the cone aperture angle as the initial energy increases. (b) Represents qualitatively the variation in the probability of different initial energies.

The weight assigned to a CoR built for an initial energy E_0 depends on which of the three physical interactions in the second plane are compatible with the measured event, which is represented by the δ functions in equation (6.8). Assuming that the bin energy width ΔE_0 is sufficiently small, the δ functions in our implementation are represented as $\delta(E_0 - \tilde{E}) = \Theta(\tilde{E}; E_0, E_0 + \Delta E_0)/\Delta E_0$, so that $\int dE_0 \Theta/\Delta E_0$ is to a good approximation equal to 1 if the event energy $\tilde{E}$ falls within the voxel of energy E_0 and and 0 otherwise. Thus, the weight of the CoR calculated with an initial energy of (the bin containing) $\tilde{E_1} + \tilde{E_2}$ is computed employing the photoelectric probability in the second interaction. Equivalently, from the measured energies, the pair production probability is used to compute the weight of the CoR obtained for an initial energy of $\tilde{E_1} + \tilde{E_2} + 2m_e c^2$. Lastly, all the possible CoRs related to a second Compton interaction are calculated, which correspond to initial energies in the range $[\tilde{E_1} + \frac{1}{2}\left(\tilde{E_2} + \sqrt{\tilde{E_2}^2 + 2m_e c^2 \tilde{E_2}}\right),\ E_{\max}]^{\dagger}$, being $E_{\max}$ the maximum voxel energy considered in the FoV.

Besides the modifications to include de spectral dimension, the rest of the code works exactly as the previous one. All numerical computations associated to the individual CoR geometries are calculated as described in the diagram shown in Figure 5.2, adapted with the terms introduced in equation (6.8). Regarding the double escape probability function $S(\vec{r_2})$, in our implementation it is precomputed by dividing the detector volume into small elements and calculating the escape probability numerically through conventional Monte Carlo techniques. The values are stored in a look-up table and called during the computation of the system and sensitivity matrices.

6.2.2 Spectral sensitivity matrix

As shown in the previous chapter, the sensitivity matrix plays an important role in the reconstruction process. Given the strong dependence of the detection probability on the energy and the position of the emission point of the photons, the employment of an accurate sensitivity matrix becomes necessary for the algorithm to be able to correctly position the source, in both the spatial and the spectral domains. An expression for the calculation of the sensitivity matrix was given in equation (6.5). Following the same procedure as in the previous chapter, the sensitivity matrix here is calculated numerically via Monte Carlo integration. Again, considering separately each of the interactions in the second plane, the partial sensitivities of the corresponding interactions can be calculated.

[†]The minimum energy comes from applying Compton kinematics to the second interaction. The maximum energy that a photon (of initial energy E_γ) can lose through a Compton interaction is $E_\gamma/(1 + m_e c^2/(2E_\gamma))$. Since the measured energy $\tilde{E_2}$ and the energy of the scattered gamma ($E_\gamma - \tilde{E_1}$) must satisfy the previous condition, we have $E_\gamma \geq \tilde{E_1} + (1/2)\left(\tilde{E_2} + \sqrt{\tilde{E_2}^2 + 2m_e c^2 \tilde{E_2}}\right)$.

The accuracy of the proposed sensitivity matrix has been verified through a comparison with the sensitivity values obtained from simulations with GATE. As a quick validation, the sensitivity at two spatial positions has been calculated through simulations for the energy range [0.2, 7] MeV. Figure 6.2 shows the comparison between the values obtained from the simulations and the ones calculated with equation (6.5). The values have been computed for the three different contributions and for the total sensitivity. In all cases, the simulated values match the integration results with very good agreement.

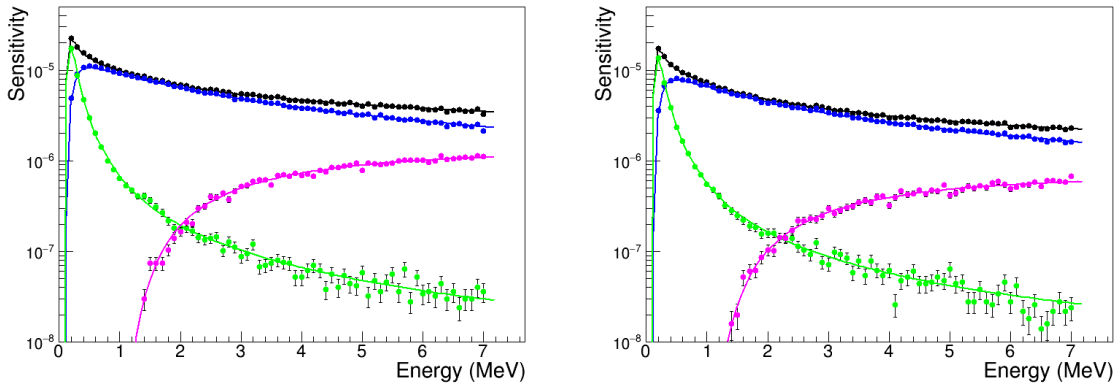

(a) (b)

Figure 6.2 Sensitivity to the possible interactions of the photon in coincidence events over a range of energies for a source placed at $x = 0$ mm (a) and $x = 30$ mm (b). The points are obtained from simulated data and the continuous lines from the integration of equation (6.4). The different colors indicate the interaction experienced by the photon in the second plane: Compton scatter (blue), photoelectric absorption (green), pair production (pink) or any of the three (black).

6.2.3 Image treatment

The implemented method yields four-dimensional images, from which the spatial or spectral distributions can be extracted. A purely spatial image can be retrieved through integration over the spectral domain; conversely, the reconstructed spectrum can be recovered by integrating over the whole spatial domain. If the integration is performed over a single spatial dimension, the resulting image is a mixed spatial-spectral representation. Along this chapter, different graphical representations of the reconstructed images are shown, for which the integrated dimensions are specified in each case.

If the distance between the source and the detector is known, the FoV may be considered with only one bin along the z dimension, being in fact an image with two spatial and one spectral dimension. This is a practicality that allows the employment of a reduced FoV in

the reconstruction, thus decreasing the computational burden. The images presented in this chapter have been reconstructed following this approach. The employment of a reduced FoV in this study is justified because it is the first test of the method imaging capabilities, although a more thorough study should in the future consider truly four-dimensional FoVs. For a smoother visualization, all images presented in this chapter have been post-processed with a Gaussian filter with a sigma equal to one voxel length.

6.3 Reconstructed images

6.3.1 Simulated sources

The reconstruction algorithm was first tested on data extracted from simulations. The simulated two-plane Compton camera consists of two identical $LaBr_3$ crystals of $25.8 \times 25.8 \times 5$ mm^3, which reproduces the experimental prototype dimensions with the latest detectors. In all simulations, the distance between the centers of the planes is set to 50 mm and all the simulated sources are placed at a distance of 70 mm from the first plane. For these tests, the simulated detectors have perfect energy resolutions.

Three different data sets have been extracted from the simulated results and employed for reconstruction. In addition to the usual *singles* and *hits*, introduced in section 3.2 and already employed in the reconstruction of images shown in chapter 5, a new data set was necessary for this study. We will refer to the new set as *ideal hits*, which, as its name indicates, is built assuming completely ideal detection of the measured events. The need for the ideal hits was not foreseen before the imaging tests were carried out, and will become clear when the resulting images are presented. In the usual hits data set, although the gamma interaction positions are perfectly determined, it is possible that the recoil electron produced in the Compton scattering escapes the detector material, taking part of the energy deposited by the initial gamma in the interaction. As will be seen along this section, the missing energy carried away by the escaping electron prevents the algorithm from finding the correct source emission energy. In order to avoid this effect, the ideals hits set is built using the same gamma interaction positions given by the hits, and forcing the complete detection of the energy deposited in the first Compton interaction, so that all the energy transferred by the incident photon is preserved. In all three data sets, only the signal events have been considered, i.e. those produced by the combination of a Compton scatter in the first plane and a subsequent interaction in the second one by a single primary gamma.

The remainder of this section is dedicated to the results obtained from three simulated sources of increasing complexity, with the three different data sets. In all cases, the simulated

sources present a spectral emission distributed between 2 and 7 MeV, and the shown images have been reconstructed in a 4D FoV of $101 \times 101 \times 1$ spatial voxels of 1 mm^3 and 99 spectral voxels, linearly distributed in the range [0.05, 9.95] MeV.

Point-like sources

The first simulated distribution consists of monoenergetic point-like sources. Six sources have been simulated separately, all placed at the same position, displaced 10 mm from the detector center in the x and y directions. The different sources emit photons of 2, 3, 4, 5, 6 or 7 MeV, respectively, with the same intensity in all cases.

Images have been reconstructed using the three simulated data sets described above. Since these sources have no spatial structure, we focus here on the spectral performance of the algorithm. An image of each source has been reconstructed independently, and its recovered spectrum extracted by integrating the image over the whole spatial domain. The spectra obtained for the six sources has been histogrammed together to compare the algorithm ability to find the source energy in the studied range. Figure 6.3a shows the spectra obtained for the six sources, grouped according to the three different data sets used for reconstruction. In the three cases, intensity maxima are recovered at the simulated energies. However, the plot shows that the values obtained for sources with higher energies are not correctly reconstructed for the singles data. An improvement is seen when the hits data are selected, and it is only with the ideal hits set that the method assigns the correct intensity to the source images at all the tested energies. Figure 6.3b shows the same results with the three described data sets, but, in this case, the intensities are not the result of the integration over the whole spatial domain; instead, they are calculated by summing the values of the voxels containing the sources and their immediate neighbors, which allows a better estimation of the intensity assigned around the exact source positions.

Looking at the results and the information contained in the three data sets, the different performance of the three lists can be understood. An improvement is obvious both between singles and hits and between hits and ideal hits, so the effect must be due to two separate factors that are overcome as the level of ideality in the data is increased. Since the simulation has perfect energy resolution and only true signal events have been selected, the main difference between singles and hits is the determination of the interaction position: in the singles list, the interaction position is determined through a weighted average over the energy depositions inside the crystal, whereas the position stored in the hits set is the exact gamma interaction point (see section 3.2). Therefore, the misplacement of the single interaction point degrades the image, especially at higher energies. Indeed, for higher energies, the recoil electron ejected from the interaction will have in average higher kinetic energy, thus

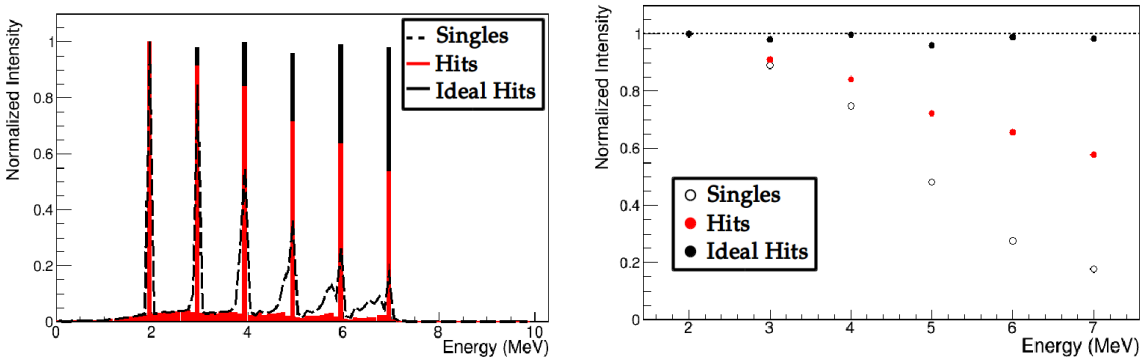

(a) (b)

Figure 6.3 Reconstructed spectra obtained for the different sets of data from the simulations. (a) Spectra after integration over the spatial domain of the whole reconstructed images. (b) Intensities of only the voxels containing the sources and their immediate neighbors.

traversing a longer distance in the crystal and leading to a bigger deviation between real and assigned impact position. The second degradation factor, related to the first one, is the possibility of the recoil electron escaping the crystal, thus carrying away part of the energy deposited by the gamma at the Compton interaction. Again, the probability for an electron to escape the crystal increases with its kinetic energy, and thus with the initial gamma energy. The ideal hits data set are built avoiding this effect (i.e. forcing full detection of the deposited energy) and thus allow the method to completely compensate the reconstructed spectrum.

Discrete energy phantom

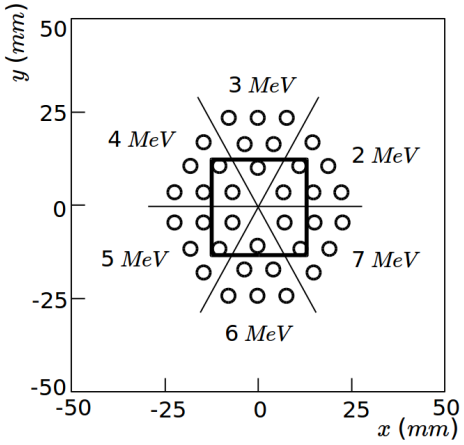

Figure 6.4 Diagram of the simulated discrete energy phantom.

This phantom is inspired in a Derenzo phantom, although in this case all sources have the same dimensions and each region corresponds to one emitted energy. The simulated phantom consists of six regions of different energy, ranging from 2 to 7 MeV with a difference of 1 MeV between regions. Each of the regions is formed by six spherical sources with 2 mm radius and the separation between the centers of any neighboring sources is 8 mm. A diagram of the simulated phantom is shown in Figure 6.4, where the footprint of the simulated detector is also depicted. Unlike the point-like sources employed previously, all sources in this phantom have been simulated and reconstructed simultaneously.

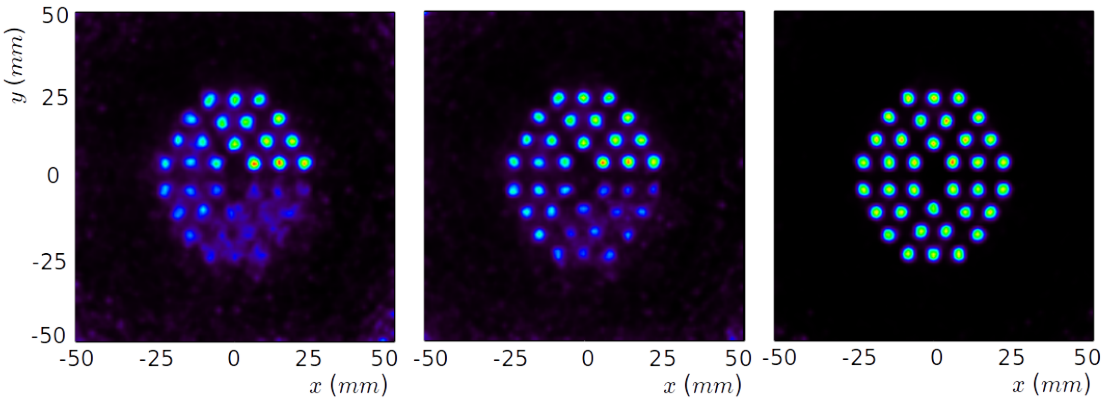

Figure 6.5 Spatial images reconstructed for the discrete energy phantom with the different data sets after integration over the energy domain. From left to right: singles, hits and ideal hits.

The phantom was reconstructed employing the three data sets from the simulation with around 50000 signal events. Several interesting aspects can be pointed out from the four dimensional reconstructed images. In the first place, the recovery of the phantom spatial distribution can be seen after integration over the spectral domain. The corresponding images are shown in Figure 6.5, in which the individual sources can be identified. In the second place, slices of specific energies can be extracted from the resulting image. In Figure 6.6, slices for the minimum and maximum emitted energies are shown to illustrate how the different regions of emission are reconstructed at their corresponding energies. Finally, when the image is integrated over the spatial domain, a reconstruction spectrum is obtained (Figure 6.7), which contains a distinct peak of intensity at each of the different energies emitted by the phantom.

The degradation effects found in the images reconstructed from the non-ideal data sets in the previous sections are also present in this case. In the image obtained from the singles data, it can be observed that the sources emitting higher energy photons are not properly reconstructed in their spherical shape (see Figure 6.6, left column bottom row). This effect is corrected when the hits data are employed, although the intensity assigned to the different

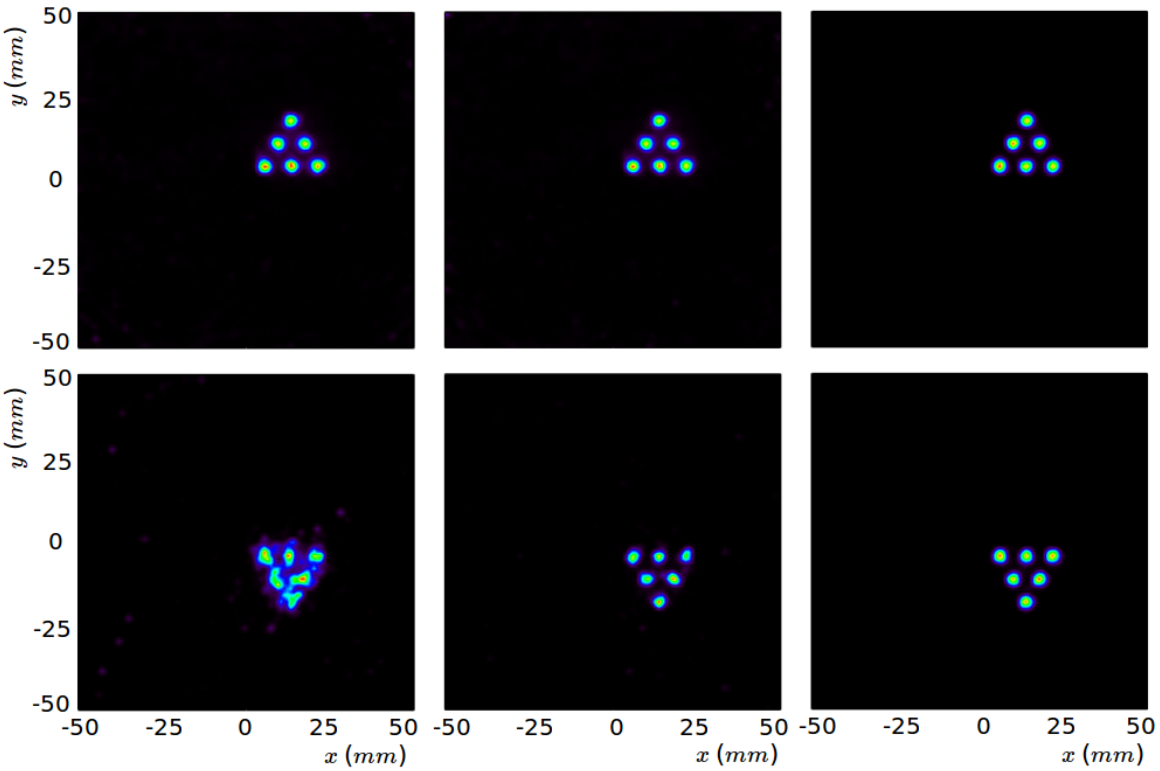

Figure 6.6 Spatial images reconstructed for the discrete energy phantom with the different data sets. Slices selected for the regions of 2 (top row) and 7 MeV (bottom row). From left to right: singles, hits and ideal hits.

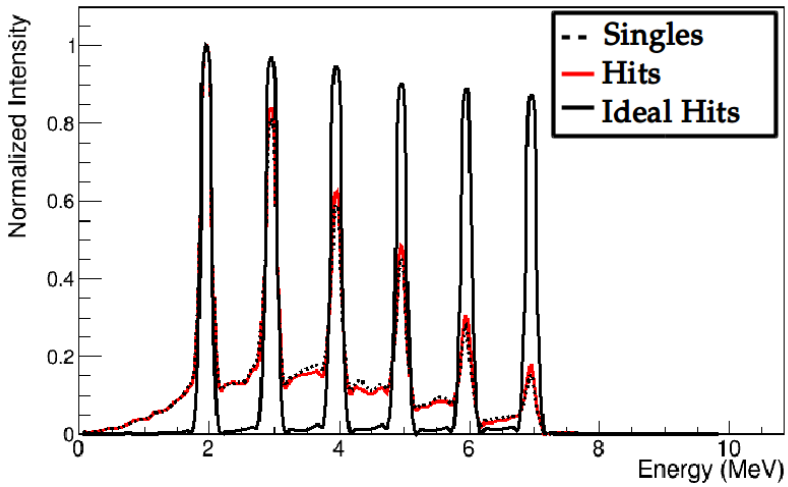

Figure 6.7 Reconstructed spectra after integration over the spatial domain.

sources is still underestimated for higher energies. In order to compensate the source intensities, the ideal hits data need to be used by the reconstruction algorithm. This can be appreciated both in the spatial domain (Figure 6.6) and, perhaps more evidently, in the

recovered spectrum. Looking at the ideal hits spectrum shown in Figure 6.7, it can be noted that the intensity is still somewhat higher at the lower energies. This small difference arises because, for each of the source energies, a residual tail of intensity appears at energies below the true emission, caused by the events with partial energy deposition: since the algorithm needs to test all possible energies, some intensity is spread into the energies between the measured value and the true emission[‡]. Given that this spread extends towards lower energies, the cumulative value of the tails induced by all sources causes an increase in the lower energy intensities. Nevertheless, the difference between the 2 and 7 MeV peaks is below 10% of the maximum value, showing that the method can accurately reconstruct the ideal events.

Continuous energy phantom

Finally, a phantom with extended spatial distribution and continuous energy emission was simulated. The spatial distribution of this phantom is inspired in the overall shape of the Bragg peak produced by a proton beam, although for this tests only photons are considered. All gammas are emitted following a thin linear path with intensity increasing until it reaches a peak, where it quickly drops (see Figure 6.9). The photons are generated in a continuous spectrum between 2 and 7 MeV, with a constant probability for the whole energy range. Of course, the simulated phantom does not correspond to the prompt gamma distribution generated in a realistic case, which is notably more complex; the goal of this test is to evaluate the imaging capabilities of the method with more complex emission distributions.

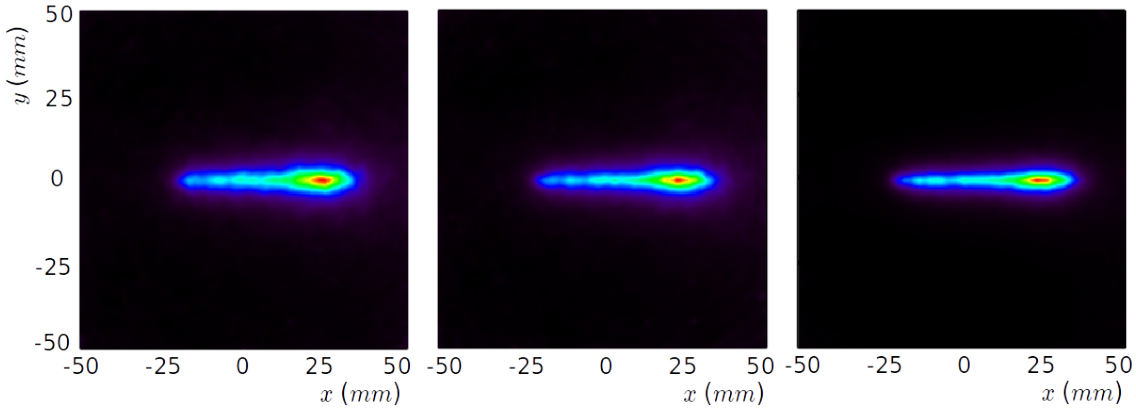

Figure 6.8 Spatial images reconstructed for the continuous energy phantom with the different data sets after integration over the energy domain. From left to right: singles, hits and ideal hits.

[‡]The reconstruction method tests all energies from $\tilde{E}_1 + \tilde{E}_2$ to $E_{\max}$, including those above the actual photon energy (E_γ). However, the weight assigned to the SM elements is higher for energies closer to the measured value (dividing terms in equations (6.7) and (6.8)), which explains the tail formation towards lower energies.

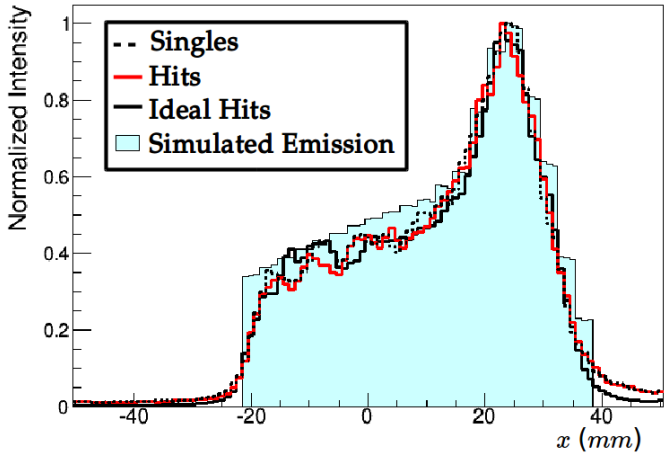

Figure 6.9 Profiles along the x direction of the emitted and reconstructed distribution of activity with the three data sets.

Images of the phantom were reconstructed, for the three simulated data sets, with around 70000 signal events. Again, different projections can be extracted from the four-dimensional images. The spatial component of the reconstructed images, obtained after integration over the spectral domain, is shown in Figure 6.8. From those images, the three data sets yield apparently similar images. Figure 6.9 depicts the profiles along the x axis obtained from the images in Figure 6.8, where the true emission distribution is also represented. The profiles show that the spatial features of the phantom are recovered with the three data sets, including both its longitudinal extension and the peak position.

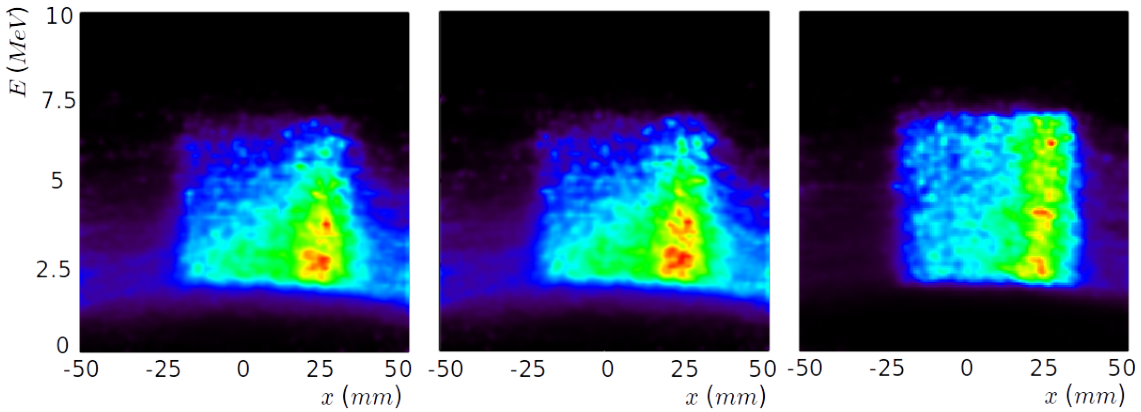

Figure 6.10 Spatial-spectral images of the continuous energy phantom after integration over the y spatial dimension. From left to right: singles, hits and ideal hits.

Taking into account that the spatial structure of the phantom is distributed only along the x dimension, it is perhaps more interesting to integrate the image over the y dimension

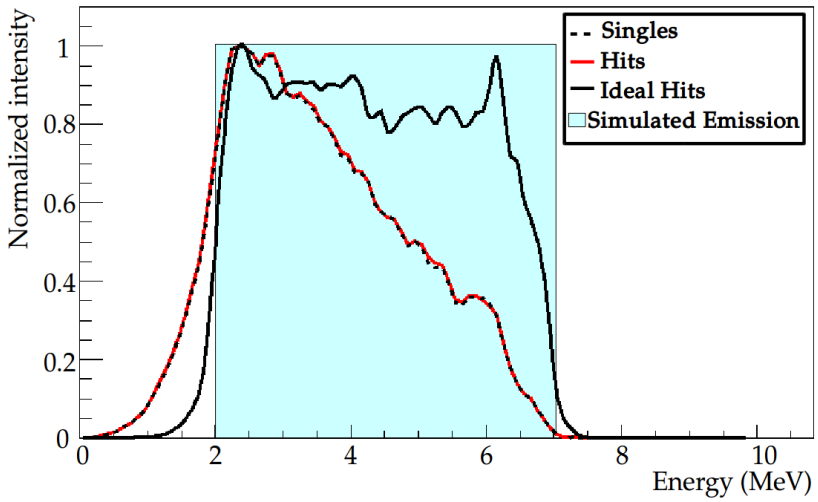

Figure 6.11 Reconstructed spectra after integration over the whole spatial domain.

in order to extract the mixed spectral-spatial representation of the result. These images are shown in Figure 6.10, where it can be appreciated that the spatial distribution of the phantom is reconstructed in the whole spectral range. In this representation, we see that again the images are degraded at higher energies due to the missing energy carried away by the recoil electron, and the true spectral emission is only recovered with the ideal hits data set. This is also visible in the reconstructed spectra shown in Figure 6.11, where the intensity at higher energies is underestimated when the singles or hits data are employed.

The results obtained with this phantom show that the spatial distribution is accurately reconstructed in the three cases. In other words, the purely spatial source information (which is usually the main goal of the reconstruction) can be extracted despite the missing energy. However, the spectral information is degraded for the singles and hits data, in which the intensity at high energies is underestimated, and the simulated emission can only be recovered from the ideal hits data.

6.3.2 Experimental sources

An important test for the method is the assessment of the algorithm capability of recovering simultaneously the position and spectral emission of an experimentally measured source distribution. For that purpose, the spectral reconstruction method was also tested with some of the experimental data already discussed in chapter 4. Specifically, two interesting data sets were selected due to their particular interest: the data measured simultaneously with a ^{22}Na and a ^{88}Y sources (see section 4.1.1) and the measurements taken at HZDR Dresden with 4.44 MeV gammas (section 4.2.4).

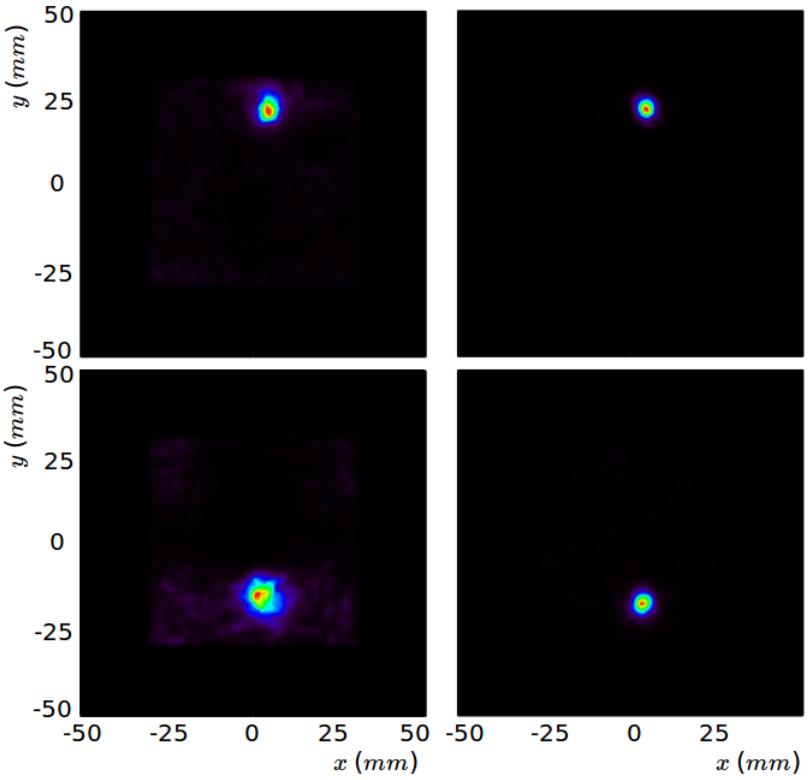

Figure 6.12 Reconstructed image of the ^{22}Na and a ^{88}Y sources together. Spatial slices at the peak energies of the two sources. Top: ^{88}Y source, summed between 875-925 keV (left) and 1800-1850 keV (right). Bottom: ^{22}Na source, summed between 475-525 keV (left) and 1250-1300 keV (right).

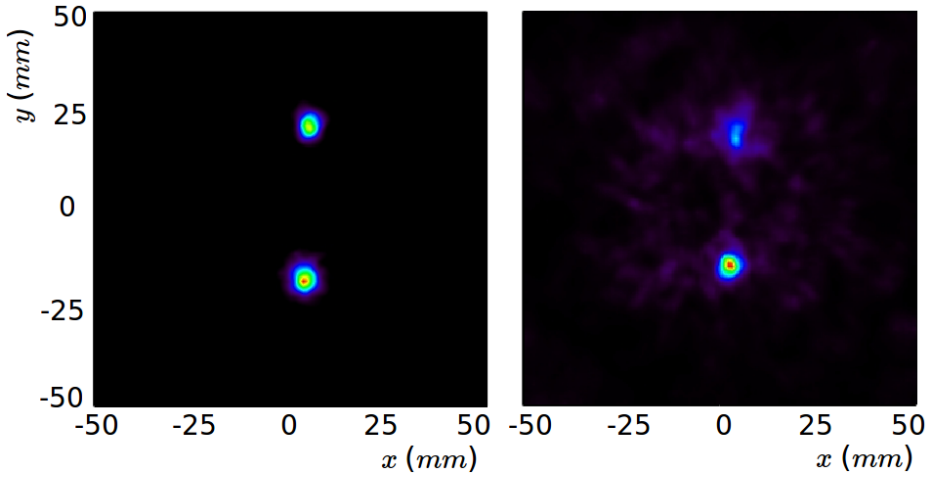

Figure 6.13 Reconstructed images of the ^{22}Na and a ^{88}Y sources together obtained with the spectral (left) and non-spectral (right) algorithms.

As already mentioned previously, the ^{22}Na spectrum has two emission peaks at 511 and 1275 keV, and ^{88}Y emits at the energies of 898 and 1836 keV. With the combined data from both sources, the spectral reconstruction method should be able to find the four emitted energies and recover one source image for each of them. The data were reconstructed employing a FoV of $101 \times 101 \times 1$ spatial voxels of 1 mm^3 and 100 spectral voxels, linearly distributed in the range [0.05, 2.55] MeV. The results obtained from the reconstructed four-dimensional image can be seen in Figures 6.12 and 6.13. Figure 6.12 shows the image slices extracted at each of the four energy peaks, where it can be appreciated that, as expected, the two energies emitted by each source yield an image that peaks at the same position. The spatial image obtained after integration over the spectral dimensions is shown in Figure 6.13 (left). In it, the two measured source positions are clearly visible and well delimited. For comparison, the right-hand side of Figure 6.13 (equivalent to Figure4.7b) shows the result obtained for these same data with the non-spectral algorithm, in which the initial gamma energy was taken as the measured summed energy. The comparison of the two images proves that the spectral method clearly outperforms the non-spectral one. This is due to the fact that the spectral algorithm is able to find the true initial energy of those events with partial energy depositions, and, therefore, their corresponding CoRs intersect the correct emission position. In contrast, when the energy is assumed as the measured value, the events with partial depositions are not properly reconstructed. Consequently, their calculated CoRs do not contain the true emission position and they add noise to the image instead.

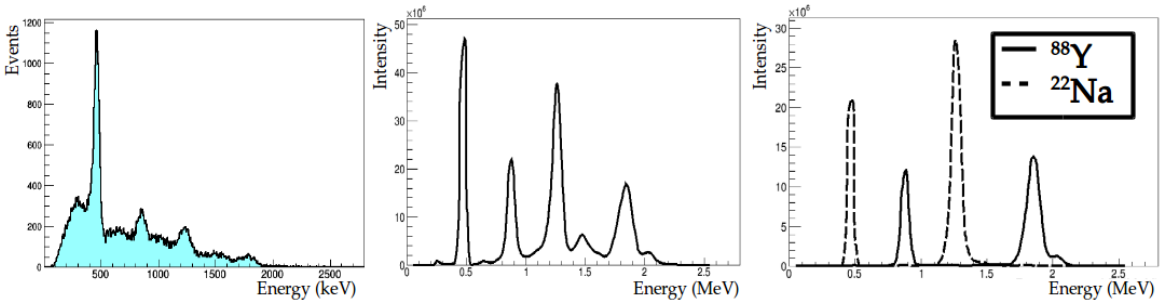

Figure 6.14 Comparison of the spectra. Left: measured spectra obtained by summing the energy depositions of the coincidence events in both planes. Center: reconstructed spectra after integration over the whole spatial domain of the reconstructed image. Right: reconstructed spectra after integration over the spatial domain only for the voxels located at the positions of the sources.

Figure 6.14 shows a comparison between the measured summed energy spectrum (left), obtained by summing the measured energy deposited in both planes for every coincidence event, and the recovered spectrum given by the spatial integration of the reconstructed image (center). The peaks corresponding to the emitted energies are more prominent in

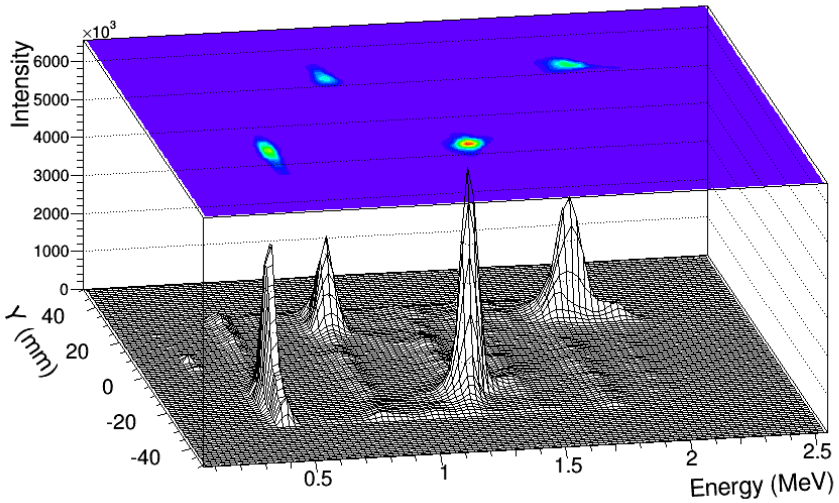

Figure 6.15 Reconstructed image of the ^{22}Na and a ^{88}Y sources together after integration over the x spatial dimension.

the recovered spectra, due to the events with only partial deposition in the summed energy spectrum that are reconstructed with the appropriate initial energy. The right-hand side plot in Figure 6.14 shows the spectra recovered when the integration of the image is performed only over the spatial voxels containing the position of each of the sources, where their respective emitted energies are clearly identified. In that image, the intensity of the different peaks is related to the emission activity of the corresponding energies, although they cannot be directly compared. In the experimental results, in contrast to the simulations, the intensity is somewhat underestimated for the lowest energies. This is due to several factors that are not considered by the method, most importantly the fact that lower energies present a higher fraction of backscatter events, their activity is reconstructed with a wider spread across voxels and they are more affected by the experimental low energy threshold. In addition, since in this case the tested energies are much lower than in simulations, the effect of escaping recoil electrons is not significant. Another interesting view is plotted in Figure 6.15, which shows the combined spatial-spectral view of the reconstructed image after integration over the spatial x dimension, where the four peaks are visible in the spatial and spectral domains simultaneously.

The previous study proves that the method is able to accurately find the emission spectrum and spatial distribution of multi-energetic radioactive sources measured in the laboratory. In order to test the algorithm with experimental data measured at high energies, a set of data taken with 4.44 MeV photons at the HZDR Dresden, not accessible in laboratory

measurements, was reconstructed. In particular, the measurement registered with the 1-3 detectors pair were chosen for this test. A four-dimensional image was reconstructed independently for each of the three measured source positions. The employed FoV is divided into $101 \times 101 \times 1$ spatial voxels of 1 mm^3 and 99 spectral voxels, linearly distributed between 0.05 and 9.95 MeV. Figure 6.16a displays the (spatial domain of) the combined

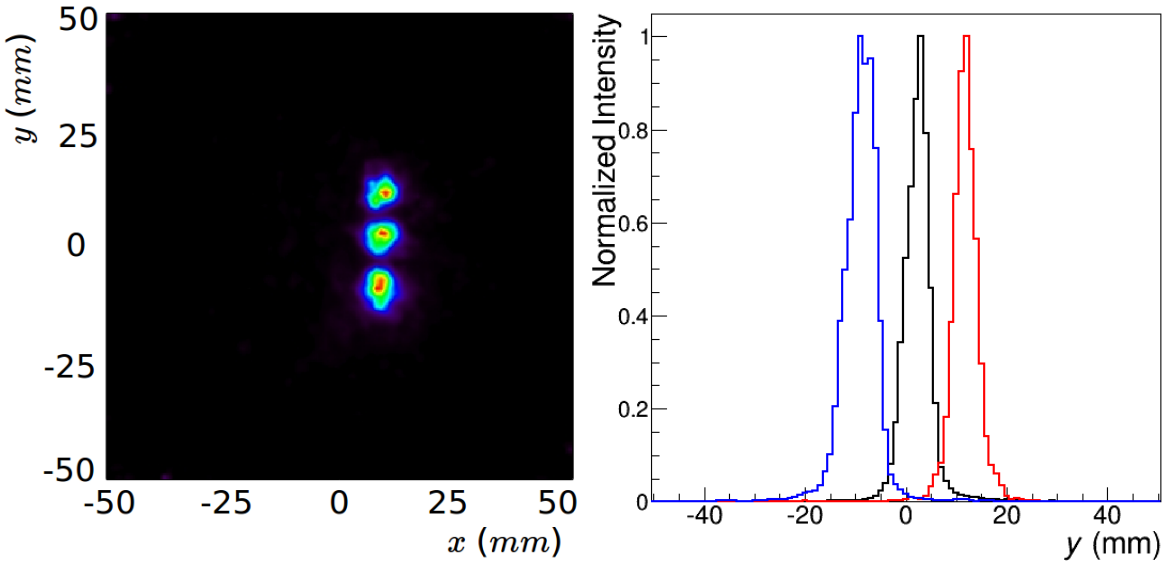

(a) (b)

Figure 6.16 Results obtained with experimental data measured from a 4.439 MeV gamma source. (a) Reconstructed image after integration over the spectral domain. (b) Profiles along the y axis at the maximum of the source images.

reconstructed images, obtained by summing the three independent images. The three sources are clearly visible, and are reconstructed at their correct position. This can also be appreciated in Figure 6.16b, where the profiles along the y axis at the maximum of the independent source images are shown. Comparing these results with those obtained previously (right-hand side images in Figure 4.17), we see that the spectral reconstruction method yields spatial images very similar to those reconstructed using the initial gamma energy as a known parameter.

The good results of the spectral reconstruction method are due to the algorithm capability of recovering the true gamma energy. This can be better appreciated in Figure 6.17, which represents the comparison between the measured summed energy spectrum and the spectrum recovered from the reconstructed image for the data measured at the central position. It is worth noting that the initial gamma energy, 4.44 MeV, has a low probability of being completely absorbed in the detector, and thus the measured spectrum does not show a clear peak at that position. Nevertheless, in the spectrum obtained from the reconstructed image, a peak is recovered precisely at the energy emitted by the source. Finally, Figure 6.18 shows

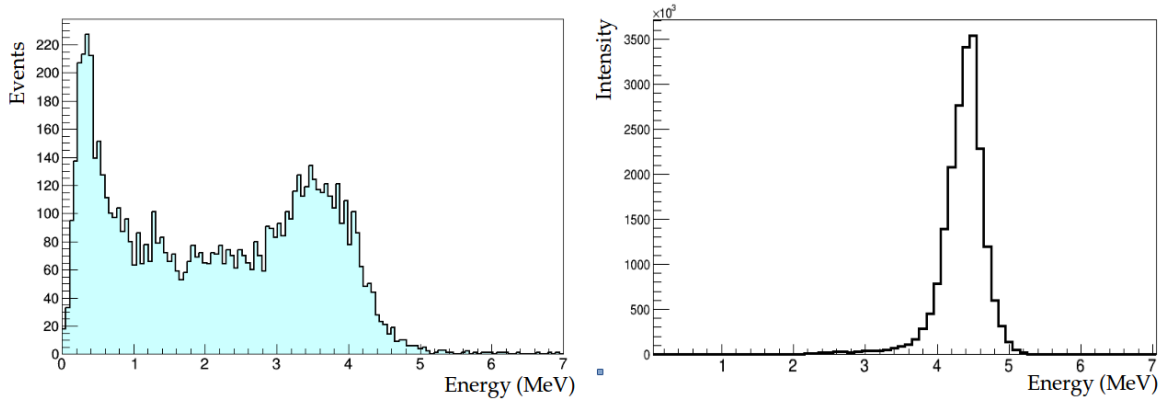

Figure 6.17 Comparison between the summed energy spectrum and the spectrum recovered by integrating over the spatial domain, where a peak is clearly visible between 4.4 and 4.5 MeV.

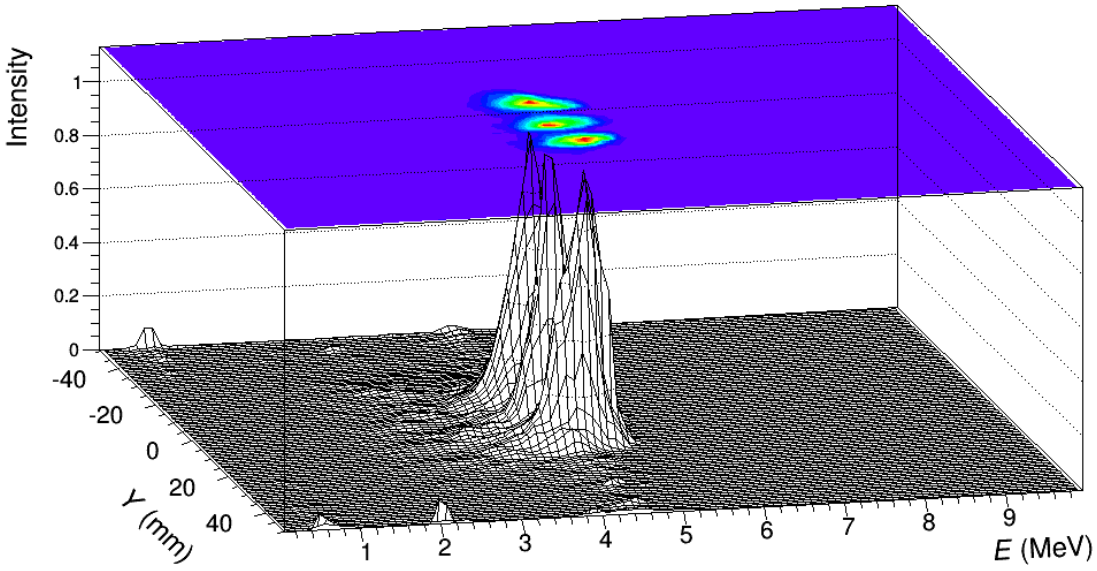

Figure 6.18 Reconstructed image for the three measured positions after integration over the x spatial dimension.

the recovered images after integration over the x spatial axis, where the three different source positions in the y axis can be seen in the spatial-spectral combined space.

6.4 Discussion

A spectral reconstruction algorithm for two-plane Compton cameras is proposed and tested in this chapter. The main concept behind its development is the possibility to associate partial depositions of energy in the second interaction with a probability for a range of plausible

incident gamma energies, which in turn yield a set of CoRs with their corresponding aperture angles. In order to do so, the SM is divided into the three possible interactions that can produce a detection in the second detector plane: photoelectric absorption, a second Compton scattering or an e^-e^+ pair production. Since the reconstruction is performed on a four-dimensional FoV, during the iterative algorithm those voxels that contain both the spatial position and the spectral emission of the source are obtained.

The performance of the proposed algorithm has been evaluated through image reconstruction of data from a variety of simulated sources. Images were first reconstructed using the singles list, which are ideal events that can be regarded as a good approximation of the best possible accessible events measured by a detector with perfect energy and intrinsic spatial resolution. Even at the singles level, the quality of the reconstructed images was lower than expected. In order to investigate where the information is lost, more ideal data sets have been employed. Images were reconstructed from the hits data set, in which the spatial coordinates are the exact interaction positions and the transferred energy is taken as the energy measured by the detector. Although this set improves the singles results, the recovered images are not fully compensated. For that reason we consider the ideal hits, employing also the exact energy lost by the gamma. In this ideal case, both the spectral and the spatial information are successfully recovered. Therefore, the algorithm performs correctly under the assumption of ideal measurements, but when singles or hits are used the reconstructed images are degraded.

From the study with point-like sources, two important factors have been found to degrade the reconstruction process at high energies with the singles and hits data sets. The first of them is the displacement of the electron dispersed in the Compton scatter from the interaction position. This displacement grows larger for higher incident energies, and it can cause an error in the position of the apex and a misalignment in the axis of the CoRs. The second and most important factor, closely related to the first one, is the missing energy carried away by escaping electrons. As the incident energy increases, so does the probability that the dispersed electron escapes the detector, taking part of the energy lost by the primary gamma. This fact can produce various effects: if an electron escapes the first detector plane, the measured energy $\tilde{E}_1$ will be smaller than that transferred in the Compton scatter, and thus the aperture angles of the CoRs will be larger than they should; if an electron escapes the second detector plane, the CoR constructed for the actual emitted energy will still reach the source position, but its probability will be incorrectly assigned. Furthermore, if an electron escapes one of the planes and reaches the other, it could trigger a false coincidence event that would add noise to the reconstructed image. Only when ideal hits from the simulations were selected, these effects were avoided and the reconstruction code was able to reconstruct all the sources and fully correct their intensities; when more realistic events are used, the

obtained spectra tend to underestimate the intensity at high energies, although the spatial information is still successfully recovered.

In order to test the performance of the algorithm in a more demanding scenario, two more complex phantoms have been defined. In the discrete energy phantom, the obtained images show that the algorithm is able to reconstruct simultaneously different individual sources at their position and energy of emission when ideal data are employed. For more realistic data, although the intensity is not correctly compensated throughout the whole energy range, in the spatial image all the sources at the different energy regions are identified. In all cases, the recovered spectra obtained from the integration of the images over the spectral domain show one peak at each of the emitted energies.

The results obtained with the continuous energy phantom prove that the algorithm can reconstruct simultaneously the spatial distribution and the spectral emission of spread sources in both domains. Regarding the spectral information, the upper and lower limits of the emission are accurately found. Again, the degradation increases for higher energies, especially when the singles and hits data are employed. Nevertheless, in the spatial domain, the algorithm was able to find in all cases the start and end points of emission in a line-distributed source, as well as the position of the peak of activity, all of them important features in prospective reconstruction of the prompt gamma creation maps during irradiation. This can be seen in the reconstructed line profiles, which are very similar in the three cases.

Finally, the reconstruction algorithm was also used with experimental data from different incident gamma energies. The tests with the two ^{22}Na and ^{88}Y sources together demonstrate the applicability of the proposed method for spectral identification of radioactive sources. By selecting the spatial slices at each of the four gamma energies emitted, the position of the sources is determined. As expected, at the two energies corresponding to one of the sources, the locations of the voxels with highest intensities coincide. Another visible feature is that the lower emitted energies yield noisier images, which can be attributed to their higher probability of producing a backscatter coincidence event with wrong ordering (events that are backscattered in the second plane and subsequently detected in the first one). Comparing the measured summed energy spectrum to the one recovered from the reconstructed image, it can be seen that the algorithm is able to find the incident energy of those events with partial energy depositions. This behaviour is even more noticeable in the case of the experimental 4.44 MeV gamma source measured at HZDR Dresden. At this energy, the probability of total energy deposition is reduced, and the measured summed energy spectrum offers little information about the incident energy of the measured photons. When the spectral reconstruction code is used, only those CoRs generated with the actual emitted energy produce a coherent image and the spectral information of the source can be recovered.

6.5 Conclusions

The proposed spectral reconstruction method can be employed for image reconstruction of data measured by a two-plane Compton camera, irrespective of the prior information about the energy of the detected gammas. The algorithm has been shown to successfully reconstruct the different source distributions tested in this work, obtained both from simulations and experimental measurements, which is a promising step towards the use of this device in hadrontherapy treatment monitoring. However, we have seen that the method can only fully reconstruct complex spectral and spatial distributions under the assumption of ideal measurements, and image degradation appears when simulated singles or hits are employed. The missing energy carried away by electrons escaping the detector has been identified as the major source of image degradation, which needs to be specifically addressed either in the experimental design or in the system matrix. Despite its current limitations, the spatial distributions of complex phantoms has been recovered in all cases. Finally, the method is able to accurately reconstruct point-like experimental sources in a broad range of energies, recovering simultaneously both their emission spectrum and spatial location.

Summary and conclusions

A factor limiting the applicability extent of hadrontherapy is the lack of a reliable real time monitoring system. Among other possible methods under investigation, Compton cameras are candidates to achieve real time treatment monitoring. The MACACO prototype designed at the IRIS group features a compact and reconfigurable multiplane Compton camera with detector planes based on $LaBr_3$ crystals coupled to SiPMs arrays. The current version of the experimental prototype can be operated with two or three detector planes, allowing simultaneous acquisition of two and three-interaction events.

One aspect addressed in this work was the characterization of the experimental prototype and the assessment of its imaging capabilities. In that sense, it has been shown that the system is capable of correctly positioning radioactive sources. The results with two planes in the laboratory confirm that gamma sources with emission energies in the range between 511 and 1836 keV are successfully reconstructed. Regarding image resolution, in that energy range better results were achieved with the highest energies tested. The study with different relative distances between source and planes yielded images with better resolution for bigger inter-plane separations and for shorter distances between source and first plane. In the three-plane operation mode, a short study showed that the initial photon energy can be extracted from experimental measurements without any prior knowledge, which allowed image reconstruction of all the measured sources. The system, assembled with three detector planes, was also tested at HZDR Dresden with 4.4 MeV photons. Although the statistics in the measurement time were insufficient for reconstruction with triple coincidences, images of the target at three different positions were successfully reconstructed with all combinations of detector pairs, demonstrating that the system is able to recover images at this energy.

Regarding the image reconstruction process, a complete physical model of the signal formation has been derived for two-plane Compton cameras and monochromatic sources of known energy. The model has been validated through a comparison against Monte Carlo simulations, where excellent agreement was found, and used to obtain an expression for the system and sensitivity matrices. The impact of the sensitivity matrix in the final reconstructed images has also been evaluated. In a comparison study against other sensitivity models in

the literature, the sensitivity model derived in this work has shown to produce better images, especially in the recovery of activity regions outside the detector footprint.

The derived physical model has been extended to include sources of unknown energy emission, which has been employed to implement a spectral reconstruction code. The spectral reconstruction code has proven capable of recovering simultaneously the spatial distribution and spectral emission of various sources without prior knowledge of the emitted photon energy. The evaluation of the code with simulated sources has shown that complex sources can be successfully reconstructed when ideal data are considered. The simulated study also showed that some degradation appears in the recovered spectrum when realistic data are employed, mainly due to the missing energy carried away by recoil electrons escaping the detector. Finally, the application of the spectral reconstruction code to experimental data has proven that the method can find both the position and the spectral emission of point-like sources in the whole tested energy range.

The results obtained in this work have helped in the identification of current shortcomings and definition of future guidelines for the project. Future developments include improvements both in hardware components of the experimental prototype and in reconstruction software. In addition to new electronic components with better time resolution, the inclusion of a tracking system to detect escaping recoil electrons is currently being considered, motivated in part by the results presented in chapter 6. The implemented reconstruction code will also serve as the basis for future enhancements. The physical model derived for two-plane Compton cameras can be extended to three-plane systems and, in order to fully exploit the potential of the experimental system, an image reconstruction method employing all two- and three-interaction events can be implemented. Other tests have been carried out with the experimental prototype alongside the development of this thesis, directly related to the work presented here. In particular, working towards the final aim of prompt gamma imaging, tests with proton beams at clinical energies have been measured, in which shifts of the Bragg peak can be identified when the spectral reconstruction method described in Chapter 6 is employed. In conclusion, although the system capacities and image reconstruction software must still be enhanced, the research carried out in this thesis has led to significant advances in the MACACO project, whose applicability for treatment monitoring in hadrontherapy will be determined in the following years.

Resumen

Introducción

La terapia hadrónica es un tipo de radioterapia que consiste en la irradiación de tumores con partículas pesadas cargadas, típicamente protones o iones ligeros. Esta técnica presenta un perfil de deposición energética diferente al de la radioterapia convencional con rayos X, debido a la naturaleza de las interacciones físicas entre las partículas que componen el haz y el cuerpo del paciente. A diferencia de los rayos X, cuya dosis depositada se atenúa a medida que el haz penetra en el interior del cuerpo, los hadrones depositan una dosis mínima en su superficie de entrada, que se incrementa paulatinamente hasta alcanzar un máximo abrupto en el punto donde son absorbidos. Este punto se conoce como *pico de Bragg*, y el tejido situado tras él no recibe radiación del haz incidente. El pico de Bragg es la principal ventaja de la terapia hadrónica, ya que, al no depositarse dosis más allá de él, permite focalizar el tratamiento en el tumor y preservar el tejido sano circundante.

Puesto que la mayor parte de la dosis se deposita en una pequeña región, para aprovechar el potencial de esta técnica es imprescindible contar con un sistema de monitorización que garantice que no se produzcan variaciones respecto al plan de tratamiento y que efectivamente se esté irradiando la zona afectada. Dada la completa absorción de las partículas del haz en el cuerpo del paciente, estas no pueden ser utilizadas para monitorización. Es posible, sin embargo, recurrir a partículas secundarias, generadas durante la irradiación, para monitorizar el tratamiento. Mediante interacciones nucleares entre las partículas del haz y los átomos del paciente, se producen principalmente dos tipos de partículas que pueden ser aprovechadas para la monitorización: positrones y fotones de alta energía, también llamados *prompt gammas*. La producción de estas partículas secundarias está correlacionada con la dosis depositada a lo largo del camino del haz. Su detección permite, a través de la reconstrucción de su mapa de creación, comparar la distribución medida con una predicción generada a partir de los planes de tratamiento. La equivalencia de las distribuciones simulada y medida dentro de unos márgenes de tolerancia consituyen un modo de monitorizar la terapia. El origen de los positrones puede ser reconstruido utilizando técnicas de tomografía por emisión

de positrones (PET, por sus siglas en inglés), ampliamente empleadas en otros ámbitos de la imagen médica. En el ámbito de la terapia hadrónica, el uso de PET tiene fundamentalmente dos inconvenientes: el tiempo de vida medio de los emisores de positrones (que hace que, dependiendo del isótopo producido, su emisión no sea inmediata, y que se dé difusión biológica de las células donde se encuentran) y la dificultad para integrar el escáner PET y la línea del haz. Los prompt gammas son producidos inmediatamente después de la irradiación (en el orden de unos pocos ns) y con un espectro de emisión característico, continuo hasta unas decenas de MeV y dominado por líneas espectrales propias de los elementos más abundantes en el tejido irradiado. Diversos métodos para la detección y reconstrucción de prompt gammas están siendo investigados para su aplicación en monitorización de terapia hadrónica. Entre ellos podemos destacar la colimación mecánica, métodos basados en la detección de su distribución temporal, espectroscopía de prompt gammas o las cámaras Compton. Puesto que esta tesis se enmarca dentro del proyecto MACACO, que tiene como fin el desarrollo de una cámara Compton compacta para monitorización de terapia hadrónica, estos dispositivos se explican con más detalle a continuación.

Cámaras Compton

Las cámaras Compton son detectores de fotones que emplean la cinemática Compton para reconstruir el punto de emisión de los fotones medidos. Su principio operacional está basado en la detección en coincidencia temporal de una interacción Compton producida por un fotón incidente y de otra interacción sufrida por el fotón dispersado. Si se conoce la energía inicial del fotón incidente y se mide la energía depositada en la dispersión Compton, la fórmula Compton (ecuación 2.1) permite calcular el ángulo que forman el fotón incidente y el dispersado. A partir de las dos posiciones de interacción medidas y el ángulo de dispersión, se puede construir una superficie cónica dentro de la cual el camino seguido por el fotón inicial debe estar contenido.

Puesto que, para construir el cono de respuesta (CoR), es necesario conocer la energía inicial del fotón, la detección de dos interacciones permite la reconstrucción de imagen únicamente si la energía de emisión de la fuente es conocida de antemano o si se produce una absorción total del fotón en el segundo plano (es decir, cuando la segunda interacción es una absorción fotoeléctrica). Si, en lugar de una absorción fotoeléctrica, la segunda interacción es de nuevo una dispersión Compton, se puede cacular la energía del fotón incidente midiendo una tercera interacción. En efecto, la posición interacción del fotón en la tercera detección permite obtener el ángulo de dispersión de la segunda interacción, con lo que la energía inicial del fotón queda determinada (ecuación 2.2). La detección de eventos triples permite

una reconstrucción más precisa, ya que posibilita el cálculo de la energía inicial de los fotones medidos. Por tanto, cuando las fuentes medidas emiten fotones de distintas energías o con un espectro desconocido, los eventos triples son en principio más favorables respecto a los dobles. Sin embargo, debido a que una interacción adicional debe ser registrada, su eficiencia de detección es significativamente menor. Con el fin de aprovechar la mayor eficiencia de los eventos dobles sin absorción total, otra posible estrategia es modificar el método de reconstrucción para incluir la dimensión espectral, de forma que la energía inicial del fotón también es inferida en la reconstrucción a partir de las medidas.

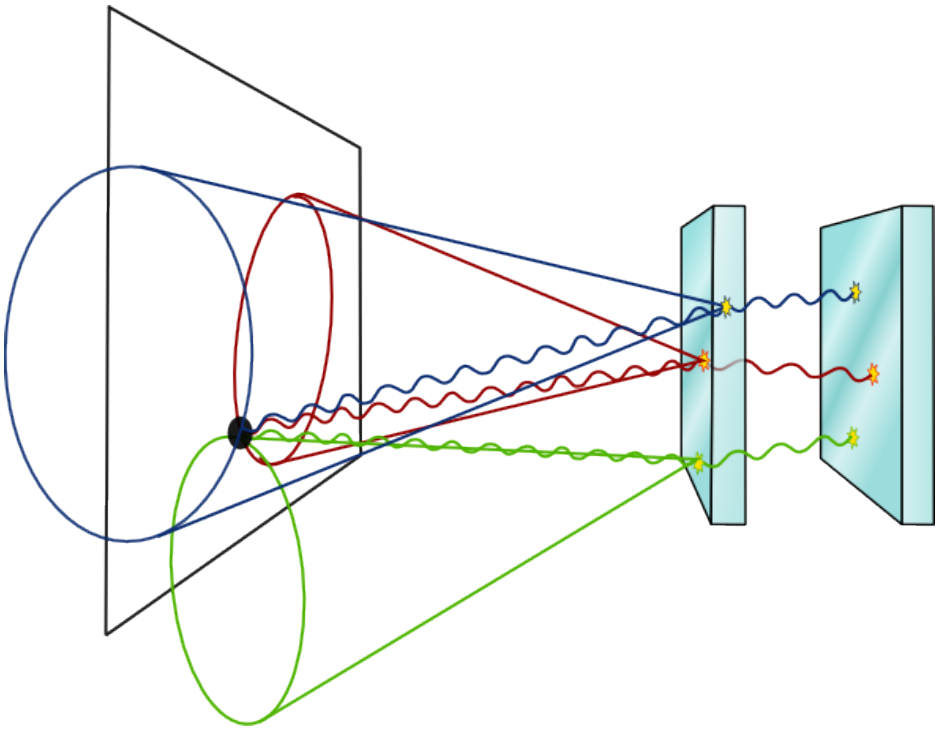

Figura R.1 Intersección en el plano imagen de superficies cónicas a partir de distintos eventos medidos.

Por cada evento detectado, un único CoR es construido y proyectado en el espacio imagen, con lo que la distribución espacial de la fuente medida se puede inferir a través las intersecciones de los distintos CoRs. Esta idea está ilustrada en la Figura R.1, que muestra la intersección de tres CoRs y el plano imagen en la posición donde tres fotones iniciales han sido emitidos. Existen diferentes algoritmos, analíticos o numéricos, para reconstruir la imagen a partir de los datos medidos. En esta tesis, la reconstrucción se ha realizado en todos los casos con el algoritmo iterativo *list-mode* MLEM, ampliamente utilizado en reconstrucción de imagen Compton.

Dispositivo experimental

El prototipo experimental diseñado en el proyecto MACACO es una cámara Compton reconfigurable que puede ser montada con dos o tres planos detectores a diferentes distancias. Cada uno de los planos consta de un cristal monolítico de bromuro de lantano dopado con cerio ((Ce)$LaBr_3$) acoplado a fotomultiplicadores de silicio (SiPMs). La Figura R.2a muestra una imagen del sistema montado con tres planos, que pueden verse ampliados en la Figura R.2b.

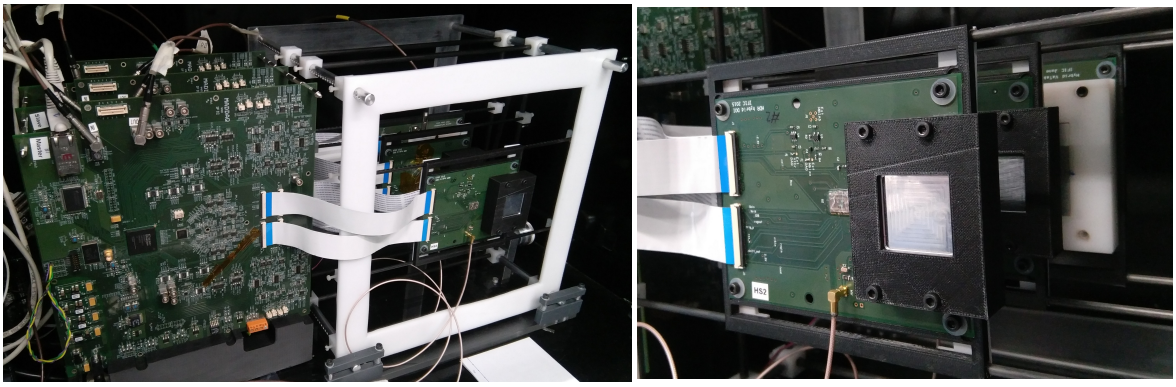

(a) (b)

Figura R.2 Imágenes del dispositivo experimental montado con tres planos. Sistema completo (a) y vista detallada de los planos detectores (b).

Durante el transcurso de esta tesis, tres generaciones de detectores han sido empleados, aunque versiones previas ya habían sido desarrolladas en el contexto del proyecto. Las características más importantes de las distintas versiones de detectores están recogidas en la Tabla R.1. La calidad de las imágenes porporcionadas por la cámara Compton depende en última instancia de la resolución energética, espacial y temporal del sistema:

- Resolución energética: determina la precisión con la cual se calcula el ángulo de dispersión Compton. Las distintas generaciones de detectores empleados han mejorado esta característica, llegando hasta resoluciones del 5.3% FWHM a una energía de 511 keV. Las resoluciones de los distintos detectores están recogidas en la Tabla R.1.

- Resolución espacial intrínseca: determina la precisión con la cual se obtienen el eje y el vértice del CoR. La resolución espacial medida en nuestros detectores es de 1.2 mm FWHM para los cristales de 5 mm de grosor y de 1.5 mm FWHM para los de 10 mm.

- Resolución temporal: puesto que el sistema trabaja en coincidencia temporal, es importante tener una buena resolución para poder distinguir los eventos producidos por un

único fotón incidente de las coincidencias aleatorias. La resolución temporal obtenida con nuestro sistema es de 41 ns FWHM. Esta resolución es baja en comparación con los valores usuales en los detectores empleados para imagen médica, y se debe a la electrónica utilizada en la fase de desarrollo del prototipo, que será notablemente mejorada en futuras versiones.

Tabla R.1 Detectores empleados en el prototipo experimental.

Tamaño del cristal (mm^3)	Versión SiPM	Área activa / total píxel (mm^2)	Resolución energética (FWHM a 511 keV)
$36.0 \times 32.4 \times 5$	S11064-050P(X1)	3×3 / 4.50×4.05	7.2
$36.0 \times 32.4 \times 10$	S11064-050P(X1)	3×3 / 4.50×4.05	7.4
$27.2 \times 26.8 \times 5$	S11830-3340MF	3×3 / 3.2×3.2	6.4
$(2\times)$ $25.8 \times 25.8 \times 5$	S13361-3050AE-08	3×3 / 3.2×3.2	5.3

Cada plano individual (cristal centelleador acoplado a SiPMs) está montado en un soporte híbrido, que alimenta a los SiPMs y contiene el ASIC (modelo VATA64HDR16 de Ideas), encargado de controlar de lectura. Cada híbrido se conecta a una tarjeta de adquisición hecha a medida, equipada con una FPGA (modelo XC3S4000 de Xilinx) que gestiona el proceso de adquisición. La primera etapa del ASIC es un preamplificador, después del cual la señal entra en un filtro semi-gaussiano que produce una señal de voltaje o de corriente. Un conversor analógico-digital (DAC) de 8 bits permite al usuario un ajuste fino del potencial de entrada del preamplificador. A través de la aplicación de los DACs, el potencial de los 64 canales individuales se puede modificar hasta 1 V en pasos de 3.5 mV, lo que permite ajustar independientemente el voltaje de cada píxel para uniformizar la respuesta en la matriz de SiPMs. Cuando un evento tiene lugar, el ASIC genera una señal que activa la secuencia de lectura. La información es transferida desde el híbrido hasta la tarjeta de adquisición, donde es amplificada y digitalizada por un conversor analógico-digital de 12 bits, formateada y enviada al ordenador.

La adquisición es controlada por ordenador mediante un programa dedicado, que se comunica con cada tarjeta de adquisición a través de un cable ethernet. Este programa permite al usuario establecer distintos parámetros antes de comenzar la toma de datos, como los umbrales o los DACs. Además, permite seleccionar dos modos de adquisición: *singles* (detectores activados independientemente) y *coincidencias* (detectores trabajando en coincidencia temporal). El modo *singles* se utiliza para comprobar el correcto funcionamiento de los planos individuales y para obtener las curvas de calibración aplicadas a los datos en

coincidencias. El modo de operación en coincidencia está controlado por una tarjeta de coincidencias específica. Cuando el sistema está montado con los tres planos, esta tarjeta permite la adquisición simultánea de eventos producidos por coincidencias dobles (entre cualquier par de detectores) o triples.

Caracterización del sistema experimental

El prototipo experimental ha sido utilizado para reconstruir imágenes de fuentes radiactivas en el laboratorio, tanto en el modo de operación de dos planos como en el de tres. Para evaluar el sistema con fotones de distintas energías, se han utilizado dos fuentes puntuales distintas: una fuente de ^{22}Na, que emite fotones de 511 y 1275 keV, y una de ^{88}Y, que emite fotones de 898 y 1836 keV. Con el fin de reconstruir los fotones de cada energía independientemente, en las medidas realizadas se seleccionan los eventos mediante un corte en el espectro de energía total medida. Por ejemplo, en el caso del ^{22}Na, este corte se establece en 600 keV, de forma que aquellos eventos que han depositado una energía total inferior al corte son clasificados como eventos producidos por un fotón inicial de 511 keV, y aquellos con deposición energética superior son clasificados como eventos de 1275 keV.

En el modo de operación con dos planos, las fuentes fueron colocadas manualmente en nuevo posiciones distintas dentro del campo de visión (FoV, por sus siglas en inglés), formando una matriz rectangular y con un espacio entre posiciones de aproximadamente 20 mm en las direcciones x e y. Las imágenes reconstruidas pueden verse en la Figura R.3, donde la fila superior corresponde a las imágenes obtenidas con la fuente de ^{22}Na y la inferior con la de ^{88}Y. Dichas imágenes han sido reconstruidas independientemente para cada posición de la fuente, y sumadas en las imágenes finales mostradas para visualizarlas juntas. En ellas, puede apreciarse que, en cada caso, la posición reconstruida de la fuente se corresponde con su posición esperada. Además, para cada medida individual, las imágenes obtenidas con las dos energías emitidas reconstruyen la fuente en la misma posición, lo que confirma que el sistema funciona correctamente. También se observa que las imágenes reconstruidas con las energías inferiores (columna izquierda) son más ruidosas que las obtenidas con energías superiores (columna derecha). Esto se debe a dos contribuciones: la primera de ellas es la contaminación por eventos generados por los fotones de más alta energía con deposiciones parciales, que pueden dar lugar a energías depositadas inferiores al corte energético y ser por tanto mal clasificados. La segunda contribución es el mayor porcentaje de eventos de *backscatter* (eventos en los que el fotón interacciona en el segundo plano antes que en el primero) para energías bajas, a los que se le asigna un orden de interacción incorrecto y por tanto añaden ruido a la imagen.

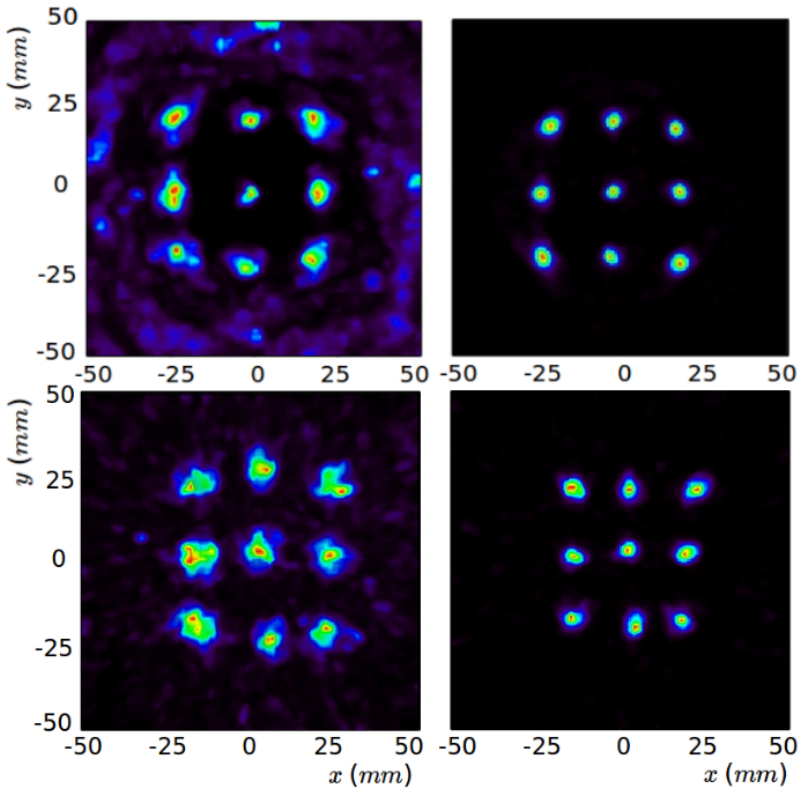

Figura R.3 Imágenes reconstruidas a partir de coincidencias dobles. Arriba: imágenes de la fuente de ^{22}Na con 511 keV (izquierda) y 1275 keV (derecha). Abajo: imágenes de la fuente de ^{88}Y con 898 keV (izquierda) y 1836 keV (derecha).

También se tomaron medidas con las mismas fuentes y el sistema montado con tres planos. Igual que en el caso de dos planos, las imágenes han sido reconstruidas para las distintas energías emitidas aplicando un corte en la energía total depositada (en este caso, medida en las tres interacciones). Las imágenes pueden verse en la Figure R.4, donde la fuente de ^{22}Na se muestra en tres posiciones diferentes (fila superior) y la de ^{88}Y en una única posición (fila inferior). A diferencia del modo con dos planos, en este caso la energía inicial de los fotones no era un parámetro conocido en el momento de la reconstrucción, sino que es calculada en cada evento a partir de los datos medidos.

Las imágenes reconstruidas a distintas energías son comparados en términos de resolución espacial. La figura de mérito calculada es la FWHM, obtenida a partir de ajustes gaussianos a los perfiles en las direcciones x e y a través del máximo en las imágenes. Los valores obtenidos para cada energía, con dos y tres planos, aparecen listados en la Tabla R.2. En las dos configuraciones, se observa una tendencia hacia mejores resoluciones espaciales en las imágenes reconstruidas con fotones de mayor energía.

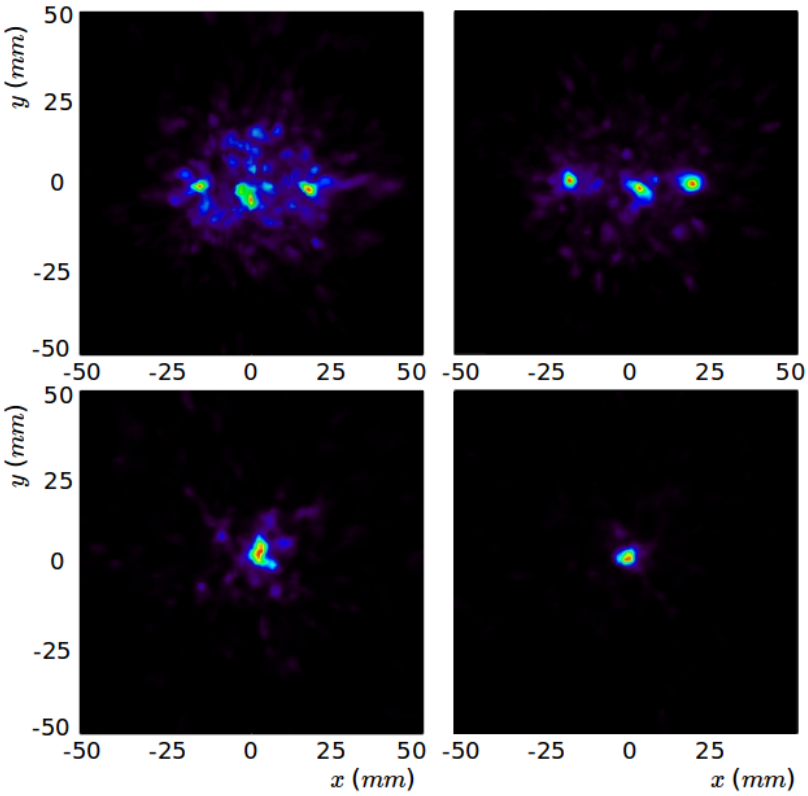

Figura R.4 Imágenes reconstruidas a partir de coincidencias triples. Arriba: imágenes de la fuente de ^{22}Na con 511 keV (izquierda) y 1275 keV (derecha). Abajo: imágenes de la fuente de ^{88}Y con 898 keV (izquierda) y 1836 keV (derecha).

Tabla R.2 FWHM a lo largo de los perfiles en x e y de las imágenes reconstruidas para fotones de diferentes energías.

	FWHM$_{x,y}$ (mm)	
Energía (keV)	2 Planos	3 Planos
511	5.2, 4.4	5.4, 5.4
898	4.0, 3.6	3.9, 4.6
1275	3.8, 3.7	3.6, 3.6
1836	2.7, 3.1	3.4, 3.0

Además de los tests realizados en el laboratorio, el sistema ha sido probado con fotones de 4.4 MeV en la instalación de aceleradores del HZDR en Dresde. Esta energía, inaccesible desde el laboratorio, es relevante en terapia hadrónica, ya que es una de las líneas prominentes en el espectro de prompt gammas, causada por la desexcitación del ^{12}C, muy abundante en el tejido orgánico. La generación de los fotones de alta energía se produce

mediante la irradiación con un haz de iones ^{15}N de un blanco de Ti implantado con H, que induce la reacción de resonancia $^{15}N(p,\alpha\gamma_{4,439})^{12}C$. Para este estudio, se tomaron datos en coincidencia con el sistema montado con tres planos. Para simular el desplazamiento del blanco, fijo en todo momento, se midió con el sistema en tres posiciones separadas 10 mm entre ellas a lo largo del eje paralelo al haz. En el tiempo de duración del test, la estadística de coincidencias triples acumulada fue insuficiente para reconstruir imágenes del blanco. En cambio, sí se detectaron datos suficientes de coincidencias dobles en las tres posibles combinaciones de pares de detectores (planos 1-2, planos 2-3 y planos 1-3). Las imágenes correspondientes están representadas en la Figura R.5, donde se puede ver que las imágenes obtenidas con los distintos pares de detectores son coherentes entre sí.

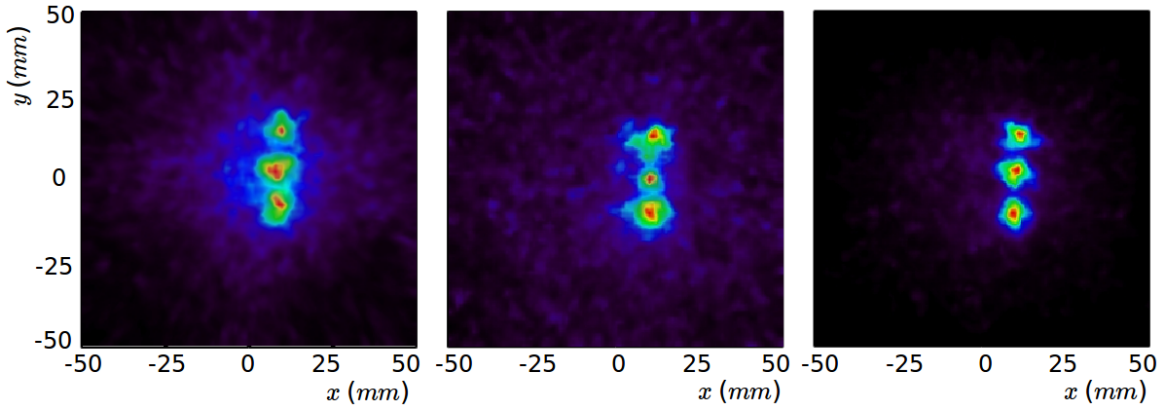

Figura R.5 Imágenes reconstruidas con los detectores en tres posiciones diferentes, con los tres pares de detectores posibles: planos 1-2 (izquierda), 2-3 (centro) y 1-3 (derecha).

Modelo físico detallado para fuentes monocromáticas

Los resultados anteriores muestran que nuestro prototipo de cámara Compton puede reconstruir fuentes experimentales de energía conocida. Con el fin de reconstruir fuentes más complejas, un modelo físico detallado debe ser considerado e incluido en el proceso de reconstrucción. Este modelo sirve para obtener una expresión de la matriz del sistema, definida como la probabilidad de que un fotón emitido desde un vóxel V sea detectado con los parámetros medidos $\{\vec{x}_1, \tilde{E}_1, \vec{x}_2, \tilde{E}_1\}$. Teniendo en cuenta todas las probabilidades físicas involucradas en la detección de un evento, en un sistema de dos planos y midiendo fuentes monocromáticas de energía conocida, la expresión para la matriz del sistema deducida en este trabajo es

$$\frac{dP(\tilde{E}_1,\vec{r}_1,\vec{r}_2|\,V)}{d\tilde{E}_1\,d^3r_1\,d^3r_2} = \int d\varphi d\xi \frac{m_e c^2 n_e^{eff}}{4\pi V} \frac{e^{-\mu_0\lambda_0}e^{-\mu_1\lambda_1}}{(E_0-\tilde{E}_1)^2|\vec{r}_1-\vec{r}_2|^2}\frac{d\sigma_0^c}{d\Omega_1}\mu_1\Theta_V. \tag{R.1}$$

donde la integral sobre φ y ξ define una superfície cónica (ver Figura 5.1). Además de la matriz del sistema, el algoritmo de reconstrucción también utiliza la matriz de sensibilidad, s_V, definida como la probabilidad total de que un fotón emitido en el voxel V sea detectado por el sistema. Empleando el mismo modelo físico, en este trabajo la matriz de sensibilidad viene dada por

$$s_V = \frac{n_e^{eff}}{4\pi V}\int_V d^3r_0 \int_{P_1} d^3r_1 \frac{e^{-\mu_0\lambda_0}}{|\vec{r}_1-\vec{r}_0|^2}\int_{P_2} d^3r_2 \frac{e^{-\mu_1\lambda_1}}{|\vec{r}_2-\vec{r}_1|^2}\frac{d\sigma_0^c}{d\Omega_1}\mu_1, \tag{R.2}$$

que es precalculada antes del proceso de reconstrucción de imagen utilizando técnicas Monte Carlo de integración numérica.

La validez de estas expresiones se ha comprobado mediante la comparación con simulaciones en GATE. La Figura R.6 representa las gráficas de sensibilidad obtenidas a partir de las simulaciones y de la ecuación deducida. Para su representación, se ha separado la sensibilidad en distintas contribuciones, una para cada posible interacción física del fotón dispersado en el segundo plano (otro Compton, absorción fotoeléctrica o producción de pares e^+e^-. En todos los casos se puede observar un gran acuerdo entre ambos resultados.

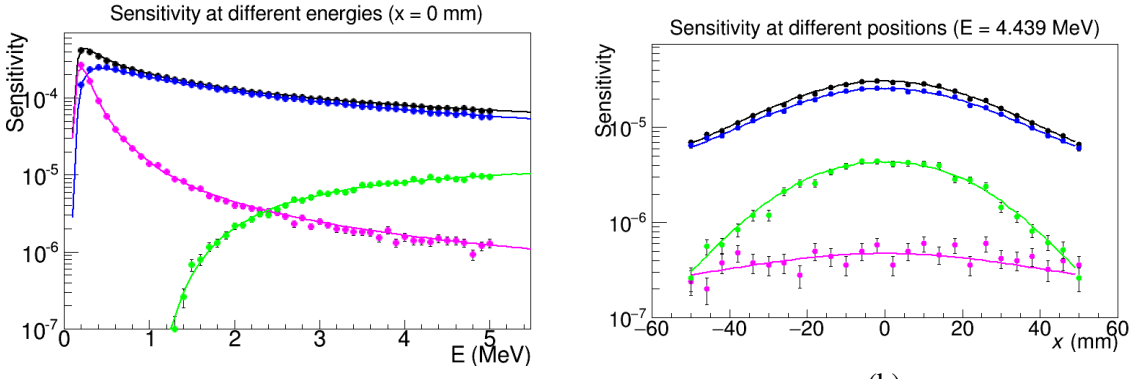

(a) (b)

Figura R.6 Sensibilidad del sistema a las distintas interacciones posibles en el segundo plano. Sensibilidad a distintas energías en una posición fija (a) y sensibilidad a distintas posiciones del FoV con una energía de 4439 keV (b). Los puntos muestran los resultados de la simulación y las líneas continuas la integración de la expresión analítica. Los colores diferentes indican las diferentes interacciones: Compton (azul), efecto fotoeléctrico (rosa), producción de pares (verde) o cualquiera (negro).

También se ha evaluado el impacto de la matriz de sensibilidad en la imagen final reconstruida, comparándola con otros modelos existentes en la bibliografía. Además de

Tabla R.3 Distribuciones de actividad reconstruidas con los distintos modelos de sensibilidad.

Fuente	Tipo de datos	Energía (keV)	Distancia entre planos (mm)
Fondo homogéneo	Simulados	4439	40
Shepp-Logan	Simulados	1275	40
37 Fuentes ^{22}Na	Experimentales	1275	80

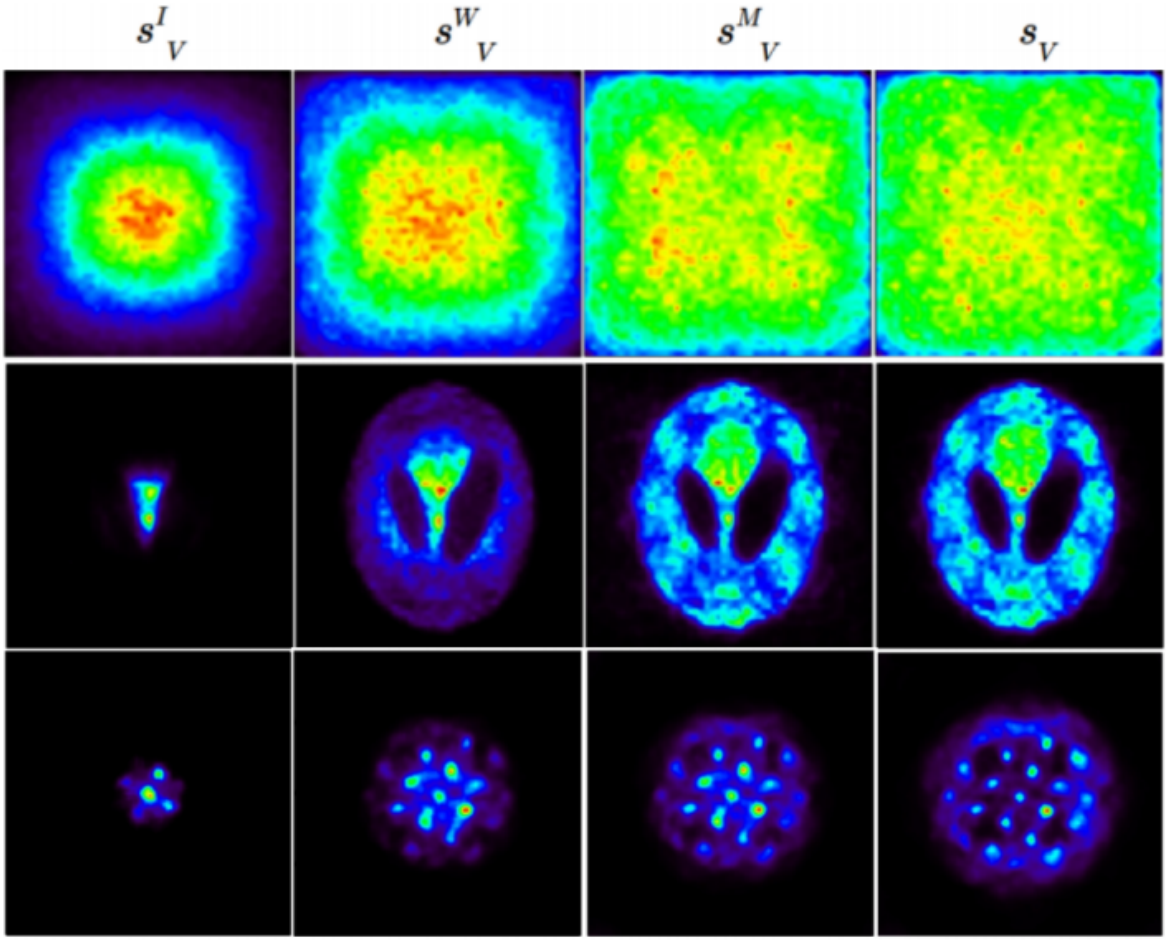

Figura R.7 Imágenes reconstruidas con los cuatro modelos de sensibilidad. Se muestran imágenes de distrintas distribuciones de actividad en cada fila. De arriba a abajo: fondo homogéneo simulado, fantoma de Shepp-Logan simulado y conjunto de 37 fuentes puntuales de ^{22}Na medido experimentalmente.

nuestro modelo y la aproximación de una sensibilidad constante en todo el FoV (s^I_V), se han implementado los modelos aproximados presentados en [102] (s^W_V) y [50] (s^M_V). Estos modelos aproximados asumen que el fotón dispersado tras la interacción Compton tiene muy alta probabilidad de producir una segunda interacción, por lo que la principal contribución

a la sensibilidad del sistema es la cobertura angular del primer plano respecto al punto de emisión inicial. Para evaluar su impacto en la imagen final, los distintos modelos han sido empleados para reconstruir fuentes con diferentes distribuciones de actividad, descritas en la Tabla R.3.

La Figura R.7 muestra las imágenes reconstruidas con cada uno de los modelos para las tres distribuciones de actividad. Cuando se emplea una sensibilidad constante, el algoritmo reconstruye la actividad emitida en la región directamente cubierta por el área del primer detector, pero la intensidad reconstruida es infraestimada en los vóxeles fuera de ella. Puede observarse que los modelos aproximados, s_V^W y s_V^M, mejoran significativamente el resultado obtenido con una sensibilidad constante. Empleando estos modelos, especialmente con s_V^M, el código puede compensar parcialmente la intensidad en las zonas fuera de la superficie del detector. Finalmente, el modelo derivado en este trabajo ha producido los mejores resultados en todos los casos, especialmente en las imágenes del conjunto experimental de fuentes. Esto se debe a que estos datos fueron tomados con una separación mayor entre los planos detectores, por lo que la premisa de los modelos aproximados no se cumple y únicamente nuestro modelo es capaz de describir correctamente la sensibilidad del sistema.

Modelo para fuentes con espectro de emisión desconocido

El modelo anterior supone que las fuentes medidas por el sistema emiten fotones con una energía conocida. Sin embargo, en algunos casos es interesante obtener imágenes de fuentes con un espectro de emisión continuo o con fotones de energía inicial desconocida, como es el caso de los prompt gammas. Con ese fin, en este trabajo se ha extendido el modelo anterior para incluir una dimensión energética en el FoV, de forma que el algoritmo reconstruye simultáneamente la distribución espacial y el espectro energético de la fuente. La base de este método es el hecho de que en la segunda interacción puede darse tanto una absorción total como parcial de la energía transportada por el fotón dispersado, lo que indica que el evento debe haber sido producido por un fotón con energía inicial igual o superior a la suma de energías medidas. Esto permite generar un CoR para cada energía inicial posible (dentro del rango considerado), cada uno de los cuales tendrá un ángulo de apertura diferente. A su vez, cada CoR tiene un peso asociado a la probabilidad de que un fotón con la energía inicial correspondiente genere un evento con los parámetros medidos. Es importante resaltar que el número de bines energéticos considerados en el FoV es finito, por lo que cada evento da lugar a un número discreto de CoRs. La Figura R.8 representa el esquemáticamente un conjunto de CoRs con distintas probabilidades asociado a un evento medido.

La matriz del sistema puede deducirse de forma análoga al modelo con energía determinada, integrando en este caso también la energía inicial. En este trabajo, la expresión que se ha utilizado es

$$\frac{dP_V}{d^3r_1 d\tilde{E}_1 d^3r_2 d\tilde{E}_2} = \int d\varphi d\xi \frac{dE_0}{4\pi V} \frac{e^{-\mu_1\lambda_1}}{|\vec{r}_2-\vec{r}_1|^2} \frac{m_e c^2}{(E_0-\tilde{E}_1)^2} n_e^{eff} \frac{d\sigma_0^c}{d\Omega_1} T^{ceg}, \tag{R.3}$$

donde T^{ceg} codifica la segunda interacción, y tiene un sumando para cada una de las tres interacciónes posibles (dispersión Compton, absorción fotoeléctrica o producción de pares):

$$\begin{aligned} T^{ceg} = & \frac{m_e c^2}{(E_0-\tilde{E}_1-\tilde{E}_2)^2} n_e^{eff} \frac{d\sigma_1^c}{d\Omega_2} \int d\varphi_2 e^{-\mu_2\lambda_2} + \mu_1^e \delta(E_0-\tilde{E}_1-\tilde{E}_2) + \\ & + \mu_1^g S(\vec{r}_2)\delta(E_0-\tilde{E}_1-\tilde{E}_2-2m_e c^2). \end{aligned} \tag{R.4}$$

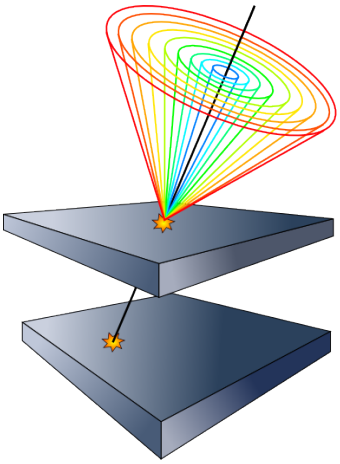

Figura R.8 Diagrama del conjunto de CoRs generados a partir de un evento medido.

El código de reconstrucción espectral ha sido probado con distintas fuentes, tanto simuladas como experimentales. Para analizar los resultados obtenidos a partir de las simulaciones, es importante entender qué tipo de datos se pueden extraer de ellas. En particular, en este estudio hemos considerado tres tipos de datos, según su nivel de idealidad:

- *Singles*: son los datos tal como podrían ser medidos por el detector, teniendo en cuenta su resolución intrínseca. Una interacción de un fotón da lugar a un único single, donde la energía y posición de interacción medidas se calculan teniendo en cuenta las interacciones del electrón de retroceso y otras posibles partículas secundarias.

- *Hits*: registran individualmente las interacciones de todas las partículas generadas. En este conjunto de datos, consideramos que la posición de interacción es el punto

exacto donde interactúa el fotón, y la energía es la depositada por éste y por todas sus partículas secundarias.

- *Hits ideales*: estos datos ideales se construyen suponiendo que toda la energía transmitida es depositada en el punto exacto de la interacción del fotón.

Una de las distribuciones de actividad simuladas para testear el código es el fantoma de energía discreta. Consiste en 6 regiones, formadas por 6 esferas de actividad homogénea, cada una de las cuales emite fotones de una energía fija entre 2 y 7 MeV, con una diferencia de 1 MeV entre regiones adyacentes (ver Figura 6.4). La Figura R.9 muestra las imágenes reconstruidas (e integradas en el dominio espectral, para visualizar únicamente el espacial) con los tres datos generados de la simulación. En todas ellas se puede identificar la posición de todas las fuentes simuladas. No obstante, en la imagen obtenida a partir de los *singles*, las regiones emisoras de energías más altas son reconstruidas con intensidades progresivamente menores y las fuentes aparecen peor definidas. En la imagen con *hits*, aunque todas las fuentes están mejor definidas, las intensidades a energías altas siguen estando subestimadas, efecto que únicamente se corrige mediante el uso de *hits ideales*. Esto puede observarse más claramente en los espectros reconstruidos, que están representados en la Figura R.10. La degradación de las imágenes se debe al desplazamiento del electrón de retroceso respecto al punto de interacción del fotón inicial. Puesto que, a medida que aumenta la energía inicial, la energía transferida al electrón también se incrementa, mayor es su desplazamiento en el detector, por lo que la posición medida en *singles* tiene mayor desviación respecto a la posición real (la registrada en los *hits*). Cuando esta energía es suficientemente grande, también aumenta la probabilidad de que el electrón escape del detector con parte de la energía. Esta energía perdida produce una desviación entre la medida y la energía transferida en la interacción Compton, por lo que el método no es capaz de encontrar la energía y posición de emisión. Cuando se emplean *hits ideales*, este efecto se corrige totalmente, demostrando que el método es capaz de reconstruir con éxito distribuciones complejas en condiciones ideales de detección.

El código de reconstrucción espectral también ha sido empleado para reconstruir datos experimentales con fotones de distintas energías. Para ello, se han utilizado datos medidos simultáneamente con las fuentes de ^{22}Na e ^{88}Y, que en conjunto emiten un total de cuatro energías distintas. La imagen reconstruida (e integrada en el dominio espectral) puede verse en la Figura R.11a, donde también se muestra la imagen reconstruida con los mismos datos y el código de reconstrucción no espectral (empleando la energía suma de cada evento como energía inicial). En el resultado obtenido con el código espectral es una imagen más nítida y menos ruidosa, donde las dos fuentes son claramente visibles. Esto se debe a que, en este

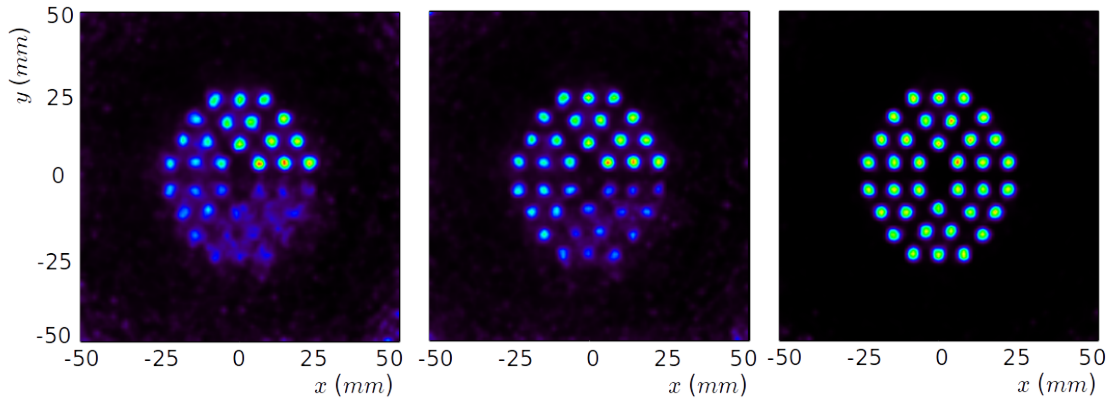

Figura R.9 Imágenes reconstruidas con el fantoma simulado. Distribución espacial obtenida tras la integración de la dimensión espectral con *singles* (izquierda), *hits* (centro) y *hits ideales* (derecha).

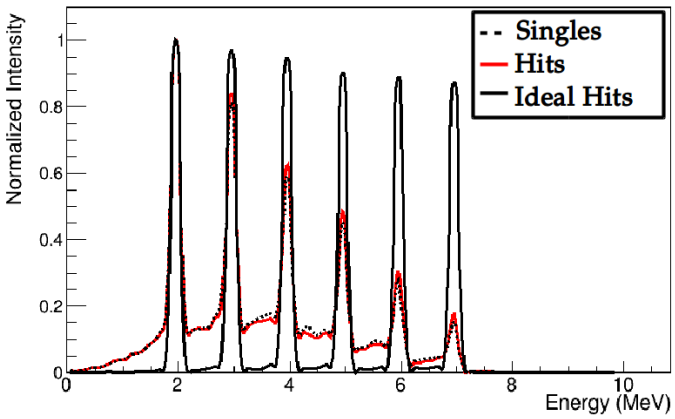

Figura R.10 Espectro reconstruido del fantoma simulado tras la integración de las componentes espaciales de la imagen.

caso, el código es capaz de encontrar la energía inicial en todos los eventos, incluyendo aquellos con deposiciones parciales. Por contra, en el código anterior, sólo los eventos con absorción total pueden ser reconstruidos correctamente, y el resto añaden ruido a la imagen. Finalmente, la Figura R.11b muestra una imagen mixta energético-espacial, donde se representan conjuntamente el espectro y posiciones medidas. En ella se puede apreciar que se recupera un pico en las cuatro energías emitidas. Como era de esperar, las dos energías emitidas por cada fuente son reconstruidas en la misma posición, confirmando que el método es capaz de reconstruir simultáneamente la distribución espacial y la emisión espectral de fuentes experimentales.

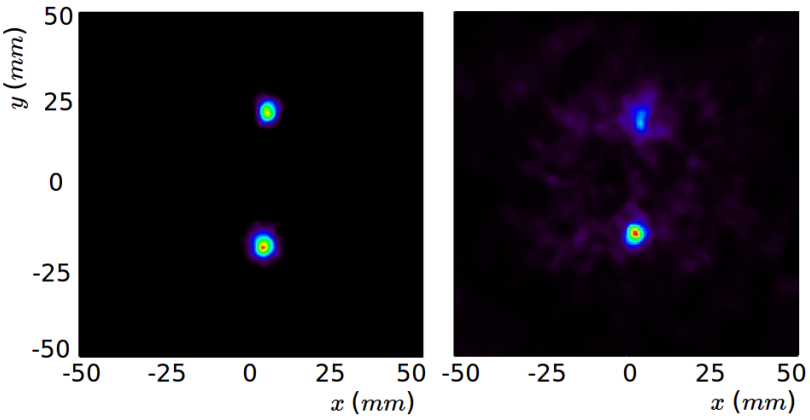

(a)

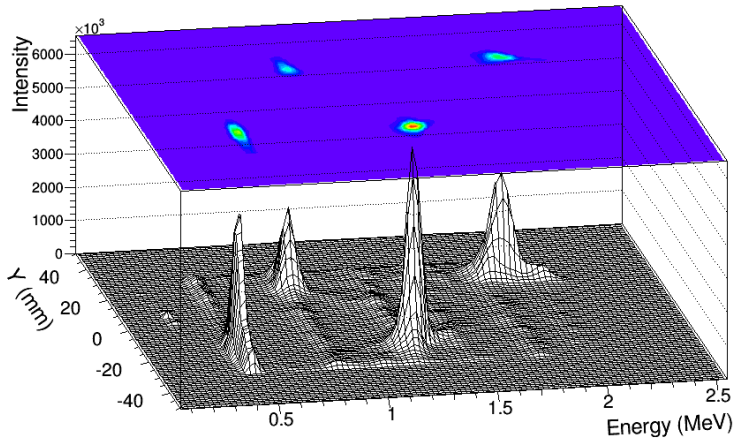

(b)

Figura R.11 Imágenes reconstruidas con el fantoma simulado. (a) Distribución espacial obtenida tras la integración de la dimensión espectral con *singles*(izquierda), *hits*(centro) y *hits ideales*(derecha). (b) Espectros tras la integración de las componentes espaciales.

Conclusiones

Un aspecto tratado en esta tesis ha sido la caracterización del prototipo experimental desarrollado por el grupo IRIS y la evaluación de sus capacidades de imagen. En ese sentido, se ha demostrado que el sistema es capaz de posicionar correctamente fuentes radiactivas en su campo de visión. Los resultados con dos planos en el laboratorio confirman que fuentes de fotones con energías de emisión en el rango entre 511 y 1836 keV son reconstruidas con éxito. Respecto a la resolución de la imagen, en ese rango de energías los mejores resultados fueron obtenidos para los fotones de más alta energía. En el estudio con distintas distancias relativas entre la fuente y los planos se obtuvieron imágenes con mejor resolución

para mayores separaciones entre planos y para menores distancias entre fuente y primer plano. En el modo de operación con tres planos, se demostró que la energía inicial del fotón puede extraerse de las medidas experimentales sin conocimiento previo, lo cual permitió la reconstrucción de imágenes de todas las fuentes medidas. El sistema también fue probado con fotones de 4.4 MeV en el centro HZDR de Dresde. Aunque la estadística acumulada en el tiempo de medida era insuficiente para la reconstrucción con coincidencias triples, imágenes del blanco en tres posiciones diferentes fueron reconstruidas con éxito con todas las combinaciones de pares de detectores, demostrando que el sistema es capaz de recuperar imágenes a esta energía.

Respecto al proceso de reconstrucción de imagen, un modelo físico completo de la formación de la señal ha sido derivada para cámaras Compton de dos planos y fuentes monocromáticas de energía conocida. El modelo ha sido validado a través de comparaciones con simulaciones de Monte Carlo, donde se vio una excelente compatibilidad, y empleado para deducir una expresión para las matrices del sistema y de sensibilidad. El impacto de la matriz de sensibilidad en las imágenes reconstruidas también ha sido evaluado. En un estudio de comparación frente a otros modelos de sensibilidad utilizados en la literatura, el modelo derivado en este trabajo ha demostrado producir mejores imágenes, especialmente en la recuperación de regiones de actividad situadas fueras de la superficie del detector.

El modelo físico ha sido extendido para incluir fuentes emisoras de energía desconocida, que a su vez ha sido empleado en la implementación de un código de reconstrucción espectral. El código de reconstrucción espectral es capaz de recuperar simultáneamente la distribución espacial y la emisión espectral de diversas fuentes sin conocimiento previo sobre la energía de los fotones emitidos. La evaluación del código con fuentes simuladas ha demostrado que fuentes complejas pueden ser reconstruidas con éxito cuando se utilizan datos ideales. El estudio con simulaciones también mostró que el espectro reconstruido se degrada cuando se consideran datos realistas, principalmente debido a la energía perdida, transportada por los electrones de retroceso que escapan del detector. Finalmente, la aplicación del código de reconstrucción espectral a medidas experimentales ha permitido encontrar tanto la posición como la emisión espectral de fuentes puntuales en todo el rango de energías probado.

Los resultados obtenidos en este trabajo han ayudado a identificar las limitaciones actuales y a definir las líneas futuras del proyecto. Futuros desarrollos incluyen mejoras en los componentes del prototipo experimental y en los programas de reconstrucción. Además de nuevos componentes electrónicos, que permitirán mejorar la resolución temporal, se está considerando la inclusión de un sistema para medir los electrones de retroceso que escapen de los detector, motivado en parte por los resultados obtenidos con el código de reconstrucción espectral. El código de reconstrucción implementado también servirá de

base para mejoras futuras. En particular, el modelo físico derivado para cámaras Compton de dos planos puede ser extendido a sistemas con tres planos y, con el objetivo de explotar al máximo el potencial del sistema experimental, un método de reconstrucción de imagen empleando todas las coincidencias dobles y triples puede ser desarrollado. En conclusión, la investigación llevada a cabo en esta tesis ha supuesto avances significativos en el proyecto MACACO, cuya aplicabilidad en monitorización del tratamiento en terapia hadrónica será determinada en los próximos años.

References

[1] AdvanSiD (2014). Application note, Introduction to SiPMs. *https://advansid.com/*.

[2] Agostinelli, S. et al. (2003). Geant4-a simulation toolkit. *Nuclear Instruments and Methods in Physics Research Section A: Accelerators, Spectrometers, Detectors and Associated Equipment*, 506(3):250 – 303.

[3] Aldawood, S., Thirolf, P., Miani, A., Böhmer, M., Dedes, G., Gernhäuser, R., Lang, C., Liprandi, S., Maier, L., Marinšek, T., et al. (2017). Development of a Compton camera for prompt-gamma medical imaging. *Radiation Physics and Chemistry*, 140:190–197.

[4] Andreyev, A., Sitek, A., and Celler, A. (2009). Stochastic image reconstruction method for Compton camera. In *2009 IEEE Nuclear Science Symposium Conference Record (NSS/MIC)*, pages 2985–2988. IEEE.

[5] Andreyev, A., Sitek, A., and Celler, A. (2011). Fast image reconstruction for Compton camera using stochastic origin ensemble approach. *Medical physics*, 38(1):429–438.

[6] Andritschke, R., Zoglauer, A., Kanbach, G., Bloser, P. F., and Schopper, F. (2005). The compton and pair creation telescope MEGA. *Experimental Astronomy*, 20(1-3):395–403.

[7] Barrio, J., Etxebeste, A., Granado, L., Muñoz, E., Oliver, J., Ros, A., Roser, J., Solaz, C., and Llosá, G. (2017). Performance improvement tests of MACACO: A Compton telescope based on continuous crystals and SiPMs. *Nuclear Instruments and Methods in Physics Research Section A: Accelerators, Spectrometers, Detectors and Associated Equipment*.

[8] Barrio, J., Etxebeste, A., Lacasta, C., Muñoz, E., Oliver, J., Solaz, C., and Llosá, G. (2015). Performance of VATA64HDR16 ASIC for medical physics applications based on continuous crystals and SiPMs. *Journal of Instrumentation*, 10(12):P12001.

[9] Basko, R., Zeng, G. L., and Gullberg, G. T. (1998). Application of spherical harmonics to image reconstruction for the Compton camera. *Physics in Medicine & Biology*, 43(4):887.

[10] Berger, M., Hubbell, J., Seltzer, S., Chang, J., Coursey, J., Sukumar, R., Zucker, D., and Olsen, K. (2010). Xcom: Photon cross section database (version 1.5). *National Institute of Standards and Technology, Gaithersburg, MD*.

[11] Bethe, H. (1930). Zur Theorie des durchgangs schneller Korpuskularstrahlen durch Materie. *Annalen der Physik*, 397(3):325–400.

[12] Bhattacharya, D., O'Neill, T., Akyüz, A., Samimi, J., and Zych, A. (2004). Prototype TIGRE Compton γ-ray balloon-borne telescope. *New Astronomy Reviews*, 48(1-4):287–292.

[13] Bloch, F. (1933). Zur Bremsung rasch bewegter teilchen beim durchgang durch Materie. *Annalen der Physik*, 408(3):285–320.

[14] Cree, M. J. and Bones, P. J. (1994). Towards direct reconstruction from a gamma camera based on Compton scattering. *IEEE transactions on medical imaging*, 13(2):398–407.

[15] Dendooven, P., Buitenhuis, H., Diblen, F., Heeres, P., Biegun, A., Fiedler, F., Van Goethem, M., Van der Graaf, E., and Brandenburg, S. (2015). Short-lived positron emitters in beam-on PET imaging during proton therapy. *Physics in Medicine & Biology*, 60(23):8923.

[16] Dogan, N. and Wehe, D. (1994). Optimization and angular resolution calculations for a multiple Compton scatter camera. pages 269–273.

[17] Etxebeste, A., Barrio, J., Muñoz, E., Oliver, J. F., Solaz, C., and Llosá, G. (2016). 3D position determination in monolithic crystals coupled to SiPMs for PET. *Physics in Medicine and Biology*, 61(10):3914.

[18] Everett, D. B., Fleming, J. S., Todd, R. W., and Nightingale, J. M. (1977). Gamma-radiation imaging system based on the compton effect. *IEEE Procedings*, 124:995–1000.

[19] Fontana, M., Dauvergne, D., Létang, J. M., Ley, J.-L., and Testa, É. (2017). Compton camera study for high efficiency SPECT and benchmark with Anger system. *Physics in Medicine & Biology*, 62(23):8794.

[20] Gillam, J., Lacasta, C., Torres-Espallardo, I., Juan, C. C., Llosá, G., Solevi, P., Barrio, J., and Rafecas, M. (2011). A Compton imaging algorithm for on-line monitoring in hadron therapy. In *Medical Imaging 2011: Physics of Medical Imaging*, volume 7961, page 79611O. International Society for Optics and Photonics.

[21] Golnik, C., Bemmerer, D., Enghardt, W., Fiedler, F., Hueso-González, F., Pausch, G., Römer, K., Rohling, H., Schoene, S., Wagner, L., and Kormoll, T. (2016). Tests of a Compton imaging prototype in a monoenergetic 4.44 MeV photon field—a benchmark setup for prompt gamma-ray imaging devices. *Journal of Instrumentation*, 11(06):P06009.

[22] Golnik, C., Hueso-González, F., Müller, A., Dendooven, P., Enghardt, W., Fiedler, F., Kormoll, T., Roemer, K., Petzoldt, J., Wagner, A., et al. (2014). Range assessment in particle therapy based on prompt γ-ray timing measurements. *Physics in Medicine & Biology*, 59(18):5399.

[23] Gong, K., Cherry, S. R., and Qi, J. (2016). On the assessment of spatial resolution of pet systems with iterative image reconstruction. *Physics in medicine and biology*, 61(5):N193.

[24] Hamamatsu (2019). Hamamatsu Photonics. *https://www.hamamatsu.com/*.

[25] Henriquet, P., Testa, E., Chevallier, M., Dauvergne, D., Dedes, G., Freud, N., Krimmer, J., Létang, J., Ray, C., Richard, M., et al. (2012). Interaction vertex imaging (ivi) for carbon ion therapy monitoring: a feasibility study. *Physics in Medicine & Biology*, 57(14):4655.

[26] Herbach, C. M., Gueorguiev, A., Kong, Y., Lentering, R., Pausch, G., Plettner, C., and Stein, J. (2009). Concept study of a two-plane Compton camera designed for location and nuclide identification of remote radiation sources. *Nuclear Science Symposium Conference Record (NSS/MIC)*, 224(13):909–911.

[27] Jan, S. et al. (2004). GATE: a simulation toolkit for PET and SPECT. *Physics in Medicine and Biology*, 49(19):4543.

[28] Jensen, A., Münter, M., and Debus, J. (2011). Review of clinical experience with ion beam radiotherapy. *The British journal of radiology*, 84(special_issue_1):S35–S47.

[29] Jiang, J., Shimazoe, K., Nakamura, Y., Takahashi, H., Shikaze, Y., Nishizawa, Y., Yoshida, M., Sanada, Y., Torii, T., Yoshino, M., Ito, S., Endo, T., Tsutsumi, K., Kato, S., Sato, H., Usuki, Y., Kurosawa, S., Kamada, K., and Yoshikawa, A. (2016). A prototype of aerial radiation monitoring system using an unmanned helicopter mounting a GAGG scintillator Compton camera. *Journal of Nuclear Science and Technology*, 53(7):1067–1075.

[30] Kang, B.-H. and Kim, J.-W. (2009). Monte Carlo design study of a gamma detector system to locate distal dose falloff in proton therapy. *IEEE Transactions on Nuclear Science*, 56(1):46–50.

[31] Kim, J.-W. (2009). Pinhole camera measurements of prompt gamma-rays for detection of beam range variation in proton therapy. *Journal of Korean Physical Society*, 55:1673.

[32] Kishimoto, A., Kataoka, J., Nishiyama, T., Taya, T., and Kabuki, S. (2015). Demonstration of three-dimensional imaging based on handheld Compton camera. *Journal of Instrumentation*, 10(11):P11001.

[33] Klein, O. and Nishina, Y. (1929). Über die Streuung von Strahlung durch freie Elektronen nach der neuen relativistischen Quantendynamik von Dirac. *Zeitschrift für Physik*, 52(11):853–868.

[34] Knopf, A.-C. and Lomax, A. (2013). In vivo proton range verification: a review. *Physics in Medicine & Biology*, 58(15):R131.

[35] Kormoll, T. (2012). Image formation. In *A Compton Camera for In-vivo Dosimetry in Ion-beam Radiotherapy, PhD Thesis*. Technische Universität Dresden.

[36] Kormoll, T., Fiedler, F., Schöne, S., Wüstemann, J., Zuber, K., and Enghardt, W. (2011). A Compton imager for in-vivo dosimetry of proton beams-A design study. *Nuclear Instruments and Methods in Physics Research A*, 626,627:114–119.

[37] Koyama, A., Nakamura, Y., Shimazoe, K., Takahashi, H., and Sakuma, I. (2016). Prototype of a single probe Compton camera for laparoscopic surgery. *Nuclear Instruments and Methods in Physics Research Section A: Accelerators, Spectrometers, Detectors and Associated Equipment*, pages –.

[38] Krimmer, J., Dauvergne, D., Létang, J., and Testa, É. (2018). Prompt-gamma monitoring in hadrontherapy: A review. *Nuclear Instruments and Methods in Physics Research Section A: Accelerators, Spectrometers, Detectors and Associated Equipment*, 878:58–73.

[39] Krimmer, J., Ley, J.-L., Abellan, C., Cachemiche, J.-P., Caponetto, L., Chen, X., Dahoumane, M., Dauvergne, D., Freud, N., Joly, B., Lambert, D., Lestand, L., Létang, J., Magne, M., Mathez, H., Maxim, V., Montarou, G., Morel, C., Pinto, M., Ray, C., Reithinger, V., Testa, E., and Zoccarato, Y. (2015). Development of a Compton camera for medical applications based on silicon strip and scintillation detectors. *Nuclear Instruments and Methods in Physics Research Section A: Accelerators, Spectrometers, Detectors and Associated Equipment*, 787:98 – 101. New Developments in Photodetection NDIP14.

[40] Kroeger, R. A., Johnson, W. N., Kurfess, J. D., Phlips, B. F., and Wulf, E. A. (2002). Three-Compton telescope: Theory, simulantions, and performance. *IEEE Transactions on Nuclear Science*, 49:1887–1892.

[41] Kurosawa, S., Kubo, H., Ueno, K., Kabuki, S., Iwaki, S., Takahashi, M., Taniue, K., Higashi, N., Miuchi, K., Tanimori, T., Kim, D., and Kim, J. (2012). Prompt gamma detection for range verification in proton therapy. *Current Applied Physics*, 12(2):364 – 368.

[42] LeBlanc, J., Clinthorne, N., Hua, C.-H., Nygard, E., Rogers, W., Wehe, D., Weilhammer, P., and Wilderman, S. (1998a). C-SPRINT: a prototype Compton camera system for low energy gamma ray imaging. *IEEE Transactions on Nuclear Science*, 45(3):943–949.

[43] LeBlanc, J., Clinthorne, N., Hua, C.-H., Nygard, E., Rogers, W., Wehe, D., Weilhammer, P., and Wilderman, S. (1998b). Experimental results from the C-SPRINT prototype Compton camera. In *1998 IEEE Nuclear Science Symposium Conference Record. 1998 IEEE Nuclear Science Symposium and Medical Imaging Conference (Cat. No. 98CH36255)*, volume 2, pages 743–746. IEEE.

[44] Li, Z., Wedrowski, M., Bruyndonckx, P., and Vandersteen, G. (2010). Nonlinear least-squares modeling of 3d interaction position in a monolithic scintillator block. *Physics in Medicine and Biology*, 55(21):6515.

[45] Llosá, G., Barrio, J., Cabello, J., Crespo, A., Lacasta, C., Rafecas, M., Callier, S., de La Taille, C., and Raux, L. (2012). Detector characterization and first coincidence tests of a Compton telescope based on LaBr3 crystals and SiPMs. *Nuclear Instruments and Methods in Physics Research Section A: Accelerators, Spectrometers, Detectors and Associated Equipment*, 695:105 – 108. New Developments in Photodetection {NDIP11}.

[46] Llosá, G., Barrio, J., Lacasta, C., Callier, S., de La Taille, C., and Raux, L. (2010). Characterization of a detector head based on continuous labr 3 crystals and sipm arrays for dose monitoring in hadron therapy. In *IEEE Nuclear Science Symposuim & Medical Imaging Conference*, pages 2148–2150. IEEE.

[47] Llosá, G., Cabello, J., Gillam, J. E., Lacasta, C., Oliver, J. F., Rafecas, M., Solaz, C., Solevi, P., Stankova, V., Torres-Espallardo, I., and Trovato, M. (2013). Second LaBr3 Compton telescope prototype. In *Advancements in Nuclear Instrumentation Measurement Methods and their Applications (ANIMMA), 2013 3rd International Conference on*, pages 1–4. IEEE.

[48] Mackin, D., Peterson, S., Beddar, S., and Polf, J. (2012). Evaluation of a stochastic reconstruction algorithm for use in Compton camera imaging and beam range verification

from secondary gamma emission during proton therapy. *Physics in Medicine and Biology*, 57(11):3537.

[49] Marta, M., Trompler, E., Bemmerer, D., Beyer, R., Broggini, C., Caciolli, A., Erhard, M., Fülöp, Z., Grosse, E., Gyürky, G., et al. (2010). Resonance strengths in the N 14 (p, γ) O 15 and N 15 (p, α γ) C 12 reactions. *Physical Review C*, 81(5):055807.

[50] Maxim, V., Lojacono, X., Hilaire, E., Krimmer, J., Testa, E., Dauvergne, D., Magnin, I., and Prost, R. (2016). Probabilistic models and numerical calculation of system matrix and sensitivity in list-mode MLEM 3D reconstruction of Compton camera images. *Physics in medicine and biology*, 61(1):243.

[51] McCleskey, M., Kaye, W., Mackin, D. S., Beddar, S., He, Z., and Polf, J. (2015). Evaluation of a multistage CdZnTe Compton camera for prompt γ imaging for proton therapy. *Nuclear Instruments and Methods in Physics Research Section A: Accelerators, Spectrometers, Detectors and Associated Equipment*, 785:163–169.

[52] Meier, D., Mikkelsen, S., Talebi, J., Azman, S., Maehlum, G., and Patt, B. (2010). An ASIC for SiPM/MPPC readout. In *IEEE Nucl, Sci. Symp. Med. Imag. Conf*, volume 1653.

[53] Min, C.-H., Kim, C. H., Youn, M.-Y., and Kim, J.-W. (2006). Prompt gamma measurements for locating the dose falloff region in the proton therapy. *Applied Physics Letters*, 89.

[54] Min, C. H., Lee, H. R., Kim, C. H., and Lee, S. B. (2012). Development of array-type prompt gamma measurement system for in vivo range verification in proton therapy. *Medical physics*, 39(4):2100–2107.

[55] Mitin, T. and Zietman, A. L. (2014). Promise and pitfalls of heavy-particle therapy. *Journal of Clinical Oncology*, 32(26):2855.

[56] Muñoz, E., Barrio, J., Bemmerer, D., Etxebeste, A., Fiedler, F., Hueso-González, F., Lacasta, C., Oliver, J., Römer, K., Solaz, C., et al. (2018b). Tests of MACACO compton telescope with 4.44 MeV gamma rays. *Journal of Instrumentation*, 13(05):P05007.

[57] Muñoz, E., Barrio, J., Bernabéu, J., Etxebeste, A., Lacasta, C., Llosa, G., Ros, A., Roser, J., and Oliver, J. F. (2018). Study and comparison of different sensitivity models for a two-plane Compton camera. *Physics in Medicine and Biology*.

[58] Muñoz, E., Barrio, J., Etxebeste, A., García-Ortega, P., Lacasta, C., Oliver, J., Solaz, C., and Llosá, G. (2017). Performance evaluation of MACACO: a multilayer Compton camera. *Physics in medicine and biology*, 62(18):7321.

[59] Nakamura, Y., Shimazoe, K., Takahashi, H., Yoshimura, S., Seto, Y., Kato, S., Takahashi, M., and Momose, T. (2016). Development of a novel handheld intra-operative laparoscopic Compton camera for 18 F-Fluoro-2-deoxy-2-D-glucose-guided surgery. *Physics in Medicine and Biology*, 61(15):5837.

[60] Nuyts, J. and Bequé, D. (2006). Image formation. In *Diagnostic Nuclear Medicine*, pages 291–310. Springer Berlin Heidelberg.

[61] Ordonez, C. E., Bolozdynya, A., and Chang, W. (1997). Doppler broadening of energy spectra in Compton cameras. In *1997 IEEE Nuclear Science Symposium Conference Record*, volume 2, pages 1361–1365. IEEE.

[62] Parodi, K., Bortfeld, T., and Haberer, T. (2008). Comparison between in-beam and offline positron emission tomography imaging of proton and carbon ion therapeutic irradiation at synchrotron-and cyclotron-based facilities. *International Journal of Radiation Oncology* Biology* Physics*, 71(3):945–956.

[63] Parra, L. C. (2000). Reconstruction of cone-beam projections from Compton scattered data. *IEEE Transactions on Nuclear Science*, 47(4):1543–1550.

[64] Pinto, M., Dauvergne, D., Freud, N., Krimmer, J., Letang, J. M., Ray, C., Roellinghoff, F., and Testa, E. (2014). Design optimisation of a TOF-based collimated camera prototype for online hadrontherapy monitoring. *Physics in Medicine & Biology*, 59(24):7653.

[65] Polf, J. C., Avery, S., Mackin, D. S., and Beddar, S. (2015). Imaging of prompt gamma rays emitted during delivery of clinical proton beams with a compton camera: feasibility studies for range verification. *Physics in Medicine & Biology*, 60(18):7085.

[66] PTCOG (2019). Patient statistics and facilities under operation. particle therapy cooperative group. *http://www.ptcog.ch*.

[67] Quarati, F., Khodyuk, I., Van Eijk, C., Quarati, P., and Dorenbos, P. (2012). Study of 138La radioactive decays using LaBr3 scintillators. *Nuclear Instruments and Methods in Physics Research Section A: Accelerators, Spectrometers, Detectors and Associated Equipment*, 683:46–52.

[68] Querol, M., Rodríguez, J., Toledo, J., Esteve, R., Álvarez, V., and Herrero, V. (2016). A programmable, multichannel power supply for SiPMs with temperature compensation loop and Ethernet interface. *Journal of Instrumentation*, 11(12):C12035.

[69] Ramilli, M. (2008). Characterization of SiPM: temperature dependencies. In *2008 IEEE Nuclear Science Symposium Conference Record*, pages 2467–2470. IEEE.

[70] Reinhardt, T. P., Akhmadaliev, S., Bemmerer, D., Stöckel, K., and Wagner, L. (2016). Absolute hydrogen depth profiling using the resonant 1H (15n, $\alpha\gamma$) 12C nuclear reaction. *Nuclear Instruments and Methods in Physics Research Section B: Beam Interactions with Materials and Atoms*, 381:58–66.

[71] Richard, M.-H., Dahoumane, M., Dauvergne, D., De Rydt, M., Dedes, G., Freud, N., Krimmer, J., Létang, J., Lojacono, X., Maxim, V., et al. (2012). Design study of the absorber detector of a compton camera for on-line control in ion beam therapy. *IEEE Transactions on nuclear science*, 59(5):1850–1855.

[72] Roellinghoff, F., Richard, M.-H., Chevallier, M., Constanzo, J., Dauvergne, D., Freud, N., Henriquet, P., Foulher, F. L., Létang, J., Montarou, G., Ray, C., Testa, E., Testa, M., and Walenta, A. (2011). Design of a Compton camera for 3D prompt-γ imaging during ion beam therapy. *Nuclear Instruments and Methods in Physics Research Section A: Accelerators, Spectrometers, Detectors and Associated Equipment*, 648, Supplement 1:S20 – S23. NIMA 4th International Conference on Imaging techniques in Subatomic Physics, Astrophysics, Medicine, Biology and Industry.

[73] Rogers, W., Clinthorne, N., Stamos, J., Koral, K., Mayans, R., Keyes, J., Williams, J., Snapp, W., and Knoll, G. (1982). SPRINT: A stationary detector single photon ring tomograph for brain imaging. *IEEE transactions on medical imaging*, 1(1):63–68.

[74] SaintGobain (2019). Saint-gobain crystals. *https://www.crystals.saint-gobain.com/*.

[75] Schardt, D., Elsässer, T., and Schulz-Ertner, D. (2010). Heavy-ion tumor therapy: Physical and radiobiological benefits. *Reviews of modern physics*, 82(1):383.

[76] Schoene, S., Enghardt, W., Fiedler, F., Golnik, C., Pausch, G., Rohling, H., and Kormoll, T. (2016). An image reconstruction framework and camera prototype aimed for Compton imaging for in-vivo dosimetry of therapeutic ion beams. *IEEE Transactions on Nuclear Science*, 1(99):1.

[77] Schönfelder, V., Diehl, R., Lichti, G. G., Steinle, H., Swanenburg., B. N., Deerenberg, A. J. M., Aarts, H., Lockwood, J., Webber, W., Macri., J., Ryan, J., Simpson, G., Taylor, B. G., Bennett, K., and Snelling, M. (1984). The imaging compton telescope comptel on the gamma ray observatory. *IEEE Trans. Nucl, Sci.*, 31:766–770.

[78] Schönfelder, V., Hirner, A., and Schneider, K. (1973). A telescope for soft gamma ray astronomy. *Nuclear Instruments and Methods*, 107:385–394.

[79] Schulz, R. J., Smith, A. R., and Orton, C. G. (2007). Proton therapy is too expensive for the minimal potential improvements in outcome claimed. *Medical physics*, 34(4):1135–1138.

[80] Seo, K. S., Kim, C. H., and Kim, J. W. (2006). Comparison of titanium hydride (tih˜ 2) and paraffin as neutron moderator material in a prompt gamma scanning system. *JOURNAL-KOREAN PHYSICAL SOCIETY*, 48(4):855.

[81] Sharma, S., Zhou, O., Thompson, R., Gabriel, P., Chalian, A., Rassekh, C., Weinstein, G. S., O'Malley Jr, B. W., Aggarwal, C., Bauml, J., et al. (2018). Quality of life of postoperative photon versus proton radiation therapy for oropharynx cancer. *International Journal of Particle Therapy*, 5(2):11–17.

[82] Shepp, L. A. and Logan, B. F. (1974). The fourier reconstruction of a head section. *IEEE Transactions on nuclear science*, 21(3):21–43.

[83] Shepp, L. A. and Vardi, Y. (1982). Maximum likelihood reconstruction for emission tomography. *IEEE transactions on medical imaging*, 1(2):113–122.

[84] Siddon, R. L. (1985). Fast calculation of the exact radiological path for a three-dimensional ct array. *Medical physics*, 12(2):252–255.

[85] Sinclair, L., Hanna, D. S., MacLeod, A. M. L., and Saull, P. R. B. (2009). Simulations of a scintillator Compton gamma imager for safety and security. *IEEE Transactions on Nuclear Science*, 56(3):1262–1268.

[86] Singh, M. (1983). An electronically collimated gamma camera for single photon emission computed tomography. part i: Theoretical considerations and design criteria. *Medical Physics*, 10:421–427.

[87] Singh, M. and Doria, D. (1983). An electronically collimated gamma camera for single photon emission computed tomography. part 2: mage reconstruction and preliminary experimental measurements. *Medical Physics*, 10:428–435.

[88] Sitek, A. (2008). Representation of photon limited data in emission tomography using origin ensembles. *Physics in Medicine & Biology*, 53(12):3201.

[89] Smeets, J., Roellinghoff, F., Prieels, D., Stichelbaut, F., Benilov, A., Busca, P., Fiorini, C., Peloso, R., Basilavecchia, M., Frizzi, T., Dehaes, J. C., and Dubus, A. (2012). Prompt gamma imaging with a slit camera for real-time range control in proton therapy. *Physics in Medicine and Biology*, 57(11):3371.

[90] Solaz, C., Barrio, J., Llosá, G., Stankova, V., Trovato, M., and Lacasta, C. (2013). Data acquisition system for the readout of SiPM arrays. In *2013 IEEE Nuclear Science Symposium and Medical Imaging Conference (2013 NSS/MIC)*, pages 1–4. IEEE.

[91] Solevi, P., Muñoz, E., Solaz, C., Trovato, M., Dendooven, P., Gillam, J. E., Lacasta, C., Oliver, J. F., Rafecas, M., Torres-Espallardo, I., and Llosá, G. (2016). Performance of MACACO Compton telescope for ion-beam therapy monitoring: first test with proton beams. *Physics in Medicine and Biology*, 61(14):5149.

[92] Stankova, V., Barrio, J., Gillam, J. E., Lacasta, C., Rafecas, M., Solaz, C., Trovato, M., and Llosá, G. (2012). Multichannel daq system for sipm matrices. In *2012 IEEE Nuclear Science Symposium and Medical Imaging Conference Record (NSS/MIC)*, pages 1069–1071. IEEE.

[93] Studenski, M. T. and Xiao, Y. (2010). Proton therapy dosimetry using positron emission tomography. *World journal of radiology*, 2(4):135.

[94] Takahashi, T., Takeda, S., Watanabe, S., and Tajima, H. (2012). Visualization of radioactive substances with a Si/CdTe Compton camera. In *Nuclear Science Symposium and Medical Imaging Conference (NSS/MIC), 2012 IEEE*, pages 4199–4204. IEEE.

[95] Tavernier, S. (2010). *Experimental techniques in nuclear and particle physics*. Springer Science & Business Media.

[96] Taya, T., Kataoka, J., Kishimoto, A., Iwamoto, Y., Koide, A., Nishio, T., Kabuki, S., and Inaniwa, T. (2016). First demonstration of real-time gamma imaging by using a handheld Compton camera for particle therapy. *Nuclear Instruments and Methods in Physics Research Section A: Accelerators, Spectrometers, Detectors and Associated Equipment*, 831:355–361.

[97] Testa, E., Bajard, M., Chevallier, M., Dauvergne, D., Le Foulher, F., Freud, N., Poizat, J. C., Ray, C., and Testa, M. (2009). Dose profile monitoring with carbon ions by means of prompt-gamma measurements. *Nuclear Instruments and Methods in Physics Research Section B: Beam Interactions with Materials and Atoms*, 267:993–996.

[98] Thirolf, P., Aldawood, S., Böhmer, M., Bortfeldt, J., Castelhano, I., Dedes, G., Fiedler, F., Gernhäuser, R., Golnik, C., Helmbrecht, S., et al. (2016). A Compton camera prototype for prompt gamma medical imaging. In *EPJ Web of Conferences*, volume 117, page 05005. Nuclear Structure.

[99] Todd, R., Nightingale, J., and Everett, D. (1974). A proposed γ camera. *Nature*, 251(5471):132.

[100] Tumer, O., Akyuz, A., Bhattacharya, D., Blair, S., Case, G., Dixon, D., Liu, C.-J., O'Neill, T., Samimi, J., White, R., et al. (1995). The TIGRE instrument for 0.3-100 MeV γ-ray astronomy. *IEEE transactions on nuclear science*, 42(4):907–916.

[101] Verburg, J. M. and Seco, J. (2014). Proton range verification through prompt gamma-ray spectroscopy. *Physics in Medicine & Biology*, 59(23):7089.

[102] Wilderman, S. J., Clinthorne, N. H., Fessler, J. A., and Les Rogers, W. (1998). List-Mode Maximum Likelihood Reconstruction of Compton scatter camera images in nuclear medicine. *Conference Record of the IEEE Nuclear Science Symposium and Medical Imaging Conference*, 3:8–14.

[103] Wilderman, S. J., Fessler, J. A., Clinthorne, N. H., LeBlanc, J., and Rogers, W. L. (2001). Improved modeling of system response in list mode EM reconstruction of Compton scatter camera images. *IEEE Transactions on Nuclear Science*, 48(1):111–116.

[104] Wilson, R. R. (1946). Radiological use of fast protons. *Radiology*, 47(5):487–491.

[105] Winkler, C., Bennett, K., Bloemen, J., Collmar, W., Connors, A., Diehl, R., Dordrecht, A. v., den Herder, J., Hermsen, W., Kippen, M., et al. (1992). The gamma-ray burst of 3 May 1991 observed by COMPTEL on board GRO. *Astronomy and Astrophysics*, 255:L9.

[106] Xu, D. and He, Z. (2007). Gamma-ray energy-imaging integrated spectral deconvolution. *Nuclear Instruments and Methods in Physics Research Section A: Accelerators, Spectrometers, Detectors and Associated Equipment*, 574(1):98–109.

[107] Zhu, X. and El Fakhri, G. (2013). Proton therapy verification with PET imaging. *Theranostics*, 3(10):731.